



Loupy, Gaëtan J.M. (2018) High fidelity, multi-disciplinary analysis of flow in realistic weapon bays. PhD thesis.

<https://theses.gla.ac.uk/9091/>

Copyright and moral rights for this work are retained by the author

A copy can be downloaded for personal non-commercial research or study, without prior permission or charge

This work cannot be reproduced or quoted extensively from without first obtaining permission in writing from the author

The content must not be changed in any way or sold commercially in any format or medium without the formal permission of the author

When referring to this work, full bibliographic details including the author, title, awarding institution and date of the thesis must be given

Enlighten: Theses

<https://theses.gla.ac.uk/>  
[research-enlighten@glasgow.ac.uk](mailto:research-enlighten@glasgow.ac.uk)



University  
of Glasgow

# **High Fidelity, Multi-Disciplinary Analysis of Flow in Realistic Weapon Bays**

by

**Gaëtan J.M. Loupy (MEng.)**

Thesis submitted in accordance with the  
requirements of the University of Glasgow for  
the degree of Doctor in Philosophy by  
Gaëtan J.M. Loupy  
December 2017

© 2017  
Gaëtan J.M. Loupy

# Abstract

To improve the stealthiness, and the efficiency of military aircraft, engineers moved carried weapons from external hand points, to weapons bays. However, the flow inside bays is turbulent, and characterised by strong broadband, and tonal noise. The open bay flow leads to variability in the released store trajectory, excites the missile, and bay structures, and reduces the aircraft stealthiness. This thesis aims to improve our understanding of real weapon bay flow, and suggests a method for quantifying the store trajectory variability.

The main spatio-temporal characteristics of cavity flows are described using post-processing methods, like, SPL, OASPL, and wavelet transform. Also, the code HMB3 is validated for simulation of cavity flows, comparing Scale Adaptive (SAS) results with experiments. To further improve the understanding of the physics driving this flow, a simple model is presented, and compared to experiments. The results are promising, and the model is able to reproduce the cavity flow fluctuations both in space and time.

To support measurements of the noise field around a cavity flow, beamforming is applied to the CFD results. This method was able of capturing the main sources of noise around the cavity, using a microphone array, and the mean flow to simulate the propagation of acoustic waves. Also, recommendations for future use of this technique are given.

Developments were carried out for this thesis, and for the first time, a CFD code is reported to simulate the complete weapon bay operation, including door operation, store release, and store aeroelasticity. The different parts of the code are strongly coupled, and work together. Thanks to new capabilities of HMB3, this thesis shows more insight on the physics behind realistic weapon bay operation. The flow establishment during door opening is described, and appears to be important for store design, only if the doors are moving very fast. Store releases are simulated, and statistical analysis of the data is performed. A statistical metric was proposed to identify the minimum number of simulations necessary for capturing the mean and standard deviation of the trajectories. Using averaged, and filtered flow data, the trajectory phases were identified and the role of the pressure field inside the cavity was clarified. In addition, the aeroelasticity of the store was computed during carriage, door opening, and release phases, showing small deformations that may lead to structural fatigue. Thanks to the efficiency of the SAS method, a large number of simulations were performed, and more than 1800 cavity travel times were simulated.

Simulation of the flow around a store in a supersonic flow, and at high attitude is described in an appendix of the thesis. Like a cavity, this flow has complex features that require advanced turbulence modelling to be simulated.

In addition, novel cavity flow controls are investigated, and described in a restricted appendix of the thesis.

# Declaration

I hereby declare that this dissertation is a record of work carried out in the School of Engineering at the University of Liverpool during the period from November 2014 to August 2015, and at the University of Glasgow during the period from September 2015 to December 2017. The dissertation is original in content except where otherwise indicated.

December 2017

.....

(Gaëtan Loupy)

In the loving memory of my father, Jean-Marie Claude,  
who passed me on his love of the Sciences.

# Acknowledgements

I would like to deeply thank my supervisor, Professor George Barakos, for his invaluable support, and knowledge, that guided, and motivated me along this long, and passionate journey. I am also thankful to Dr. Massimo Biava, and Dr. Mark Woodgate, for their expertise, that helped me through my work adding features to HMB, and their answers to all my questions.

I was very pleased to be supported by MBDA UK Ltd., that was very supportive towards my work. I am grateful to Nigel Taylor, for his enthusiasm, and deep interest to the outcomes of this thesis, through numerous meetings at Liverpool, Glasgow, and Bristol. I extend my gratitude to David Pike, and Melanie Peiris of MBDA UK Ltd. for their help providing the structural models. The use of the EPSRC funded ARCHIE-WeSt High Performance Computer (EPSRC grant no. EP/K000586/1) is also gratefully acknowledged.

In addition, I would like to thank all the members of the CFD lab that contributed to a family, and stimulating work environment. The time spend with Antonio, Guilia, Clément, Massimo, Marina, and others from Liverpool, and Glasgow University was a great value.

Most importantly, I gratefully acknowledge the support of my family, including Christine, and Jean-Marie, who supported me in every hard situations, and Solange, and Jacques, who took care of me like their son. I thank Lucas, who was always present with love, and support, during this long journey.

# Publications

## Book Chapters

- Loupy, G. and Barakos, G., *Multi-Disciplinary Analysis of Flow in Weapon Bays, Progress in Hybrid RANS-LES Modelling: Papers Contributed to the 6th Symposium on Hybrid RANS-LES Methods, 26-28 September 2016, Strasbourg, France*, edited by Y. Hoareau, S.-H. Peng, D. Schwamborn, and A. Revell, Springer International Publishing, 2018.

## Journal Papers

- Babu, S., Loupy, G., Dehaeze, F., Barakos, G., and Taylor, N., “Aeroelastic simulations of stores in weapon bays using Detached-Eddy Simulation,” *Journal of Fluids and Structures*, Vol. 66, October 2016, pp. 207-228, doi:10.2514/6.2017-3252.
- Loupy, G. and Barakos, G., “Processing and Analysis Methods for Transonic Cavity Flow,” *Physics of Fluids*, Vol. 29, No. 7, July 2017, doi:10.1063/1.4995461.
- Loupy, G., Barakos, G., and Taylor, N., “Cavity Flow Over a Transonic Weapon Bay During Door Operation,” *Journal of Aircraft*, August 2017, doi:10.2514/1.C034344
- Loupy, G. and Barakos, G., “Acoustic Field Around a Transonic Cavity Flow,” *International Journal of AeroAcoustics*, Vol. 16, No. 6, September 2017, doi:10.1177/1475472X17730459.
- Loupy, G., Barakos, G., and Taylor, N., “Assessment of Store Release Variability from Weapon Bay using Scale Adaptive Simulation,” *AIAA Journal*, November 2017, doi:10.2514/1.J056485.
- Loupy, G., Barakos, G., and Taylor, N., “Multi-Disciplinary Simulations of Stores in Weapon Bays using Scale Adaptive Simulation,” *Journal of Fluids and Structures*, 2017, Submitted.

## Papers in Conference Proceedings

- Loupy, G. and Barakos, G., “Cavity Flow Over a Transonic Weapon Bay During Door Operation,” *Proceedings of the RAS Applied Aerodynamics Conference*, Bristol, UK, 19-21 July 2016.
- Loupy, G. and Barakos, G., “Acoustic Field Around a Transonic Cavity Flow,” *Proceedings of the Fourth International Workshop Computational Experiment in Aeroacoustics*, Svetlogorsk, Russia, 21-24 September 2016.

- Loupy, G. and Barakos, G., “Multi-Disciplinary Analysis of Flow in Weapon Bays,” *Proceedings of the 6th Symposium on Hybrid RANS-LES Methods*, Strasbourg, France, 26-28 September 2016.
- Loupy, G. and Barakos, G., “Modelling of Transonic Shallow Cavity Flows and Store Release Simulations from Weapon Bays,” *Proceedings of the 35th AIAA Applied Aerodynamics Conference*, Paper No. AIAA 2017-3252, American Institute of Aeronautics and Astronautics Inc, 5-9 January 2017, doi:10.2514/6.2017-3252.
- Loupy, G. and Barakos, G., “Multi-Disciplinary Simulations of Stores in Weapon Bays using Scale Adaptive Simulations,” *Proceedings of the 36th AIAA Applied Aerodynamics Conference*, American Institute of Aeronautics and Astronautics Inc, 8-12 January 2018.
- Loupy, G. and Barakos, G., “Understanding of Transonic Cavity Flow,” 6th European Conference on Computational Mechanics, 11-15 June 2018, To be presented.

# Contents

<b>Abstract</b>	<b>i</b>
<b>Declaration</b>	<b>ii</b>
<b>Acknowledgements</b>	<b>iv</b>
<b>Publications</b>	<b>v</b>
<b>1 Introduction</b>	<b>1</b>
1.1 Background and Motivation . . . . .	1
1.1.1 Cavity Flow Physics - Fundamental Ideas . . . . .	5
1.1.2 Weapon Bay Doors Opening - Literature Findings . . . . .	9
1.1.3 Aeroelasticity of Store in Weapon Bays . . . . .	11
1.1.4 Store Releases from Weapon Bays . . . . .	14
Experimental Works . . . . .	14
Computational works . . . . .	20
1.1.5 Cavity Flow Control . . . . .	25
1.2 Thesis Objectives . . . . .	29
1.3 Thesis Outline . . . . .	29
<b>2 Mathematical Models and CFD Methods</b>	<b>33</b>
2.1 CFD Method . . . . .	33
2.2 Variable Extrapolation-MUSCL Approach . . . . .	34
2.3 Turbulence Modelling . . . . .	36
2.3.1 The Reynolds-Averaging . . . . .	36
2.3.2 RANS and URANS . . . . .	37
2.3.3 $k-\omega$ and Shear Stress Transport (SST) Model . . . . .	39
2.3.4 Scale-Adaptive Simulation (SAS) . . . . .	39
2.4 Overset Grid Method . . . . .	41
2.5 Methods of Data Analysis . . . . .	41
2.5.1 Pressure Signals . . . . .	41
2.5.2 Time Frequency Analysis - Morlet Wavelet Method . . . . .	42
2.5.3 Noise Directivity . . . . .	44
2.5.4 Solution Monitoring . . . . .	44

<b>3</b>	<b>Validation of the CFD Method</b>	<b>46</b>
3.1	Geometric and Computational Model . . . . .	46
3.2	Experimental Results . . . . .	48
3.3	Validation Results . . . . .	51
3.3.1	Averaged Flow . . . . .	51
3.3.2	Spatio-Temporal Validation . . . . .	55
<b>4</b>	<b>Beamforming Analysis for Transonic Cavity Flows</b>	<b>57</b>
4.1	Beamforming Method . . . . .	57
4.1.1	Noise Propagation Model . . . . .	60
4.1.2	Acoustic Arrays . . . . .	61
4.2	Results and Discussion . . . . .	64
<b>5</b>	<b>Modelling of the Cavity Flow Resonance</b>	<b>71</b>
<b>6</b>	<b>Geometry and Conditions</b>	<b>81</b>
6.1	Geometry . . . . .	81
6.2	Frames of Reference . . . . .	85
<b>7</b>	<b>Coupled Aeroelastic Computation of Store in Weapon Bays</b>	<b>86</b>
7.1	Fluid-Structure Interaction Modelling . . . . .	86
7.1.1	Structural Modes . . . . .	86
7.1.2	CFD/CSD Interpolation . . . . .	89
7.1.3	Computation of the Modal Loads and Amplitudes . . . . .	91
7.1.4	Deformation of the Surface Mesh . . . . .	93
7.1.5	Volume Mesh Deformation . . . . .	95
7.2	Results and Discussion . . . . .	96
7.3	Chapter Summary . . . . .	101
<b>8</b>	<b>Simulations of Weapon Bay Doors Opening</b>	<b>103</b>
8.1	Computations of Static Doors . . . . .	104
8.2	Computations for Dynamic Door Opening . . . . .	106
8.3	Noise Field for Dynamic and Static Door Cases . . . . .	110
8.4	Computations with Store at Carriage . . . . .	117
8.5	Chapter Summary . . . . .	121
<b>9</b>	<b>Computation of Store Release from Weapon Bays</b>	<b>122</b>
9.1	6DoF Method . . . . .	122
9.2	Validation of the 6DoF Method . . . . .	124
9.2.1	External Store Release . . . . .	124
	Model Geometry and Release Conditions . . . . .	124
	Decoupled Analysis . . . . .	124
	Store Loads and Trajectory . . . . .	126
9.2.2	Internal Store Release . . . . .	128
9.3	Computational Model for Store Release . . . . .	132
9.4	Results and Discussion . . . . .	134
9.4.1	Statistical Analysis of the Trajectories . . . . .	134

9.4.2	Mean Flow . . . . .	137
9.4.3	Filtered Loads . . . . .	140
9.4.4	Releases with Aeroelasticity . . . . .	142
	Store Release Process . . . . .	143
	Results and Discussion . . . . .	144
9.4.5	Aeroelastic Store Releases with Static Doors . . . . .	148
9.4.6	Influence of the Store Properties on the Release Trajectory . . . . .	155
9.5	Chapter Summary . . . . .	164
<b>10</b>	<b>Conclusions</b>	<b>166</b>
10.1	Conclusions from Current Work . . . . .	166
10.2	Future Work . . . . .	168
<b>A</b>	<b>Flowfield Around an Isolated Store at High Pitch Angle</b>	<b>170</b>
A.1	Geometry and Conditions . . . . .	170
A.2	Computational Mesh . . . . .	170
A.3	Flowfield Visualisation and Flow Physics . . . . .	176
A.4	Mesh Convergence . . . . .	184
A.5	Summary of Work . . . . .	191
<b>B</b>	<b>Proper Orthogonal Decomposition for Engineering Applications</b>	<b>193</b>
B.1	POD Principle . . . . .	193
B.2	Modified POD Process . . . . .	195
B.3	Creation of the MATLAB Input Files . . . . .	197
	B.3.1 Process of MATLAB File Generation . . . . .	197
B.4	Running a Reconstruction with MATLAB . . . . .	198
	B.4.1 GUI Execution . . . . .	198
	B.4.2 Batch Execution . . . . .	199
	B.4.3 Output . . . . .	200
	B.4.4 Interpolation parameters . . . . .	200
B.5	Test Case : Clean Cavity Without Doors . . . . .	202
	B.5.1 Reconstruction grids . . . . .	202
	B.5.2 Reconstruction . . . . .	205
<b>C</b>	<b>Post-processing Codes</b>	<b>216</b>
C.1	Beamforming . . . . .	216
C.2	Cavity Flow Model . . . . .	233
	<b>References</b>	<b>239</b>

# List of Figures

1.1	Store release from the F-35 . . . . .	1
1.2	Examples of weapon bays . . . . .	2
1.3	Examples of weapon bays . . . . .	3
1.4	Examples of unsafe store trajectory <sup>[16]</sup> . . . . .	4
1.5	Open and closed cavity flow configurations at subsonic speeds <sup>[19]</sup> . . .	5
1.6	Experimental SPL at the aft wall of an ideal cavity <sup>[14]</sup> . . . . .	6
1.7	Joint time-frequency analysis of the pressure at front wall <sup>[29]</sup> . . . . .	7
1.8	Schlieren image of cavity shear layer <sup>[29]</sup> . . . . .	8
1.9	Geometry used to study fully and half open complex weapon bays. . .	10
1.10	RMS pressure along cavity ceiling for dynamically moving doors <sup>[33]</sup> .	10
1.11	cavity with model store installed in wind tunnel <sup>[39]</sup> . . . . .	11
1.12	In flight setup used by Probst <i>et al.</i> <sup>[39]</sup> . . . . .	12
1.13	Flight test geometry <sup>[46]</sup> of B-1B store release . . . . .	15
1.14	Flight test results <sup>[46]</sup> for B-1B store release . . . . .	16
1.15	CTS experiments <sup>[50]</sup> . . . . .	17
1.16	Instantaneous schlieren image of GBU-38 at carriage <sup>[52]</sup> . . . . .	18
1.17	Vertical and roll angle variability <sup>[16]</sup> . . . . .	21
1.18	Comparison of GBU-12 trajectory between CFD and wind tunnel <sup>[60]</sup>	22
1.19	Trajectory variability with and without blowing at front wall <sup>[62]</sup> . . .	23
1.20	Classification of flow control types <sup>[68]</sup> . . . . .	26
1.21	Spoiler tested by Saddington <i>et al.</i> <sup>[78]</sup> . . . . .	27
1.22	Summary of the computations performed to simulate the weapon bay operation. . . . .	32
2.1	Computation of the wavelet envelope $ \overline{W_{\Psi}^y} $ . . . . .	43
2.2	Convolution of an input vector field (a) with noise field (b) to produce an LIC image (c) <sup>[129]</sup> . . . . .	45
3.1	Schematic view of the M219 cavity with doors. . . . .	46
3.2	Boundary conditions and blocking at the mid-span of the computa- tional domain. . . . .	47
3.3	M219 with door SPL and OASPL for three experimental signals. . . .	48
3.4	SPL and OASPL at the ceiling mid-span and at different time with envelope. . . . .	49
3.5	Time-frequency plots for the ceiling mid-span using experimental data <sup>[32]</sup> . . . . .	50
3.6	M219 with door SPL at ceiling mid-span for CFD and experiments. . .	52

3.7	OASPL, and mean $C_p$ along the M219 with doors ceiling mid-span. . . . .	52
3.8	Noise along the no doors M219 cavity ceiling mid-span computed with a medium mesh. . . . .	53
3.9	Time averaged stream-wise velocity at the mid-span of the cavity along vertical lines. . . . .	54
3.10	BIW at the cavity ceiling centre-line for modes 1 and 2. . . . .	54
3.11	BIW amplitude at the cavity ceiling centre-line for modes 1 and 2. . . . .	55
3.12	Mode modulation SPL for modes 1 and 2. . . . .	56
4.1	Beamforming principle with a planar wave propagation. . . . .	58
4.2	In phase and of of phase superposition of the signals with time delay. . . . .	59
4.3	Main and side lobes obtained with beamforming around two speakers. . . . .	60
4.4	Validation of the beamforming analysis. . . . .	62
4.5	Schematic view of the microphone arrays. . . . .	62
4.6	Reconstruction of three noise sources at shear layer. . . . .	63
4.7	BISPL at the mid-span of the cavity over a large frequency band (a), and centred on the two first cavity modes in windows of 10Hz (b)-(c). . . . .	64
4.8	Noise source reconstruction at the mid-span of the cavity over a large frequency band between 10 and 1300Hz for different noise propagation model. Multi-spiral array with 31 microphones, placed at $Z/L=1.5$ . . . . .	65
4.9	Comparison between OASPL and BIW along lines. Multi-spiral array with 31 microphones, placed at $Z/L=1.5$ . . . . .	66
4.10	Noise source reconstruction at the mid-span of the cavity over a large frequency band between 10 and 1300Hz for different multi-spiral array positions. Multi-spiral array with 31 microphones. . . . .	67
4.11	Noise source reconstruction at the mid-span of the cavity over a large frequency band between 10 and 1300Hz for different array shapes. Array of 31 microphones placed at $Z/D=1.5$ . . . . .	67
4.12	Noise source reconstruction at the mid-span of the cavity over a large frequency band between 10 and 1300Hz for different array density. Multi-spiral array placed at $Z/L=1.5$ . . . . .	68
4.13	Noise field at the mid-span of the M219 cavity without doors over a large frequency band between 10 and 1300Hz. Multi-spiral array of 31 microphones placed at $Z/D=1.5$ . . . . .	69
5.1	(a) Standing waves schematic, (b) Reflections and resulting pressures in cavity. . . . .	71
5.2	Absolute pressure wave speed $c^n$ along the cavity length. . . . .	74
5.3	SPL at the aft wall of the M219 cavity. $L=0.51m$ . . . . .	75
5.4	SPL at aft wall of the cavity for different input signals. . . . .	76
5.5	Scalogram at 95% of the cavity length. High frequency input applied to the unsteady resonator. . . . .	77
5.6	BIW at ceiling mid-span for experimental and unsteady resonator. . . . .	78
5.7	BIW envelope at ceiling mid-span for experimental and unsteady resonator. . . . .	78

5.8	Tonal amplitude modulation at $X/L=0.95$ . . . . .	79
6.1	Schematic view of the vented cavity with store. . . . .	82
6.2	Geometry, cavity axes, and the store at carriage position. . . . .	83
6.3	Fin geometry. . . . .	83
7.1	Structural modes 1 to 4 of the free root fin . . . . .	88
7.2	Ejector Release Unit (ERU) position and structural modelling . . . . .	89
7.3	Structural modes 1 to 6 of the body at carriage . . . . .	90
7.4	Structural modes 1 to 6 of the body in free air . . . . .	90
7.5	Body and fins structure of the store. Grid points represented by spheres. . . . .	91
7.6	Aeroelastic coupling strategy. . . . .	92
7.7	2D example of surface mesh deformation with body and fin. . . . .	94
7.8	Selection of the points to interpolate from to compute the IDW weights. . . . .	96
7.9	SPL along the cavity ceiling mid-span with aeroelastic store. . . . .	97
7.10	Deformations of the body at carriage and shear layer. . . . .	97
7.11	Spectrum of body modal forces, and tail acceleration. $M_i$ are cavity modes. $Y_l$ and $Z_i$ are respectively vertical and span-wise body structural modes. . . . .	99
7.12	Deformations in the fin root reference frame, for the TE tip of the fins. . . . .	100
7.13	Spectra of fin 4 acceleration with and without body aeroelastics. . . . .	102
7.14	Spectra of fin modal forces, and acceleration at the trailing edge tip of the fin. $M_i$ are cavity modes. $F_i$ are fin structural modes. . . . .	102
8.1	Time averaged Mach Number at $X/L=0.85$ for the LD7 cavity. . . . .	104
8.2	OASPL along the cavity ceiling mid-span. . . . .	105
8.3	Time averaged $U_{RMS}$ at the middle section of the doors. . . . .	106
8.4	Shear layer momentum of the time averaged flow on the cavity mid-span. . . . .	106
8.5	Mach Number and LICs between 5 and 90 degrees for dynamic and static cases. Plane at cavity mid-span . . . . .	107
8.6	Force on the front and aft walls for static and dynamic doors. . . . .	108
8.7	Shear layer momentum thickness $\theta(x,y)$ integrated over the cavity opening. Fixed doors results are used for the static envelope. . . . .	109
8.8	Loads on doors and cavity ceiling for dynamic and static cases. . . . .	110
8.9	OASPL field during the doors opening between 5 and 110 degrees. . . . .	111
8.10	Averaged OASPL lines at the mid-span for fast, medium, slow, and static doors cases. . . . .	112
8.11	Pressure BIW envelope along the ceiling mid-span for dynamic opening and mode 1 to 3. . . . .	113
8.12	SPL at $X/L=0.95$ of the ceiling mid-span for different door speed. . . . .	114
8.13	3D Noise directivity for different fixed door angle. Iso-surface at 2 cavity depths from the shear layer. . . . .	115
8.14	Noise propagation from the main sources of noise taking into account the flowfield with doors at 110 degrees. Five sources are shown at positions A,B,C,D,E. . . . .	116
8.15	Noise directivity for different door angle and door velocity. . . . .	116
8.16	Mach number and LIC at mid-span during door opening. . . . .	118

8.17	Force on the cavity walls during medium speed door opening. . . . .	119
8.18	Force on the store during medium speed door opening. . . . .	119
8.19	Deformation of the store during medium speed door opening. . . . .	120
9.1	Wing store configuration and ejector position. . . . .	124
9.2	Comparison of trajectories from a decoupled approach and wind tunnel data <sup>[154]</sup> . WT : Wind tunnel. NUM : Decoupled simulation. . . . .	125
9.3	Store trajectory released from the wing at different time instances. . .	126
9.4	Trajectories comparison between HMB3 and wind tunnel data <sup>[154]</sup> . WT: Wind tunnel. . . . .	127
9.5	Geometry, cavity axis, and store at carriage position. . . . .	129
9.6	Store position during release simulation using HMB3. . . . .	130
9.7	Sequence of separating store CFD 2400 computed with the coupled 6DoF and HMB3. . . . .	130
9.8	Sequence of separating store computed with HMB3 . . . . .	131
9.9	Trajectory of full and half stroke cases. Vertical dashed bars denote $W_e$ . . . . .	133
9.10	Convergence of the averaged trajectory. . . . .	135
9.11	Number of converged release permutations as function of the number of releases used for the statistics. . . . .	136
9.12	Force and moment coefficients during full and half stroke releases. Vertical dashed bars denote $W_e$ . . . . .	136
9.13	Averaged and standard deviation of translations and rotations with half and full stroke releases. . . . .	138
9.14	Averaged store loads, and pressure coefficient at cavity mid-span. . . .	139
9.15	Flow momentum at the cavity mid-span. . . . .	140
9.16	Decomposition of the HS2600 store forces in pressure and viscous components. . . . .	141
9.17	Original and filtered pitch for the case HS2600. . . . .	141
9.18	MFRT for the different releases and force/moment coefficients. The horizontal lines represent the cavity tones 1, 2 and 3. . . . .	141
9.19	Filtered force and moment during full and half stroke releases. . . . .	143
9.20	Tail displacement due to the carriage, and the free flight structural modes during store release HS10000. . . . .	144
9.21	Converged release permutations number in function of the number of releases. . . . .	145
9.22	Average and standard deviation of store trajectory during release. . . .	145
9.23	Average and standard deviation of store deformations during release. Fins deformations are shown at the tip of the fin trailing edge. . . . .	147
9.24	Number of converged release permutations in function of the number of releases in the statistics. (5% criterium, store aeroelasticity and doors included) . . . . .	149
9.25	Average and standard deviation of store trajectory during aeroelastic releases with and without doors. . . . .	149
9.26	$C_p$ field at the mid-span of the cavity during releases with and without doors averaged from all available releases. . . . .	151

9.27	Average and standard deviation of store deformations during release with and without doors. Fins deformations are shown at the tip of the fin trailing edge. . . . .	152
9.28	OASPL field at $X/L=0.85$ during releases with and without doors averaged using all available releases. . . . .	153
9.29	Snapshots of the weapon bay operation computed using HMB. $C_p$ field over the surfaces. . . . .	154
9.30	Store displacements for different store configurations. . . . .	156
9.31	Store attitude for different store configurations. . . . .	157
9.32	Pressure coefficients on the store for different store configurations. . . . .	158
9.33	Loads on the isolated store in free-stream at Mach 0.85. . . . .	160
9.34	Store trajectory during releases C4 and C5 in function of time. . . . .	160
9.35	Store forces during releases C4 and C5 in function of time. . . . .	161
9.36	Instantaneous Mach number and $C_p$ on the store during the release C5. . . . .	162
9.37	Instantaneous Mach number and $C_p$ on the store during the release C5. . . . .	163
9.38	Froude number during releases C4 and C5. . . . .	164
A.1	Store geometry. . . . .	171
A.2	Grid slice at the fins. . . . .	172
A.2	Grid slice at the fins. . . . .	173
A.3	Grid slice at the fins. . . . .	174
A.3	Grid slice at the fins. . . . .	175
A.3	Grid slice at the fins. . . . .	176
A.4	Total pressure along the store length using $k-\omega$ -SST (Left) and $k-\omega$ -SST $P_k$ Limiter (Right). Results on very fine grid. . . . .	177
A.4	Total pressure along the store length using $k-\omega$ -SST (Left) and $k-\omega$ -SST $P_k$ Limiter (Right). Results on very fine grid. . . . .	178
A.4	Total pressure along the store length using $k-\omega$ -SST (Left) and $k-\omega$ -SST $P_k$ Limiter (Right). Results on very fine grid. . . . .	179
A.5	Total pressure along the store length using EARSM (Left) and SAS (Right). Results on very fine grid. . . . .	180
A.5	Total pressure along the store length using EARSM (Left) and SAS (Right). Results on very fine grid. . . . .	181
A.5	Total pressure along the store length using EARSM (Left) and SAS (Right). Results on very fine grid. . . . .	182
A.6	Load polar for pitch between 0 and 15 degrees on the coarse grid. Results obtained using steady state CFD and RANS equations. . . . .	183
A.7	Total pressure at $X/L_s = 0.85$ for different grid densities, and for the EARSM turbulence model. . . . .	185
A.7	Total pressure at $X/L_s = 0.95$ for different grid densities, and for the EARSM turbulence model . . . . .	186
A.8	Total pressure at $X/L_s = 0.85$ for different grid densities, and for the SAS turbulence model. . . . .	187
A.8	Total pressure at $X/L_s = 0.95$ for different grid densities, and for the SAS turbulence model. . . . .	188

A.9	Load on the store using EARSM (Dashed lines, square) , and SAS (Continuous lines, circle) turbulence models. . . . .	189
A.10	Load convergence using EARSM, and SAS turbulence models. . . . .	189
A.11	Load convergence using EARSM, and SAS turbulence models. . . . .	190
A.12	OASPL along the path of the main vortices, and at the wake. Result scaled for ISA sea level. SAS on very fine grid. . . . .	191
B.1	Cumulative energy contained in the POD modes. . . . .	194
B.2	Example of POD modes for a cavity flowfield. . . . .	195
B.3	POD generation and reconstruction processes. Go : gigaoctet, Mo : megaoctet. . . . .	196
B.4	POD Reconstruction GUI. . . . .	199
B.5	Influence of the smoothing parameter on the velocity interpolation at $y = 0, z = 0$ . Comparison with the POD_ORIGINAL reconstruction. . . . .	201
B.6	Reconstruction time with MLS in function of the smoothness parameter. . . . .	201
B.7	Geometry of a clean cavity without doors. . . . .	202
B.8	POD_COARSE distribution of points around the cavity region. . . . .	203
B.9	POD_MEDIUM distribution of points around the cavity region. . . . .	203
B.10	POD_FINE distribution of points around the cavity region. . . . .	203
B.11	POD_VERY_FINE distribution of points around the cavity region. . . . .	204
B.12	POD_ORIGINAL Reconstruction of Mach number at centerline . . . . .	204
B.13	Energy of the POD reconstruction, as a function of the number of modes. . . . .	204
B.14	Reconstructions POD_COARSE (Spheres) and POD_ORIGINAL (Background color) at the same CFD time of 80 with 151 modes. Reconstruction at the front, middle, and rear end of the cavity. . . . .	205
B.15	Reconstructions POD_COARSE (Spheres) and POD_ORIGINAL (Background color) at the same CFD time of 80 with 151 modes. Reconstruction at the cavity mid-span, port, and starboard side. . . . .	206
B.16	Minimum distance between points in the coarse, medium and fine grids on the plane facing the flow ( $X=\text{constant}$ ). . . . .	207
B.17	Temporal reconstructions of $u(t)$ at two probes at the mid-span of the shear layer using POD_COARSE (a-b), POD_MEDIUM (c-d) and POD_FINE (e-f). . . . .	210
B.18	Temporal reconstructions of $u(t)$ at two probes at the shear layer using POD_COARSE (a-b), POD_MEDIUM (c-d) and POD_FINE (e-f). . . . .	211
B.19	Spacial reconstructions of $u(x)$ at shear layer. . . . .	212
B.20	Spacial reconstructions of $v(x)$ at shear layer. . . . .	213
B.21	Spacial reconstructions of $w(x)$ at shear layer. . . . .	214
B.22	1D example of the effect of the point density of the Inverse Distance Weighting interpolation. . . . .	215
B.23	Position of the reconstruction axis in the POD_COARSE case. The closer value is alternating between $z=0.0$ and $z=0.037$ . . . . .	215

# List of Tables

1.1	Summary of works on door effects on cavity flows. . . . .	11
1.2	Summary of works about aeroelasticity on store in cavity. . . . .	14
1.3	Summary of experimental store release studies . . . . .	19
1.4	Summary of numerical store release studies . . . . .	25
1.5	Summary of passive flow control studies of cavity flows. . . . .	28
3.1	Details of the M219 computations. . . . .	47
3.2	Available signals for CFD comparison. . . . .	48
4.1	Details of the microphone arrays . . . . .	63
6.1	Simulated door opening speeds . . . . .	81
6.2	Mesh size for each solid . . . . .	84
7.1	Modal frequencies of the store. Rossiter’s modes are based on Mach of 0.85 and cavity length of 3.59m using equation 1.1 . . . . .	87
7.2	Computed aeroelastic cases . . . . .	97
8.1	Computed cases with doors . . . . .	103
8.2	Cavity mode frequency for dynamic and static doors in Hz. . . . .	114
9.1	Full-scale store and ejector characteristics <sup>[154]</sup> . . . . .	125
9.2	Full-scale store and ejector characteristics <sup>[50]</sup> . . . . .	129
9.3	List of computations carried out to validate internal store release. . . . .	129
9.4	List of computations carried out to demonstrate the trajectory variability. . . . .	132
9.5	List of carried elastic releases. . . . .	144
9.6	List of carried elastic releases with doors. . . . .	148
9.7	List of computations carried out to study the effect of store parameter on the trajectory. Parameters in red are changed compared to the baseline. . . . .	155
A.1	Grid density and simulated cases. Performed simulations are marked with X. . . . .	171
B.1	Time needed for the MATLAB POD reconstruction . . . . .	208

# Nomenclature

## Latin

$a$	Wavelet dilatation or scale (1/s)
$A_f$	Pressure wave amplitude (Pa)
$A_t$	Absorption coefficient (-)
$b$	Wavelet translation parameter (s)
$c$	Sound speed (m/s)
$c_j^{n-}, c_j^{n+}$	Upstream, and downstream wave speed at point j and time n (m/s)
$C_l, C_m, C_n$	Rolling, pitching and yawing moment coefficients (-)
$C_p$	Pressure coefficient (-)
$c_{travel}$	Averaged velocity along a trajectory (m/s)
$\mathbf{c}_w$	Wave velocity vector (m/s)
$C_x, C_y, C_z$	Axial, side and normal force coefficients (-)
$D$	Cavity depth (m)
$DI$	Directivity (dB)
$d_{mis}$	Store diameter (m)
$d_{off}$	Minimum distance between a trajectory, and a microphone (m)
$d_{ref}$	Reference length (m)
$d_{travel}$	Distance between a source and a microphone (m)
$e$	Specific internal energy (J)
$E$	Total Energy (J)
$e(\omega)$	Steering vector
$f$	Frequency (Hz)
$f_d$	Door opening frequency (Hz)
$f_i$	Body forces (m/s <sup>2</sup> )
$f_N$	Maximum pressure wave frequency (Hz)
$f_m$	Frequency of Rossiter mode $m$ (Hz)
$f_m^s$	Modal force on solid $s$ for the $m$ -th mode (N/m.kg)
$Fr$	Froude number (-)
$f_{tt}$	Cavity travel time frequency (Hz)
$\mathbf{F}, \mathbf{G}, \mathbf{H}$	Flux vector in x, y, x directions
$g$	Gravity acceleration (9.80m/s <sup>2</sup> )
$I$	Local noise intensity (W/m <sup>2</sup> )
$I_x, I_y, I_z$	Moment of inertia of the store (kg.m <sup>2</sup> )
$i, j, k$	Cell index (-)

$k$	Specific turbulent kinetic energy ( $m^2/s^2$ )
$k_t$	Thermal conductivity ( $W/mK$ )
$L$	Cavity length ( $m$ )
$L_{vK}$	von Karman length scale ( $m$ )
$L_s$	Store length ( $m$ )
$m$	Rossiter mode number (-)
$m_s$	Mass of the store ( $kg$ )
$M$	Number of sensors (-)
$M_\infty$	Free-stream Mach number (-)
$N_i$	Number of inner timesteps (-)
$n_s$	Number of CFD points on solid $s$ (-)
$n_{sp}$	Number of shared points (-)
$n_m^s$	Number of modes for solid $s$ (-)
$N_p$	Number of points along the cavity length (-)
$N_r$	Number of reflections (-)
$p$	Pressure (Pa)
<b>P</b>	Primitive Variable
$p, q, r$	Roll, pitch and yaw rates ( $deg/s$ )
$\mathbf{p}(p, t)$	Pressure vector at a point $p$ , and at a time $t$ ( $N/m^2$ )
$\mathbf{P}(p)$	Position of node $p$ ( $m$ )
$P_{i,j}^n$	$i$ -th wave reflection amplitude at point $j$ , and time $n$ ( $Pa$ )
$p_{ref}$	International standard minimum audible sound ( $2.10^{-5} Pa$ )
$q_i$	Heat flux vector ( $W/m^2$ )
$Q$	Adimensional flow momentum (-)
$Q_f$	Noise directivity factor (-)
$Q_{SAS}$	SAS source term ( $kg/m^3 s^2$ )
$q_s$	Free-stream dynamic pressure ( $Pa$ )
<b>R</b>	Vector of conserved residuals
$R$	Specific gas constant ( $287.058 J/kg^{-1} K^{-1}$ )
<b>R</b>	Rotation matrix (-)
$R_k$	Cross spectral matrix
$\mathbf{R}_{i,j,k}$	Flux residual vector
$r_m$	Distance between a noise source, and a microphone ( $m$ )
$Re_L$	Reynolds number based on cavity length (-)
$R_w$	Reflection coefficient (-)
$S$	Reference area ( $m^2$ )
<b>S</b>	Source term
$S_t$	Strouhal number (-)
<b>U</b>	Velocity vector ( $m/s$ )
$u, v, w$	Velocity components ( $m/s$ )
$t$	Time (s)
<b>t</b>	Translation matrix ( $m$ )
$T$	Temperature ( $K$ )

$T_{ref}$	Reference temperature (273.15K)
$T_S$	Sutherland temperature (110.4K)
$U_\infty$	Free-stream Velocity (m/s)
$u_i$	Velocity vector (m/s)
$u_j^n$	Axial flow-field velocity at point j and time n (m/s)
$V_0$	Initial velocity of a sound wave (m/s)
$V_{i,j,k}$	Volume of the cell i,j,k (m <sup>3</sup> )
$W$	Cavity width (m)
$\mathbf{W}$	Vector of conserved variables
$W_{dB}$	Wavelet Amplitude (dB)
$W_e$	Maximum envelope width
$w_i(\mathbf{x})$	Interpolation weight (-)
$W_\Psi^y$	Wavelet transform
$\mathbf{w}_{i,j,k}$	Vector of conservative variables
$\mathbf{x}$	Position vector (m)
$x_i$	Position vector (m)
$X, Y, Z$	Earth reference coordinates (m)
$X_b, Y_b, Z_b$	Store reference coordinates (m)
$X_{dp}, Y_{dp}, Z_{dp}$	Port side door reference coordinates (m)
$X_{ds}, Y_{ds}, Z_{ds}$	Starboard side door reference coordinates (m)
$X_f, Y_f, Z_f$	Fins reference coordinates (m)
$y_m$	Signal of microphone m
$Z(\omega)$	Beamformer output
$Z_{steel}, Z_{air} = \rho c$	Acoustic impedance (kg/m <sup>2</sup> s)

## Greek

$\alpha$	Rossiter phase shift (-)
$\alpha_m^s$	Model amplitude of mode m of solid s (-)
$\delta_{ij}$	Kronecker (-)
$\Delta f_{ref}$	Reference frequency (Hz)
$\Delta m$	Beamforming time delay (s)
$\Delta \mu$	Average statistical convergence index (-)
$\Delta \sigma$	Standard deviation statistical convergence index (-)
$\gamma$	Ratio of specific heats of air (-)
$\kappa_v$	Rossiter convection velocity coefficient (-)
$\mu$	Molecular Viscosity (Pa.s)
$\mu_{ref}$	Viscosity at that reference temperature (1.716 · 10 <sup>-5</sup> kg/ms)
$\mu_t$	Eddy Viscosity (Pa.s)
$\mu(t, n)$	Average of n trajectories
$\omega$	Specific turbulence dissipation rate (1/s)
$\omega_m$	Pulsation (2πf) (1/s)

$\Psi(t)$	Mother wavelet (-)
$\phi, \theta, \psi$	Roll, pitch and yaw angles ( <i>deg</i> )
$\phi_p, \phi_s$	Port side and starboard door angle ( <i>deg</i> )
$\phi_m^s$	Normalised m-th mode displacement of solid s ( <i>m/kg</i> )
$\phi^s$	Normalised displacement of solid s ( <i>m/kg</i> )
$\rho$	Density ( <i>kg/m<sup>3</sup></i> )
$\sigma$	Standard deviation
$\tau_{ij}$	Viscous stress tensor ( <i>N/m<sup>2</sup></i> )
$\theta$	Momentum thickness ( <i>m</i> )
$\zeta_m$	Damping coefficient (-)

### Acronyms

<i>ADT</i>	Alternate Digital Tree
<i>AEDC</i>	Arnold Engineering Development Center
<i>AFSEO</i>	Air Force Seek Eagle Office
<i>AGARD</i>	Advisory Group for Aerospace Research and Development
<i>AIAA</i>	American Institute of Aeronautics and Astronautics
<i>AIMS</i>	Airframe Integration of Modern Stores
<i>AFSEO</i>	Air Force Seek Eagle Office
<i>ALE</i>	Arbitrary Lagrangian-Eulerian
<i>BILU</i>	Block Incomplete Lower-Upper
<i>BISPL</i>	Banded Integrated Sound Pressure Level
<i>BIW</i>	Banded Integrated Wavelet
<i>B-L</i>	Baldwin-Lomax
<i>CAA</i>	Computational Aeroacoustics
<i>CBUSH</i>	Generalized Spring and Damper Connection
<i>CFD</i>	Computational Fluid Dynamics
<i>CFL</i>	CourantFriedrichsLewy
<i>CG</i>	Gravity Center
<i>CSD</i>	Computational Solid Dynamics
<i>CTS</i>	Captive Trajectory System
<i>DDES</i>	Delayed Detached Eddy Simulation
<i>DERA</i>	Defense Evaluation and Research Agency
<i>DES</i>	Detached Eddy Simulation
<i>EARSM</i>	Explicit Algebraic Stress <i>k-<math>\omega</math></i> model
<i>ERU</i>	Ejector Release Unit
<i>FFT</i>	Fast Fourier Transforms
<i>FS</i>	Full Stroke
<i>FSM</i>	Fin Structural Mode
<i>GBU</i>	Guided Bomb Unit

<i>HiFEX</i>	High Frequency Excitation
<i>HMB</i>	Helicopter Multi-Block
<i>HS</i>	Half Stroke
<i>IDW</i>	Inverse Distance Weighing
<i>IDDES</i>	Improved Delayed Detached Eddy Simulation
<i>IHAAA</i>	Institute of High Performance Computing Application to Air Armament
<i>ISA</i>	International Standard Atmosphere
<i>JDAM</i>	Joint Direct Attack Munition
<i>LE</i>	Leading Edge
<i>LES</i>	Large Eddy Simulation
<i>LIC</i>	Linear Integral Convolution
<i>MDCFD</i>	Minimum Domain CFD
<i>MEM</i>	Maximum Entropy Method
<i>MFRT</i>	Minimum Frequency to Reconstruct Trajectory
<i>MILES</i>	Monotone Integrated Large Eddy Simulation
<i>MMTD</i>	Miniature Munition Technology Demonstrator
<i>MLS</i>	Moving Least Square
<i>MUSCL</i>	Monotone Upwind Schemes for Scalar Conservation Laws
<i>MUSIC</i>	MULTiple Signal Classification
<i>NASA</i>	National Aeronautics and Space Administration
<i>NAVAIR</i>	Naval Air System Command
<i>NED</i>	North East Down
<i>NICS</i>	Navy Internal Carriage and Separation
<i>NTRS</i>	NASA Technical Reports Server
<i>OASPL</i>	Overall Sound-Pressure Level
<i>PIV</i>	Particle Image Velocimetry
<i>POD</i>	Proper Orthogonal Decomposition
<i>PSD</i>	Power Spectral Density
<i>RK4</i>	Runge-Kutta method 4th order
<i>RM</i>	Rossiter Mode
<i>RMS</i>	Root Mean Square
<i>S-A</i>	Spalart-Allmaras
<i>SAS</i>	Scale Adaptive Simulation
<i>SMAG</i>	Smagorinsky
<i>SPL</i>	Sound Pressure Level
<i>SST</i>	Shear Stress Transport
<i>SVD</i>	Singular Value Decomposition
<i>TE</i>	Trailing Edge
<i>TetrUSS</i>	Tetrahedral Unstructured Software System
<i>UCAV</i>	Unmanned Combat Air Vehicle
<i>URANS</i>	Unsteady Reynolds-Averaged Navier-Stokes
<i>6DoF</i>	Six-Degree of Freedom

# Chapter 1

## Introduction

### 1.1 Background and Motivation

High-speed flows inside cavities are encountered in all vehicles, trains, cars, aircraft etc. In aviation, the growing demand of stealth operation of unmanned and manned combat aircraft, pushed engineers to move externally carried stores to weapon bays like the ones found on the F-35 (Figure 1.1) and the B-52 (Figure 1.2c).

Cavity flows generate strong acoustic fields, comprising broadband and tonal noise, called Rossiter modes<sup>[13]</sup>. The flow unsteadiness is the consequence of a complex interaction between the turbulent shear layer spanning the weapon bay, and reflected waves at the aft bay wall<sup>[14]</sup>. To date, studies on cavity flows focused on idealised bays, commonly modelled as prismatic cavities. Nevertheless, actual aircraft bays are more and more complex, as can be seen figures 1.2 and 1.3. The cavities are sealed with doors (Figure 1.2a), include hydraulic lines (Figure 1.2d), structural ribs



(a) GBU-12 drop test<sup>[1]</sup>



(b) GBU-32 Pitch down<sup>[2]</sup>

Figure 1.1: Store release from the F-35



(a) Tupolev Tu-2 (1941)<sup>[3]</sup>



(b) Boeing B-52 (1952)<sup>[4]</sup>



(c) Boeing B-52 (1952)<sup>[5]</sup>



(d) General Dynamics F-111 (1964)<sup>[6]</sup>



(e) Rockwell B-1B (1974)<sup>[7]</sup>



(f) Lockheed Martin F-22 (1997)<sup>[8]</sup>



(g) Boeing X-32 (2000)<sup>[9]</sup>

Figure 1.2: Examples of weapon bays

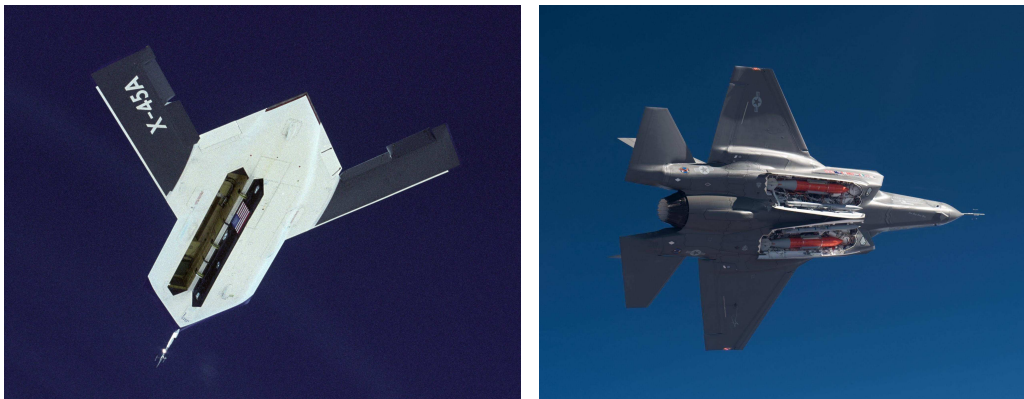
(a) Boeing X-45 (2002)<sup>[10]</sup>(b) Lockheed Martin F-35 (2006)<sup>[11]</sup>(c) Lockheed Martin F-35 (2006)<sup>[12]</sup>

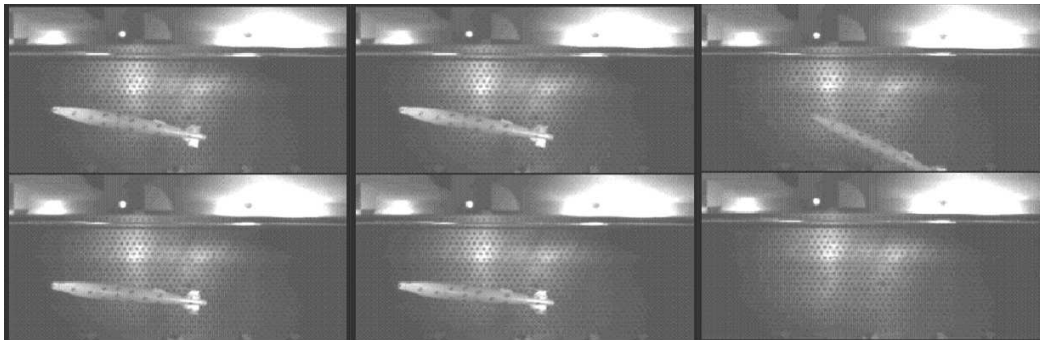
Figure 1.3: Examples of weapon bays

(Figure 1.2f), and store ejectors (Figure 1.2c). In addition, several stores are packed in the bays (Figure 1.2e), leading to different flow conditions for each combination. The F-35 weapon bay geometry is the most complex, being shallow and very different from a prismatic shape (Figure 1.3c). The first step towards increasing the complexity of the cavity geometry is to add the bay doors. The doors are known to modify the cavity flow behaviour, while their effect, when dynamically moving, is not known. The design of the weapon bays and of the stores may thus be improved by knowing the actual transient flow fluctuations, and the duration of the cavity flow establishment during door operation.

Once the doors are open, the resonant cavity flow may effect a store separation. The store is subject to unsteady loads, driving its trajectory (Figure 1.4), and this environment leads to store trajectory variability that may be difficult to predict. Unsafe store releases from cavities were reported by the US Army, where a GBU-12 came back to hit a B-52 tail<sup>[15]</sup>. Further releases showed substantial variability, but none of them reproduced the accident. In addition, the cavity tones may excite the store and



(a) Release of a GBU-12 from the weapon bay of a B-52 shows a large pitch up shortly after release



(b) Snapshots of two different releases at nominally identical conditions. Top : drop 1; Bottom : drop 2; Time progress from left to right

Figure 1.4: Examples of unsafe store trajectory <sup>[16]</sup>

aircraft structures, that may induce structural fatigue and failure.

To alleviate these drawbacks, researchers tested a broad range of passive and active flow control devices with various levels of success. Nevertheless, few solutions guarantee noise reduction, steady shear layer, and reduced vortex shedding from the bay, which may impact downstream parts of the aircraft. To improve on the current situation, the bay flow physics must first be understood to design better flow control devices. Unfortunately, the prediction of the cavity tonal frequencies, and amplitudes is still difficult without Computational Fluid Dynamics (CFD) or experiments.

This complex engineering problem requires fast and accurate design and analysis tools. Flight tests are accurate, but very expensive. Wind tunnel tests suffer from scaling effects, and store release measurements are difficult. For simulations, this multidisciplinary problem requires CFD, Computational Structural Dynamics (CSD), Computational Aeroacoustics (CAA) and store flight mechanics. In addition, the cavity flow is not deterministic and turbulence simulation instead of modelling <sup>[17]</sup> is the key for accurate predictions. The main motivation of this work is to develop accurate and fast methods for cavity flows that will lead to better understanding of its physics.

### 1.1.1 Cavity Flow Physics - Fundamental Ideas

Cavity flows are categorised according to the flow topology. In closed cavities (Figure 1.5a), the flow-stream separates from the leading edge of the cavity, but does not have enough energy to cross it. The flow attaches on the cavity ceiling, and separates further downstream to attach at the trailing edge. This topology creates two strong vortices located at the front, and at the aft of the cavity. In open cavities (Figure 1.5b), the free-stream flow separates at the leading edge, and bridges the cavity, before impacting the aft wall. This creates a large re-circulation inside the cavity. In between, transitional flows occur. Plentovich *et al.* [18] experimentally determined the boundaries between the different topology for subsonic and transonic flows. The boundaries depend on the length to depth ratio  $L/D$ , the Mach number, and the width to depth ratio  $W/D$ , of the cavity. Overall the  $L/D$  ratio which defines the boundary between transitional and closed flow increases with the Mach number and the  $W/D$  ratio.

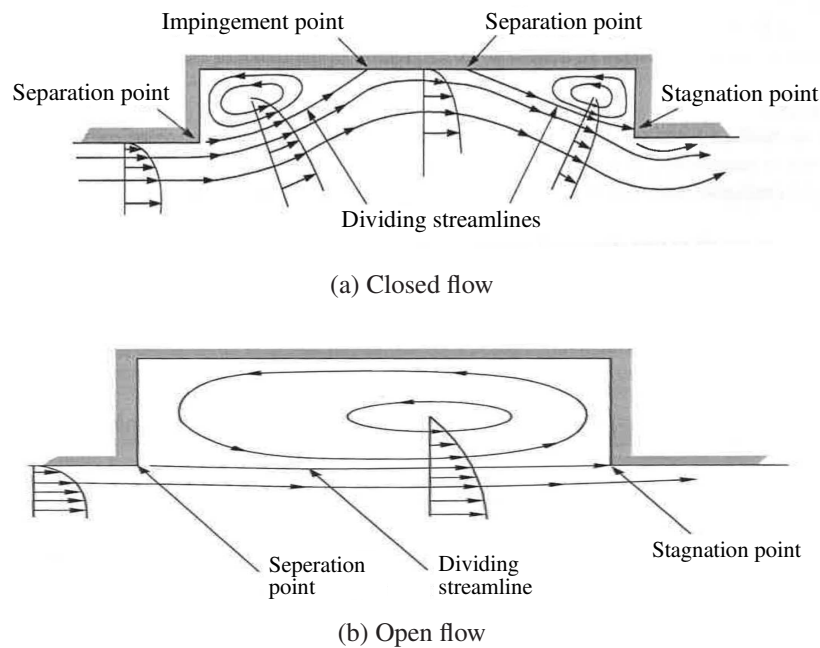


Figure 1.5: Open and closed cavity flow configurations at subsonic speeds<sup>[19]</sup>.

This section focuses on the physics of open cavity flows typically encountered in fighter weapon bays at transonic speeds. The cavity acoustics is characterised by strong broadband and tonal noise (Figure 1.6), and had been studied over the last 70 years using experiments, and more recently CFD. Plumlee *et al.* [20] were some of the first researchers to propose a model for the generation of the cavity tones. They

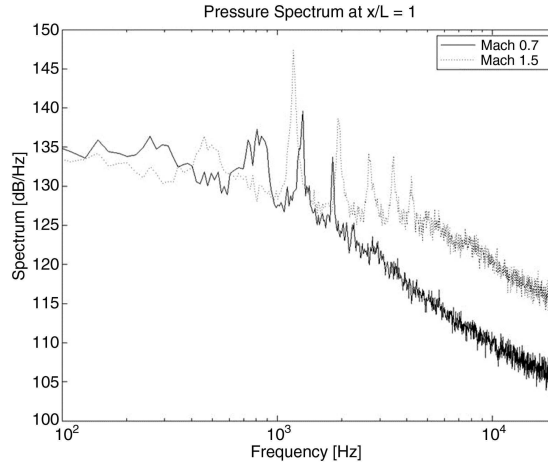


Figure 1.6: Experimental SPL at the aft wall of an ideal cavity <sup>[14]</sup>.

suggested that the turbulence growing in the shear layer provided a broadband noise source driving the cavity oscillations. The cavity response was to amplify small bands of frequencies, depending on the geometry and conditions. For transonic to supersonic speeds, the tones are not harmonic, and cannot be described by normal resonance concepts<sup>[21]</sup>.

Rossiter <sup>[13]</sup> proposed a different model based on an acoustic feedback loop. Using shadowgraph images, he spotted vortices shed periodically from the front lip of the cavity. The vortices were travelling along the cavity length at the shear layer, generating acoustic waves when reaching the downstream wall. These acoustic waves travel upstream and interact with the shear layer, resulting in shedding of new vortices. He proposed a formula based on those observations for estimating the tonal frequencies, that was further modified by Heller <sup>[22]</sup> according to:

$$f_m = \frac{U_\infty}{L} \left[ \frac{m - \alpha}{M_\infty \left( 1 + \left( \frac{\gamma - 1}{2} \right) M_\infty^2 \right)^{-1/2} + 1/\kappa_v} \right] \quad (1.1)$$

where  $f_m$  is the frequency of mode  $m$ ,  $U_\infty$  is the free-stream velocity,  $M_\infty$  is the free-stream Mach number,  $L$  is the cavity length,  $\alpha$  represents a phase shift between the propagation of the vortices from the front lip, and the acoustic radiations from the cavity aft wall, and  $\kappa_v$  is the convection velocity coefficient of the vortices at the shear layer.  $\alpha$  is a non dimensional number defined using Rossiter experiments that shown that the cavity frequencies lied in a sequence of the form  $m - \alpha$ . These empirical constants have been tuned to fit experiments, and have the values  $\alpha = 0.25$  for a phase shift of a quarter of a wavelength, and  $\kappa_v = 0.57$  for vortices travelling at 57% of the

free-stream velocity. This formula can be used to estimate the tonal frequencies for Mach numbers between 0.4 to 1.4, but does not indicate if a mode is active or not. In addition, further experiments at a wide range of Mach numbers [23, 22, 24] did not confirm the vortex shedding, suggesting that this is not an important phenomenon at all conditions. More recently, experimental data [14, 25] suggest that equation 1.1 can be valid even if  $\kappa_v$  is different from the value found by Rossiter. As pointed out by Rossiter, this model is “merely an attempt to give a simple explanation of what is undoubtedly a highly complex motion” [13].

Tam *et al.* [21] improved a model developed by Bilanin *et al.* [26]. They considered an acoustic monopole radiating noise located downstream of the cavity. The acoustic waves were travelling upstream along the shear layer, and were also reflected by the cavity ceiling, and by the upstream wall. Using a “distributed receptivity” model considering the shear layer thickness, the acoustics waves excited the shear layer instability waves. Handa *et al.* [27] developed a model for the acoustic feedback mechanism of deep cavity flows considering the superposition of two pressure waves. One generated at the trailing edge of the cavity due to the shear layer impact on the aft wall, and the other generated by acoustic reflections at the ceiling of the cavity. Both models predicted the cavity tonal frequencies, but not their amplitudes. Only the model of Alvarez *et al.* [28] predicted if cavity modes may exist, or not in a given cavity. They considered the scattering process at the ends of the cavity, along with the propagation of reflected waves for the central cavity region.

Thanks to improvements in measuring methods, data for cavity flows became

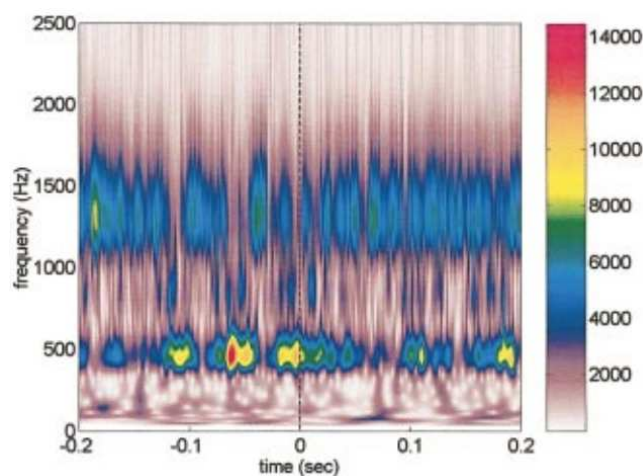
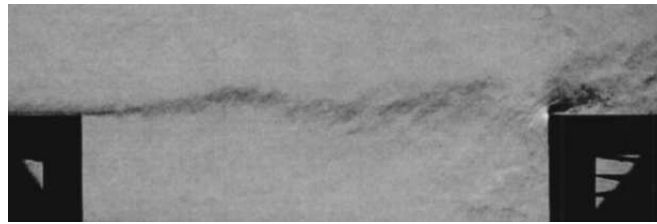
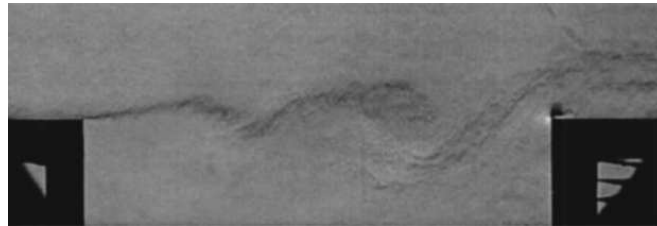


Figure 1.7: Joint time-frequency analysis of the pressure at front wall [29].



(a) Dominant mode 1



(b) Dominant mode 3

Figure 1.8: Schlieren image of cavity shear layer<sup>[29]</sup>.

more and more accurate. Using joint time-frequency methods <sup>[29]</sup>, and high definition shadowgraph <sup>[14]</sup>, the understanding of the smaller cavity flow fluctuations was improved. The amplitude of the cavity tones is not constant in time, and the dominant tone may become quiet in favour of another one. This is called mode switching (Figure 1.7), during which, the shape of the shear layer varies depending on the dominant tone (Figure 1.8). In addition, the noise spectra showed a non linear quadratic interaction between the tones, generating small peaks, of negligible amplitude compared to the main tones <sup>[30]</sup>. Numerous reflected acoustic waves were also identified travelling back and forth along the cavity length. Previous cavity flow models missed these unsteady characteristics and the amplitude of the tones, showing that a part of the physics was still missing.

Modelling ideal cavity flows is crucial for understanding the mechanisms driving their unsteadiness, and to design new control methodologies. Nevertheless, actual weapon bays have complex geometric features whose effects cannot be modelled by the simple models described in this section. To understand the physics of those real world cases, experimental or numerical investigations are required. In the following sections, attempts to understand the weapon bay flow, door operation, store aeroelasticity, and store release are presented. Then, different passive flow controls methods employed for cavity flows are described.

### 1.1.2 Weapon Bay Doors Opening - Literature Findings

During the store release process, the bay doors open and close, establishing a transient flow behaviour. So far, researchers neglected the dynamics of the doors and focused on cases with fixed doors.

Regarding the flow conditions, and the geometries used by researchers, fixed doors held at 90 degrees on each side of an ideal cavity had different effects. Murray *et al.* [31] experimentally tested doors at Mach number 1.50 on a cavity of L/D ratio of 9. Adding the doors, the cavity modes become weaker, and the broadband noise was dominant. Barakos *et al.* [17] simulated the M219 cavity [32] of L/D ratio of 7 at a Mach number 0.85 using Detached Eddy Simulation (DES). In that case, the doors resulted in a strong amplification of the second cavity mode, and to a slightly weaker first mode, in agreement with experiments [32]. Sheta *et al.* [33] obtained the same result with a Delayed Detached Eddy Simulation (DDES) of a cavity of L/D ratio of 6 at Mach number 1.44. A half opened bay, with one door held at 90 degrees, and one closed door was described by Murray *et al.* [31] and Sheta *et al.* [33]. Both obtained a strong amplification of the cavity modes, due to the sheltered part of the cavity that enhanced the acoustic feedback path. In addition, Murray found a dramatic decrease of the broadband noise.

Sheta *et al.* [33] studied the effect of doors held at an angle of less than 90 degrees. This reduced the space available for the shear layer to move, and resulted in a reduction of the fluctuations inside the cavity. On the other hand, Bacci *et al.* [34] performed DDES simulations with doors held at 90 and 110 degrees. The cavity length to depth ratio was 5.66 and the Mach number 0.85. In their case, the shear layer was not influenced by the doors, and the flowfield fluctuations were unchanged.

The effect of the bay doors on store loads had been experimentally studied by the end of the 80' by Blair *et al.* [35]. The cavity length to depth ratio was 14 (closed cavity flow), and the Mach number 2.65. The store loads were measured at different vertical stations without doors, and with doors held at 45, 90, and 135 degrees. The doors at 45 degrees reduced the opening area and the store loads, while the doors at 135 degrees had small effect. On the other hand, the doors at 90 degrees resulted in significant increase of the store loads inside the cavity due to the doors containing high pressure within the cavity. Flow visualisation, and unsteady pressure measurements were missing to draw clear conclusions from this study.

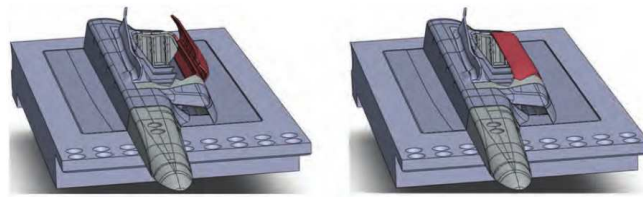
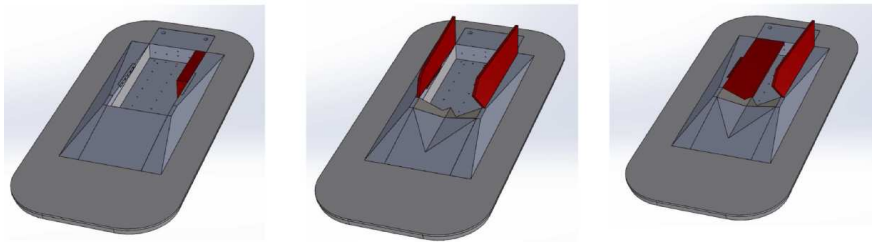
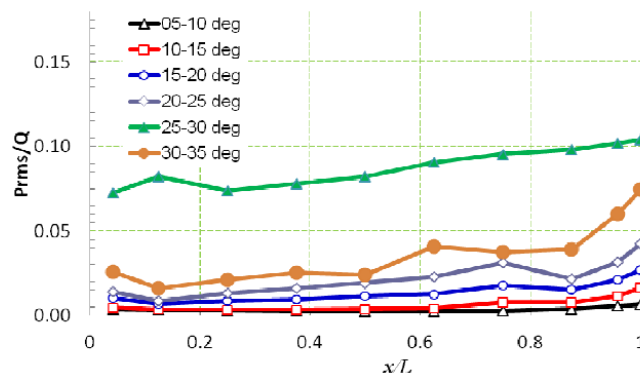
(a) F-35 weapon bay used by Kannepali *et al.* [36](b) Weapon bay geometry used by Casper *et al.* [37]

Figure 1.9: Geometry used to study fully and half open complex weapon bays.

Figure 1.10: RMS pressure along cavity ceiling for dynamically moving doors<sup>[33]</sup>

More complex geometries were investigated with static doors (Figure 1.9). Kannepali *et al.* [36] performed Monotone Integrated Large Eddy Simulation (MILES) of the F-35 weapon bay with doors at Mach 1.5 (Figure 1.9a). Panickar *et al.* [38] worked on a similar geometry using wind tunnel experiments at Mach 0.75 and 1.5. Both sets of results suggest a large amplification of the tones, and a reduction of the broadband noise when closing one of the two doors. Similar door configurations mounted in a complex cavity by Casper *et al.* [37], showed the same differences as Panickar *et al.* [38] between fully and half open cavity (Figure 1.9b). This also agreed with the result of Murray *et al.* [31] and Sheta *et al.* [33] on ideal cavities, and shows that ideal cavities are good enough to capture essential physics due to the doors.

The influence of moving doors on the cavity flow has so far been researched by

Sheta *et al.* [33] using CFD. The doors were opened between 5 to 35 degrees at Mach 1.44 over a prismatic cavity of length to depth ratio of 6. The doors were inserted in the computational domain using the chimera technique. It was shown that the OASPL level reached a peak at 30 degrees of door opening (Figure 1.10). Any description of the flow topology was missing to understand the origin of this peak, and a longer CFD signal was required to obtain the full opening.

Understanding the flow physics involved during door opening, may help optimise the store release process, minimising the effect of the flow fluctuations on the store, and supporting a safe, and stealthy store separation. Table 1.1 summarises the different CFD door studies. However, no experiments are published for their validation, as the geometric scaling makes a realistic opening difficult in wind tunnels.

Study	Geometry	L/D	W/D	Mach	Method	Door Opening
Blair <i>et al.</i> [35] (1989)	Prism	14.0	3.1	2.65	Exp.	Open 45, 90 and 135 deg
Barakos <i>et al.</i> [17] (2009)	M219	5.0	1.0	0.85	DES	Open 90deg
Kannepali <i>et al.</i> [36] (2011)	Complex F-35	-	-	1.50	MILES	Open, half open
Murray <i>et al.</i> [31] (2012)	Prism	9.0	2.0	1.50	Exp.	Open, half open
Panickar <i>et al.</i> [38] (2013)	Complex F-35	-	-	0.75, 1.50	Exp.	Open, half open
Bacci <i>et al.</i> [34] (2015)	UCAV 1303 with M219	5.7	1.4	0.85	DDES (Fluent)	Open 90, 135deg
Casper <i>et al.</i> [37] (2016)	Prism and complex	7.0	3.5	0.80	Exp.	Open, half open
Sheta <i>et al.</i> [33] (2017)	Prism	6.0	2.0	1.44	DDES (Loc/CHEM)	Open 45, 90 deg, half open, dynamic 5 $\Rightarrow$ 35 degrees

Table 1.1: Summary of works on door effects on cavity flows.

### 1.1.3 Aeroelasticity of Store in Weapon Bays

As the bay doors begin to open, carried stores are subjected to unsteady loads that may produce aeroelastic deformations. Flight tests were reported by Probst *et al.* [39] using an SUU-41 POD mounted on a F-16 (Figures 1.11 and 1.12). The aircraft flew at altitudes between 10.000 to 29.000 ft and Mach numbers were between 0.5 to 0.93. The cavity was 1.02m long with an L/D ratio of 4. A store model, with canards and fins was placed at different carriage positions inside the cavity. Kulite sensors were mounted on the cavity walls to measure the pressure fluctuations. Accelerometers were

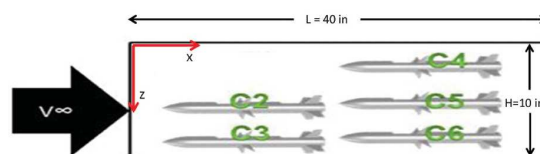
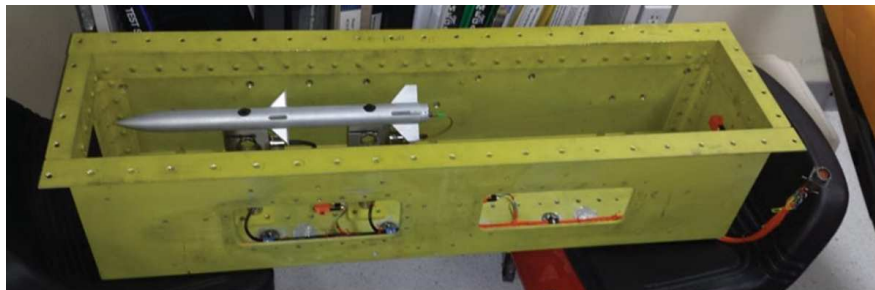


Figure 1.11: cavity with model store installed in wind tunnel [39]



(a) SUU-41 pod mounted on the F-16 wing

(b) Cavity with the missile model at  $X/L=0.28$ Figure 1.12: In flight setup used by Probst *et al.* [39].

also placed on the cavity ceiling and on the store model. Forces acting on the store were measured with load cells. Pressure, forces, and acceleration signals were compared in the frequency domain, showing how the store was responding to the cavity flow at different positions. The store loads were noticeably influenced by the tonal fluctuations with strong peaks at the second and third cavity flow modes. The missile accelerations resulted in strong peaks at cavity modes. However, the store mounting structure for each store position was different, and was driving the structural characteristics of the system. In addition, the loads signals were polluted by the structural vibration leading to uncertainty in the obtained data.

Wagner *et al.* [40] performed wind tunnel experiments with two different stores. A first store was represented by a cylinder held on two supporting rods. The second was a tunable natural frequency store with a nose and a tail [41]. Experiments conducted at transonic and supersonic Mach numbers showed store acceleration peaks both at its natural structural frequencies, and at cavity modes. Near mode matching, the

store response was variable with the store vibrations decreasing by a factor of two for a variation of cavity tone frequencies of about 1%. Switching to a complex cavity geometry increased the span-wise vibrations due to further asymmetries in the cavity flow<sup>[42]</sup>. Nevertheless, this experiment is limited to low Reynolds Numbers compared to in flight conditions, and the scaled structures may not be representative of actual full size stores. Furthermore, scaled structures may not reproduce instability phenomena encountered at full scale.

This is where the versatility of Computational Fluid Dynamics (CFD) can aid the analysis of stores in full size weapon bays. CFD and Computational Structural Dynamics (CSD) can be loosely coupled if the deformations of the surfaces are assumed to be small enough to keep a rigid CFD grid. Arunajatesan *et al.*<sup>[43]</sup> employed this technique for a generic finned store in a cavity of L/D 4.5 at Mach 0.6. Maximum surface displacements of 0.025mm were seen, that were small enough to use this method. Nevertheless, store deformations of the order of few millimeters are seen in flight, that could not be simulated with their technique.

For better accuracy, a strong fluid/structure interaction method was used by Babu *et al.*<sup>[44]</sup> transferring the loads from CFD to CSD grids, and sending back the deflections to the CFD grid. This method takes into account the flow and structural history. This work employed Scale Adaptive Simulation (SAS)<sup>[45]</sup> for a cavity of L/D 7 at Mach 0.85. With this method, Babu computed the deformations of the fins for a full size store, for different vertical positions from the cavity ceiling. Fin tip displacements, up to 2.5 mm were found for the store placed at the shear layer. The fins were mainly excited at the structural frequencies which were much higher than the cavity modal frequencies. Nevertheless, the missile body aeroelasticity also has to be added to show its influence on the fins deformations.

Table 1.2 summarises the aeroelastic cases found in the literature. There is only two CFD studies of this problem, and further work is required to obtain a model fully representative of the experiments, including both the body and the fins deformations.

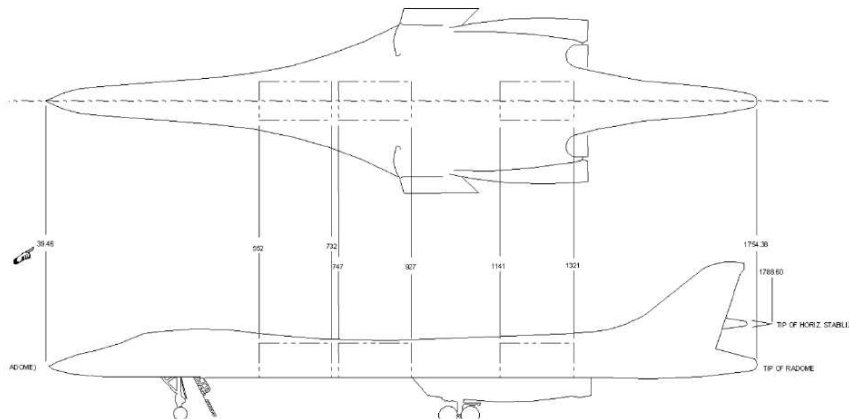
### 1.1.4 Store Releases from Weapon Bays

#### Experimental Works

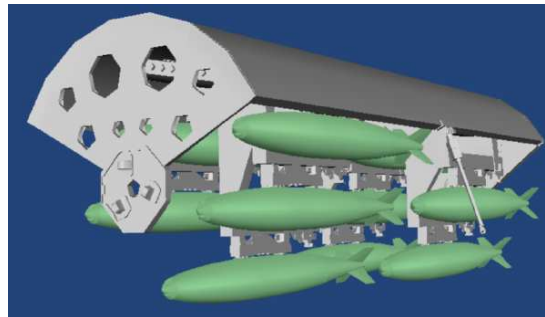
The unsteady flow around a weapon bay affects the loads on the released stores, and leads to store trajectory variability. To guarantee the clearance of a store for weapon

Study	Cavity length (m)	L/D	Store Position	Mach	Method
Arunajatesan <i>et al.</i> <sup>[43]</sup> (2013)	0.46	4.5	Carriage	0.6	Sigma CFD - Loosely coupled CSD
Wagner <i>et al.</i> <sup>[40]</sup> (2015)	0.13	3.3	Shear layer	0.59, 2.47	Exp., ideal cavity
Babu <i>et al.</i> <sup>[44]</sup> (2016)	3.33	7.0	Carriage, Shear layer, Outside	0.85	DES S-A - Strongly coupled CSD
Wagner <i>et al.</i> <sup>[41]</sup> (2016)	0.21	7.0	Shear layer	0.58, 1.47	Exp., ideal cavity
Casper <i>et al.</i> <sup>[42]</sup> (2017)	0.21	7.0	Shear layer	0.58, 0.87	Exp., ideal and complex cavities
Probst <i>et al.</i> <sup>[39]</sup> (2017)	1.02	4.0	Carriage	0.50, 0.93	Flight test

Table 1.2: Summary of works about aeroelasticity on store in cavity.



(a) B-1B general configuration



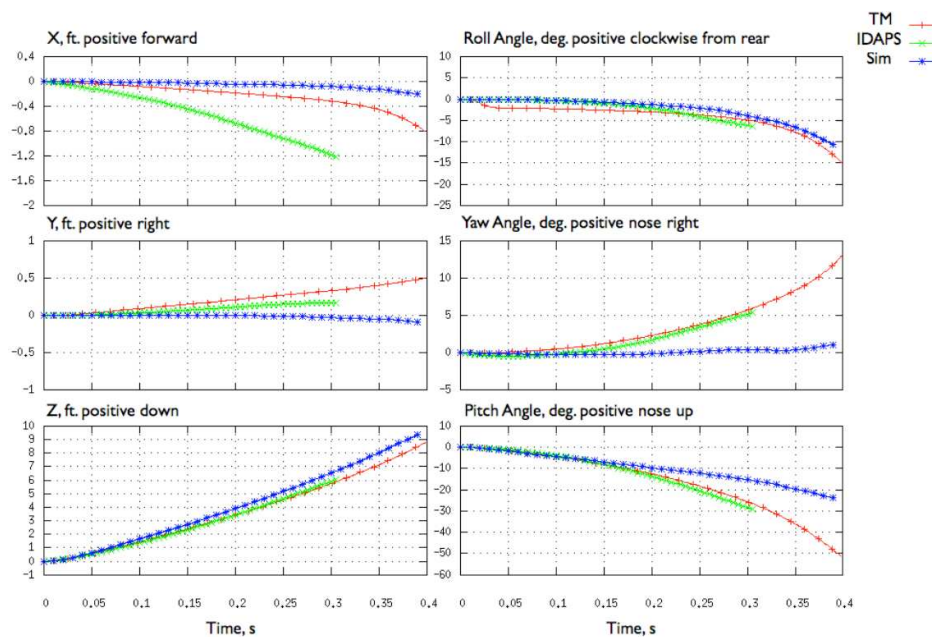
(b) Carriage system

Figure 1.13: Flight test geometry <sup>[46]</sup> of B-1B store release

bays release, the statistics of the trajectories have to be known. With the need of validation for computational techniques, the Institute of High Performance Computing Application to Air Armament (IHAAA) worked with the Air Force Seek Eagle Office (AFSEO) to perform flight test of GBU-38 release from the B-1B weapon bays <sup>[46]</sup>. This project was also in collaboration with the Naval Air System Command (NAVAIR), and the Air Force AEDC to demonstrate and validate computational tools to simulate time-accurate store release trajectories from weapon bays.



(a) Image from digital camera



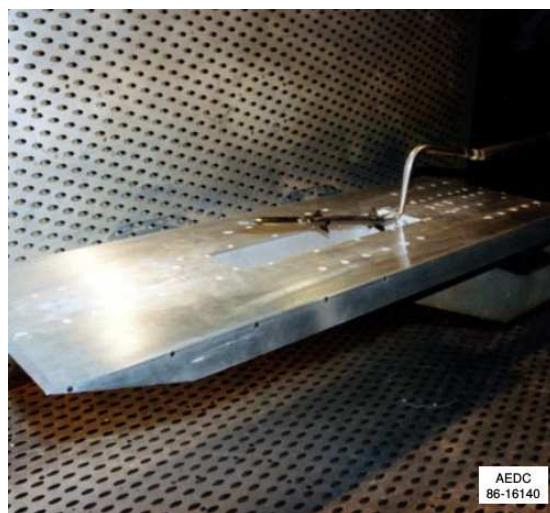
(b) Comparison of telemetry, photogrammetry, and simulations trajectories.

Figure 1.14: Flight test results <sup>[46]</sup> for B-1B store release

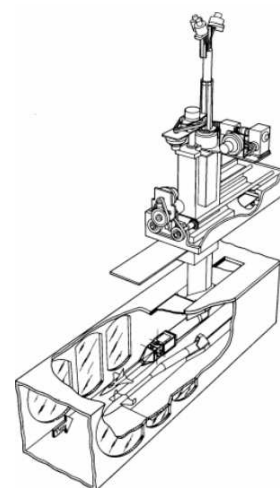
The B-1B is a bomber equipped with three weapon bays placed along the fuselage (Figure 1.13a). The experiments were performed with six GBU-38 carried inside the third cavity, with the two forward bays closed. Six stores were packed in the cavity and all were released one after the other (Figure 1.13b). Twelve high speed video cameras were placed around the cavity to generate photogrammetry data of the trajectories (Figure 1.14a). On-board computers recorded the flight

conditions including Mach number, altitude, and angle of attack. Additionally, the stores were equipped with a telemetry kit recording accelerations, rate gyro components, and temperature. A total of eighteen stores were released during the test campaign. The results showed the same trends between the trajectories obtained from photogrammetry, and accelerometers (Figure 1.14b). Nevertheless, discrepancies appeared due to problems with the camera position, orientation and lens distortion. Besides, noise polluted the telemetry system and biased the obtained trajectories. This project included CFD simulations to compare with the flight data. All attempts to simulate this case [47, 48, 49] have showed that the cavity flow effect was negligible, and the trajectories were repeatable in time. This may be due to a spoiler at the leading edge of the cavity that was deflecting disturbances away from the opening. This case is not suitable as validation for the present work, for few reasons. First, the weapon bay aerodynamics is influenced by the engine intake on either sides, and complex features included in the cavity. Consequently, the simulation of this case requires the complete aircraft geometry that is not openly available. Furthermore the contribution of the ejector to the initial motion was measured with large errors [48]. In addition, only two trajectories were published, and the trajectory variability was not assessed. Although effective, this case shows that flight test outcomes can be limited compared to the invested cost and effort.

Wind tunnel tests are an alternative, and are also important for CFD validation.



(a) Cavity installed in the wind tunnel



(b) Schematic of the captive trajectory system

Figure 1.15: CTS experiments [50]

Some of the available data is described in the following paragraphs. Experimental store releases from weapon bays were carried out between 1997 and 1998 at the Arnold Engineering Development Center (AEDC) [50]. Transonic, and low supersonic tests at Mach number 0.95 and 1.20 were performed in a closed circuit wind tunnel, with a square test section of 1.21m and 3.81m long. Ideal cavities 0.46m long, 0.10m width, and of L/D 9.0 and 4.5 were installed on a flat plate of 1.19m long (Figure 1.15a). The employed store was an AIM-9L one-tenth of full scale model, and was moved by a captive trajectory system (CTS) (Figure 1.15b). The store had five degrees of freedom with the rolling angle disabled. Aerodynamic loads on the store were measured with a small six-components internal strain-gage balance. After an ejector stroke, the store was released with a full size translational downward velocity of 9.14m/s, and a pitch, nose-down velocity of 57deg/s. The store was moved feeding a six degree of freedom (6DoF) flight mechanics model with averaged forces. The CTS system worked with a move-pause sequence, so the dynamics of the store/shear layer interaction was not well captured. Nevertheless, this is the best and closest case to the current study to validate CFD code.

Boeing performed wind tunnel tests for the Airframe Integration of Modern Stores (AIMS) program in 2006 [51]. A one-tenth of a full-scale Mk-82 JDAM store was released from a generic X-45 bay inserted in a flat plate. The High Frequency Excitation (HiFEX) bay was 0.43m long, 0.07m wide, and the length to depth ratio was 7.2. The cavity was installed in a 1.22m square section, at 0.45m from the bottom wall. The store length was 0.3m, its weight 234g, its pitch and yaw moments were  $1.69g.m^2$ , and its roll moment was  $0.05g.m^2$ . The store was free to move during the release, and the trajectory was captured on video. The wind tunnel Mach number was 0.8, but there is uncertainty on the experimental conditions as the flowfield was not measured around the cavity. Furthermore, wall blowing was used to prevent the flow from become sonic, but the blowing flow rate was not measured. The results indicated very large variability, and two stores hit the cavity model. Nevertheless, the uncertainty on the experimental conditions, and the very small store inertia due to scaling, exclude this case from being used for CFD validation.

Murray *et al.* [52] carried out wind tunnel releases of a 1/15<sup>th</sup> GBU-38 store at Mach number 1.49. The trajectory of the store was measured using Particle Image Velocimetry (PIV) applied to high speed camera images (Figure 1.16). The pressure fluctuations were measured in the cavity, and were compared with the trajectories to

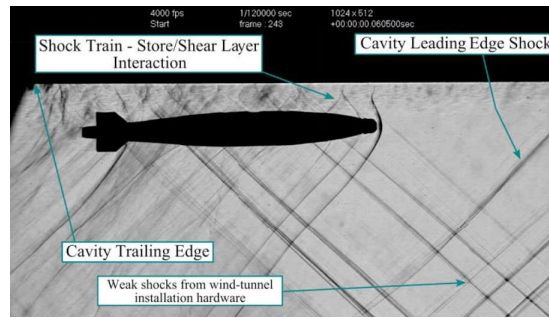


Figure 1.16: Instantaneous schlieren image of GBU-38 at carriage<sup>[52]</sup>

identify any phase relationship. Five drops were presented, two with a high ejection force, and three with a low ejection force, respectively resulting in residence times in the shear layer of 2ms, and 5ms. The store was mass scaled and weighed 48g. Large pitch angle variability was shown, and the phase relationship between the store release and the pressure oscillation in the cavity was different for each test. This case missed the span-wise displacement, the roll, and yaw angle to give the complete description of the trajectories.

More recently, experiments were conducted by Flora *et al.*<sup>[53]</sup> and Merrick *et al.*<sup>[54]</sup> at supersonic speeds. The tests were conducted in a variable density blow-down tunnel with a test section of  $0.06m^2$  and 0.41m long. The cavity placed on the ceiling was 0.17m long, and the ratio  $L/D$  was 4.5. Simple spheres and an Mk-82 store made of water ice were released without ejection stroke to maximise the cavity flow effect. The spheres weighed 6.9g and were of a diameter of 2.4cm. The Mach numbers were 2.9 and 2.2, and the total pressure was fixed to different values between 1 and 20 psia. The total pressure was determined to scale the store weight to fit in flight conditions. The store material density was equivalent to titanium for the smaller total pressure, and was equivalent to rubber, pine and balsa increasing the total pressure. At Mach 2.9<sup>[53]</sup>, the shear layer lifted the sphere that was not able to cross it, hitting the cavity aft wall. Small and large spoiler placed at the cavity leading edge, thickened the shear layer, and made possible for the sphere to safely clear the cavity at 4 psia. At the same conditions the Mk-82 store was pitching up while interacting with the shear layer, and was not cleared. Adding the spoiler, the pitch up motion reduced, and the store was able to clear. At Mach 2.2<sup>[54]</sup>, the sphere was dropped 8 times at 1 psia, showing large trajectory variability, and hit the cavity most of the times. Increasing the total pressure to 3.5 psia was equivalent to decreasing sphere mass, and the re-circulation inside the cavity was stronger, pushing the store upstream. This is the best existing case

Study	Bay Geometry, Length	Store	Mach	Method	Available Components	Release Measurements
Dix <i>et al.</i> <sup>[50]</sup> (2000)	Prism L/D 4.5, 4.57m	AIM-9L, 88kg	0.95	Wind tunnel, CTS	9 traj. $x, y, z, \theta, \psi$	Position, velocity, acceleration from CTS
Cary <i>et al.</i> <sup>[51]</sup> (2006)	Prism L/D 7.2, 0.43m	Mk-82 JDAM, 234g	0.80	Wind tunnel, FR	5 traj. $x, y, z, \phi, \theta, \psi$	High speed camera
Atkins <i>et al.</i> <sup>[46]</sup> (2008)	Complex B-1B, 5.49m	GBU-38, 250kg	0.88	Flight test, FR	2 traj. $x, y, z, \phi, \theta, \psi$	12 high speed cameras, flight conditions, telemetry (accelerations, rate gyro).
Murray <i>et al.</i> <sup>[52]</sup> (2009)	Prism L/D 6.0, 0.37m	GBU-38, 48g	1.49	Wind tunnel, FR	5 traj. $x, z, \theta$	High speed camera, Kulite transducer
Flora <i>et al.</i> <sup>[53]</sup> (2014)	Prism L/D 4.5, 0.17m	Mk-82, Sphere, 6.9g	2.90	Wind tunnel, FR	5 traj. $x, z$	High speed camera
Merrick <i>et al.</i> <sup>[54]</sup> (2016)	Prism L/D 4.5, 0.17m	Sphere, 6.9g	2.22	Wind tunnel, FR	10 traj. $x, z$	High speed camera

**CTS: Captive Trajectory System, FR: Free Release**

Table 1.3: Summary of experimental store release studies

to validate a CFD code for store trajectory variability in supersonic flow. However, the flow conditions and the store aspect ratio are too far from the thesis assumptions.

### **Computational works**

CFD studies of store releases appeared in the last ten years using more or less accurate methods. The two most used approaches are the grid method, and the time accurate simulation [55].

The grid method consists in measuring the time averaged loads on the store at different positions and attitudes by means of wind tunnel testing or CFD. This database is used to build the grid of aerodynamic influence. Then the trajectory is computed feeding a 6DoF model with loads interpolated from the grid of aerodynamic influence. This approach is very fast as the initial conditions can be easily changed, and the measurements have to be done once. First attempts tried to simplify the problem by reducing the need of CFD simulations. For example, Johnson *et al.* [56] developed a low fidelity model to obtain the forces and the moments on the store using Minimum Domain CFD (MDCFD). First, the steady flowfield around a F/A-22 aircraft was computed without the store. Then, a near field domain was defined, containing a Miniature Munition Technology Demonstrator (MMTD) store, and a portion of the aircraft. The unsteady flow was resolved in the near field domain, and its boundaries were interpolated from the aircraft steady flowfield. The grid was computed for different store positions averaging the unsteady flowfield. In comparison to experiments, the translations were well captured, but the orientations were not correctly predicted due to the averaging of the pressure fluctuations. An other attempt to apply the grid method by Smith *et al.* [57] for the release of a Small Smart Bomb (SSB) from a Boeing X-45A lead to similar results.

Finney [55] compared the grid method with the Navy Internal Carriage and Separation (NICS) experimental data. During the experiments, a Mk-82 store was held at different positions around a cavity to measure the loads. The comparison of the experiments with steady RANS Spalart-Allmaras computations showed large loads discrepancies, as the solution did not converge well due to the steady state assumption that was not realistic. The grid method was fed with the steady CFD loads to reproduce the trajectories performed with the captive trajectory system (CTS). The experimental trajectories fell within the standard deviation bound of the CFD trajectories for some

position and attitude components. However, significant discrepancies were visible, for the span-wise displacement and the roll angle.

This method was also used by Davis *et al.* [16] to study the separation of a GBU-38 from the HiFEX cavity at Mach 0.8. The grid of influence was built at the cavity mid-span using CFD computations, and a 3DoF was used ignoring span-wise displacements. The results showed significant discrepancies, but similar trends compared to time accurate trajectory simulations. The grid method could be used as a rough estimate of the trajectory, but is not accurate enough for store clearance certification that must account for cavity flow fluctuations, and their flow interactions with the store.

The time accurate method coupled CFD with 6DoF. At each timestep, the loads were integrated from the CFD flow. Then a 6DoF method computed the store displacements and attitudes using the CFD loads. Finally, the displacements were applied to the CFD grid to compute the next timestep. Davis *et al.* [16] simulated the release of the GBU-38 from the HiFEX cavity at Mach 0.80. CFD was performed using SST  $k - \omega$  turbulence model on an unstructured overlapping grid using the USM3D code from NASA. Three releases with large variability agreed with wind tunnel observations (Figure 1.17). None of the released stores were back inside the cavity as seen during the experiments. Further releases were simulated with variation of the ejection speed, store mass, store inertia, and flow velocity. Nevertheless, more simulations were required to build a statistical parametric study.

The Beggar CFD code of the Air Force SEEK EAGLE Office (AFSEO) was first employed by Johnson *et al.* [58] to simulate the release of a Smart Small Bomb

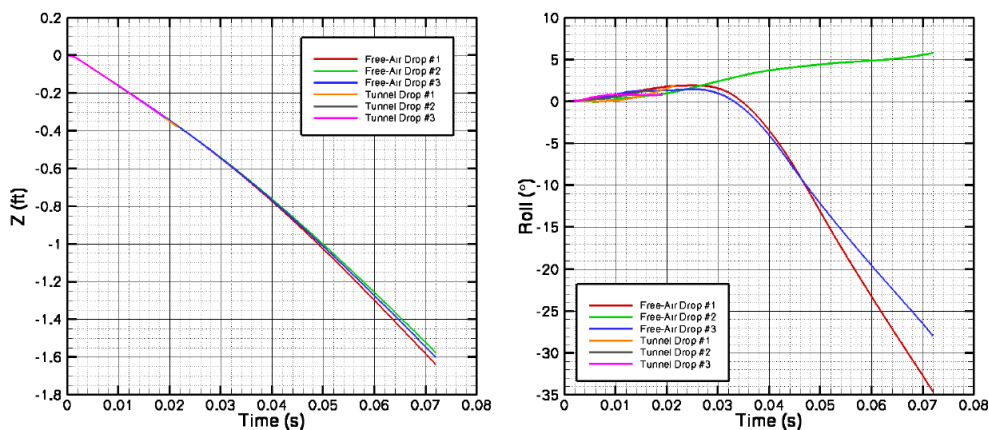


Figure 1.17: Vertical and roll angle variability [16]

from the bay of an F-111 aircraft. Simulations performed at Mach 0.80 and 0.95 were performed using second order spacial discretisation and first order time integration of Euler's equations. The CFD results matched wind tunnel and flight test experiments for the vertical and axial positions. On the other hand, the span-wise translation, and the store attitudes showed large discrepancies between CFD and experiments. This may be due to the Euler equations for the flowfield which is not suitable for cavity flows [59].

Lee *et al.* [60] and Crowe *et al.* [61] used Beggar to simulate store release from the F-35. The geometry included the complete aircraft fuselage, the bay doors, and the complex F-35 weapon bay (Figure 1.18). The computations were performed using overlapping grids with DES with the Baldwin-Lomax model. GBU-12 and GBU-32 stores were released at a simulated altitude of 15000ft and at free-stream Mach number of 0.80. Overall, the simulated trajectories had similar trends compared to the wind tunnel tests. The release of the GBU-12 was repeated once and showed variability, but more simulations were required to build an understanding of how stores are released from complex cavity.

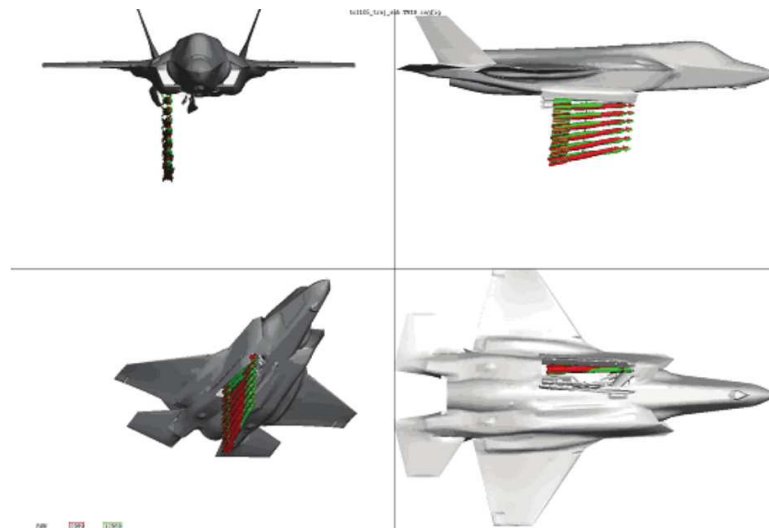


Figure 1.18: Comparison of GBU-12 trajectory between CFD and wind tunnel [60]

A CFD code used by Kim *et al.* [62] was also used to simulate releases using the  $k - \omega$  SST and DES models. The CFD was compared to the AEDC wind tunnel test described above. An AIM-9L store was released from an ideal cavity at Mach 0.95 using chimera grids. Four drops at different time instances showed small trajectory variability due to changes in the store loads. The same drops were repeated four

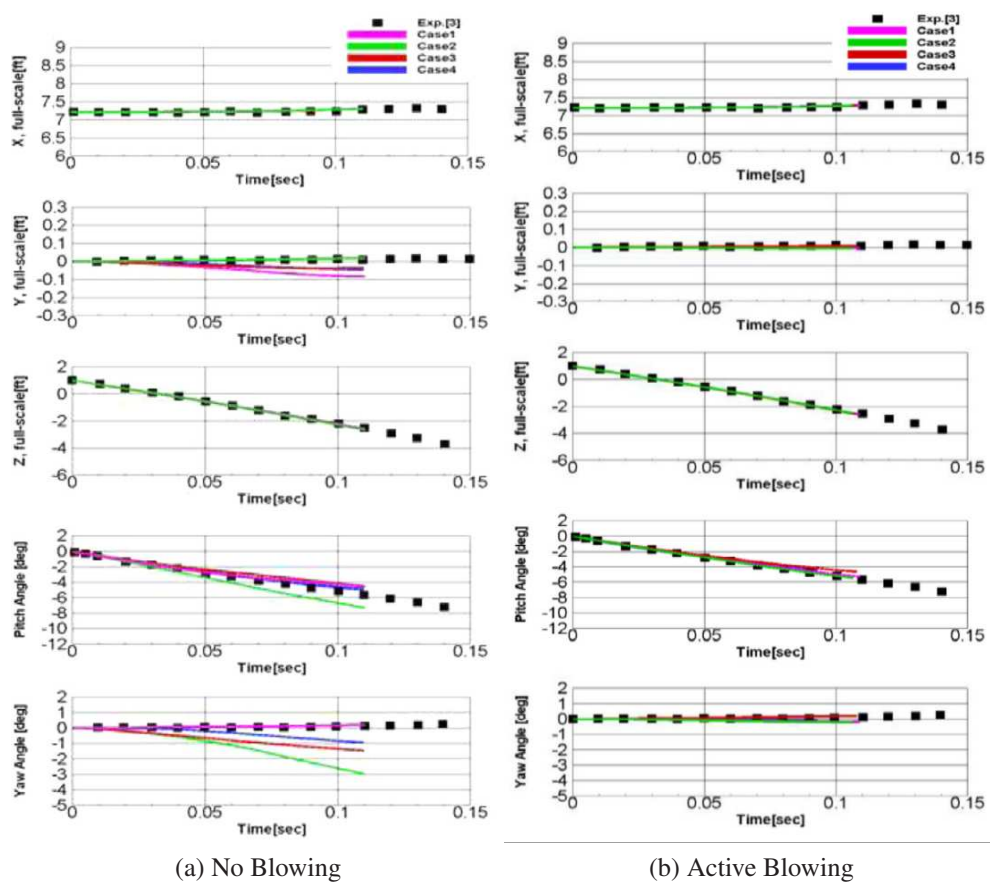


Figure 1.19: Trajectory variability with and without blowing at front wall <sup>[62]</sup>

times with a steady blowing at the leading lip of the cavity that appeared to reduce the variability (Figure 1.19) due to a reduction of the flowfield fluctuations. As the previous studies, this case requires more releases to define the trajectory envelope and estimate an average trajectory, in order to statically assess the active control effect.

The CFD code OVERFLOW developed by NASA was also used to simulate store releases using structured chimera grids and 6DoF. Westmoreland <sup>[63]</sup> was the first to use this method to compute the release of a GBU-38 store from an ideal cavity of  $L/D$  4.5. The Mach number was 0.95, and the store was released at four different instances in time, with and without stroke. The trajectories suggested large variability without stroke, and the fins hit the cavity walls for two cases. This was due to large yawing angles up to 12 degrees inside the cavity. Adding the stroke reduced the variability, and all the releases were successful. This is the first study showing that cavity flow fluctuations alter the store trajectories. Nevertheless, the study lacks depth, and the computations were not enough to understand the cause of the variability due to the

rich spectral content of the load signals.

<sup>[64]</sup> also used this code for 2D simulations, and failed to represent the 3D variability. Flora *et al.* <sup>[53]</sup> and Merrick *et al.* <sup>[54]</sup> used their supersonic experiments described above to validate OVERFLOW. The computations were performed using the SST-DDES turbulence model. Overall, the code captured the trend of the trajectories varying the total pressure. However, the simulated trajectories did not capture the upstream motion of the sphere at the early stage of the release. This suggests that the CFD underestimated the re-circulation inside the cavity. This code did not prove to be able to capture the trajectory variability for this case, as every experimental condition was computed only once.

More recently, a CFD code was used by Yan *et al.* <sup>[65]</sup> to perform the release of the AGARD store from the M219 cavity. The Mach number was 1.35, and the SST-IDDES turbulence model was employed. Due to the cost of IDDES, only one release was computed. In addition, the store was very large, heavy, and was ejected with a force much larger than the aerodynamics forces. That work should have considered multiple releases of a smaller and lighter store more likely to be influenced by the cavity flow. Due to the large size of the store, the cavity flow feedback loop was disrupted while the store was crossing the shear layer.

Study	Bay Geometry	Store	Mach	Turbulence model	Code	Method
Johnson <i>et al.</i> <sup>[56]</sup> (2004)	Complex F/A-22	MMTD	0.90, 1.30	-	-	GM
Johnson <i>et al.</i> <sup>[58]</sup> (2004)	Complex F-111	SSB	0.80, 0.95	Euler	Beggar	TA
Smith <i>et al.</i> <sup>[57]</sup> (2006)	Complex BX-45A	SSB	0.80	-	-	GM
Lee <i>et al.</i> <sup>[47]</sup> (2008)	Complex B-1B	GBU-38	0.88	DES S-A	Beggar	TA and GM
Sickles <i>et al.</i> <sup>[48]</sup> (2008)	Complex B-1B	GBU-38	0.88	DES SST	NXAIR	TA and GM
Spinetti <i>et al.</i> <sup>[49]</sup> (2008)	Complex B-1B	GBU-38	0.88	DES S-A	Beggar	TA
Wastmoreland <sup>[63]</sup> (2009)	Prism L/D 4.5	GBU-38	0.95	-	Overflow	TA
Davis <i>et al.</i> <sup>[16]</sup> (2009)	Prism L/D 7.0 and 8.0	Mk-82, GBU-38	0.80	SST $k - \omega$ , RANS	USM3D	TA and GM
Finney <sup>[55]</sup> (2010)	Prism L/D 4.5	Mk-82	0.85	Steady S-A	TetrUSS	GM
Lee <i>et al.</i> <sup>[60]</sup> (2010)	Complex F-35B	GBU-12, GBU-32	0.80	Baldwin-Lomax model	Beggar	TA
Crowe <i>et al.</i> <sup>[61]</sup> (2010)	Complex F-35B	GBU-12	0.80	S-A DES	Beggar	TA
Kraft <i>et al.</i> <sup>[64]</sup> (2011)	Rectangular L/D 4.5	GBU-38	0.95	SST-DDES	Overflow	TA
Flora <i>et al.</i> <sup>[53]</sup> (2014)	Prism L/D 4.5	Mk-82, Sphere	2.90	SST-DDES	Overflow	TA
Kim <i>et al.</i> <sup>[62]</sup> (2015)	Prism L/D 4.5	AIM-9L	0.95	$k - \omega$ SST-DES	-	TA
Merrick <i>et al.</i> <sup>[54]</sup> (2016)	Prism L/D 4.5	Sphere	2.22	SST-DDES	Overflow	TA
Yan <i>et al.</i> <sup>[65]</sup> (2017)	Prism L/D 7.0	AGARD	1.35	SST-IDDES	-	TA

**TA: Time Accurate - GM: Grid Method**

Table 1.4: Summary of numerical store release studies

There are more and more numerical tools available, capable to simulate store releases as shown table 1.4. However, due to the cost of DES and LES required for cavity flow simulations, a very small amount of data was produced, and the physics that drive the store trajectory is still to be understood. For example the simulation of the GBU-32 release from the B-1B by Sickles *et al.* [48] took 33 days for a single release. As shown by Babu *et al.* [66] Scale-Adaptive Simulations (SAS) [45] can reduce this time almost by an order of magnitude, and resolve well the cavity flow. This means that practical calculations of store releases are in reach with current computer technology. The only way to go further, is to perform a statistical study simulating a large number of releases to understand which flow structures drive variability. The knowledge to be gained on these releases may help design future cavity bays with flow control.

### 1.1.5 Cavity Flow Control

Since the problems arising from cavity flows were first observed, efforts were put forward to mitigate them. Despite more than 70 years of work, the problem is not trivial, and cavity flow control remains an active research area. The ideal control method has to weaken both the tonal and the broadband noise for better stealth. In addition, the shear layer has to be steady for safer store release, and shedding of vortical structures away from the cavity must be reduced and not impact aircraft structures. Cavity flow control methods were categorised by Cattafesta III *et al.* [67] as passive and active class (Figure 1.20). Active control methods use actuators altering the flow, in open, or closed loop. A summary of previous studies on active flow control can be found in the work by Cattafesta III *et al.* [67] and Rowley *et al.* [68]. The present survey focuses on passive flow control, involving the modification of the geometry, or the addition of static devices to alter the cavity flow.

One of the most effective passive control methods is the modification of the cavity aft wall by rounding [69, 70], or slanting [71, 72, 17]. This leads to significant noise reduction, of the order of 10 dB as measured on the M219 cavity [32], and to less radiated noise [73, 74]. Also both broadband, and tonal noise was reduced. The main effect of a slanted wall is to direct the reflected acoustic waves out of the cavity, breaking the feedback loop driving the oscillations [75]. In addition, a slanted wall alleviates the impact of the shear layer on the aft wall, and reduces the amplitude of the radiated pressure waves [24]. Malhotra *et al.* [76] tried to vertically offset the aft wall

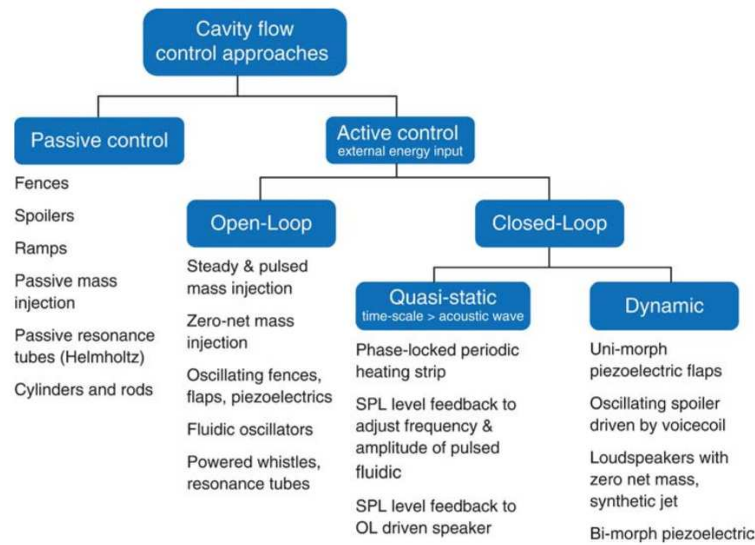


Figure 1.20: Classification of flow control types<sup>[68]</sup>

to reduce the effect of the shear layer impact on the cavity. Three offsets between 0 and 10% of the cavity depth were tested at Mach 1.71, and a reduction of the broadband and tonal noise was reported. Nevertheless, more cavity tones were present.

Roberts *et al.*<sup>[77]</sup> modified the front and aft walls of a prismatic cavity adding perforated plates coupled with a backing volume. The experiments were carried out at transonic speeds with six different perforated arrays at the front and aft of the cavity. Each array was characterised by an absorption coefficient depending on each frequency. Using a single array was very effective in weakening the dominant tone by 14 dB. However, a small frequency band was influenced, and the OASPL decreased by only 2dB. Using two arrays at the front and the aft of the cavity, single peaks were further damped, and the broadband noise slightly decreased outside the bandwidth of the selected arrays. The main drawback of this solution is that only a small frequency band can be controlled, and bay tones vary within the flight envelope.

Multiple spoilers were also extensively studied by researchers, including flat-top<sup>[79, 72, 80, 81]</sup>, saw-tooth<sup>[71, 75, 82, 73, 83, 84, 85]</sup>, and square-tooth designs<sup>[78]</sup> (Figure 1.21). Overall, this solution was as effective as slanting the aft wall, on the aft part of the cavity. The shear layer was lifted, reducing the generated noise when impacting the aft wall, and the tones shifted to higher frequencies<sup>[32]</sup>. On the other hand, milder effects were reported for the front of the cavity using spoilers. Saddington *et al.*<sup>[78]</sup> performed experimental comparisons between flat-top, saw-tooth, square tooth spoilers, and a leading edge wedge for transonic cavities. All spoilers lead to

similar OASPL reduction of about 8dB, with a slightly better result for the square tooth design.

In a similar way, transverse rods were placed at the leading edge of the cavities to modify the behaviour of the shear layer as it bridges the bay [87, 80, 86, 81, 90]. This solution was slightly less effective than slanting the wall of the M219 cavity [32, 73], and more effective than the saw-tooth spoiler. Overall, the noise reduction increases with the rod diameter as measured by Smith *et al.* [88]. As for the saw-tooth spoilers, they lift the shear layer helping to reduce the noise generated at aft wall. Furthermore, the vortex shedding downstream a rod is believed to energise the shear layer. Consequently, it is less likely to breakdown, and bridges the cavity more easily [89].

Spoilers and rods contribute a drag component, and lead to shedding more vortices downstream the cavity. Perforated plates are very effective in reducing single tones, but at limited flight conditions. The modification of the aft wall geometry by slanting or rounding is the most effective solution to date. Nevertheless, after OASPL reductions by 10dB, the noise levels remain large for all cases listed in table 1.5, and further work is needed for quieter bays.

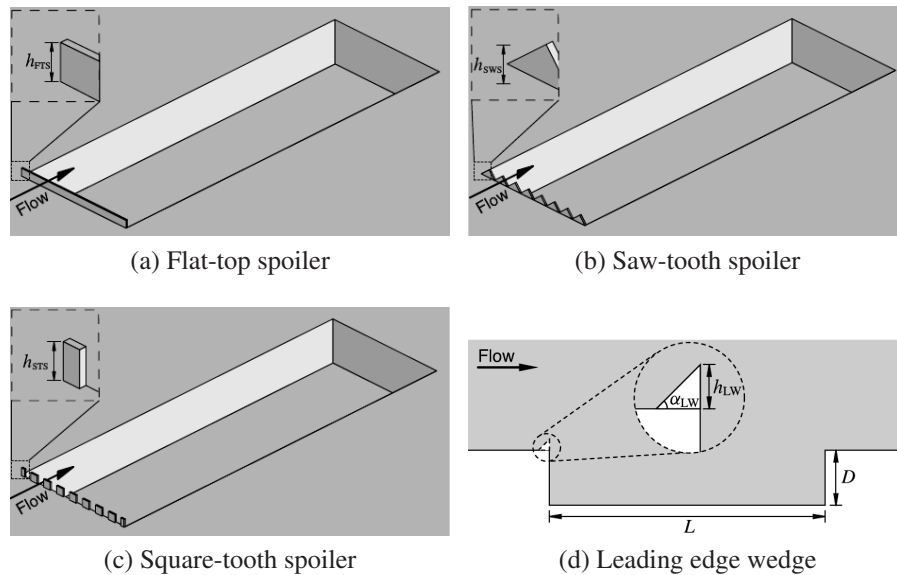


Figure 1.21: Spoiler tested by Saddington *et al.* [78]

Study	L/D	W/D	Mach	Method	Device
<b>Aft Wall Modifications</b>					
Shaw <i>et al.</i> (1988) <sup>[71]</sup>	6.8, 10.3	-	0.70 – 2.00	Exp.	Slanted wall
Baysal <i>et al.</i> (1994) <sup>[72]</sup>	4.5	2D	0.95	URANS/Mod B–L	Slanted wall
Zhang <i>et al.</i> (1998) <sup>[69]</sup>	3.0	2D	1.50	URANS/ $k-\omega$	Slanted, rounded wall
Nightingale <i>et al.</i> (2005) <sup>[32]</sup>	5.0, 10.0	1.0	0.85	Exp.	Slanted wall
Lawson <i>et al.</i> (2009) <sup>[73, 17]</sup>	5.0	1.0	0.85	DES/S–A	Slanted wall
Roberts <i>et al.</i> (2012) <sup>[77]</sup>	5.0	1.3	0.90	Exp.	Perforated plate with backing volume
Das <i>et al.</i> (2016) <sup>[70]</sup>	3.6	2.0	0.90	Exp., $k-\omega$ SST	Slanted, rounded wall
Malhotra <i>et al.</i> (2016) <sup>[76]</sup>	2.0, 3.0	-	1.71	Exp.	Wall vertical offset
<b>Inflow Spoilers</b>					
Rossiter <i>et al.</i> (1963) <sup>[79]</sup>	-	-	0.30 – 2.00	Exp.	Flat-top
Shaw <i>et al.</i> (1988) <sup>[71]</sup>	6.8, 10.3	-	0.70 – 2.00	Exp.	Saw-tooth
Baysal <i>et al.</i> (1994) <sup>[72]</sup>	4.5	2D	0.95	URANS/Mod B–L	Flat-top
Ukeiley <i>et al.</i> (2004) <sup>[80]</sup>	5.6, 9.0	2.0	0.60, 0.75	Exp.	Flat-top
Nightingale <i>et al.</i> (2005) <sup>[32]</sup>	5.0, 10.0	1.0	0.85	Exp.	Saw-tooth
Schmit <i>et al.</i> (2005) <sup>[86]</sup>	5.0	1.0	0.85, 1.19	Exp.	Saw-tooth
Ashworth (2008) <sup>[82]</sup>	5.0	1.0	0.85	DES/S–A	Saw-tooth
Levasseur <i>et al.</i> (2008) <sup>[81]</sup>	5.0	1.0	0.85	LES/SMAG	Flat-top
Lawson <i>et al.</i> (2009) <sup>[73]</sup>	5.0	1.0	0.85	DES/S–A	Flat-top & saw-tooth
Flora <i>et al.</i> (2014) <sup>[53]</sup>	4.5	1.0	2.90	Exp.	Saw-tooth
Saddington <i>et al.</i> (2016) <sup>[78]</sup>	5.0	2.0	0.71	Exp.	Flat-top & saw-tooth & square-tooth
Duben <i>et al.</i> (2017) <sup>[83]</sup>	7.1	1.8	0.80	DES	Flat-top & saw-tooth with venting
Abdrashitov <i>et al.</i> (2017) <sup>[84]</sup>	7.0	-	0.75	DDES, Exp.	Saw-tooth with venting
Luo <i>et al.</i> (2017) <sup>[85]</sup>	Complex cavity		1.5	IDDES	Saw-tooth
<b>Inflow Rods</b>					
Arunajatesan <i>et al.</i> (2002) <sup>[87]</sup>	5.6	2D, 1.0	0.60	HYB/ $k-\epsilon$	Rod
Smith <i>et al.</i> (2002) <sup>[88]</sup>	4.8	1.9	0.90	Exp.	''
Ukeiley <i>et al.</i> (2004) <sup>[80]</sup>	5.6, 9.0	2.0	0.60, 0.75	Exp.	''
Nightingale <i>et al.</i> (2005) <sup>[32]</sup>	5.0, 10.0	1.0	0.85	Exp.	''
Schmit <i>et al.</i> (2005) <sup>[86]</sup>	5.0	1.0	0.85, 1.19	Exp.	''
Comte <i>et al.</i> (2008) <sup>[89]</sup>	0.4	0.4	0.80	LES	''
Levasseur <i>et al.</i> (2008) <sup>[81]</sup>	5.0	1.0	0.85	LES/SMAG	''
Lawson <i>et al.</i> (2009) <sup>[73]</sup>	5.0	1.0	0.85	DES/S–A	''
Omer <i>et al.</i> (2015) <sup>[90]</sup>	1.0	1.0	0.45	Exp., DES	Rod placed at multiple locations

Table 1.5: Summary of passive flow control studies of cavity flows.

## 1.2 Thesis Objectives

In light of the literature survey, the fundamental mechanism of cavity flow still needs investigation before tackling real-world designs. This project aims for a better understanding of the mechanisms driving real weapon bay flows.

- The first objective is to develop a better understanding of the fundamental physics behind cavity flows using a simple model.
- Then, the project aims to find a way to apply the beamforming method to localise the sources of noise around a cavity flow, with a limited number of probes. This makes it possible for researchers to measure the noise level far from the cavity, without intrusive techniques.
- In terms of applied research, this thesis pursues the development of a numerical framework, that could compute the complete weapon bay operation, within a short time for engineering applications.
- The transient flowfield is described during the door opening, and for fixed doors, to determine if doors have to be taken into account for bay design.
- Aeroelastic simulations are performed to quantify the store deformations during the weapon bay operation. This aims to identify fatigue issues that may arise from the pressure fluctuations, and to determine the relationship between the pressure field and the store deformations.
- Store releases are performed from carriage position in order to develop a better understanding of the physics involved in terms of statistics, and store trajectory variability. This also aims to understand the aeroelasticity, doors, and store properties effects on the releases.
- Finally, this thesis shows novel cavity flow control methods, in order to reach lower noise levels than a cavity with slanted cavity wall.

## 1.3 Thesis Outline

The thesis is organised as follows:

Chapter 1 presents the motivation behind the current work, a literature review, and the objectives of the study.

Chapter 2 presents background information of the study, and includes the governing equations of the flow, the turbulence models, and the CFD solver. The post-processing of the CFD data is also described.

Chapter 3 validates SAS using the M219 cavity experiments. Grid convergence, and the ability of SAS to capture the differences between different cavity configurations are also presented. The flow fluctuations are validated using the wavelet transform method.

Chapter 4 describes the beamforming technique applied to CFD results for the M219 cavity. Multiple microphone arrays are tested at different positions, and of different shapes, and density. Furthermore, recommendations are given regarding noise propagation model.

Chapter 5 presents a cavity flow model based on a standing wave resonator, influenced by the shear layer turbulence. Comparisons of the modelled unsteady pressure field with the M219 experiments are presented. Novel ideas and insight on the tone generation mechanism are drawn from the obtained results.

Chapter 6 presents the cases used for the numerical study of the weapon bay flow. These include a prismatic weapon bay, doors, and a finned store.

Chapter 7 presents the coupled aeroelastic method, and the simulations of elastic store within weapon bays. The store is held at carriage and at shear layer, and the relationship between the store deformations, and the cavity flow is established.

Chapter 8 presents CFD simulations of cavities with door opening. Static doors configurations are computed for different door angles, and are compared in terms of flowfield, noise, and loads between each other. Then, three door opening speeds are tested, and the transient flow is detailed. The effect of a store at carriage on the cavity flow establishment is also presented. Additionally, the elastic deformations of the store during door opening are compared to static cases.

Chapter 9 shows the use of SAS to study store trajectory variability for releases from weapon bays. A statistical metric is proposed to identify the minimum number of simulations necessary to capture the mean and standard deviation of the trajectories. Using averaged flow data, the trajectory phases are identified and the role of the pressure field inside the cavity is clarified. Then, filtering the simulation results, reveals the physics behind the trajectory variability. Furthermore, the aeroelastic effects on the

release are statistically measured.

The last chapter “Chapter 10” summarises the findings in terms of fundamental, and applied knowledge gained on transonic cavity flows. Directions for future work are also given.

Appendix A discusses the CFD results for the external aerodynamics of an isolated store at supersonic speed. Mesh convergence, and the turbulence models effects are presented.

Appendix B presents the use of POD for reconstructing the velocity variables. An example test case is provided.

Appendix C shows the codes used for beamforming, and cavity flow modelling.

A restricted appendix D concerns cavity flow control, and interested readers should contact the thesis supervisor Prof. George Barakos ([george.barakos@glasgow.ac.uk](mailto:george.barakos@glasgow.ac.uk))

Figure 1.22 summarises all the computations made to validate and simulate the weapon bay operation, with the corresponding chapter in the thesis. This does not include the cavity flow control, and the isolated store.

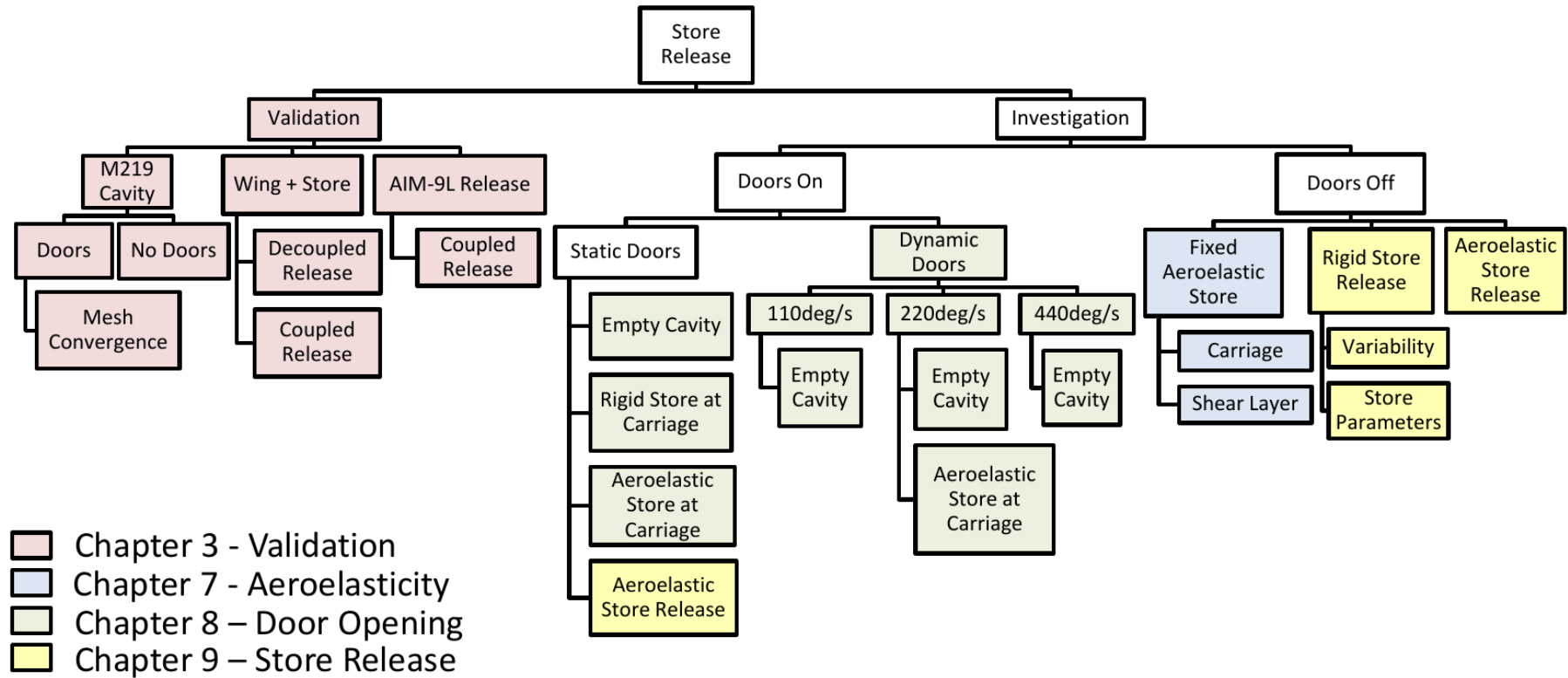


Figure 1.22: Summary of the computations performed to simulate the weapon bay operation.

# Chapter 2

## Mathematical Models and CFD

### Methods

This chapter presents the employed simulation tools, and post-processing techniques used for this project. First, the Helicopter Multi-Block (HMB3) flow solver developed at the University of Glasgow is presented including the governing equations, and the description of turbulence models. Then, the methods of data analysis and post-processing methods are described.

#### 2.1 CFD Method

The HMB [91, 92, 93] is used as the CFD solver for the present work. It solves the Unsteady Reynolds Averaged Navier-Stokes (URANS) equations in integral form using the arbitrary Lagrangian Eulerian (ALE) formulation, first proposed by Hirt *et al.* [94], for the time-dependent domains with moving boundaries:

$$\frac{d}{dt} \int_{V(t)} \mathbf{W} dV + \int_{\partial V(t)} (\mathbf{G}_i(\mathbf{W}) - \mathbf{G}_v(\mathbf{W})) \mathbf{n} dS = \mathbf{S}_{\text{source}}, \quad (2.1)$$

where  $V(t)$  is the time dependent control volume,  $\partial V(t)$  its boundary,  $\mathbf{W}$  is the vector of conserved variables  $[\rho, \rho u, \rho v, \rho w, \rho E]^T$ , where the variables  $\rho, u, v, w, P$  and  $E$  have their usual meaning of density, three components of velocity, pressure, and total energy, respectively.  $\mathbf{G}_i$  and  $\mathbf{G}_v$  are the inviscid and viscous fluxes, including the effects of the time dependent domain, and  $\mathbf{n}$  is the outward pointing unit normal vector.

The Navier-Stokes equations are discretised using a cell-centred finite volume approach on a multi-block grid. The spatial discretisation of these equations leads to a

set of ordinary differential equations in time,

$$\frac{d}{dt}(\mathbf{W}_{i,j,k} V_{i,j,k}) = -\mathbf{R}_{i,j,k}(\mathbf{W}_{i,j,k}), \quad (2.2)$$

where  $i, j, k$  represent spatial components,  $\mathbf{R}$  is the flux residual vectors, and  $V$  is the volume of the cell. To evaluate the convective fluxes, Osher's <sup>[95]</sup> approximate Riemann solver is used for the present computations, while the viscous terms are discretised using a second order central differencing spatial discretisation. The Monotone Upstream-centred Schemes for Conservation Laws (MUSCL) developed by van Leer <sup>[96]</sup> is used to provide second order accuracy in space. HMB uses the alternative form of the van Albada limiter <sup>[97]</sup> activated in regions where large gradients are encountered, mainly due to shock waves, avoiding the non-physical spurious oscillations. An implicit, dual-time stepping method is employed to performed the temporal integration <sup>[93]</sup>. The solution is marching in the pseudo-time to achieve fast convergence, using a first-order backward difference. The linearised system of the Navier-Stokes equations is solved using the Generalised Conjugate Gradient (GCG) method with a Block Incomplete Lower-Upper (BILU) factorisation as a preconditioner <sup>[98]</sup>. Multi-block structured meshes are used for HMB, which allow easy sharing of the calculation load in parallel computing. Structured multi-block hexa meshes are generated using ICEM-Hexa<sup>TM</sup>.

## 2.2 Variable Extrapolation-MUSCL Approach

Second-order spatial accuracy for the convective flux of the Navier-Stokes equations can be achieved using upwind schemes. This process is based on the Godunov's first-order scheme <sup>[99]</sup> developed for the Lagrangian equations of ideal compressible flow, and followed by van Leer <sup>[100]</sup>. The Monotone Upstream-centred Scheme for Conservation Laws is referred to in the literature as the MUSCL approach, and was developed by van Leer <sup>[96]</sup>. This scheme builds on a first-order, Total Variation Diminishing (TVD) scheme for a second-order spatial accuracy. Instead of replacing the original state quantities by piecewise constant functions, MUSCL uses a linear function. These linear distributions make possible to attain second-order accuracy. The state quantities at the interfaces can be obtained from an extrapolation of the neighbouring cells. To illustrate this idea, the extrapolation values at the right face of  $j + 1/2$  within cell  $j + 1$  is shown, where an uniform spacing in one dimension

is used. The superscripts L and R refer to the left and right sides at the considered interface,

$$\mathbf{F}_{j+1/2}^L = \mathbf{F}_j + \Phi(r_j) \left[ \frac{k_1}{2} (\mathbf{F}_{j+1} - \mathbf{F}_j) + (1 - k_1) \nabla \mathbf{F}_j \bullet \mathbf{r}_{f_j} \right]. \quad (2.3)$$

$$\mathbf{F}_{j+1/2}^R = \mathbf{F}_{j+1} - \Phi(r_{j+1}) \left[ \frac{k_1}{2} (\mathbf{F}_{j+1} - \mathbf{F}_j) + (1 - k_1) \nabla \mathbf{F}_{j+1} \bullet \mathbf{r}_{f_{j+1}} \right]. \quad (2.4)$$

In Eqns. 2.3 and 2.4, the vectors  $\mathbf{r}_{f_j}$  and  $\mathbf{r}_{f_{j+1}}$  represent the distances between the cell-centre face  $j + 1/2$  and the cell-centre volumes  $j$ , and  $j + 1$ , respectively. The parameter  $k_1$  is used to provide different spatial accuracy and properties of the MUSCL-scheme. The value of  $k_1$  in the standard HMB is set up to zero which corresponds a linear interpolation at the interface against an upstream and a downstream cell, providing a 2nd-order upwind scheme.

To reconstruct the gradients  $\nabla \mathbf{F}_j$  and  $\nabla \mathbf{F}_{j+1}$  at cell-centre volumes  $j$  and  $j + 1$ , HMB uses a second-order finite difference approximation:

$$\nabla \mathbf{F}_j \bullet \mathbf{r}_{f_j} = \frac{1}{4} \left( \mathbf{F}_{j+1} - \mathbf{F}_{j-1} \right). \quad (2.5)$$

$$\nabla \mathbf{F}_{j+1} \bullet \mathbf{r}_{f_{j+1}} = \frac{1}{4} \left( \mathbf{F}_{j+2} - \mathbf{F}_j \right). \quad (2.6)$$

This formulation is less expensive than Green-Gauss or Least Squares methods <sup>[101]</sup>, and it does not require to exchange data for parallel executions. So, this presents a compromise between accuracy and computational time.

The limiter function is represented as  $\Phi(r)$ , and  $r_j = \frac{\mathbf{F}_j - \mathbf{F}_{j-1}}{\mathbf{F}_{j+1} - \mathbf{F}_j}$  and  $r_{j+1} = \frac{\mathbf{F}_{j+1} - \mathbf{F}_j}{\mathbf{F}_{j+2} - \mathbf{F}_{j+1}}$  are the ratio of successive gradients. This scheme has the properties of monotonicity, so does not produce non-physical solutions, such as expansion shocks which correspond to a negative entropy variation. In addition, the entropy condition is satisfied in the sense of Lax <sup>[102]</sup>. Introducing the limiter function  $\Phi(r_j)$ , first and high-order schemes can be combined. In fact, if  $\Phi(r_j) = 0$  the first-order is activated but if  $\Phi(r_j) = 1$  a higher-order scheme is activated, which is at least second-order of accuracy. The HMB solver uses the alternative form of the van Albada limiter <sup>[97]</sup> namely,

$$\Phi(r) = \frac{2r}{r^2 + 1}. \quad (2.7)$$

Indeed, this limiter is activated in regions where large gradients are found due to shock waves and thin boundary layers, avoiding non-physical spurious oscillations. It is interesting to note that this limiter function is not second order TVD because this limiter cannot guarantee the following inequality for any  $r \in (1,2)$ ,

$$1 \leq \Phi(r) \leq r. \quad (2.8)$$

The advantages of using this limiter function is that is differentiable for any value of  $r$ .

## 2.3 Turbulence Modelling

Understanding turbulent flow behaviour has brought out an enormous interest in many fields of science. In weapon bays, the flow is very turbulent due to the shear layer spanning the cavity length, and the shedding of vortical structures. Despite the widespread development of computers which allowed to boost the number of works in turbulence modelling, we still do not understand in detail turbulent flow behaviour. The Navier-Stokes equations, which were introduced in the early 19<sup>th</sup> Century by Navier and Stokes, present a few exact solutions due mainly to their non-linearity and variety of boundary conditions. The result of this complexity implied the introduction of simplifications and assumptions. Reynolds identified one of the most famous dimensionless parameter in turbulence, the Reynolds number (Re), that expresses the relative importance of inertial and viscous forces <sup>[103]</sup>. A turbulent flow can be characterised by the following features: chaotic motion, non-repeatability, large range of length and time scales, diffusion and dissipation, three dimensionality and rotationality <sup>[104]</sup>.

### 2.3.1 The Reynolds-Averaging

In presenting different turbulent models, it is important to begin with key concepts, such as the Reynolds decomposition and averaging. The Reynolds decomposition of  $u(x,t)$ , separates the averaged and the fluctuating or random parts, of a signal obtained from a turbulent flowfield. These quantities can be expressed as,

$$u(x,t) = \bar{u}(x) + u'(x,t), \quad (2.9)$$

where  $\bar{u}(x)$  and  $u'(x,t)$  are averaged and fluctuating parts, respectively. The averaged part represents a steady quantity, while that the fluctuation part represents a random

with mean zero. This decomposition is used to rewrite the Navier-Stokes equations introducing this formulation. This process has to be followed by the adoption of an averaging method. This entire formulation is widely known as Reynolds average.

### 2.3.2 RANS and URANS

In this work the averaged Navier-Stokes equations were used. In a turbulent flow, the fields of density, velocity, pressure, and temperature vary randomly in time. Reynolds approach involves separating the flow quantities into stationary and random parts. The quantities are then presented as a sum of the mean flow value and the fluctuating part. The Reynolds-Averaged Navier-Stokes Equations can be derived employing the Reynolds decomposition and averaging mass, momentum, and energy equations. The compressible Reynolds-Averaged Navier-Stokes equations (also known as the Favre-Averaged Navier-Stokes Equations) <sup>[105]</sup> can be written as follows:

$$\frac{\partial \bar{\rho}}{\partial t} + \frac{\partial}{\partial x_j} (\bar{\rho} \hat{u}_j) = 0. \quad (2.10)$$

$$\frac{\partial (\bar{\rho} \hat{u}_i)}{\partial t} + \frac{\partial}{\partial x_j} (\bar{\rho} \hat{u}_i \hat{u}_j) = -\frac{\partial \bar{P}}{\partial x_i} + \frac{\partial \bar{\sigma}_{ij}}{\partial x_j} + \frac{\partial \tau_{ij}}{\partial x_j}. \quad (2.11)$$

$$\frac{\partial (\bar{\rho} \hat{E})}{\partial t} + \frac{\partial}{\partial x_j} (\bar{\rho} \hat{u}_j \hat{E}) = \frac{\partial}{\partial x_j} (\bar{\sigma}_{ij} \hat{u}_i + \overline{\sigma_{ij} u_i''}) - \frac{\partial}{\partial x_j} (\bar{q}_j + c_p \overline{\rho u_j'' T''} - \hat{u}_i \tau_{ij} + \frac{1}{2} \overline{\rho u_i'' u_i'' u_j''}). \quad (2.12)$$

where  $\hat{E} = \hat{E} + \frac{\bar{P}}{\bar{\rho}}$  is the total enthalpy,  $\bar{q}_j = -\overline{k_T \partial T / \partial x_j} \approx -\frac{c_p \hat{\mu}}{Pr} \frac{\partial \hat{T}}{\partial x_j}$  is the heat flux vector, and the viscous stress tensor is:

$$\bar{\sigma}_{ij} \approx 2\hat{\mu} \left( \hat{S}_{ij} - \frac{1}{3} \frac{\partial \hat{u}_k}{\partial x_k} \delta_{ij} \right). \quad (2.13)$$

The Reynolds stress tensor is defined as  $\tau_{ij} = -\overline{\rho u_i'' u_j''}$ , defined in tensor notation. The term  $c_p$  represents the heat capacity at constant pressure, and  $Pr$  is the Prandtl number (around 0.72 for air). The overbar represents the conventional time-average mean. The hat represents the Favre or density-weighted average defined as:  $\hat{f} = \frac{\overline{\rho f}}{\bar{\rho}}$  where  $f = \bar{f} + f' = \hat{f} + f''$ . The Sutherland's Law is used here to relate the dynamic viscosity  $\hat{\mu}$  with the temperature of an ideal gas <sup>[106]</sup>:

$$\hat{\mu} = \mu_0 \left( \frac{\hat{T}}{T_0} \right)^{3/2} \left( \frac{T_0 + S}{\hat{T} + S} \right), \quad (2.14)$$

where  $\mu_0 = 1.716 \times 10^{-5}$  kg/(ms),  $T_0 = 273.15$  K, and  $S = 110.4$  K. Finally, the equation of state is written as:

$$\bar{P} = (\gamma - 1) \left( \bar{\rho} \hat{E} - \frac{1}{2} \bar{\rho} (\hat{u}^2 + \hat{v}^2 + \hat{w}^2) - \bar{\rho} k \right), \quad (2.15)$$

where  $\gamma$  is the heat capacity ratio and is often taken as 1.4 for air and  $k$  is the local turbulent kinetic energy  $k = [(\hat{u}'')^2 + (\hat{v}'')^2 + (\hat{w}'')^2]/2$ . We noted that there are more unknowns variables than equations. In fact, this is addressed via turbulence models. This problem is known in the literature as the *turbulence closure problem* [104]. So the following terms need to be modelled:

$$\begin{aligned} & \tau_{ij}, \\ & \overline{c_p \rho u''_j T''}, \\ & \overline{\sigma_{ij} u''_i}, \\ & \frac{1}{2} \overline{\rho u''_i u''_i u''_j}. \end{aligned} \quad (2.16)$$

Note that most turbulence models use the Boussinesq eddy viscosity hypothesis, which states that the Reynolds stress tensor  $\tau_{ij}$  can be calculated as a product of the mean strain rate tensor  $\hat{S}_{ij}$  and the dynamic eddy viscosity  $\hat{\mu}_t$ .

$$\tau_{ij} = 2\hat{\mu}_t \left( \hat{S}_{ij} - \frac{1}{3} \frac{\partial \hat{u}_k}{\partial x_k} \delta_{ij} \right) - \frac{2}{3} \bar{\rho} k \delta_{ij}, \quad (2.17)$$

where  $\hat{S}_{ij} = (\partial \hat{u}_i / \partial x_j + \partial \hat{u}_j / \partial x_i) / 2$ , and  $\hat{\mu}_t$  is the eddy viscosity obtained by the turbulence model. Likewise, a Reynolds analogy is used to model the turbulent heat flux:

$$\overline{c_p \rho u''_j T''} \approx - \frac{c_p \hat{\mu}_t}{Pr_t} \frac{\partial \hat{T}}{\partial x_j}, \quad (2.18)$$

where  $Pr_t$  is the turbulent Prandtl number and often taken to be constant (around 0.9 for air). Finally, the molecular diffusion and turbulent transport in the energy equation are often modelled together, for example:

$$\overline{\sigma_{ij} u''_i} - \frac{1}{2} \overline{\rho u''_i u''_i u''_j} \approx \left( \hat{\mu} + \frac{\hat{\mu}_t}{\sigma_k} \frac{\partial k}{\partial x_j} \right) \quad (2.19)$$

where  $\sigma_k$  is a coefficient associated with the turbulence model.

HMB3 has so far been validated for cavity flows and for a range of turbulence models. Unsteady Reynolds Averaged Navier-Stokes (URANS) models described above [107] failed to simulate cavity flows, showing large noise discrepancies, and over-predicting the strength of the vortices in the cavity. Today, Detached Eddy Simulation

(DES) <sup>[108]</sup> and Large Eddy Simulation (LES) <sup>[109]</sup> are by far the most common approach to account of the effect of turbulence of cavity flows. Lawson <sup>[73, 110]</sup> shown good agreement with experimental data of the M219 cavity <sup>[32]</sup> both in terms of noise, and flowfield. Nevertheless, DES and LES are still expensive especially when several computations of store releases are necessary, as they require small timestep and very fine grids. Promising results with Scale Adaptive Simulation (SAS) method <sup>[45]</sup> encouraged Babu *et al.* <sup>[66]</sup> to use this approach for weapon bay flows. Their results suggest that SAS captures the essential physics of the weapon bay, and at the same time, provides a significant reduction in CPU time by almost an order of magnitude. For this reason SAS is also used in the present work.

### 2.3.3 $k$ - $\omega$ and Shear Stress Transport (SST) Model

In 1988, Wilcox <sup>[111]</sup> developed the popular  $k$ - $\omega$  turbulence model to close the RANS equations with two transport equations for  $k$  and  $\omega$ . This model uses as second transported variable the specific turbulent dissipation frequency  $\omega$ , which is function of the scale of turbulence. The eddy viscosity is obtained by,

$$\mu_t = \rho \frac{k}{\omega}. \quad (2.20)$$

In 1994, Menter <sup>[112]</sup> proposed the hybridization of the  $k$ - $\omega$  turbulence model and the  $k$ - $\epsilon$  turbulence model. The aim was to combine the robust and accurate formulation of the  $k$ - $\omega$  model near the wall with the lack of sensitivity to free-stream values of the  $k$ - $\epsilon$  model far away from it. The transport equation for  $k$  and  $\omega$  of SST turbulence model are as follows:

$$\frac{\partial(\rho k)}{\partial t} + \frac{\partial(\rho u_j k)}{\partial x_j} = P - \beta^* \rho \omega k + \frac{\partial}{\partial x_j} \left[ (\mu + \sigma_k \mu_t) \frac{\partial k}{\partial x_j} \right] \quad (2.21)$$

$$\frac{\partial(\rho \omega)}{\partial t} + \frac{\partial(\rho u_j \omega)}{\partial x_j} = \frac{\gamma}{\nu_t} P - \beta \rho \omega^2 + \frac{\partial}{\partial x_j} \left[ (\mu + \sigma_\omega \mu_t) \frac{\partial \omega}{\partial x_j} \right] + 2(1 - F_1) \frac{\rho \sigma_\omega}{\omega} \frac{\partial k}{\partial x_j} \frac{\partial \omega}{\partial x_j} \quad (2.22)$$

A detailed description of the  $k$ - $\omega$  and  $k$ - $\omega$  SST models can be found in <sup>[111, 113, 112]</sup>.

### 2.3.4 Scale-Adaptive Simulation (SAS)

While Detached Eddy Simulation (DES) is capable of accurately predicting cavity flows <sup>[73, 110]</sup>, it still takes a considerable amount of time on a large number of

processors. Since its introduction by Menter *et al.* <sup>[114, 115, 116]</sup> in 2003, the SAS approach has gained popularity due to its LES-like behaviour in highly separated flow regions and found place in several studies. A detailed explanation of the theory and description of the model was given by Menter and Egorov <sup>[45]</sup>. Following on, work by Egorov *et al.* <sup>[117]</sup> presented the application of the SAS model, and its implementation in ANSYS-FLUENT and ANSYS-CFX, for a range of complex flows.

The governing equations of the SST-SAS model differ from those of the SST-RANS model<sup>[112]</sup> by the additional SAS source term  $Q_{SAS}$ , in the right side of the transport equation 2.22 for the turbulence eddy frequency, given by:

$$Q_{SAS} = \max \left[ \rho \zeta_2 \kappa S^2 \left( \frac{L}{L_{vK}} \right)^2 - C \frac{2\rho k}{\sigma_\Phi} \max \left( \frac{1}{\omega} \frac{\partial \omega}{\partial x_j} \frac{\partial \omega}{\partial x_j}, \frac{1}{k} \frac{\partial k}{\partial x_j} \frac{\partial k}{\partial x_j} \right), 0 \right] \quad (2.23)$$

where  $L$  is the length scale and  $L_{vK}$  is the von Karman length scale,

$$L = \frac{\sqrt{k}}{c_\mu^{1/4} \omega}, \quad L_{vK} = \frac{\kappa S}{|U''|} \quad (2.24)$$

with  $S = \sqrt{2S_{ij}S_{ij}}$  and  $S_{ij} = (\partial u_i / \partial x_j + \partial u_j / \partial x_i) / 2$  the strain rate tensor. The second derivative  $|U''|$  is generalised to 3D using the magnitude of the velocity Laplacian,

$$|U''| = \sqrt{\sum_{(i)} \left( \frac{\partial U_i}{\partial x_j \partial x_j} \right)^2} \quad (2.25)$$

and the constants are  $\zeta_2 = 3.51$ ,  $\sigma_\Phi = 2/3$ ,  $C = 2$ , and  $\kappa = 0.41$  the von Karman constant.

SAS is an improved URANS model that produce wider spectral content for unsteady flows by adjusting the turbulence length scale to the local flow inhomogeneities and balancing the contributions of modelled and resolved parts of the turbulent stresses. For steady flows, the turbulent kinetic energy  $k$ , and the length scale  $L$  are small, leading to  $Q_{SAS} = 0$ . Therefore, the model acts like the SST  $k-\omega$  model. However, for flows with transient instabilities like those with large regions of separation, larger values of  $k$  lead to an increase of  $Q_{SAS}$ , reducing the eddy viscosity according to the locally resolved vortex size represented by the von Karman length scale. This expands the turbulent spectra captured in the simulation towards the high frequencies. The SAS model can resolve the turbulent spectrum down to the grid limit and avoids RANS-typical single-mode vortex structures. For example, the RANS simulation of the wake behind a cylinder at high Reynolds will mainly contain periodic, and large vortices, while SAS simulation will give a larger range of structures down to the grid resolution,

like a DES, or LES simulation <sup>[118]</sup>. For cavity flows, this improves the simulation of the high frequency fluctuations of the flowfield that drive the acoustic resonance.

## 2.4 Overset Grid Method

Overset grids can be used with HMB <sup>[92, 119]</sup> to model the relative motion between different mesh components. This method has been widely employed for isolated rotor blades <sup>[120]</sup>, and complete helicopter configurations <sup>[92]</sup>. For the present work, an overset grid method is employed to explore its capabilities with moving doors and store.

The overset grid method, also referred to as chimera method, is based on structured composite grids with hexahedral elements, consisting of independently generated, overlapping, non-matching, sub-domains. A hierarchical approach is employed allowing to interpolate the solution variables based on an user-specified hierarchy of sub-domains. The interpolation between composite grids depends on a localisation procedure, that includes a localisation pre-processing and a chimera search which aim is to minimise the number of searches due to potential mesh overlap. Three methods are available to control the interpolation needed for the chimera solution; zero order single-neighbour, inverse distance, and variable-distribution reconstruction-based interpolation. Further information about the implementation of the overset grid method in HMB can be found in <sup>[119]</sup>.

## 2.5 Methods of Data Analysis

This section presents the techniques used to analyse the unsteady flow data. CFD flow-field files are written at specific instances in time, and flow “probes” at specific mesh points are sampled at every time step.

### 2.5.1 Pressure Signals

The Power Spectral Density (PSD), Overall Sound-Pressure Level (OASPL) and Band-Integrated Sound-Pressure Level (BISPL) are the basis of comparisons between experimental and numerical unsteady pressure data. The PSD is used to study the frequency content of a signal at a given location and is based upon the unsteady

pressure  $p'$ , where  $p' = p - \bar{p}$ . The PSD was calculated using the Burg Estimator<sup>[121]</sup> (also known as Maximum Entropy Methods or MEM) as it produces better resolved peaks for short signals than traditional Fast Fourier Transforms (FFT)<sup>[122]</sup>. For a description of the PSD in terms of decibels (dB), the natural definition is that of the Sound-Pressure spectrum Level (SPL)<sup>[123]</sup>:

$$SPL(f) = 10 \text{ LOG}_{10} \left[ \frac{PSD(f) \Delta f_{ref}}{p_{ref}^2} \right] \quad (2.26)$$

where  $\Delta f_{ref}$  is a reference frequency, usually set to 1 Hz and  $p_{ref}$  is the international standard for the minimum audible sound, which has the value of  $2 \times 10^{-5}$  Pa<sup>[123]</sup>.

The variation in pressure levels along the cavity floor was studied using the Root-Mean-Square (RMS) of the unsteady pressure,  $p'_{rms}$ , and can be obtained using the following equation:

$$p'_{rms} = \sqrt{\frac{1}{N} \sum (p')^2} \quad (2.27)$$

Although  $p'_{rms}$  is measured in Pascal (or any other unit of pressure), it is customary in cavity flow studies to report it as the Overall Sound-Pressure Level(OASPL)<sup>[123]</sup>:

$$OASPL = 20 \text{ LOG}_{10} \left[ \frac{p'_{rms}}{p_{ref}} \right] \quad (2.28)$$

which has the units of decibels. BISPL plots show the energy content within a particular frequency range and are calculated using the following equation:

$$BISPL = 20 \text{ LOG}_{10} \left[ \left( \int_{f_1}^{f_2} PSD(f) \right)^{1/2} \cdot \frac{1}{p_{ref}} \right] \quad (2.29)$$

where  $f_1$  and  $f_2$  are the lower and upper limits of the desired frequency range. For cavity flow studies, the BISPL plots are centred around the Rossiter Modes.

### 2.5.2 Time Frequency Analysis - Morlet Wavelet Method

The cavity flow is highly unsteady, and its dynamics must be understood to gain insight into its physics. The continuous Morlet wavelet transform is a method for time-frequency analysis<sup>[124]</sup>, that reveals the temporal fluctuations of the different frequencies present in the flow. The wavelet transform  $W_{\Psi}^y(f, t)$  is a convolution of the signal  $s(t)' = s(t) - \bar{s}$  with a scaled mother wavelet  $\Psi(t)$  conserving the sign of the signals in time and frequency:

$$W_{\Psi}^y(a, b) = \frac{1}{\sqrt{c_{\Psi} |a|}} \int_{-\infty}^{\infty} s'(t) \Psi \left( \frac{t-b}{a} \right) dt. \quad (2.30)$$

In the above equation,  $a$  is called the dilatation or the scale,  $b$  the translation parameter,  $c_\Psi = \sqrt{\pi/\beta}$  and  $\beta = \omega_0^2$ . The dilatation  $a$  is related to the frequency  $f$  of the wavelet, the translation parameter  $b$  is related to the time shift  $t$  of the wavelet. The mother, or Gabor wavelet  $\Psi(t)$  is given by :

$$\Psi(t) = e^{-\frac{\beta t^2}{2}} e^{j\omega t} \quad (2.31)$$

Band Integrated Wavelets (BIW) plots show the energy content within a particular frequency range and are calculated using the following equation:

$$BIW(t) = \int_{f_1}^{f_2} W_\Psi^y(f, t)^2 \quad (2.32)$$

where  $f_1$  and  $f_2$  are the lower and upper limits of the desired frequency range.

The wavelet envelope  $|\overline{W_\Psi^y}|$  is the amplitude of the frequency in time, and is determined using the maximum of the absolute value of the wavelet transform  $\overline{W_\Psi^y}$  over windows equal to half a period of the frequency (Figure 2.1). The wavelet amplitude in decibels  $W_{dB}$  is given by:

$$W_{dB}(f, t) = 20 \text{ LOG}_{10} \left[ \frac{|\overline{W_\Psi^y}(f, t)|^2}{P_{ref}} \right] \quad (2.33)$$

In the same way, the Band Integrated Wavelets amplitude in decibel  $BIW_{dB}$  is given by:

$$BIW_{dB}(t) = 20 \text{ LOG}_{10} \left[ \int_{f_1}^{f_2} \frac{|\overline{W_\Psi^y}(f, t)|^2}{P_{ref}} \right] \quad (2.34)$$

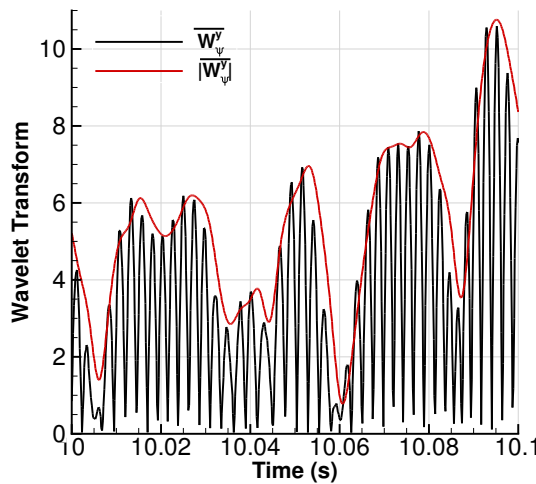


Figure 2.1: Computation of the wavelet envelope  $|\overline{W_\Psi^y}|$ .

### 2.5.3 Noise Directivity

The local noise intensity is defined as:

$$I = \frac{p_{RMS}^2}{\rho c} \quad (2.35)$$

with  $\rho$  the density, and  $c$  the sound speed. A noise directivity factor is then defined over a surface around the source of noise, as the ratio of the local noise intensity  $I$  divided by the average noise intensity  $I_{av}$  on the scanned surface:

$$Q_f = \frac{I}{I_{av}} \quad (2.36)$$

Then, the directivity  $DI$  is computed on every CFD point of the scanned surface:

$$DI = 10 \log_{10}(Q_f). \quad (2.37)$$

The directivity depends both on the noise emitted by every point inside the cavity, and on the distribution of the noise sources.

### 2.5.4 Solution Monitoring

In this work, the time is expressed in terms of cavity travel times, which is the time it takes for a flow particle moving at  $U_\infty$  to run the cavity length  $L$ .

The boundaries of the shear layer are defined as the strictly positive values of the momentum  $Q$ , product between the flow momentum, and the local contribution to the displacement thickness. The negative values due to the cavity flow re-circulation are imposed to zero:

$$Q = \max\left(0, \frac{\rho u}{\rho_\infty U_\infty} \left(1 - \frac{u}{U_\infty}\right)\right) \quad (2.38)$$

The thickness of the shear layer is given by the momentum thickness  $\theta$ :

$$\theta(x, y) = \int_{-D}^{\infty} Q(x, y, z) dz \quad (2.39)$$

with  $z$  the normal to the shear layer, and  $D$  the cavity depth.

Streamlines and particle tracing methods are efficient and common tools for visualising flowfields. They give an intuitive description of the flowfield by showing the path that particles follow in the three dimensional environment. However, results often depend greatly on the number of seeding particles and their initial position, and may give an incomplete description of the flowfield by missing small, isolated features.

Imaging of vector fields was carried out through the use of Line Integral Convolution (LIC). LIC is an image processing technique first introduced by Cabral and Leedom <sup>[125]</sup> in 1993 and has been used by Khanal *et al.* <sup>[126, 127, 128]</sup> to study the flow behaviour in cavities with passive flow control devices and a cavity with a store. The principle of the method can be described as the computation of small, local streamlines from a cloud of points randomly distributed inside the domain. It can process dense 2D or 3D vector fields and found applications in many domains from image processing to the representation of fluid flows.

The standard algorithm applicable to fluid mechanics starts from a textured image of the domain, which is usually a white noise (Figure 2.2a). The velocity vector field is used to calculate local streamlines which originate in the centre of each pixel and moves in both the positive and negative directions. The output image is the result of the one dimensional convolution of the random field and the kernel function filter, computed along the local streamlines (Figure 2.2c). An exact integral of the convolution kernel is used to normalise the output of the convolution and avoid distortion in brightness and contrast due to the filter shape.

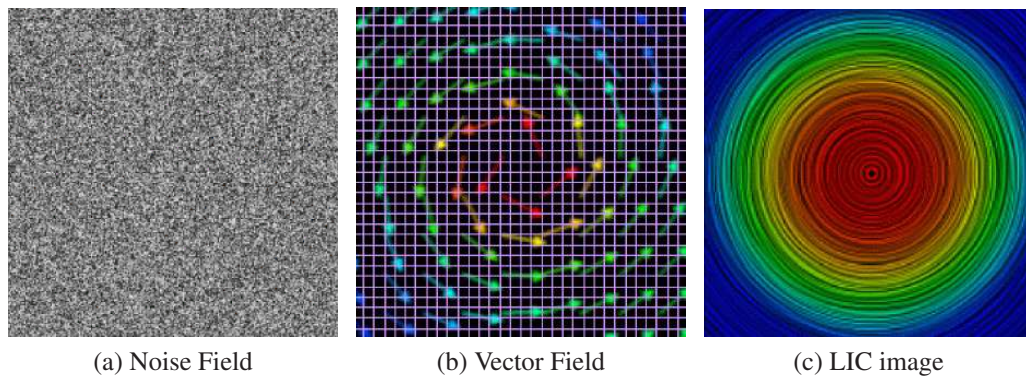


Figure 2.2: Convolution of an input vector field (a) with noise field (b) to produce an LIC image (c) <sup>[129]</sup>.

# Chapter 3

## Validation of the CFD Method

### 3.1 Geometric and Computational Model

Simulations were carried out for the M219 cavity [32]. M219 has a length to depth ratio of 5, a width to depth ratio of 1, and a length of 0.51m. Experiments were carried out by Nightingale *et al.* [32] at Mach 0.85, and a Reynolds number  $Re_L$ , based on the cavity length, of 6.5 million. Two cavities are computed, one has two doors attached

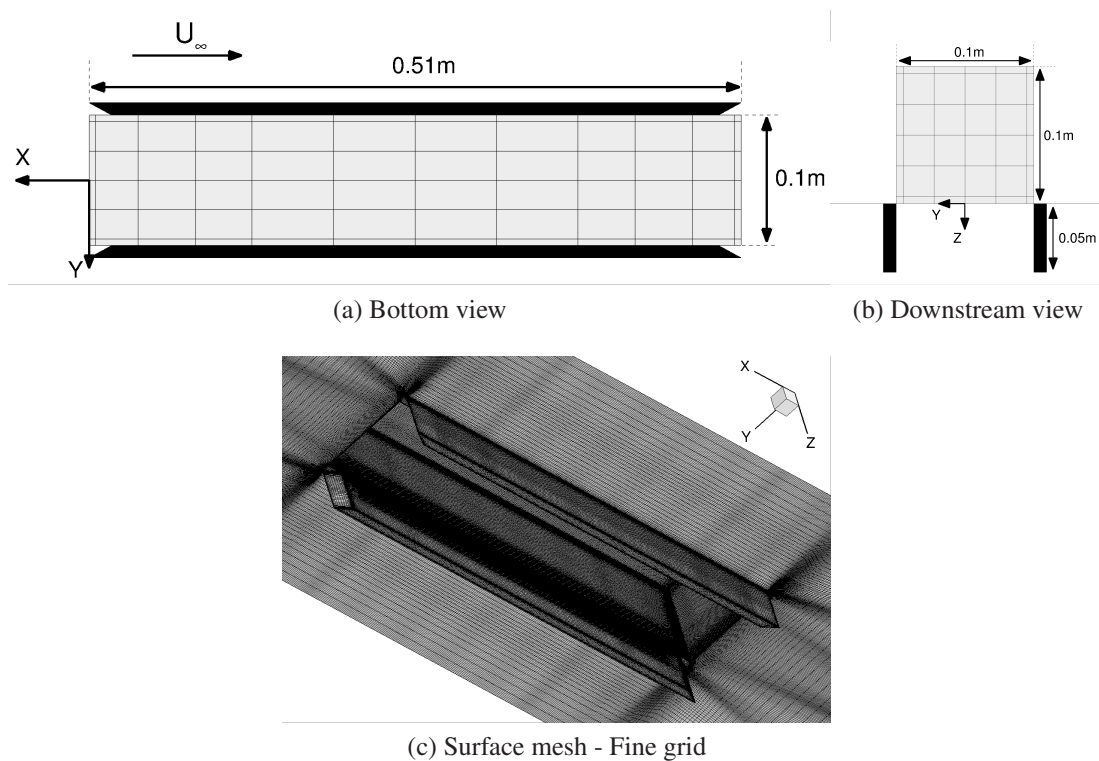


Figure 3.1: Schematic view of the M219 cavity with doors.

at its sides at an angle of 90 degrees (Figure 3.1), and the other has no doors. Data was obtained using Kulite<sup>TM</sup> pressure transducers at the cavity ceiling. CFD results for three grid densities of 13, 22 and 34 million points are compared to the experimental data for the cavity with doors. The computations used a dimensionless time-step of 0.01, and the SAS model <sup>[114]</sup> are presented in table 3.1.

Name	Door Angle (deg)	Grid size ( $10^6$ cells)	Cavity Travel Times
Coarse	90	13.2	25
Medium	90	22.3	25
Fine	90	33.9	30
No doors	-	23.0	30

Table 3.1: Details of the M219 computations.

The computational domain (Figure 3.2) considers the cavity placed on a flat plate extending 1.5 cavity lengths ahead and aft the cavity, and followed by symmetry boundary conditions about the Z axis. The domain is 8 cavity lengths long in the stream-wise direction. This particular setup was found to be adequate for simulating the M219 experiments and was adopted by most participants of the cavity flow workshop <sup>[130]</sup>. This setup is used for all computations in the thesis.

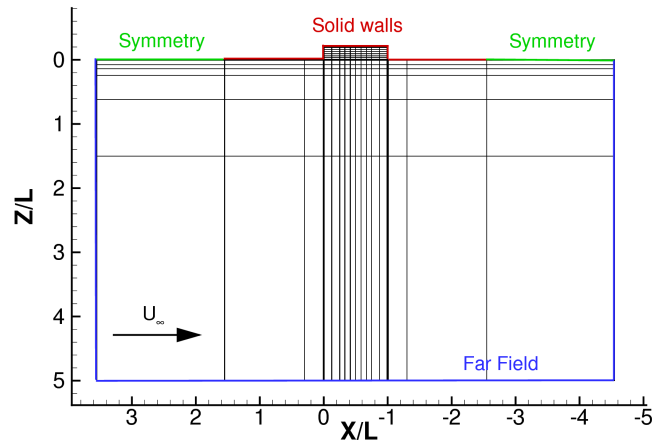


Figure 3.2: Boundary conditions and blocking at the mid-span of the computational domain.

## 3.2 Experimental Results

For the clean cavity configuration, a signal of 1910 travel times is available. Three tests at the same conditions, named S1, S2 and S3 were performed for the M219 cavity with doors. They were sampled at different frequencies and have different durations. Table 3.2 presents a summary.

Name	Signal length (Travel Time)	Sampling (kHz)	Date
No Doors	1910	6.00	Oct 1991
Doors S1	1831	31.25	Sep 1999
Doors S2	16798	6.00	Mar 2001
Doors S3	1910	6.00	Sep 1999

Table 3.2: Available signals for CFD comparison.

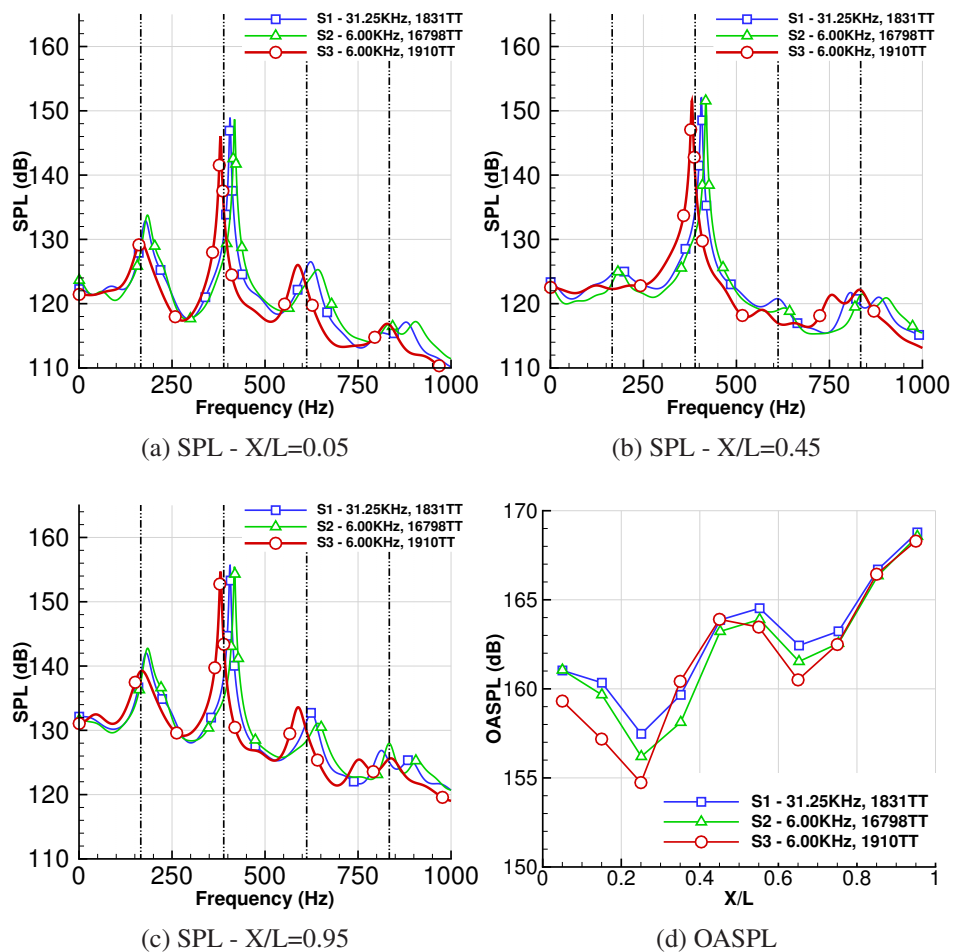


Figure 3.3: M219 with door SPL and OASPL for three experimental signals.

Figure 3.3 shows the SPL and OASPL at the ceiling mid-span for the different experimental data sets computed using the raw data. Vertical lines represent the Rossiter modes<sup>[22]</sup>. The SPL shows strong tones close to Rossiter modes 1, 2, 3 and 4 and a strong broadband noise. There is a finite number of tones of different amplitudes, and their distribution is not harmonic. S1 and S2 have similar SPL, and show less than 2dB differences in the OASPL. However, run S3 is different by 40dB in frequency, and 4dB in amplitude for the tones (Figure 3.3a). In addition, the OASPL is 3dB lower at the cavity front. In the following, run S2 is employed as it is the longest signal, and it agrees with the over-sampled signal S1 obtained two years earlier<sup>[32]</sup>.

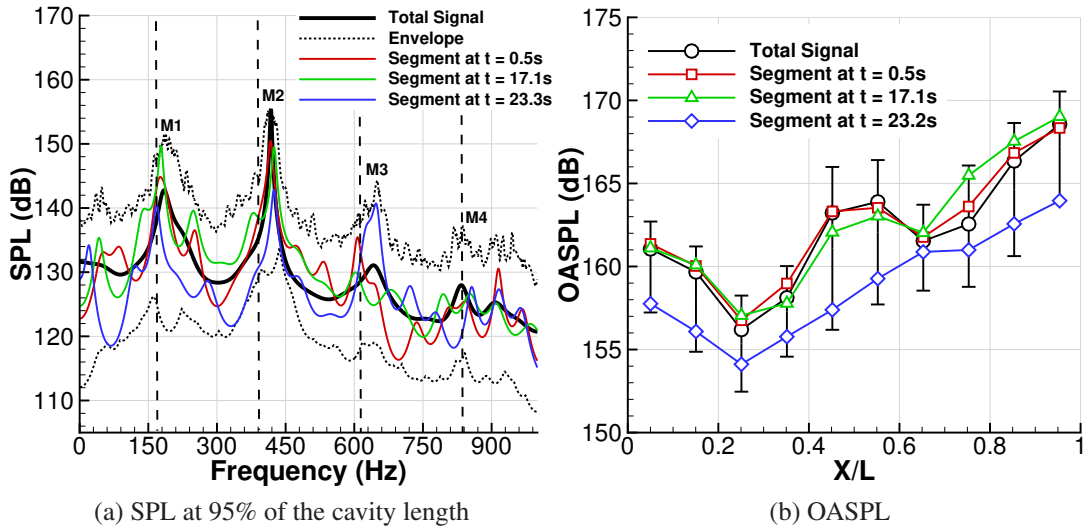


Figure 3.4: SPL and OASPL at the ceiling mid-span and at different time with envelope.

Since the CFD simulations are run for a typical length of 25 travel times, and run S2 spans 16798 travel times, the signal is analysed as follows. The experiment is divided in windows of 25 travel times, and the minima and maxima over all the windows are reported in figure 3.4 as the envelope shown with the SPL and OASPL. The envelope is wider than 20dB in SPL, and wider than 10dB in OASPL showing large fluctuations of the noise amplitude over large time scales. The SPL and OASPL computed for signal sections of 25 travel times for three selected windows are shown. The time  $t=23.3s$  shows a large decrease of modes 1 and 2, while mode 3 is amplified. This shows that energy can move between tones, and this is called mode switching<sup>[29]</sup>. These changes are related to the shape of the shear layer in time, and show that the noise field fluctuates over large time scales.

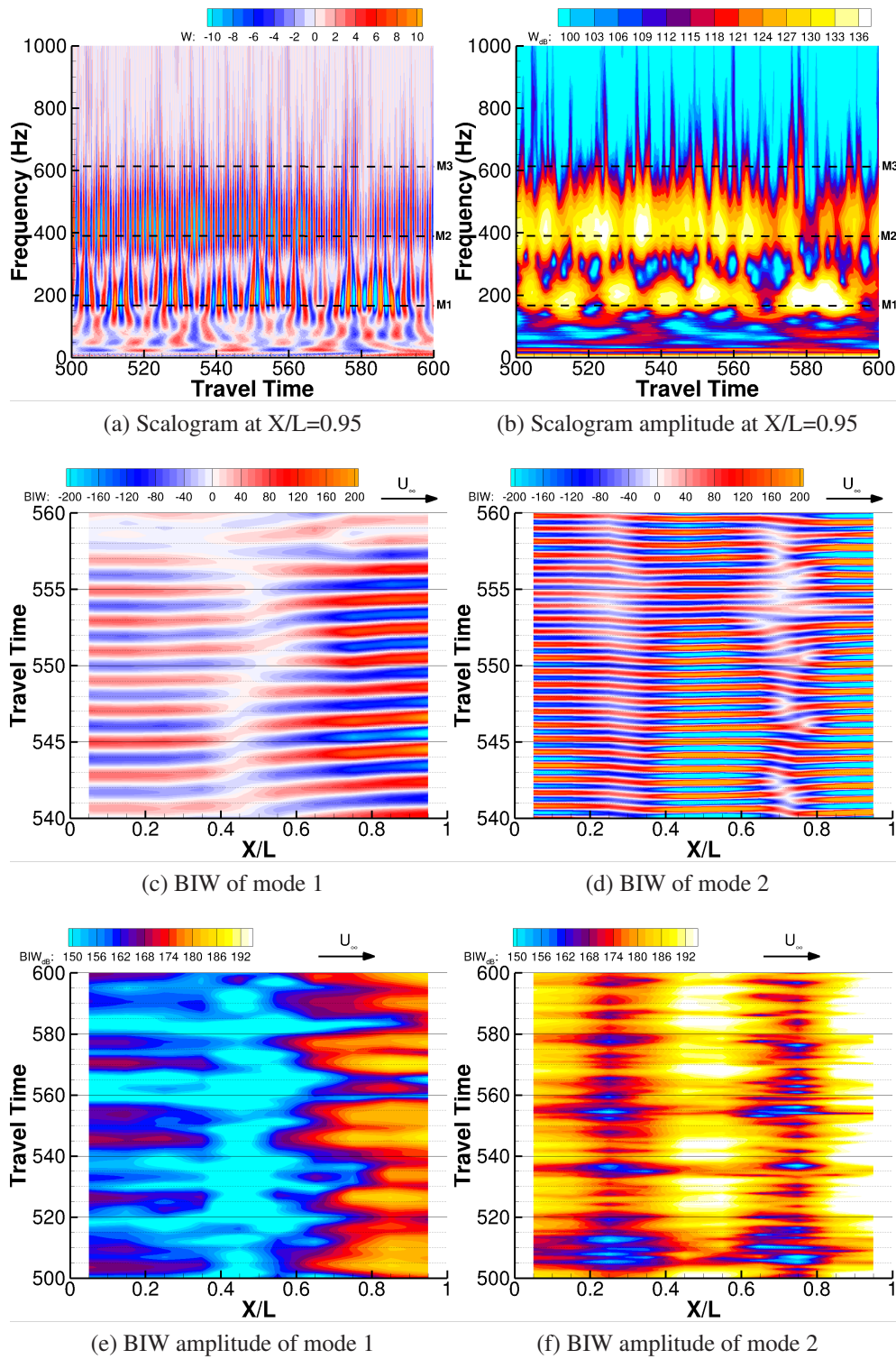


Figure 3.5: Time-frequency plots for the ceiling mid-span using experimental data <sup>[32]</sup>.

To dissect the pressure fluctuations over small time scales, Kegerise [29] used the wavelet transform to decompose the pressure signal in the frequency-time space. Figure 3.5a shows an example for the experimental pressure at a point at 95% of the ceiling mid-span of the M219 with doors. The pressure shows strong fluctuations at the tonal frequencies over small time scales. In addition, their amplitude appears to be modulated in time (Figure 3.5b). For example, the first mode shows a maximum amplitude at travel time 580, while the second mode has a maximum at travel time 520. The pressure probes are analysed for several points along the cavity length, and the BIW is represented in figures 3.5c and 3.5d along the ceiling mid-span. The scalogram is integrated in windows of 20Hz centred on cavity modes 1 and 2. There are standing wave oscillations, characterised by nodes (minima of amplitude), and antinodes (maxima of amplitude). Furthermore, neighbouring antinodes are opposed in phase with opposite fluctuation. For example the fluctuation sign between the front and the back of the cavity is always opposed for the first mode (Figure 3.5c). Figures 3.5e and 3.5f show that the amplitude modulation of the modes globally affects the entire cavity length with simultaneous maximum, and minimum amplitude between the front and the rear of the cavity.

Cavity flow fluctuations are the summation of small time scales (order of a cavity travel time), and larger time scales (order of hundreds cavity travel times) that create a non periodic flow as seen since the first experiments of Rossiter [13]. Other researchers suggest that these flows are pseudo-periodic [14]. Measurements of cavity flows are difficult as multiple signals of the same cavity flow will not necessarily give exactly the same result. Numerical simulation and modelling are also difficult, as multiple time scales have to be correctly simulated to obtain an accurate cavity flow representation.

## 3.3 Validation Results

### 3.3.1 Averaged Flow

Figure 3.6 shows the SPL comparison between CFD and experiments at three points at 5%L, 45%L, and 95%L on the cavity ceiling mid-span, for the M219 cavity with doors. Vertical black lines represent Rossiter's modes. The SPL results are in better agreement with the test data when the fine grid is used, capturing both tonal and broadband noise.

The time averaged  $C_p$  (Figure 3.7a) at the ceiling, and at the mid-span of the

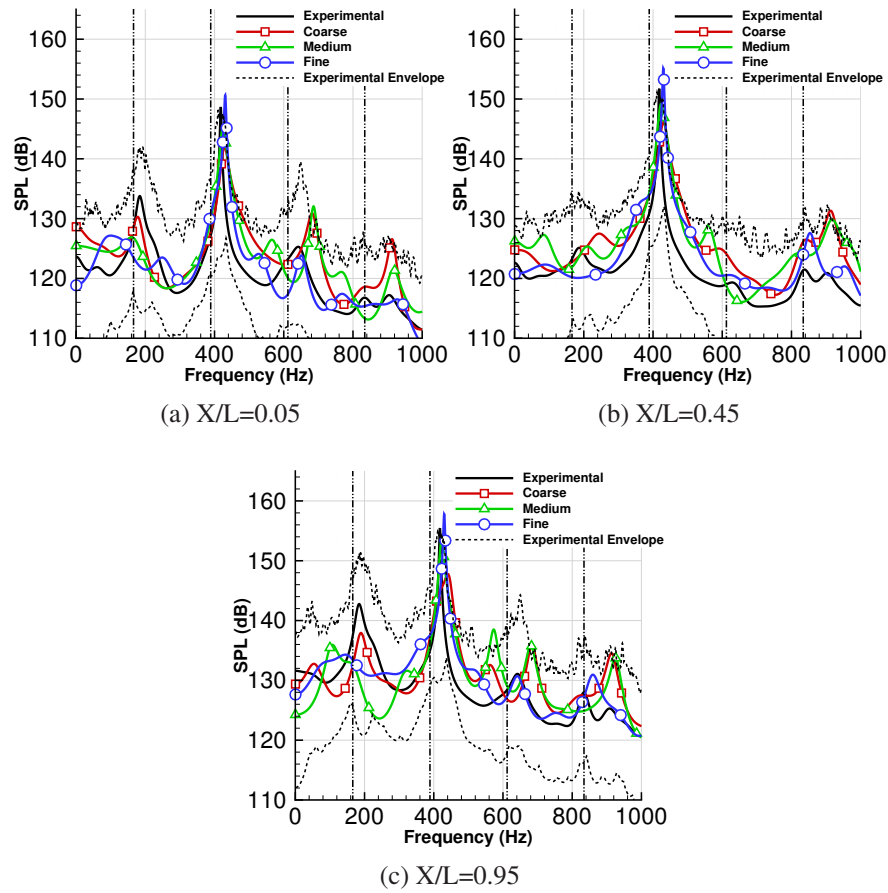


Figure 3.6: M219 with door SPL at ceiling mid-span for CFD and experiments.

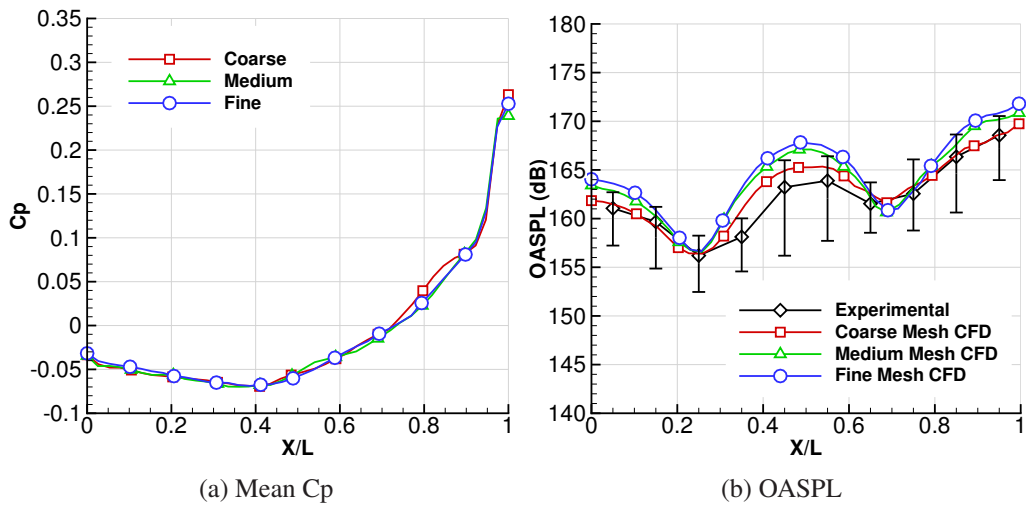


Figure 3.7: OASPL, and mean  $C_p$  along the M219 with doors ceiling mid-span.

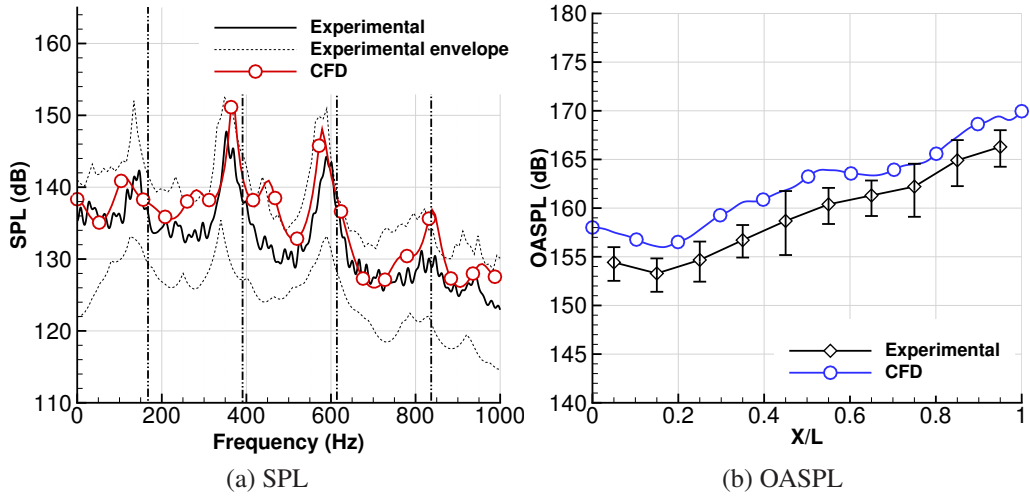


Figure 3.8: Noise along the no doors M219 cavity ceiling mid-span computed with a medium mesh.

cavity, shows grid convergence, with negligible changes between the different grid densities. The OASPL, on figure 3.7b is shown with vertical bars, computed as the signal envelope shown in figure 3.6. The second Rossiter mode is dominant, with a W shape of the OASPL, as captured by the CFD and the experiments <sup>[131]</sup>. There is convergence towards the fine mesh solution, with a small relative difference of 1 dB between medium and fine grids.

The CFD results are compared with experiments for a cavity without doors in figure 3.8. Overall, the CFD captured well the differences between the door and no door configurations, including the strong increase of the second cavity mode with the doors, suggesting that SAS <sup>[114]</sup> is a suitable method for simulating this flow. Both cases with and without doors show a small overestimation of the OASPL, all along the cavity length. A large number of simulations performed with various models <sup>[132, 130, 133]</sup> had similar overestimation. This may be due to experimental errors, the signal length, limitations of the SAS <sup>[114]</sup> and DES <sup>[109]</sup> approaches, and simplifications in the CFD setup for this case. Further discussion related to the differences between LES and DES predictions is given in the work of Nayyar *et al.* <sup>[59]</sup>.

The time averaged stream-wise velocity is compared in figure 3.9 between CFD and PIV experiments <sup>[134]</sup> for the M219 cavity without doors. The CFD results agree well with the experiments for the stream-wise velocity component, showing the development of the shear layer along the cavity length.

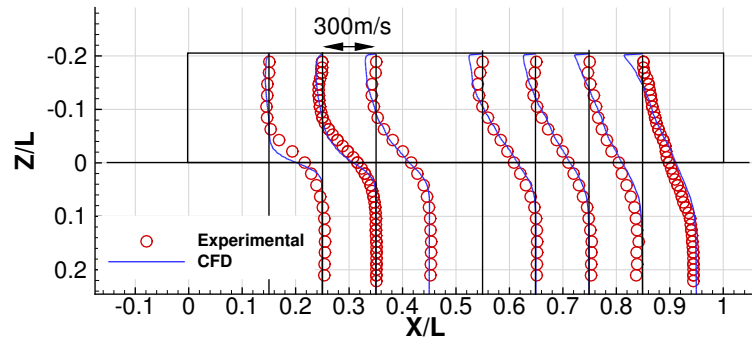


Figure 3.9: Time averaged stream-wise velocity at the mid-span of the cavity along vertical lines.

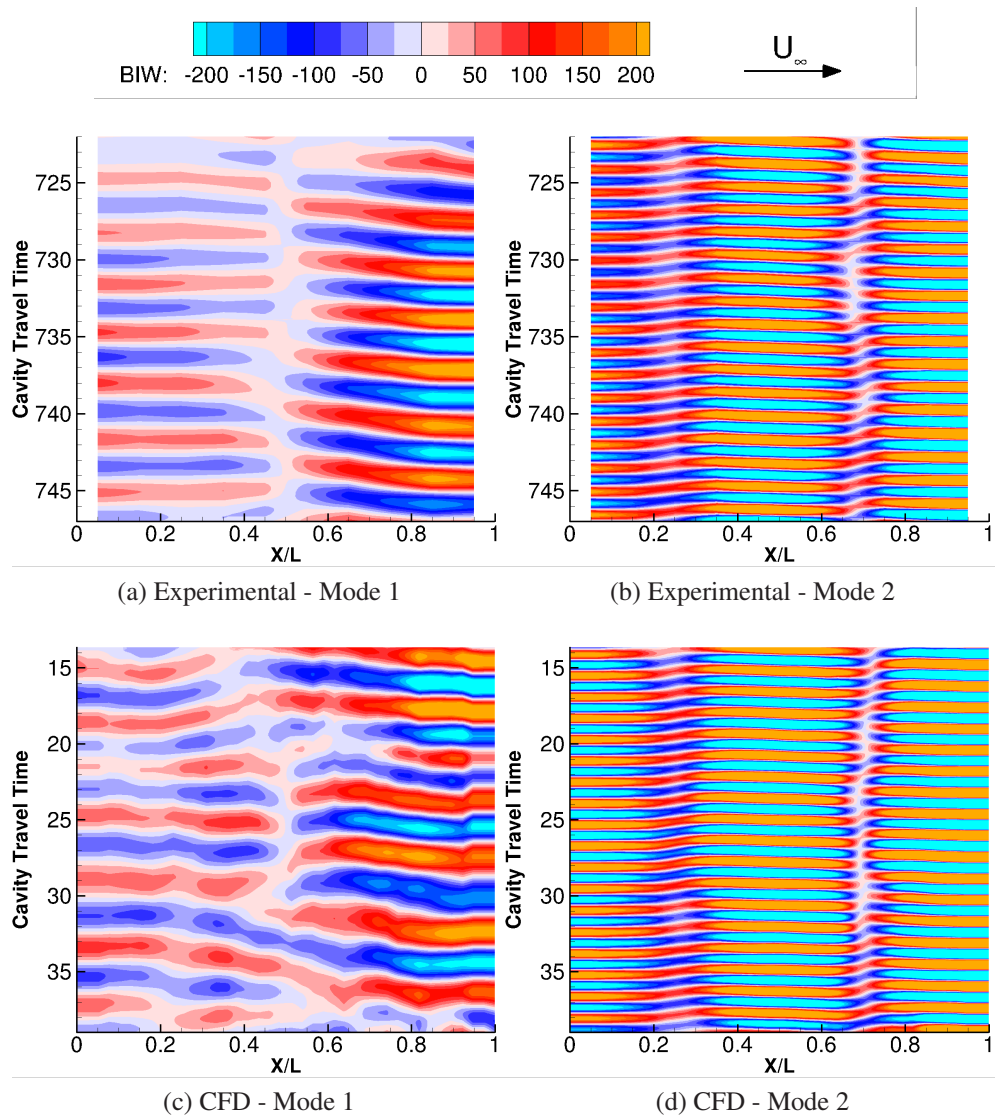


Figure 3.10: BIW at the cavity ceiling centre-line for modes 1 and 2.

### 3.3.2 Spatio-Temporal Validation

The wavelet transform is used to perform spatio-temporal validation of the CFD signals. The pressure probes are analysed, and the Banded Integral Wavelet (BIW) is given in figure 3.10 for 25 travel times, along the ceiling centre line. The BIW is integrated in windows of 20Hz centred on the first, and second cavity modes. There is a fair agreement of the CFD with the experiments, showing standing wave oscillations with respectively a tick, and a W shape for modes 1 and 2.

The BIW amplitude is shown in figure 3.11. The CFD signal agrees with the experiments showing the characteristic shape of the first mode, with two antinodes at the front, and the aft wall. The second mode shows the W shape seen on the OASPL.

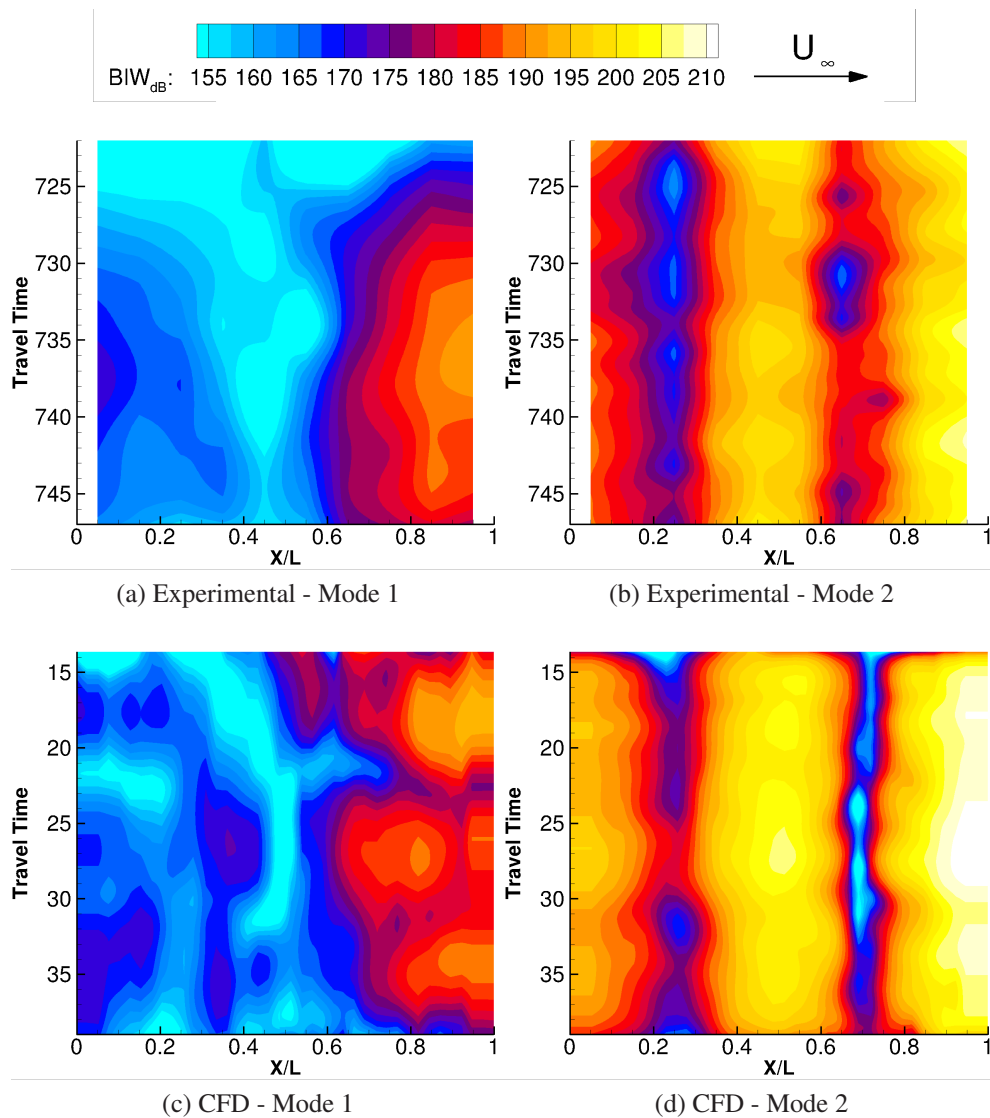


Figure 3.11: BIW amplitude at the cavity ceiling centre-line for modes 1 and 2.

Also, both experiments and CFD show global fluctuations of the amplitude along the cavity length.

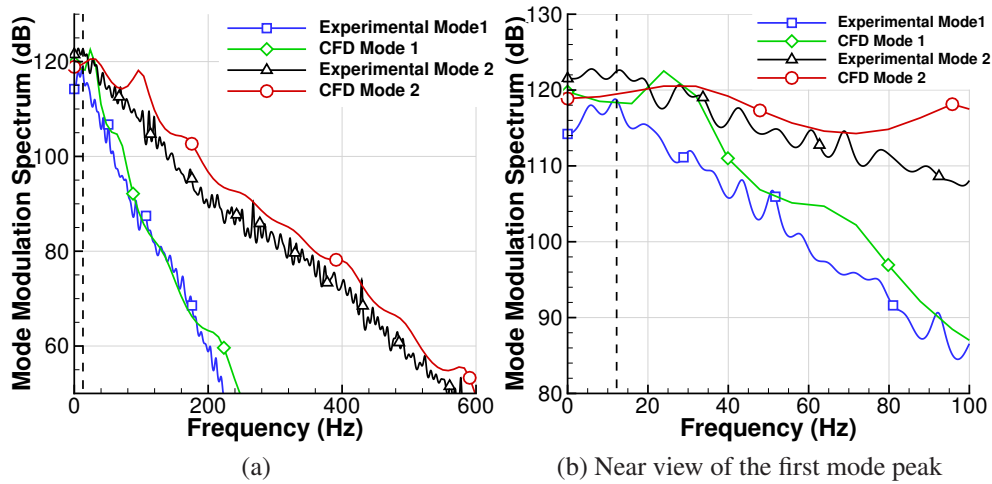


Figure 3.12: Mode modulation SPL for modes 1 and 2.

Figure 3.12 shows the spectrum of the cavity tonal amplitude modulation (BIW envelope) at 95% of the cavity length for modes 1 and 2. The experimental signal is characterised by decreasing modulation amplitude with the frequency. The first mode modulation has a peak at a very small frequency indicated with a vertical dashed line, as shown by Kegerise *et al.* [29]. SAS results fairly agree with the experiments, capturing the modulation noise decay as the frequency increases. Overall, the SAS turbulence model shows a reasonable agreement with experiments for the transonic cavity pressure field on average, and in terms of spatio-temporal components.

Considering 10 points per wavelength inside the cavity, the coarse, medium, and fine grids can respectively capture frequencies up to 10, 12, and 14kHz which is much larger than the higher cavity tone frequency. As a consequence, the damping by SAS is limited for the frequencies of interest, and the CFD result compares well with experiments.

## Chapter 4

# Beamforming Analysis for Transonic Cavity Flows

To further understand cavity flows, recent works applied novel experimental techniques, like the pressure sensitive paint <sup>[135]</sup> that can give pressure fluctuations over all cavity surfaces. Nevertheless, the peaks of the sound pressure level at the shear layer, are still difficult to measure without intrusive techniques. In principle, one can use the source term that depends on the velocity derivatives from the Poisson equation of fluctuating pressure to find the sources of noise. However, transonic cavity flows are subject to a compressible flow where this cannot be applied. This thesis uses an other technique called beamforming to find the sources of noise due to the cavity flow. The beamforming technique, was used by Long <sup>[136]</sup> to decompose the pressure signals in coherent, and uncorrelated noise using a linear microphone array on the cavity ceiling. The present work applies this technique to reconstruct the noise sources using a microphone array in the far-field, which may help researchers to capture the acoustic field far from the walls using a limited number of probes.

### 4.1 Beamforming Method

Cavity flows are characterised by high levels of noise. Typically, single microphone measurements, cannot distinguish between pressure contributions from different sources. Measurements from an acoustic array, instead, allow to determine the location of the acoustic sources, by means of a combination of the individual microphone signals <sup>[137]</sup>. This technique is useful for wind tunnel testing as it is not possible to

measure the pressure at every point of the flow-field. The output of the beamforming algorithm is a noise map, which shows the power detected at each scanned grid point in terms of decibels below the peak power. Given an array with  $M$  microphones, the waveform output of the  $m$ -th sensor will differ from the reference sensor of the array by a time delay. Therefore, the beamformer waveform output  $z(t)$  can be written as the weighted sum of the sensor waveform outputs:

$$z(t) \triangleq \sum_{m=0}^{M-1} y_m(t - \Delta_m), \quad (4.1)$$

where  $y_m(t)$  is the signal of the  $m$ -th microphone of the array, and  $\Delta_m$  the time delay. The time delay is defined as  $\Delta_m \triangleq \frac{r_m - r_0}{c}$ , where  $r_m$  is the distance from the assumed source position  $\vec{x}_0$  and the  $m$ -th sensor, and  $c$  is the speed of sound (Figure 4.1).

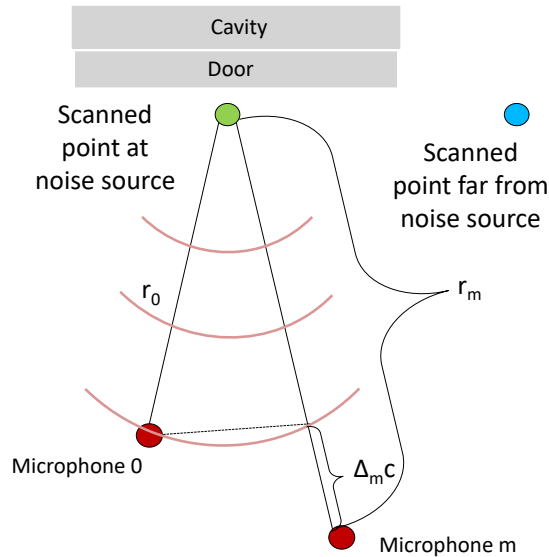
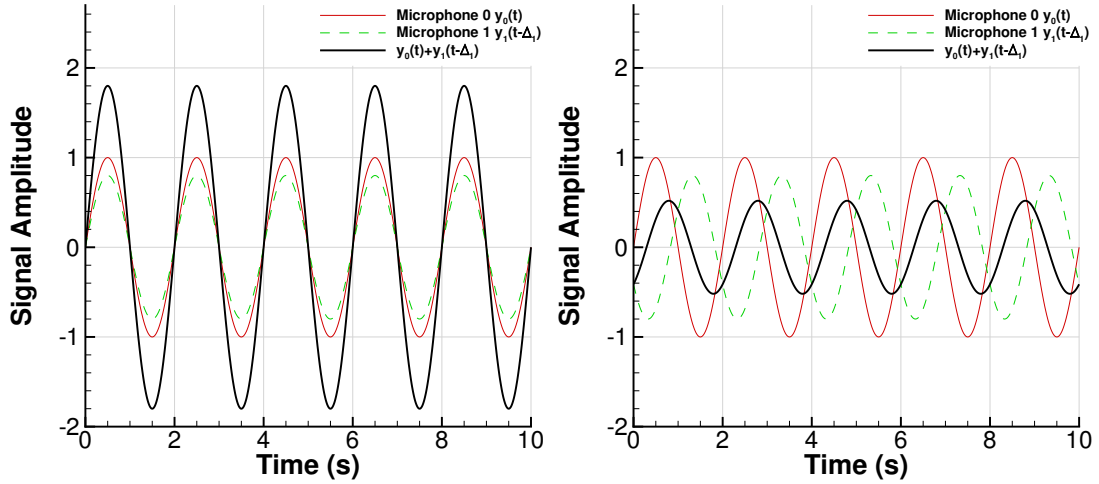


Figure 4.1: Beamforming principle with a planar wave propagation.

Scanning the noise at a point close to a source (Figure 4.2a), and if the signals are shifted in time using the time delay, they will put in phase, leading to a constructive interference and a strong output. However, scanning the noise far from source (Figure 4.2b), it is not likely that the time delays lead to in phase superposition of the signals, and the beamforming output is smaller.

The conventional beamforming computes the output using the frequency representation of  $z(t)$  obtained by a Fourier transformation of the microphones signals.

$$Z(\omega) = \mathcal{F} \left\{ \sum_{m=0}^{M-1} y_m(t - \Delta_m) \right\} = \sum_{m=0}^{M-1} Y_{\omega} e^{-j\Delta_m \omega}. \quad (4.2)$$



(a) Beamforming performed close to a noise source (b) Beamforming performed far from a noise source

Figure 4.2: In phase and out of phase superposition of the signals with time delay.

If we define as  $Y(\omega_k)$  an  $M \times 1$  vector of complex numbers containing the signal amplitude and phase, at a frequency  $\omega_k$ , for each array sensor, and  $e(\omega_k)$  as the *steering*  $M \times 1$  vector containing the weight and phase delay information of the sensors for an assumed source location  $\vec{x}_0$ . Then we can write

$$Z(\omega_k) = e(\omega_k)^\dagger Y(\omega_k) = e_k^\dagger Y_k, \quad (4.3)$$

where  $k$  is the  $k$ -th frequency bin we can detect in the digital signal processing and  $^\dagger$  is the Hermitian transpose operator.

The power detected at the  $k$ -th frequency bin is defined as

$$P_k \triangleq |Z_k|^2 = Z_k Z_k^*. \quad (4.4)$$

Therefore, using the definitions introduced before:

$$P_k = e_k^\dagger \left( Y_k Y_k^\dagger \right) e_k = e_k^\dagger R_k e_k \quad (4.5)$$

where  $R_k$  is the cross spectral matrix. This thesis uses the MULTiple Signal Classification (MUSIC) Algorithm to compute the cross spectral matrix  $R_k$  [138]. The eigenvalues are ordered by increasing values in  $R_k$ . The larger  $L$  values contain the energy from the tonal source subspace, while the broadband noise subspace is contained in the  $M - L$  smaller values. The MUSIC cross spectral matrix  $R_{k,MUSIC}^{-1}$  is built using the  $M - L$  weaker eigenvectors:

$$R_{k,MUSIC}^{-1} = \sum_{m=0}^{M-L-1} v_m v_m^\dagger \quad (4.6)$$

where  $v_m$  is the  $m^{th}$  eigenvector. This cross spectral matrix is formed only of broadband noise eigenvectors, and the output power is computed as:

$$P_{k,MUSIC}^{-1} = e_k^\dagger R_{k,MUSIC}^{-1} e_k \quad (4.7)$$

The output shows lower values at the locations of the tonal sources. Then the noise map is plotted with the inverse of  $P_{k,MUSIC}^{-1}$ .

The results are characterised by the main lobe width around the noise source, that has to be as narrow as possible to increase the source location accuracy. The side lobes appear around the main lobe at relatively lower levels that have to be as low as possible. The MUSIC algorithm is known to improve the response characteristics for noisy signals over linear techniques, reducing the size of the side lobes. Figure 4.3 shows an example of beamforming analysis using the MUSIC algorithm with small side lobes around the noise sources. A Matlab script using this algorithm is given in appendix C.1.

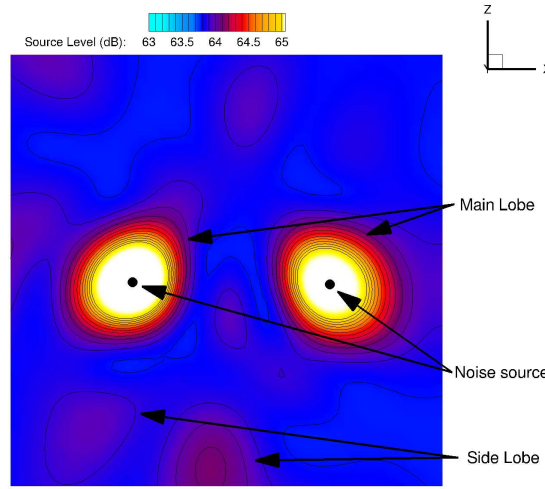


Figure 4.3: Main and side lobes obtained with beamforming around two speakers.

#### 4.1.1 Noise Propagation Model

A sound wave around a transonic cavity flow travels in a non-uniform flow-field and his path is influenced by the free-stream velocity. Consequently, the path to go from a source to a microphone is not a straight line. To use the beamforming algorithm, the distance between a source and a microphone has to take into account the path of the noise, and the noise propagation model is defined by trial and error as follows.

It is assumed that the noise sources radiate uniformly around them. The sound wave emitted in the direction of the microphone with a velocity  $V_0$  of norm equal to the speed of sound  $c$  is considered. The trajectory of the wave is computed taking into account the transport by the flow-field. The length of the trajectory  $d_{travel}$  is the distance to go from the source to the microphone, and  $c_{travel}$  the mean velocity along the trajectory. Then, the initial velocity of the sound wave  $V_0$  is modified to reduce the offset distance  $d_{off}$  between the trajectory and the microphone:

$$V_0 = V_0 - d_{off} \frac{c_{travel}}{d_{travel}} \quad (4.8)$$

The initial velocity is normalised to a norm  $c$  and a new wave is launched with the new initial velocity. This process is repeated until a trajectory reaches the microphone. Furthermore, the wave does not have a constant velocity along the trajectory, therefore, the equivalent distance  $r_m$  along the trajectory at a constant velocity  $c$  is given by:

$$r_m = d_{travel} \frac{c}{c_{travel}} \quad (4.9)$$

This beamforming algorithm has been validated on a simple case of two speakers in front of an array of 40 microphones without free-stream. The microphone signals were sampled at 48kHz and recorded during 3 seconds. Figure 4.4 shows the microphone array in white dots and the beamforming result for the frequency of 1800Hz generated by the speakers. The space is scanned for sources in a cube of 1m side around the speakers. The speaker's positions are correctly found at 0.51m in front of the microphone array. However, the lobes shown in the figure 4.4 are large in the sound propagation direction. More microphones distributed along the sound propagation direction are needed to reduce the lobe size.

### 4.1.2 Acoustic Arrays

This chapter uses different microphone arrays to show the effect of their position, density, and shape with the beamforming technique (Table 4.1). Two array shapes that give accurate source identification for far-field noise are tested <sup>[139]</sup>: the multi-spiral design (Figure 4.5a), composed of spirals equally rotated about the origin, and the Dougherty log-spiral design (Figure 4.5b), built with microphones equally spaced along a logarithmic spiral. The multi-spiral design is tested with 16, 21, 31, 61, and 101 microphones, and for different vertical positions. In the XY plane, the array centre

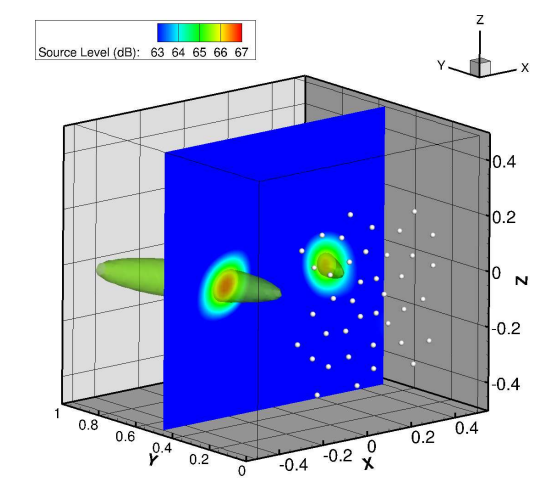
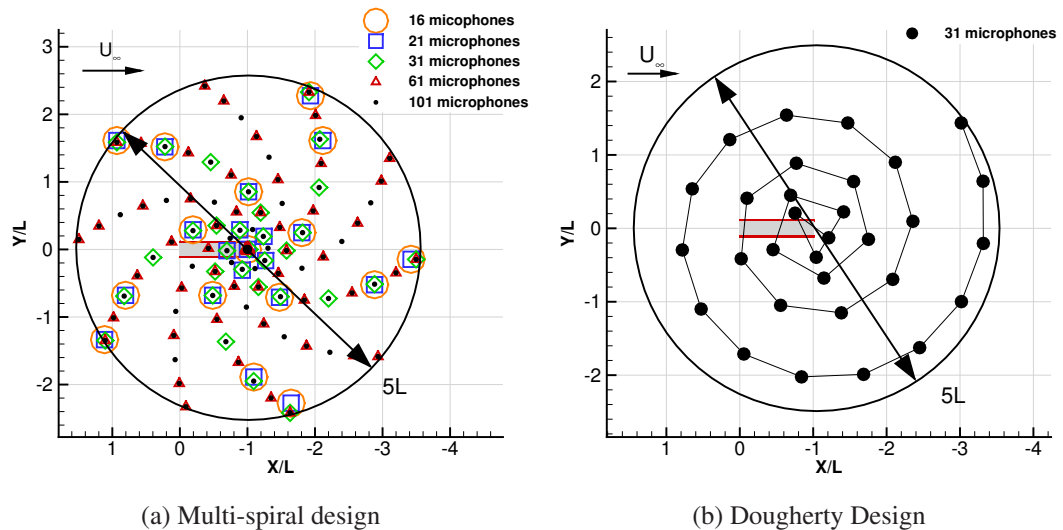


Figure 4.4: Validation of the beamforming analysis.



(a) Multi-spiral design

(b) Dougherty Design

Figure 4.5: Schematic view of the microphone arrays.

is placed at the aft wall of the cavity to take into account the flow-field that moves the focus point of the array upstream. Those arrays could be fitted within the DERA Bedford wind-tunnel where this cavity was experimentally tested, and the section was 2.44m by 2.74m with the cavity plate 1m away from the ceiling.

No wind tunnel data is available to validate the beamforming algorithm with the microphone arrays arranged around a cavity. To perform a validation, three noise sources of equal intensity are placed along the shear layer, at the front, the middle, and the aft of the cavity. The sources radiate a noise at 400Hz that corresponds to the dominant cavity mode of the present case. The signals received by the microphones are computed using the propagation model described in section 4.1.1, and the mean

Shape	Z/L	Nb microphone
Multispiral	0.6	31
Multispiral	0.9	31
Multispiral	1.2	31
Multispiral	1.5	16
Multispiral	1.5	21
Multispiral	1.5	31
Multispiral	1.5	61
Multispiral	1.5	101
Dougherty	1.5	31

Table 4.1: Details of the microphone arrays

flow computed with CFD. Here the multi-spiral and the Dougherty arrays of 31 probes placed at  $Z/L=1.5$  are employed. Finally, beamforming is applied with the simulated microphone signals. The reconstructions are shown figure 4.6, with the sources marked with black crosses. Both arrays localise all noise sources, surrounded by lobes spreading along the vertical axis. However, the Dougherty design is slightly worse, with larger lobes.

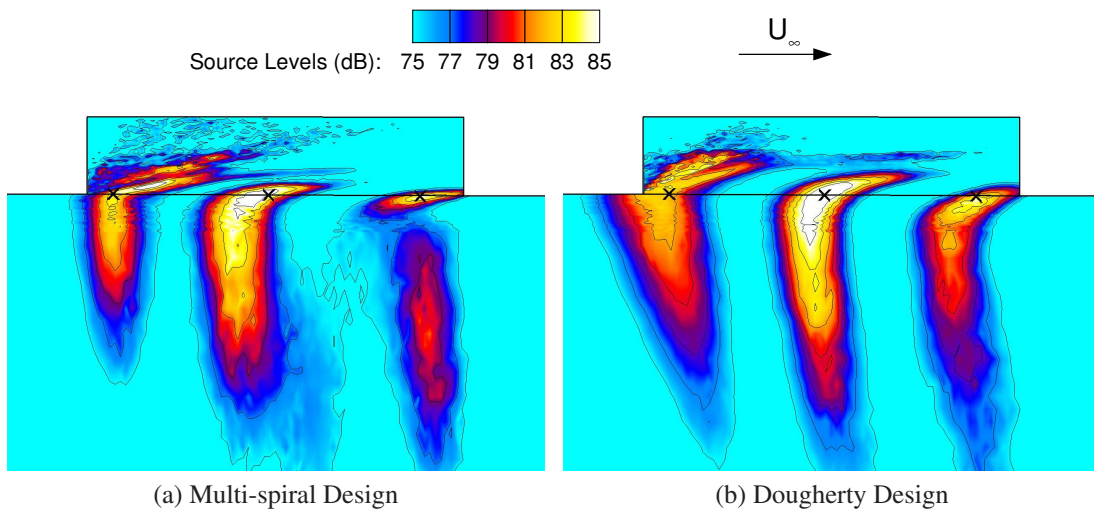


Figure 4.6: Reconstruction of three noise sources at shear layer.

## 4.2 Results and Discussion

Using the full CFD flow-field of the M219 cavity with doors, the noise field is computed and shown in figure 4.7 at the mid-span of the cavity. Between 10 and 1300Hz (Figure 4.7a), two main sources of noise are localised at the mid-length, and at the aft of the shear layer, due to the strong second cavity mode. The BISPL, is also integrated around cavity modes 1 and 2 in windows of 10Hz width (Figures 4.7b and 4.7c). All modes show alternating high and low noise levels along the cavity length, corresponding to the nodes, and the antinodes of standing waves. The nodes of the dominant second mode are shown with circles, and the antinodes with crosses, in figures 4.7 to 4.12. The cavity modes are mainly produced along the shear layer, as

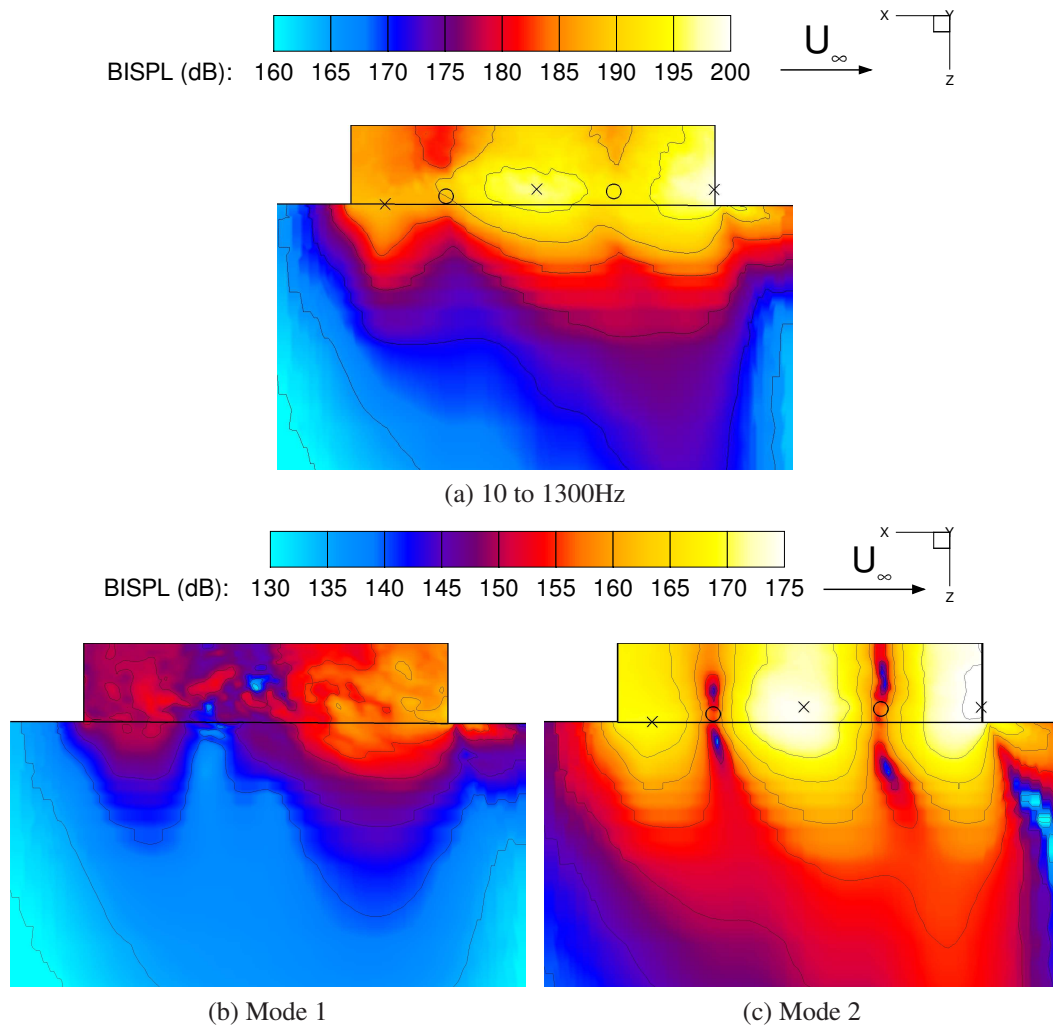


Figure 4.7: BISPL at the mid-span of the cavity over a large frequency band (a), and centred on the two first cavity modes in windows of 10Hz (b)-(c).

seen by the peaks of the different modes close to the black line at  $Z=0$ .

Experiments are limited to pressure probes placed on the wall, so they miss some important characteristics of the noise field as described above. The beamforming is applied to the CFD results, with the objective to obtain results comparable to the BISPL computed using all the CFD points on the mesh. The static pressure is considered at the microphone, as the hydrodynamic fluctuations are negligible far from the cavity. The noise is reconstructed on a rectangular grid of  $90 \times 81$  points at the mid-span of the cavity using the multi-spiral array with 31 microphones, placed at  $Z/L=1.5$ . Figure 4.8 shows the effect of the level of accuracy of the flow-field used to transport the sound waves. First, a zero velocity flow-field is assumed, and the pressure waves propagate along straight lines from the scanned points to the microphones at the speed of the sound (Figure 4.8a). The noise in this case is not correctly localised, with a

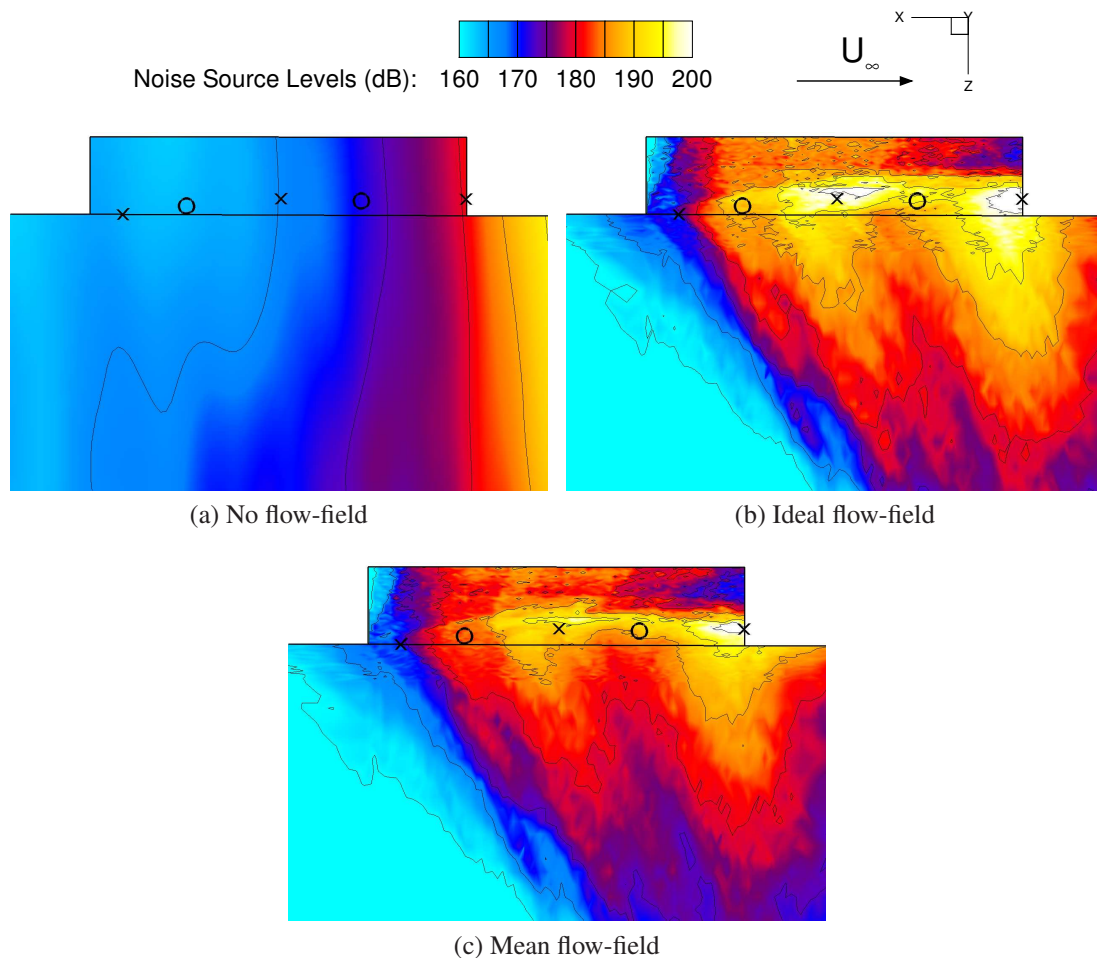


Figure 4.8: Noise source reconstruction at the mid-span of the cavity over a large frequency band between 10 and 1300Hz for different noise propagation model. Multi-spiral array with 31 microphones, placed at  $Z/L=1.5$ .

peak appearing downstream the cavity. Assuming that pressure waves are travelling in an ideal flow-field (Figure 4.8b) with zero velocity in the cavity, and free-stream outside, the noise is more accurately localised around the shear layer, mainly at the second, and at the third antinodes of the second cavity mode (Second and third crosses in figure 4.8b). Nevertheless, the sources of noise are surrounded by large lobes along the vertical direction.

Employing the CFD mean flow-field to transport the waves (Figure 4.8c), the sources of noise are localised at the same axial position compared to the ideal flow-field case (Figure 4.9b). However, the lobes are smaller for the mean flow-field case, as the thickness of the shear layer, is taken into account, giving a more precise vertical localisation of the noise sources (Figure 4.9a). The source of noise at the front of the cavity is weaker than for the other parts of the cavity, and is hidden by the lobes of the stronger noise sources. In the following, the mean flow is used for all beamforming results.

Figure 4.10 shows the influence of the vertical position of the multi-spiral array of 31 probes. The array closer to the cavity at  $Z/L=0.6$  (Figure 4.10a), did not capture the sources at the shear layer, and the noise field close to the microphone array was not correctly reconstructed. Moving the array farther from the cavity, improves the reconstruction. The two main noise sources at 50%L and at 100%L of the shear layer are more visible (Figure 4.10d), and compares better with the BISPL. When the array

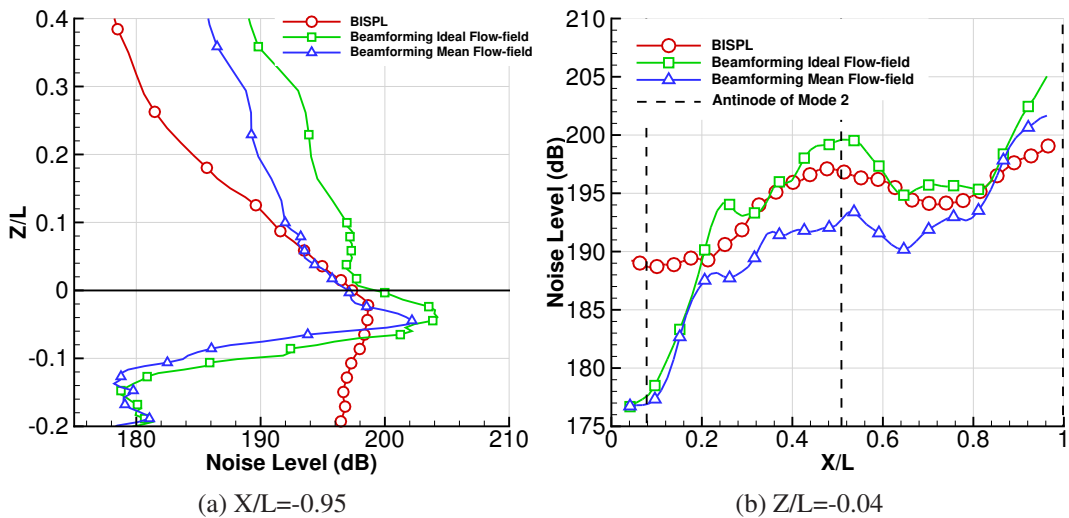


Figure 4.9: Comparison between OASPL and BIW along lines. Multi-spiral array with 31 microphones, placed at  $Z/L=1.5$ .

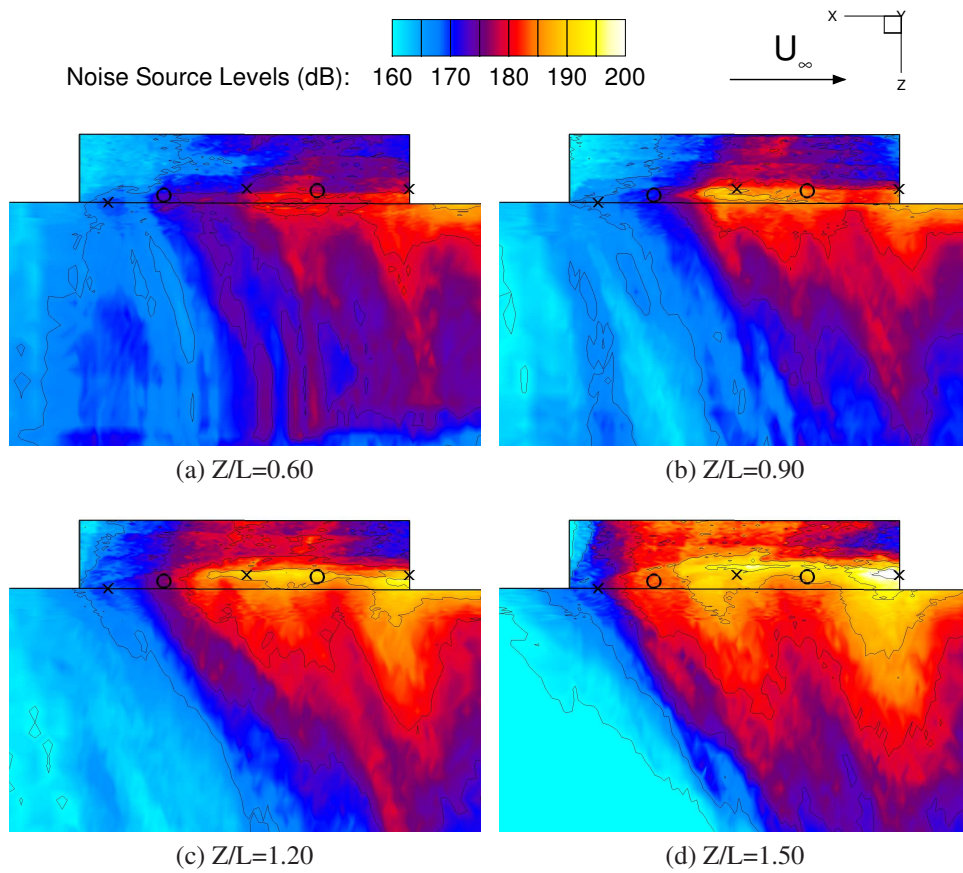


Figure 4.10: Noise source reconstruction at the mid-span of the cavity over a large frequency band between 10 and 1300Hz for different multi-spiral array positions. Multi-spiral array with 31 microphones.

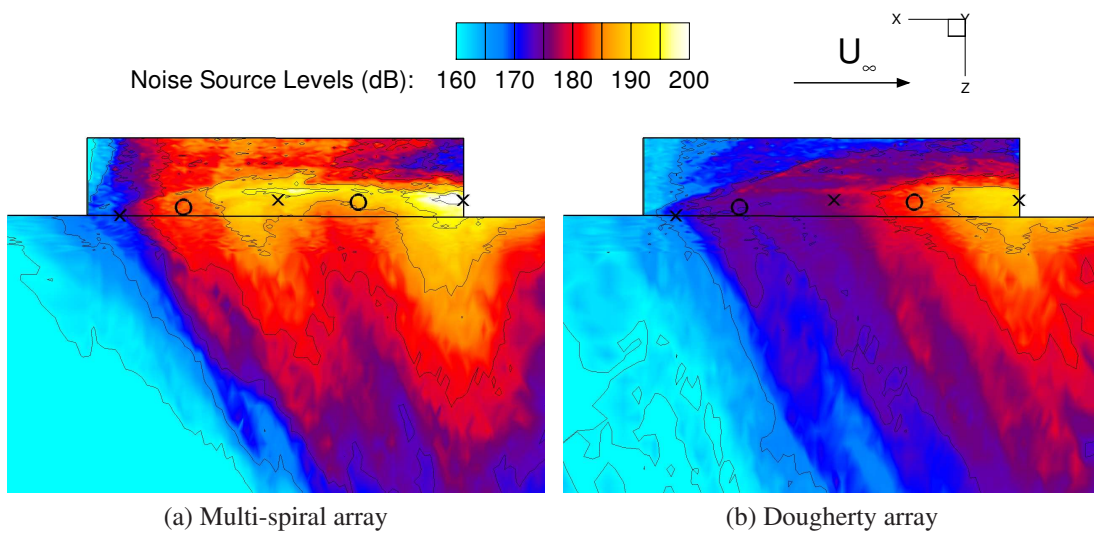


Figure 4.11: Noise source reconstruction at the mid-span of the cavity over a large frequency band between 10 and 1300Hz for different array shapes. Array of 31 microphones placed at  $Z/D=1.5$ .

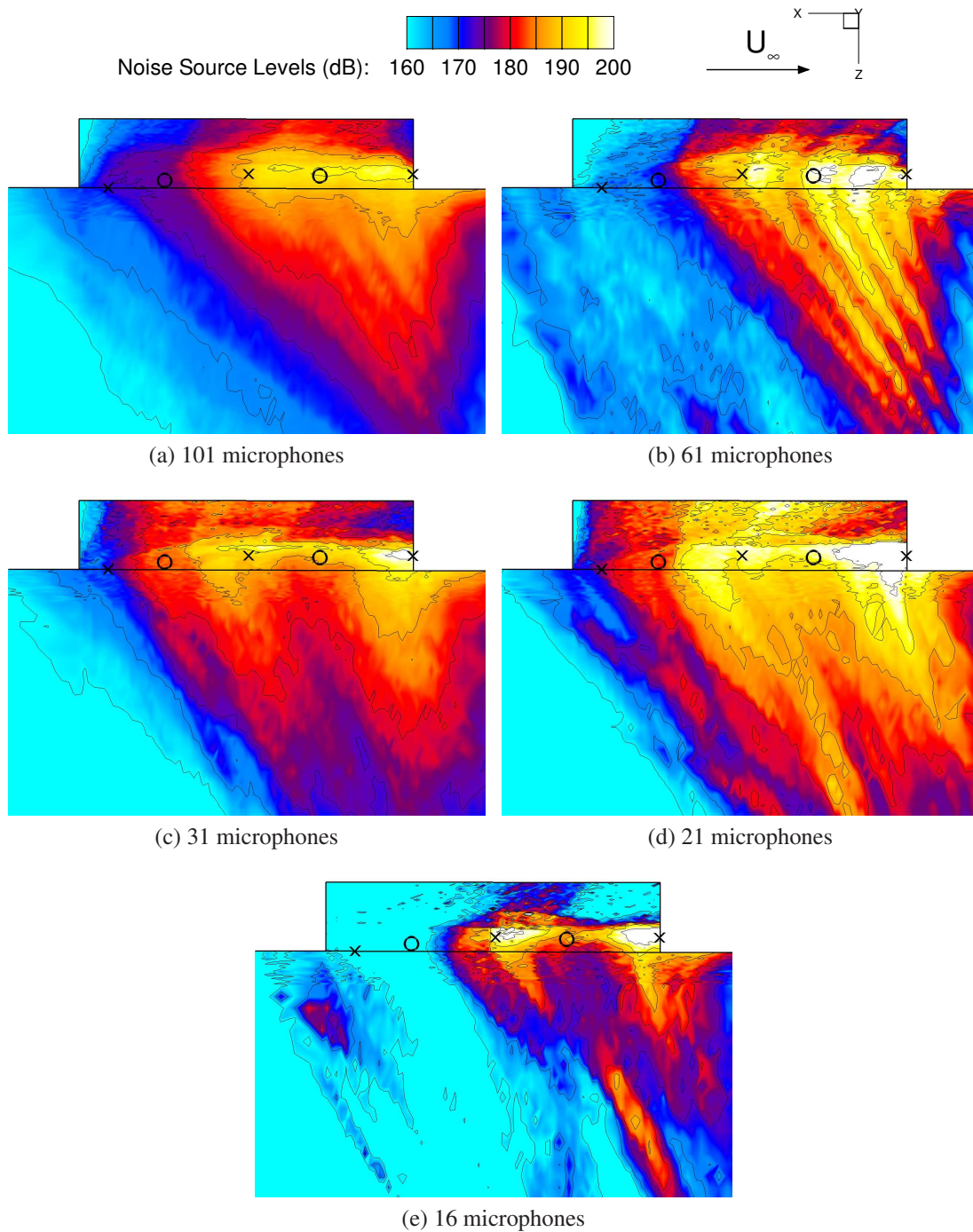


Figure 4.12: Noise source reconstruction at the mid-span of the cavity over a large frequency band between 10 and 1300Hz for different array density. Multi-spiral array placed at  $Z/L=1.5$ .

is too close to the cavity, the near field influences the resulting reconstruction, leading to errors <sup>[140]</sup> (Figures 4.10a, 4.10b, and 4.10c).

Figure 4.11 shows the beamforming for the multi-spiral and the Dougherty arrays of 31 microphones, placed at  $1.5L$  from the cavity. The Dougherty design reconstruction did not capture the noise source at  $50\%L$  of the shear layer, and globally is less accurate than the multi-spiral array reconstruction. This may be the consequence of the lower density of microphones close to the perimeter of the Dougherty array, which reduces its bandwidth.

Figure 4.12 shows that the accuracy of the beamforming depends on the number of microphones. When a large number of microphones are used, the strong broadband noise is amplified when summed over all microphones, and hides the main sources (Figures 4.12a and 4.12b). On the other hand, with a small number of microphones, the broadband noise increases the lobe size (21 microphones, figure 4.12d), and leads to non physical noise sources below the cavity for 16 microphones (Figure 4.12e). The best configuration tested here had 31 microphones (Figure 4.12c).

Figure 4.13 compares the BISPL and the beamforming for the M219 cavity without doors. Both the beamforming, and the BISPL, show the reduction of the noise source amplitude at the mid-length of the cavity, caused by a weaker second cavity mode, without the doors.

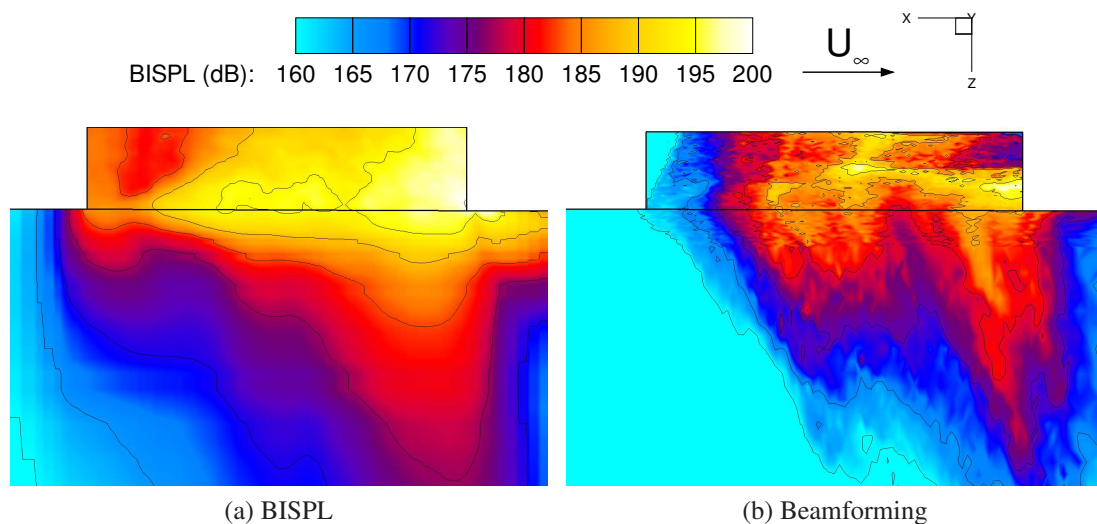


Figure 4.13: Noise field at the mid-span of the M219 cavity without doors over a large frequency band between 10 and 1300Hz. Multi-spiral array of 31 microphones placed at  $Z/D=1.5$ .

---

In summary, the beamforming proved to be capable to capture the noise field around the cavity using a limited number of probes, providing the mean CFD flow-field to compute the propagation of the noise. This technique could be used in wind tunnels, coupling microphone array measurement, and PIV data. This method provides meaningful results if the array is far enough from the cavity. In addition, the optimal number of microphones must be determined so that the array captures the tonal sources of noise. A large number of microphones may amplify the broadband noise, and hide the tones, while with a small number of microphones, the array can not localise the main sources. The shape of the array also influences the results and should have a large density of microphone on its periphery. As a result, further cavity flow physics, and more data could be obtained for CFD validation.

# Chapter 5

## Modelling of the Cavity Flow Resonance

Rossiter's cavity flow model <sup>[13]</sup> assumes a hydrodynamic interaction, between the periodic shedding of vortices, travelling downstream at the shear layer convective speed of  $\kappa_v U_\infty$ , and the reflected acoustics waves travelling upstream at the speed of sound  $c$ .  $\kappa_v$  is Rossiter's convective velocity.

Based on the observation of standing waves in cavity flows, and the presence

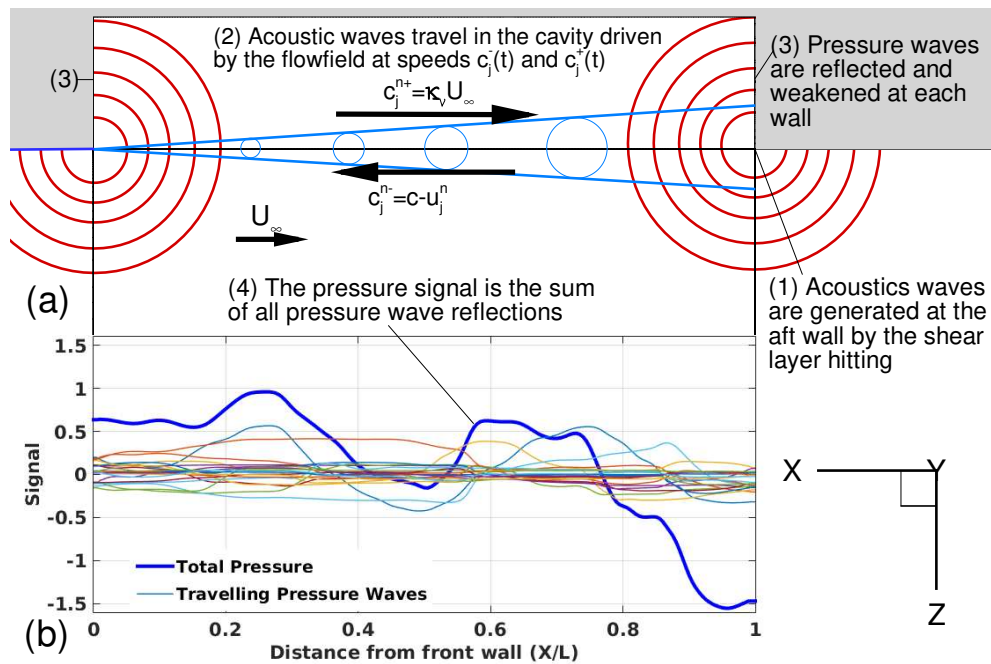


Figure 5.1: (a) Standing waves schematic, (b) Reflections and resulting pressures in cavity.

of numerous reflected waves in experiments [24, 141, 142, 14], it is assumed that the main mechanism driving the tone generation is similar to that of an one-dimensional standing wave resonator. Other papers made this assumption including Casper *et al.* [42] who considered an upstream wave travelling at the speed of sound  $c$ , and a downstream travelling wave at  $0.57U_\infty$ . This simple model was able to separately reproduce the mode shape of every mode by imposing its frequency in a simple standing wave formula. However, the flow dynamics including the modulation of the tones, the existence of the modes, and the non periodicity of the flow were not predicted. The simplest resonator in fluid dynamics is a pipe closed at both ends, where pressure waves  $P_i(x, t)$  are alternatively reflected at each ends, and travel at the speed of the sound along the pipe. The superposition of the pressure waves leads to strong pressure fluctuations, of frequency defined by the pipe length.

In a similar fashion, the cavity resonance is represented by a one dimensional standing wave resonator, shown in figure 5.1. The space is uniformly discretised using  $N_p$  points, and the pressure of the  $i$ -th reflected wave at a point  $j$ , and at the  $n$ -th timestep is denoted by  $P_{i,j}^n$ . The front wall is localised at  $j=0$ , and the aft wall at  $j = N_p$ . First, the pressure waves generated as the shear layer impacts the downstream corner (position (1) in figure 5.1), and the pressure is given by:

$$P_{0,N_p}^n = \sum_{f=1}^{f_N} A_f \sin(2\pi f t_n + 2\pi R_i) \quad (5.1)$$

In the above,  $f$  is the wave frequency,  $f_N$  the frequency of the last wave,  $A_f$  the wave amplitude,  $R_i$  a random phase shift for each frequency, and  $t_n$  the time at timestep  $n$ . In shallow cavity flows, the amplitude  $A_f$  of the broadband noise decreases with the frequency, and the modes are usually seen up to the Rossiter mode 5 depending on the case. To produce a signal  $P_{0,N_p}^n$  representative of turbulent flow, the maximum pressure wave frequency  $f_N$  is set to a large value, here 3kHz, and the wave amplitude  $A_f$  was set to linearly decrease with frequency:

$$A_f = A_0 \frac{f_N - f}{f_N} \quad (5.2)$$

As the amplitude of this signal depends on various parameters, including the Mach Number, or the thickness of the incoming shear layer, an arbitrary amplitude, found by trial and error,  $A_0 = 3920Pa$  is set for the output to fit as best as possible the CFD amplitude. The pressure waves travel towards the opposite wall (position (2) in

figure 5.1), and are alternatively reflected (position (3) in figure 5.1) at the front, and at the aft walls, assuming an absorption by the reflection defined as:

$$P_{i+1,0}^{n+1} = R_w A_t P_{i,0}^n \quad \text{at the front corner} \quad (5.3)$$

$$P_{i+1,N_p}^{n+1} = R_w A_t P_{i,N_p}^n \quad \text{at the aft corner} \quad (5.4)$$

with  $R_w$  the reflection coefficient at the wall defined as <sup>[143]</sup>:

$$R_w = \frac{Z_{steel} - Z_{air}}{Z_{steel} + Z_{air}} = 0.98 \quad (5.5)$$

with respectively  $Z_{steel}$ , and  $Z_{air}$  the steel (for the cavity walls), and air acoustic impedance.  $A_t$  is an absorption coefficient, assuming losses during the pressure wave travelling due to the viscosity, the turbulent flow, and the acoustic damping. This coefficient is set to 0.95 here for the purposes of demonstrating the method.

The waves are numerically transported using the equation,

$$\frac{\partial P}{\partial t} + c(x,t) \frac{\partial P}{\partial x} = 0 \quad (5.6)$$

discretised using an upwind scheme of third order <sup>[144]</sup>,

$$P_{i,j}^{n+1} = P_{i,j}^n - c_j^{n+1} \Delta t \frac{2P_{i,j+1}^n + 3P_{i,j}^n - 6P_{i,j-1}^n + P_{i,j-2}^n}{6\Delta x} \quad (5.7)$$

with  $\Delta x$  the grid spacing,  $\Delta t$  the timestep, and  $c_j^n$  the wave speed at the point  $j$ . Here, all velocities are defined as positive from the front wall to the aft wall. The upstream, and downstream travelling waves move out of sync at velocities defined, respectively as:

$$c_j^{n-} = -c + u_j^n \quad \text{and} \quad c_j^{n+} = \kappa_v U_\infty \quad (5.8)$$

with  $c$  the sound speed, and  $u_j^n$  the axial flowfield velocity along the propagation path of the pressure waves. Acoustics waves generated at aft wall by the impact of transported vortices in the shear layer, propagate upstream at the speed  $c_j^{n-}$  that includes the effect of the shear layer flowfield  $u_j^n$ . The present formulation of  $c_j^{n+}$  follows from Rossiter who assumed that the downstream travelling pressure waves were transported by the shed vortices at a speed proportional to the free-stream velocity. The assumption  $c_j^{n+} = c + u_j^n$  gave large over estimation of the Rossiter mode frequencies, and was rejected. The reflected pressure wave  $P_{i,j}^n$  is removed from the computation when its amplitude becomes weaker than 5% of  $P_{0,N_p}$ . Reducing this limit further does not influence the final result. Finally, the resulting pressure signal  $P_{i,j}^n$  is the sum of all reflections (curve

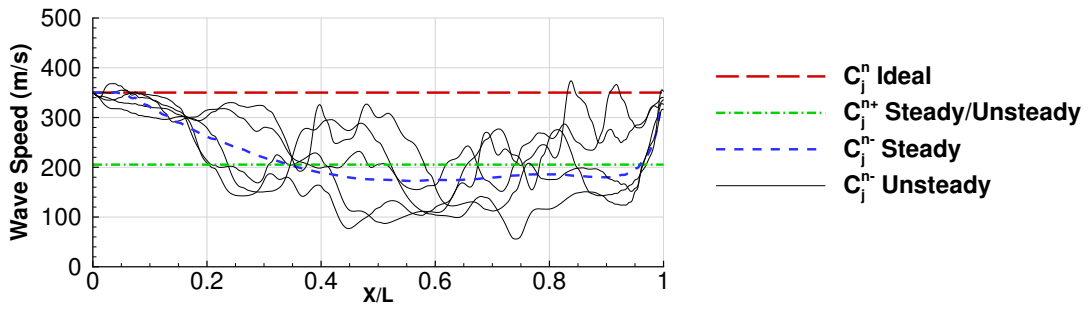


Figure 5.2: Absolute pressure wave speed  $c_j^n$  along the cavity length.

(4) in figure 5.1):

$$P_{t,j}^n = \sum_{i=1}^{N_r} P_{i,j}^n \quad (5.9)$$

with  $N_r$  the number of reflections.

The analysis is applied here to the M219 cavity without doors, with  $\Delta x = 0.0025m$  and  $\Delta t = 1.10^{-6}s$ . Three different assumptions on the velocities  $c_j^{n+}$  and  $c_j^{n-}$  driving the pressure wave propagation are tested. In figure 5.2, the unsteady speeds are only presented for selected time steps. First, the ideal wave resonator models the pressure waves travelling through a medium with  $c_j^{n+} = -c_j^{n-} = c$ , like a pipe closed at both ends. The sound pressure level in figure 5.3a shows an infinite number of linearly spaced tones following the formula:

$$f_m = \frac{m}{2L}c \quad (5.10)$$

with  $L$  the cavity length, and  $c$  the sound speed.

To reduce the tonal frequencies, the steady flow resonator considers pressure waves travelling at a reduced speed with respect to the mean stream-wise flow computed with CFD. The upstream travelling waves consider  $u_j^{n+}$  along a line in the shear layer at  $Y=0$  and  $Z/L=-0.04$ , where the tonal noise is maximum, as shown in figure 4.7a. The downstream travelling waves move along with the shed vortices at about 69% of the free-stream velocity. This value was chosen to fit as best as possible the experimental frequencies by try and error. The smaller the wave speed, the lower the resulting tonal frequencies. The steady flow resonator improves the results (Figure 5.3b) with a better estimation of cavity tone frequencies, within 40Hz. However, an infinite number of tones are predicted, not in agreement with experiments.

The accuracy of the analysis is improved using unsteady flow data to drive the pressure wave propagation. The CFD signal used to validate  $k-\omega$  SAS turbulence

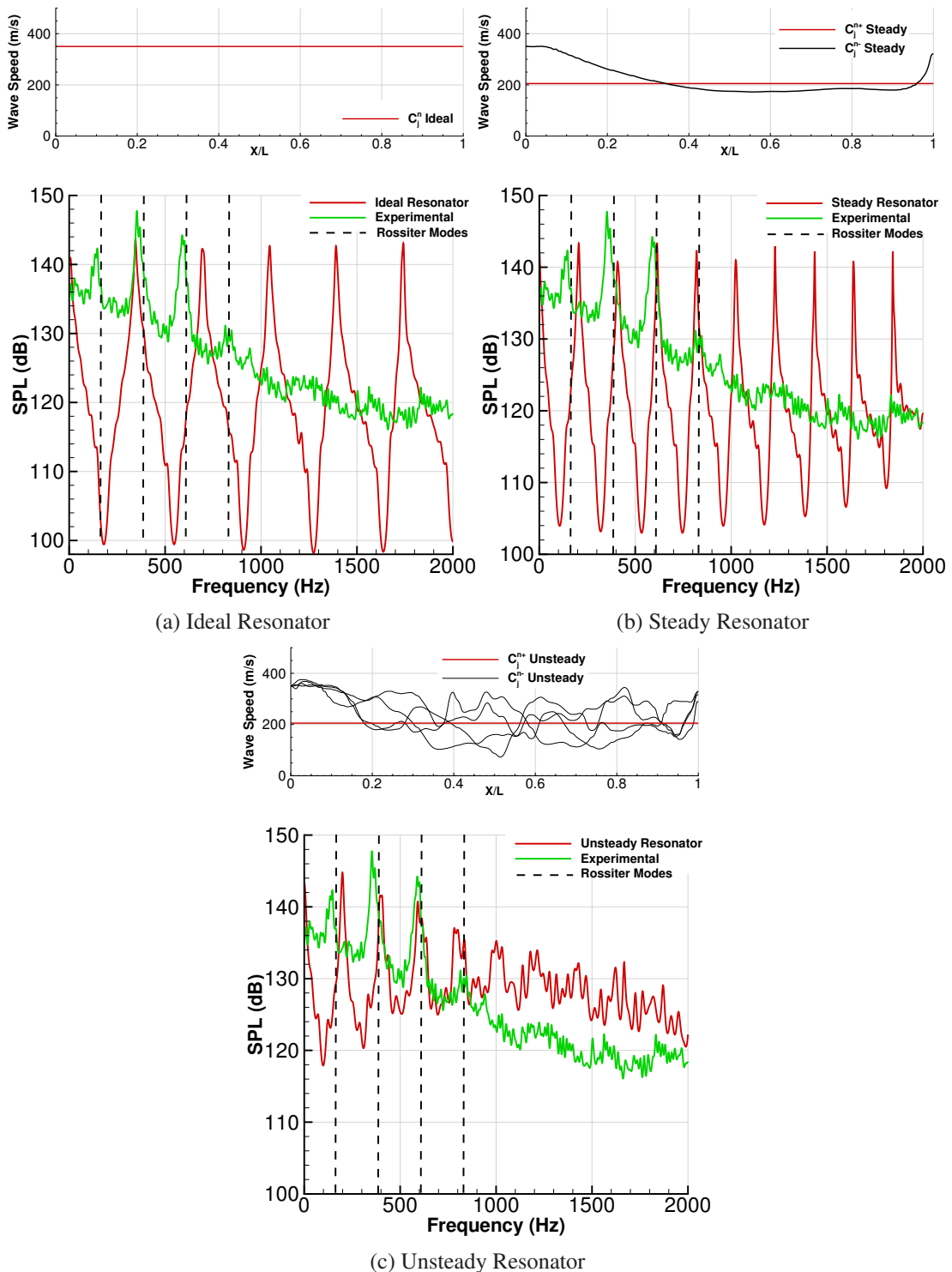


Figure 5.3: SPL at the aft wall of the M219 cavity.  $L=0.51\text{m}$ .

model with experiments, is looped to a length of 500 travel times. As for the steady resonator, the flowfield velocity is extracted along a line in the shear layer at  $Y=0$  and  $Z/L=-0.04$ . The upstream pressure waves propagate here at an unsteady velocity that

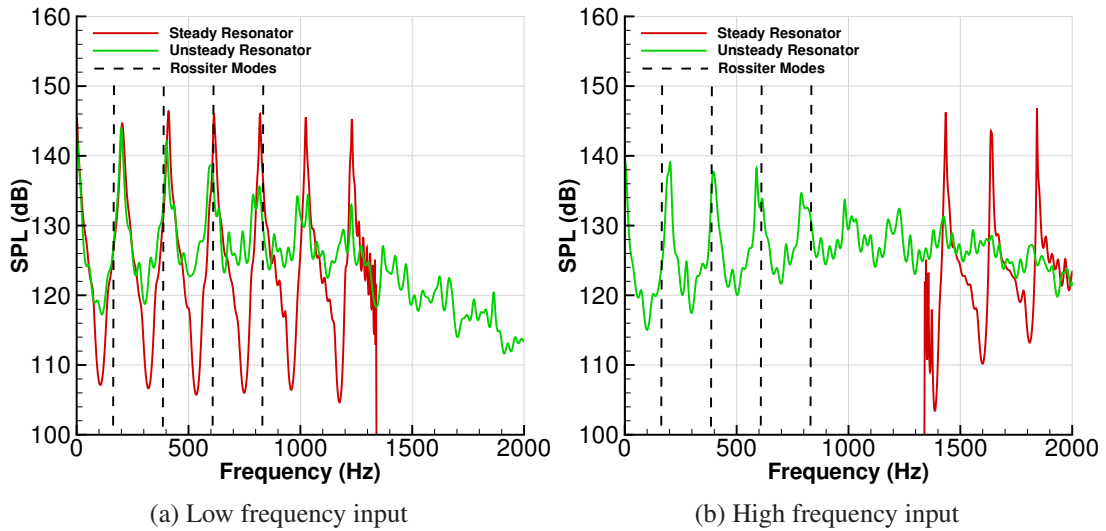


Figure 5.4: SPL at aft wall of the cavity for different input signals.

varies between 0 and 400m/s. The sound pressure levels in figure 5.3c show better agreement between the analysis and the experiments. The unsteady flow resonator predicts a finite number of modes, and broadband noise for the higher frequencies. This shows that the modal amplitudes are driven by the turbulence around the cavity. Rossiter<sup>[13]</sup> and Heller<sup>[22]</sup> demonstrated, experimentally, that a laminar shear layer lead to louder tones than a turbulent one. This agrees with the present model.

In figure 5.4, steady and unsteady resonators are used with two different signal inputs. The low frequency signals contain wavelengths larger than half a cavity length, and the high frequency signals contain wave lengths smaller than this limit. This wave length is equivalent to a frequency  $f_L$  of 1370Hz for a cavity length of 0.51m. The steady resonator provides a similar output for both inputs, with peaks and broadband noise limited to the frequency range of the input signal. However, the unsteady resonator generates a very different answer. With low frequency input (Figure 5.4a), the peaks are dumped from the third mode, and broadband noise appears above  $f_L$ . Employing the high frequency input, unexpected fluctuations arise (Figure 5.4b). The peaks above  $f_L$  are totally dumped in favour of broadband noise, and high amplitude peaks appear at the Rossiter mode frequencies. This suggests that the flowfield turbulence modifies the resonance mechanism, moving the energy from the high frequencies to the cavity modes. The high frequency resonance is disabled by the wave speed unsteadiness, that makes the upstream and the downstream waves not to be in phase, as their wavelengths are comparable, or smaller than the length scale of

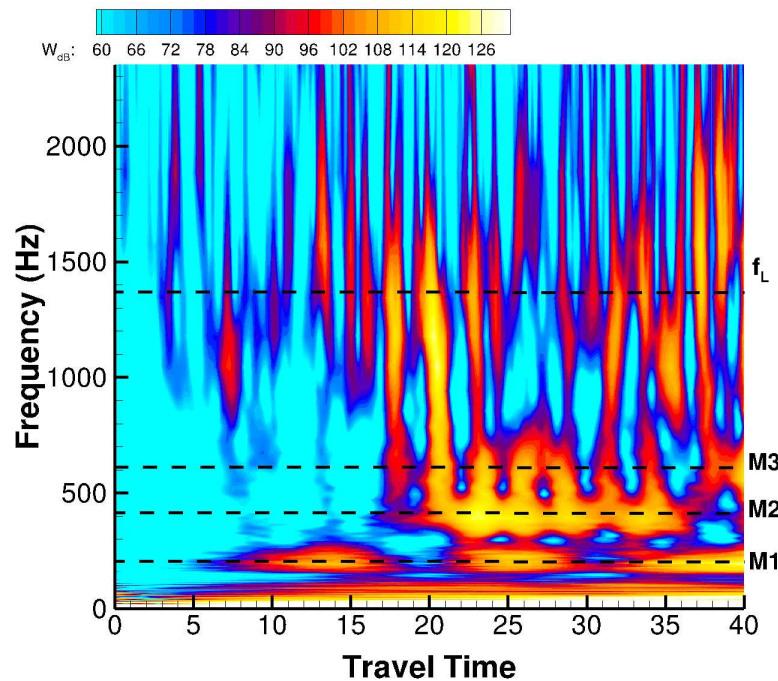


Figure 5.5: Scalogram at 95% of the cavity length. High frequency input applied to the unsteady resonator.

the flow fluctuations. This promotes broadband noise for high frequencies.

Figure 5.5 shows the output of the the unsteady resonator using the high frequency input. The wavelet transform is shown in function of the travel time at 95% of the cavity length. Lower frequency noise arises quickly, and after 5 travel times, the first cavity mode appears. The second and third modes appear after 17 travel times. This transfer from high to low frequencies may explain why cavity flows are so noisy, and fast to settle [145]. Overall, the available literature suggests that the shear layer hits the aft wall producing high frequency pressure waves reflecting inside the cavity. This wave superposition generates strong cavity modes at low frequencies due to the flowfield turbulence. Then, the cavity modes excite the shear layer motion, and this further amplifies the low frequencies in the pressure waves produced at aft wall. This feedback loop further amplifies the resonance, and the cavity modes lock to their final frequencies.

The Banded Integral Wavelets (BIWs) are shown for modes 1 to 3 for the unsteady flow resonator and the experimental results along the ceiling mid-span (Figures 5.6). The scalogram is integrated in windows of 20Hz centred on the cavity modes. There is a good agreement of the unsteady resonator with the experiments, showing standing waves of similar shape.

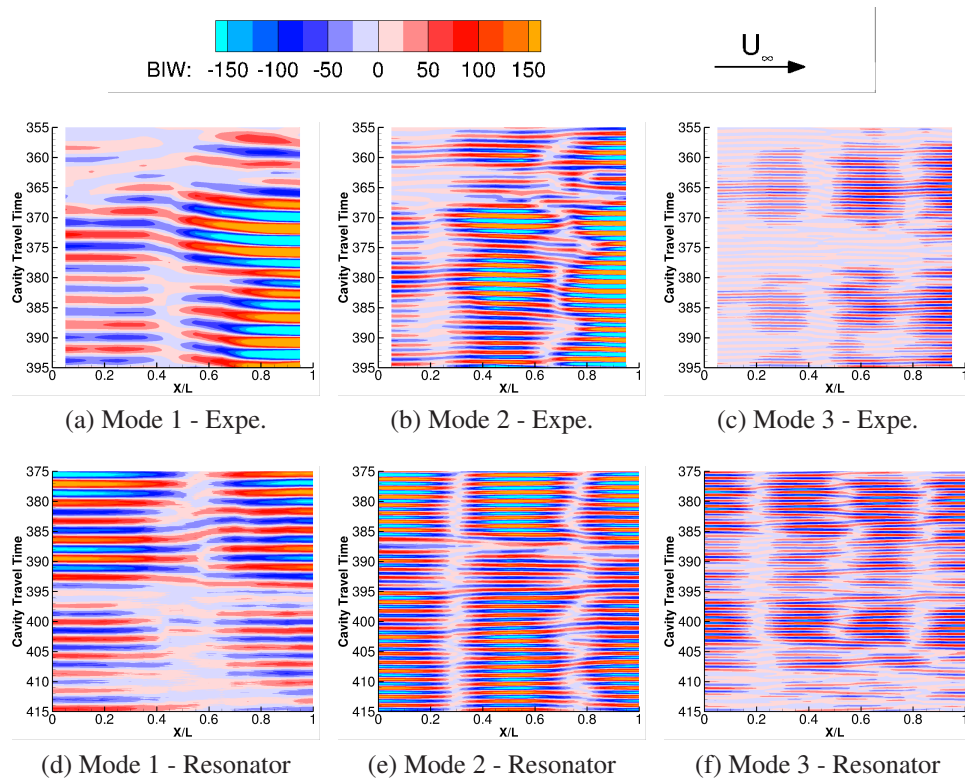


Figure 5.6: BIW at ceiling mid-span for experimental and unsteady resonator.

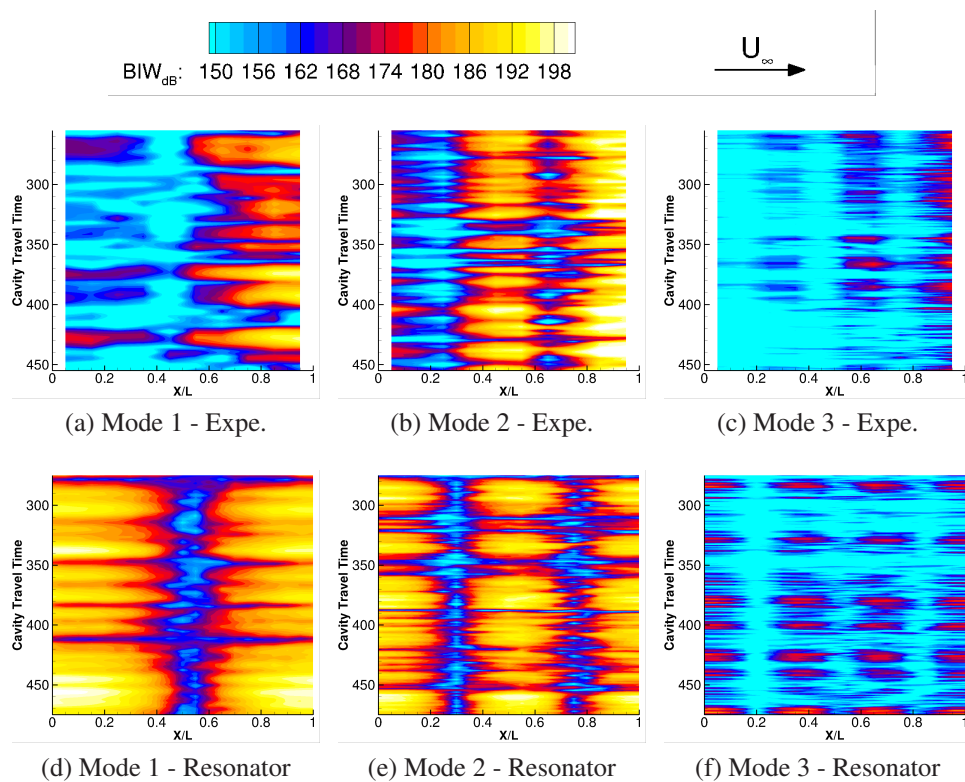


Figure 5.7: BIW envelope at ceiling mid-span for experimental and unsteady resonator.

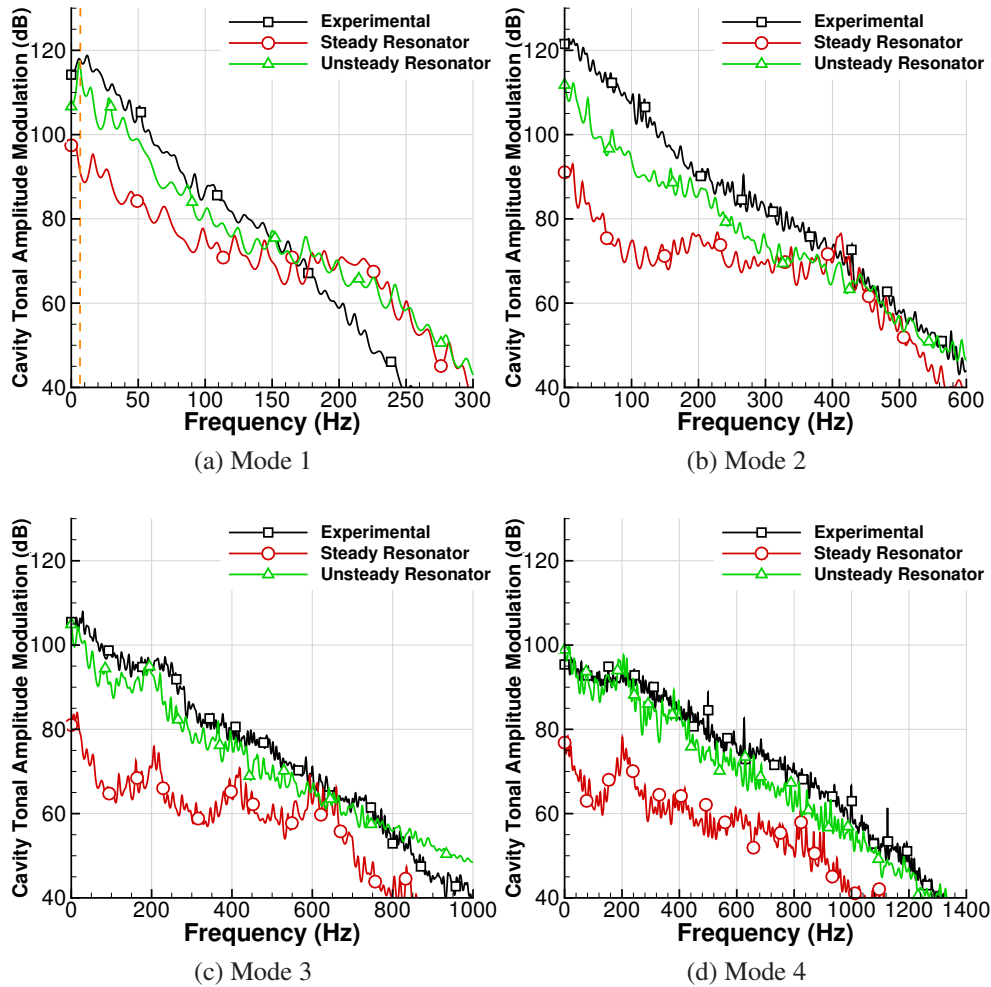


Figure 5.8: Tonal amplitude modulation at  $X/L=0.95$ .

The BIW envelope is shown in figure 5.7. The unsteady resonator predicts the tonal amplitude modulation, and the mode shapes. As the analysis does not include the noise fluctuations associated to the shear layer turbulence, and the noise radiating from all cavity surfaces, the gradient of noise between the front and the aft of the cavity is not well captured.

Figure 5.8 shows the spectrum of the cavity tonal amplitude modulation (BIW envelope) at 95% of the cavity length for modes 1 to 4. The experimental signal is characterised by decreasing modulation amplitude with the frequency. The first mode modulation has a peak at a very small frequency as shown by Kegerise *et al.* [29] (Vertical dashed line in figure 5.8a). The steady resonator fails to fit the experiments with under-prediction of the low frequencies. On the other hand, the unsteady resonator agrees well for the modes 1, 3 and 4, while the mode 2 modulation is only

slightly underestimated. Using the steady resonator, the third mode modulation shows peaks at 200, 400 and 600Hz, and the fourth mode at 200Hz. Those peaks are dumped by the unsteadiness of the flowfield in favour of broadband noise.

This analysis gives an accurate picture of the transonic cavity flow dynamics, showing that the wave superposition is the main mechanism driving the cavity flow resonance. However, the relative modal amplitudes are not exactly represented here compared to the experiments, highlighting a missing part of the physics. In future work, the pumping action at the aft wall will be taken into account. The tonal pressure fluctuations and the shear layer motion<sup>[14]</sup> have to be coupled to generate the pressure at aft wall  $P_{0,N_p}$  regarding the pressure history.

In summary, the cavity dynamics were modelled as a standing wave resonator, influenced by the shear layer flow. This study suggests that the generation mechanism of cavity noise proposed by Rossiter can be complemented with the superposition of the pressure waves reflecting, and travelling inside the bay. The time averaged flow-field drives the tonal frequencies, while the flow-field fluctuations drive their amplitude, and feed the broadband noise. More importantly, the production of cavity tonal noise by high frequencies may be the trigger of the cavity flow resonance. For the first time, the tonal dynamics of the cavity flow are fully represented by a model with the standing wave-like oscillations and their modulation. This explains why past cavity flows models considering a small number of pressure reflections were not able to capture the cavity dynamics.

This new modelling will help the understanding of experimental, and numerical observations of the noise field. For example, the efficiency of a rod placed at the leading edge of a cavity is increasing with its diameter<sup>[88]</sup>. This could be the consequence of the Von Karman sheet that includes large enough vortices to disturb the resonance of the low frequency modes. Closing one door of a weapon bay, the tones are amplified and shifted to higher frequencies with a reduction of the broadband noise<sup>[36, 38]</sup>. This is explained by the shield part of the cavity where the acoustic waves can travel in a more steady flow, leading to a noise field closer to the steady resonator model.

This also defines guidelines for cavity flow control. The first way to alleviate the resonance is by reducing the generation of acoustic waves at the aft wall. The second way is to force the presence of large enough perturbations in the shear layer to disable the tonal resonance in favour of broadband noise.

# Chapter 6

## Geometry and Conditions

This chapter presents the geometry used to simulate the aeroelasticity of stores in weapon bays, the door opening, and the store trajectory variability. In this work, all computations were carried out using Scale-Adaptive Simulation with a timestep equal to 1% of the cavity length travel time (0.12ms). The free-stream Mach number was 0.85, and the Reynolds number based on the cavity length ( $Re_L$ ) 6.5 million. The conditions approximated an aircraft flying at 3000ft,  $T = 8.51deg$ ,  $p = 89900Pa$ ,  $\rho = 1.11kg/m^2$ , and  $U_\infty = 286m/s$ .

### 6.1 Geometry

A prismatic cavity 3.59m long, 1.03m wide, and of length to depth ratio of 7.0 is considered (Figure 6.1). This L/D ratio is more representative of actual fighter weapon bays than the M219 cavity (L/D=5).

The doors are modelled as solid flat plates with a thickness of 0.3% of the cavity depth, a width of 46% of the cavity width, and a length of 98% of the cavity length

Name	Speed (deg/s)	Travel time	Strouhal
Slow	110	80	0.023
Medium	220	40	0.047
Fast	440	20	0.094

Table 6.1: Simulated door opening speeds

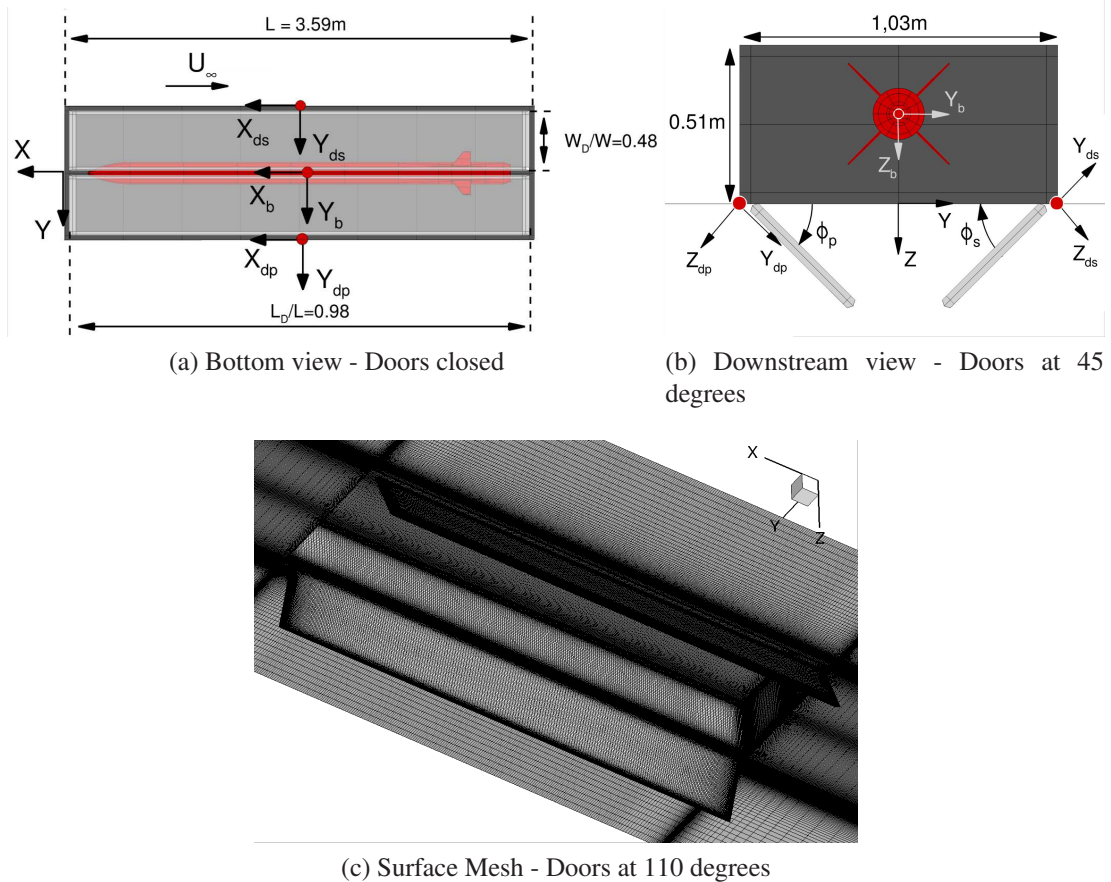


Figure 6.1: Schematic view of the vented cavity with store.

(Figure 6.1). These dimensions allow for cavity venting when doors are fully closed.  $\phi_s$  and  $\phi_p$  are the starboard and port side door angles, with zero degrees corresponding to the closed doors position. CFD results at different configurations with static doors are tested and compared against computations for dynamic opening. Static door configurations include cases at 20, 45, 90 and 110 degrees. The effect of the dynamic door opening is assessed by computing the door operation for angles between 0 and 110 degrees. Three opening frequencies were computed, 110, 220 and 440 degrees/sec, and their opening was respectively equivalent to 80, 40 and 20 travel times at 3000 ft of altitude. They are respectively termed slow, medium and fast opening. Modern fighters complete the door opening during approximately 1 second, for a cavity length of about 4 meters. This corresponds using the selected CFD conditions to a Strouhal number of 0.027 at a speed of  $U_\infty = 286\text{m/s}$ . The opening Strouhal number compares

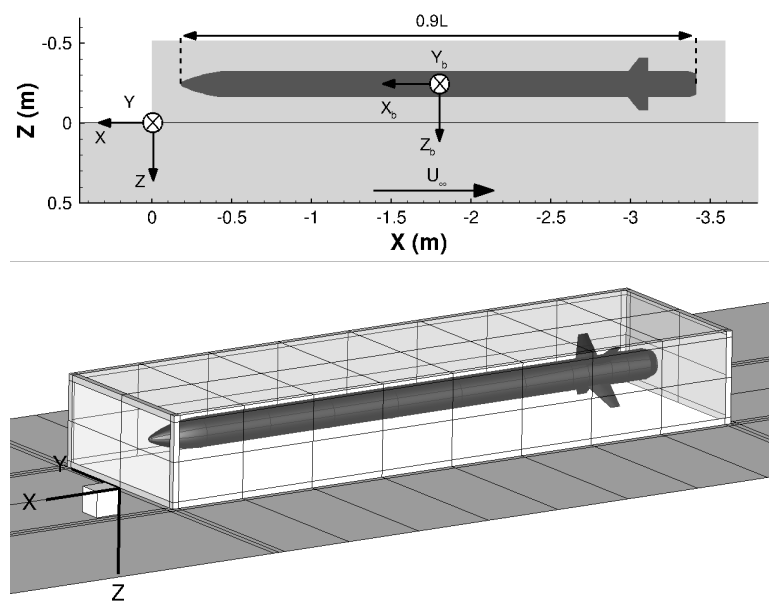


Figure 6.2: Geometry, cavity axes, and the store at carriage position.

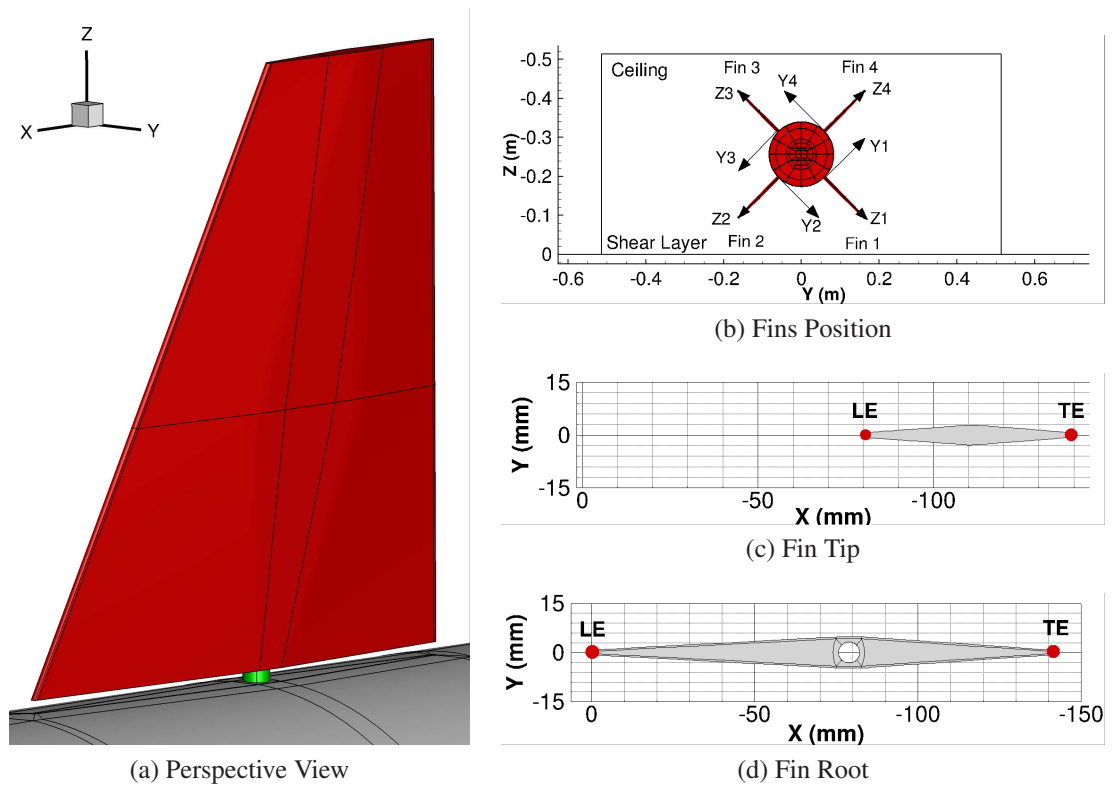


Figure 6.3: Fin geometry.

the door opening frequency  $f_d$ , and the travel time frequency  $f_{tt}$  as:

$$St_{opening} = \frac{f_d}{f_{tt}} = \frac{f_d L}{U_\infty} \quad (6.1)$$

where  $L$  is the cavity length, and  $U_\infty$  is the free-stream velocity. The simulated slow, medium, and fast opening, give Strouhal numbers of 0.023, 0.047 and 0.094. The slow opening is the most representative of actual aircraft cavities, but faster studies are also considered, since to maintain stealth, the cavity exposure should be minimised.

The store had a mass  $m_s$ , was 90% of the cavity length, and had four fins in a cross configuration (Figure 6.2) <sup>[146]</sup>. The fins were supported by a rod so that they can rotate, with respect to the store body (Figure 6.3). The flow was resolved in the gap between the fins and the store body. The non dimensional moments of inertia  $I/(m_s.L_s^2)$  were  $4,0.10^{-4}$  about the roll axis and  $7,3.10^{-2}$  about the pitch and yaw axes, with the centre of gravity located at mid length of the store. Without doors, the carriage position was at mid cavity depth ( $Z/D=-0.50$ ), while the store was carried at  $Z/D=-0.56$  allowing space for closing the doors.

The computations begin with a transitional phase where the cavity flow settles. The first 10 cavity travel times of the flow, or equivalently 130ms, are ignored, and then, the flow is sampled and stored for analysis.

All simulations were performed using the chimera technique <sup>[119]</sup> assuming one independent grid by object. Table 6.2 summarises the number of blocks, and the size of each grid component.

Name	Nb. of Blocks	Nb. of Points ( $10^6$ )
Cavity	1668	28.9
Door x 2	384	2.8
Store	816	7.1

Table 6.2: Mesh size for each solid

## 6.2 Frames of Reference

A frame of reference is attached to each solid object (cavity, door, fins, store). The cavity is attached to the earth system using the North East Down (NED) convention where,  $X$  is positive pointing north ahead of the store,  $Y$  is positive east and perpendicular to the  $X$  axis, and  $Z$  is positive towards the earth centre (Figure 6.1). The zero is defined at the mid-span of the front bay lip.

The store system  $X_b, Y_b, Z_b$  is right-handed and coincident with the earth system for the store at carriage, with respect to the roll, pitch and yaw axes (Figure 6.2). The moments are computed about the gravity center at the mid-span of the store.

The door systems  $X_{ds}, Y_{ds}, Z_{ds}$  (starboard door) and  $X_{dp}, Y_{dp}, Z_{dp}$  (port door) are right-handed and coincident with the earth system when closed, with respect to the roll, pitch and yaw axes. The moments are computed about the red dots of figure 6.1.

Each fin uses a local reference, where  $X$  is positive north, away of the fin,  $Z$  is positive from root to tip and perpendicular to the  $X$  axis, and  $Y$  is positive towards the port side the fin (Figure 6.3).

The force ( $C_{force}$ ) and moment coefficients ( $C_{moment}$ ) are computed using:

$$C_{force} = \frac{F}{\frac{1}{2}\rho_{\infty}U_{\infty}^2S} \quad \text{and} \quad C_{moment} = \frac{M}{\frac{1}{2}\rho_{\infty}U_{\infty}^2d_{ref}S} \quad (6.2)$$

where  $F$  and  $M$  are forces and moments,  $d_{ref}$  is the reference length, and  $S$  is the reference area. For the store,  $d_{ref}$ , the store diameter, and  $S = \pi d_{ref}^2/4$  is the store reference area. For the cavity walls and doors,  $d_{ref} = L$ , the cavity length, and  $S = WD$  is the aft wall area.

# Chapter 7

## Coupled Aeroelastic Computation of Store in Weapon Bays

This chapter presents the method for store aeroelasticity within weapon bays. Then, results for a fixed store at carriage, and shear layer position are discussed. The aeroelasticity of stores during door opening, and store release are respectively discussed in chapters 8 and 9.

### 7.1 Fluid-Structure Interaction Modelling

The aeroelastic framework of HMB3 is based on the modal method <sup>[44]</sup>. This method uses structural modes computed using NASTRAN <sup>[147]</sup> and a mesh deformation module based on the inverse distance weighting interpolation.

#### 7.1.1 Structural Modes

For the structural deformations, the modal approach is used to lower the computational cost. It expresses solid deformations as functions of the structure's eigenmodes. The body and fin structural modes are obtained using NASTRAN <sup>[147]</sup>. The structural model include 23000 points on the missile body and 27148 points on each fin. The models provided by MBDA UK Ltd. represent the complete structure, including the internal parts inside the body. The structural equations are solved with the eigenvalue analysis SOL103 method of NASTRAN <sup>[147]</sup>. Four fin modes are visualised in figure 7.1 (modes F1 to F4 of table 7.1).

Mode	Mode name	Frequency (Hz)	Closer Rossiter mode (number / Hz)
Free Root Fin			
1	F1	144.1	5 / 149.2
2	F2	158.1	5 / 149.2
3	F3	232.0	8 / 244.6
4	F4	923.6	30 / 939.0
Body at Carriage			
1	Y1	25.5	1 / 23.6
2	Z1	25.9	1 / 23.6
3	Y2	28.9	1 / 23.6
4	Z2	29.9	1 / 23.6
5	Y3	82.8	3 / 86.8
6	Z3	112.1	4 / 118.5
7	Y4	127.8	4 / 118.5
8	Z4	197.6	7 / 213.1
9	Y5	214.8	7 / 213.1
10	Z5	218.8	7 / 213.1
Body in Free Air			
1	FAZ1	43.4	2 / 55.2
2	FAY1	47.1	2 / 55.2
3	FAZ2	121.3	4 / 118.5
4	FAY2	148.2	5 / 150.0
5	FAZ3	259.4	8 / 244.6
6	FAZ4	440.4	14 / 434.0

Table 7.1: Modal frequencies of the store. Rossiter's modes are based on Mach of 0.85 and cavity length of 3.59m using equation 1.1

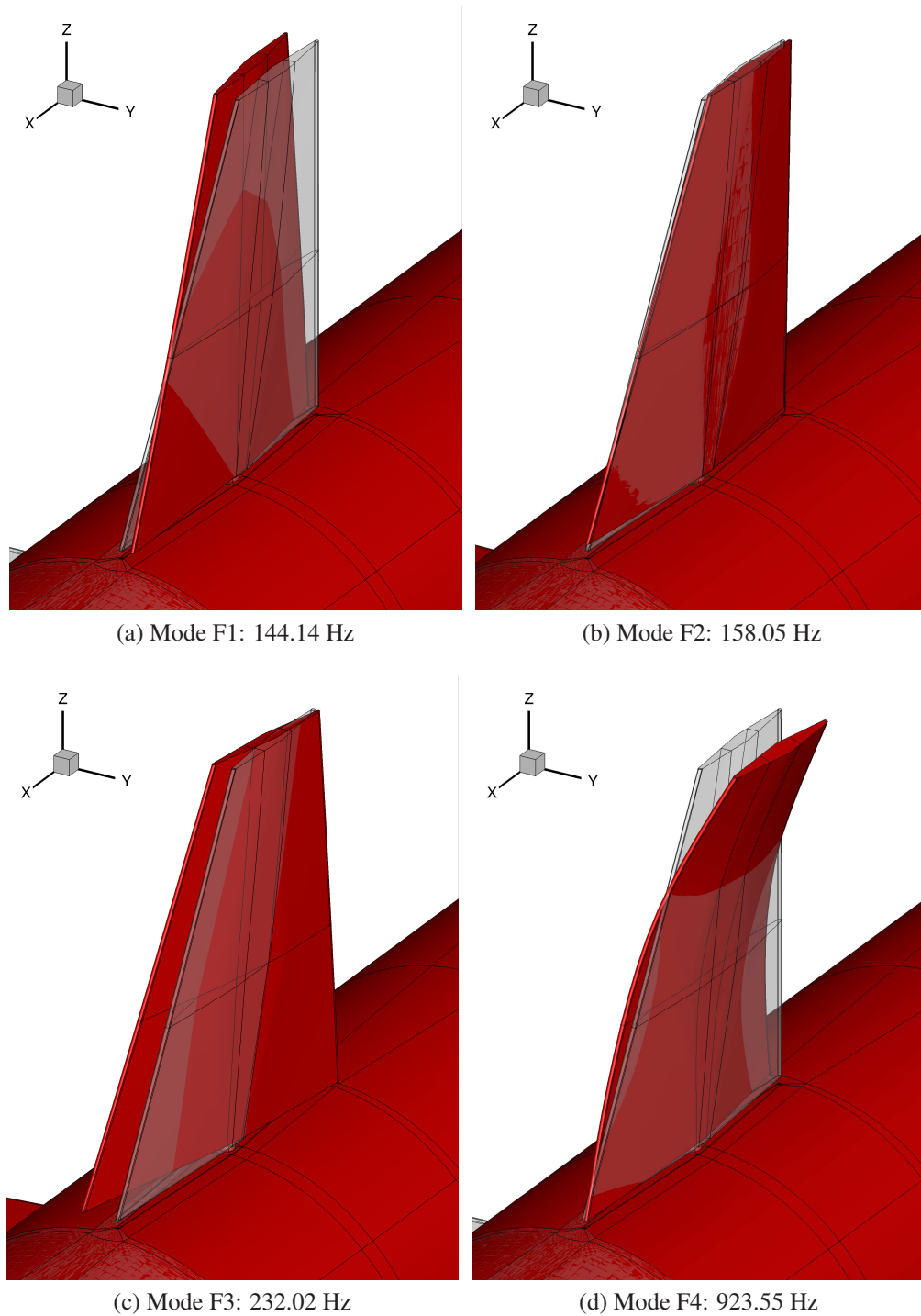


Figure 7.1: Structural modes 1 to 4 of the free root fin

At carriage, the store cannot move freely. The motion of the body is constrained by the ejector release unit (ERU) holding the store at two points. The holders are modelled by two elastic elements (CBUSH) fixed to the ceiling and to the store by multiple point connections (Figure 7.2). The forward, and the aft hangers are

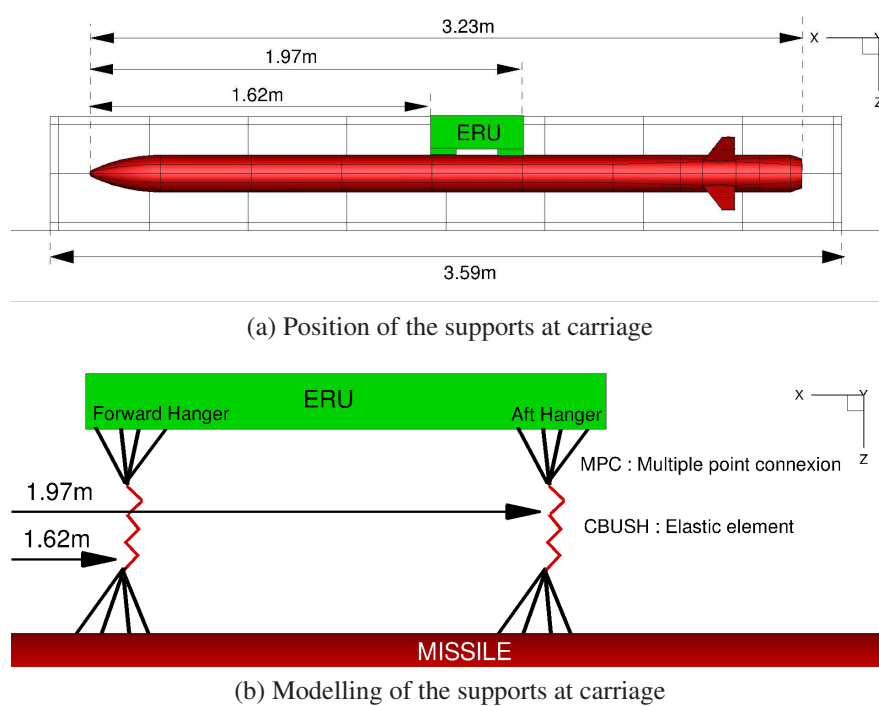


Figure 7.2: Ejector Release Unit (ERU) position and structural modelling

respectively placed at  $0.45\%L$  and at  $0.55\%L$  from the store nose. Ten carriage modes are listed in table 7.1, and figure 7.3 shows the first six of them. At carriage, the modes and frequencies of the store are different from free flight. After the store is released from the ERU, the store can freely deform, and six structural modes, shown figure 7.4, were computed.

### 7.1.2 CFD/CSD Interpolation

At the beginning of each computation, the structural modes are interpolated from the CSD to the CFD grid. The interpolation is performed with the Moving Least Square method (MLS). This method is accurate as loads integrations and displacement computations are carried out on the CFD grid without interpolation.

Also, the different solids in contact have to be identified relatively to each other (Figure 7.5) to be able to compute the motion of each fin (object 3) shown in blue, relatively to the body (object 1) shown in green. Then, all shared points between fins and body are identified. Finally, a zone of size  $R$  from the shared points called patch (object 2) is defined on each fin. In the present case,  $R$  was arbitrary defined to include the complete rod in the patch.

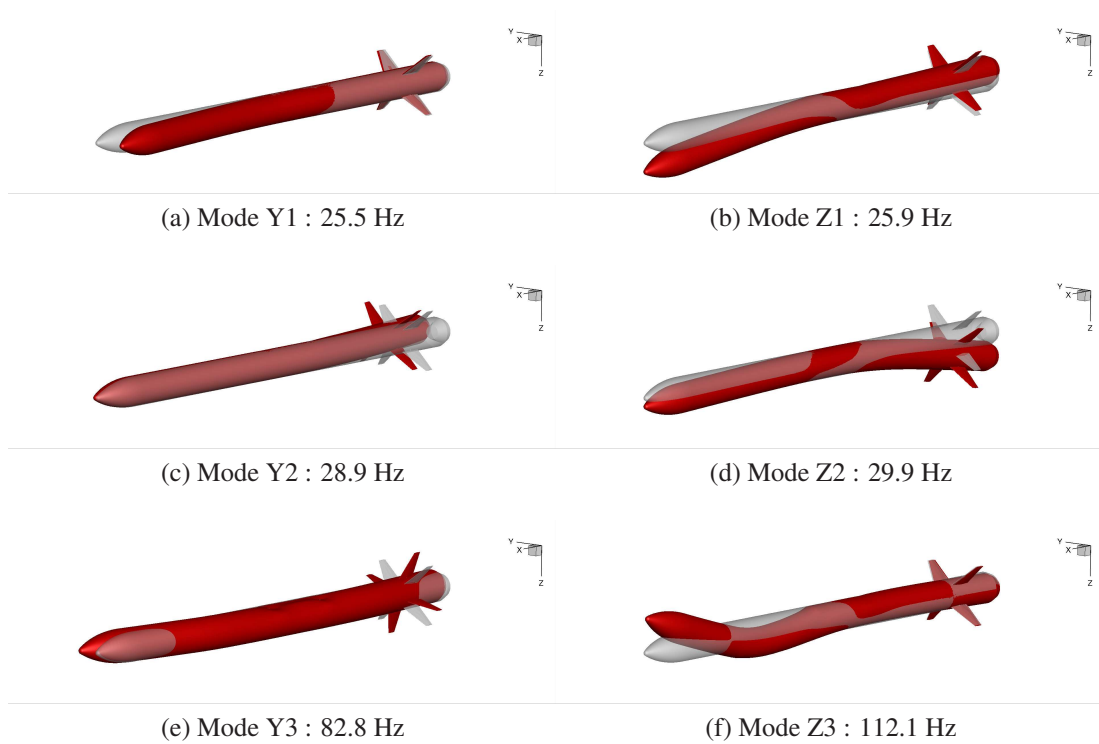


Figure 7.3: Structural modes 1 to 6 of the body at carriage

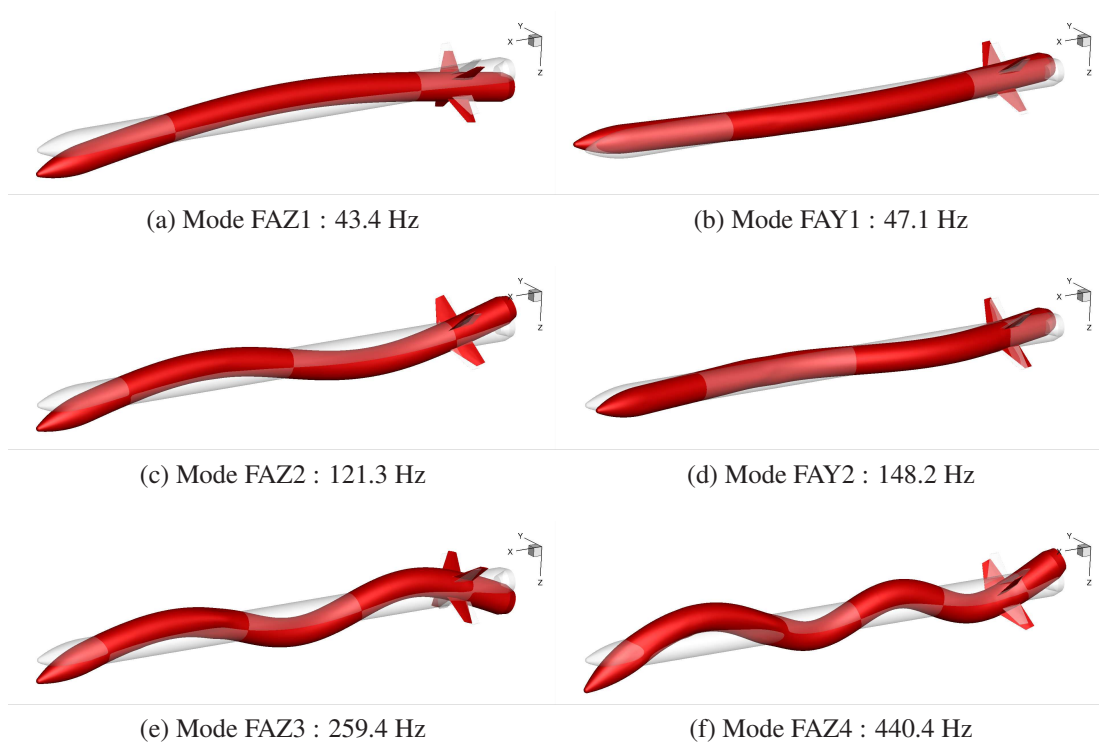


Figure 7.4: Structural modes 1 to 6 of the body in free air

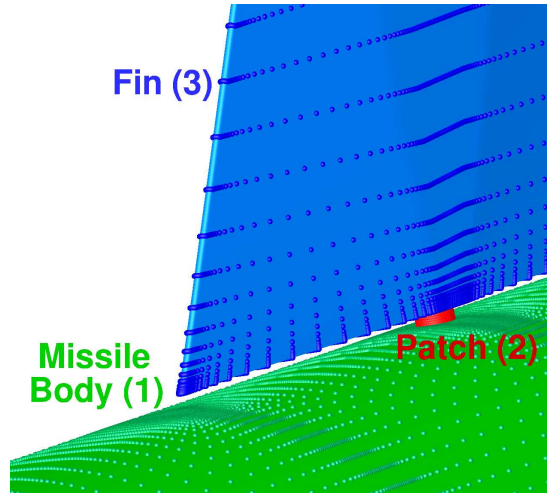


Figure 7.5: Body and fins structure of the store. Grid points represented by spheres.

### 7.1.3 Computation of the Modal Loads and Amplitudes

The CFD computation is performed on the deformed mesh to obtain the solution at  $t + \Delta t$ . The pressure is then summed over the undeformed mesh points to compute the modal loads  $f_m^s(t)$  on the solid ( $s$ ) for the  $m$ -th mode at time  $t$ :

$$f_m^s(t) = \sum_{p=1}^{n_s} \mathbf{p}(p,t) \cdot \phi_m^s(p) \quad (7.1)$$

with  $n_s$  the number of CFD points on the solid  $s$ ,  $\mathbf{p}(p,t)$  the pressure at a point  $p$  in  $N/m^2$ , and  $\phi_m^s(p)$  the mode displacement at the point  $p$  for the  $m$ -th mode of the solid  $s$  normalised by the generalised mass set to 1kg. The modal load unit is  $N/m.kg$ .

The shape of the solid  $s$ ,  $\phi^s(t)$ , is described as a sum of eigenvectors  $\phi_m^s$  :

$$\phi^s(t) = \phi_0^s + \sum_{m=1}^{n_m^s} \alpha_m^s(t) \phi_m^s \quad (7.2)$$

with  $n_m^s$  the number of modes on the solid  $s$ , and  $\phi_0^s$  the undeformed shape. The problem is then reduced to solving for the coefficient  $\alpha_m^s$ . In the modal approach, the coefficient can be obtained by solving the following differential equation:

$$\frac{\partial^2 \alpha_m^s}{\partial t^2} + 2\zeta_m \omega_m \frac{\partial \alpha_m^s}{\partial t} + \omega_m^2 \alpha_m^s = f_m^s(t) \quad (7.3)$$

For stability purposes, the analysis is started with a strong damping coefficient of  $\zeta_m = 0.7$  for each mode. The high starting damping in the equation is used to control the oscillations created by the step that appear at the beginning of the simulation, due to the sudden change in the forces applied to a second order system. Once the solid

reaches an acceptable level of deformation, the damping is gradually brought to a final value of  $\zeta_m = 0.1$ , or lower.

Then, equation 7.3 is explicitly solved using the leap-frog method. To ensure stability of the numerical scheme chosen to solve the structural equation, each timestep is solved in  $N_i$  inner timesteps of size  $\Delta t_i = \Delta t/N_i$ . The modal force at the time  $t_i = t + i\Delta t_i$  is :

$$f_m^s(t_i) = f_m^s(t) + \frac{i(f_m^s(t + \Delta t) - f_m^s(t))}{N_i} \quad (7.4)$$

The m-th amplitude  $\alpha_m^s$  is then assessed for inner timestep  $t_i + 1$  :

$$[\alpha_m^s]_{t_{i+1}} = [\alpha_m^s]_{t_i} + \left[ \frac{\partial \alpha_m^s}{\partial t_i} \right]_{t_i} \Delta t_i + \frac{1}{2} \left[ \frac{\partial^2 \alpha_m^s}{\partial t_i^2} \right]_{t_i} \Delta t_i^2 \quad (7.5)$$

The time derivative of the amplitudes are then computed as:

$$\left[ \frac{\partial^2 \alpha_m^s}{\partial t_i^2} \right]_{t_{i+1}} = [f_m^s]_{t_i} - \omega_m^2 [\alpha_m^s]_{t_i} - 2\zeta \omega_m \left[ \frac{\partial \alpha_m^s}{\partial t_i} \right]_{t_i} \quad (7.6)$$

$$\left[ \frac{\partial \alpha_m^s}{\partial t_i} \right]_{t_{i+1}} = \left[ \frac{\partial \alpha_m^s}{\partial t_i} \right]_{t_i} + \frac{1}{2} \left( \left[ \frac{\partial^2 \alpha_m^s}{\partial t_i^2} \right]_{t_i} + \left[ \frac{\partial^2 \alpha_m^s}{\partial t_i^2} \right]_{t_{i+1}} \right) \Delta t_i \quad (7.7)$$

A flow chart showing the different steps of the method is shown figure 7.6.

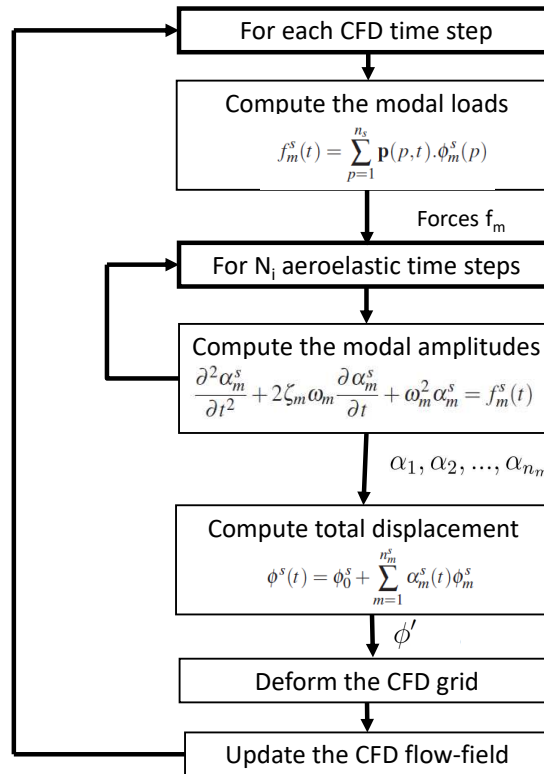


Figure 7.6: Aeroelastic coupling strategy.

### 7.1.4 Deformation of the Surface Mesh

The displacement of the surface of each solid is computed using equation 7.2. Then, the surface mesh is deformed for each solid body, beginning by the store body where the displacements are applied to all surface points. Then, the fin motion due to the body displacement is computed with the method presented in figure 7.7.

For each fin (f) to deform, the displacement due to the body (b) is computed as:

$$\phi^f = \mathbf{R}\mathbf{P} + \mathbf{t} \quad (7.8)$$

with  $\mathbf{R}$  and  $\mathbf{t}$ , respectively, the mean rotation matrix, and the translation vector of the shared points between the fin and the body, and  $\mathbf{P} = [x, y, z]$  the position of the points of fin f (Figure 7.7c).

The translation vector is the mean displacement of the  $n_{sp}$  shared points between the body and the fin:

$$\mathbf{t} = \frac{1}{n_{sp}} \sum_{p=1}^{n_{sp}} \phi^b(p) \quad (7.9)$$

with  $\phi^b(p)$  the displacement of the point p imposed by the body. The centroids of the shared points are computed on the original position A, and at the position B imposed by the body:

$$\mathbf{C}_A = \frac{1}{n_{sp}} \sum_{p=1}^{n_{sp}} \mathbf{P}(p) \quad (7.10)$$

$$\mathbf{C}_B = \frac{1}{n_{sp}} \sum_{p=1}^{n_{sp}} (\mathbf{P}(p) + \phi^b(p)) \quad (7.11)$$

The optimal solid rotation to go from position A to position B is computed with the Singular Value Decomposition technique (SVD). This method is fast and easy to implement <sup>[148]</sup>. The centres of rotation A and B are sent to the origin. Then, a covariance matrix  $\mathbf{H}$  is computed:

$$\mathbf{H} = \sum_{p=1}^{n_{sp}} (\mathbf{P}(p) - \mathbf{C}_A)(\mathbf{P}(p) + \phi^b(p) - \mathbf{C}_B)^T \quad (7.12)$$

The singular value decomposition of the matrix is computed as:

$$[\mathbf{U}, \mathbf{S}, \mathbf{V}] = SVD(\mathbf{H}) \quad (7.13)$$

The rotation matrix is then given by:

$$\mathbf{R} = \mathbf{V}\mathbf{U}^T \quad (7.14)$$

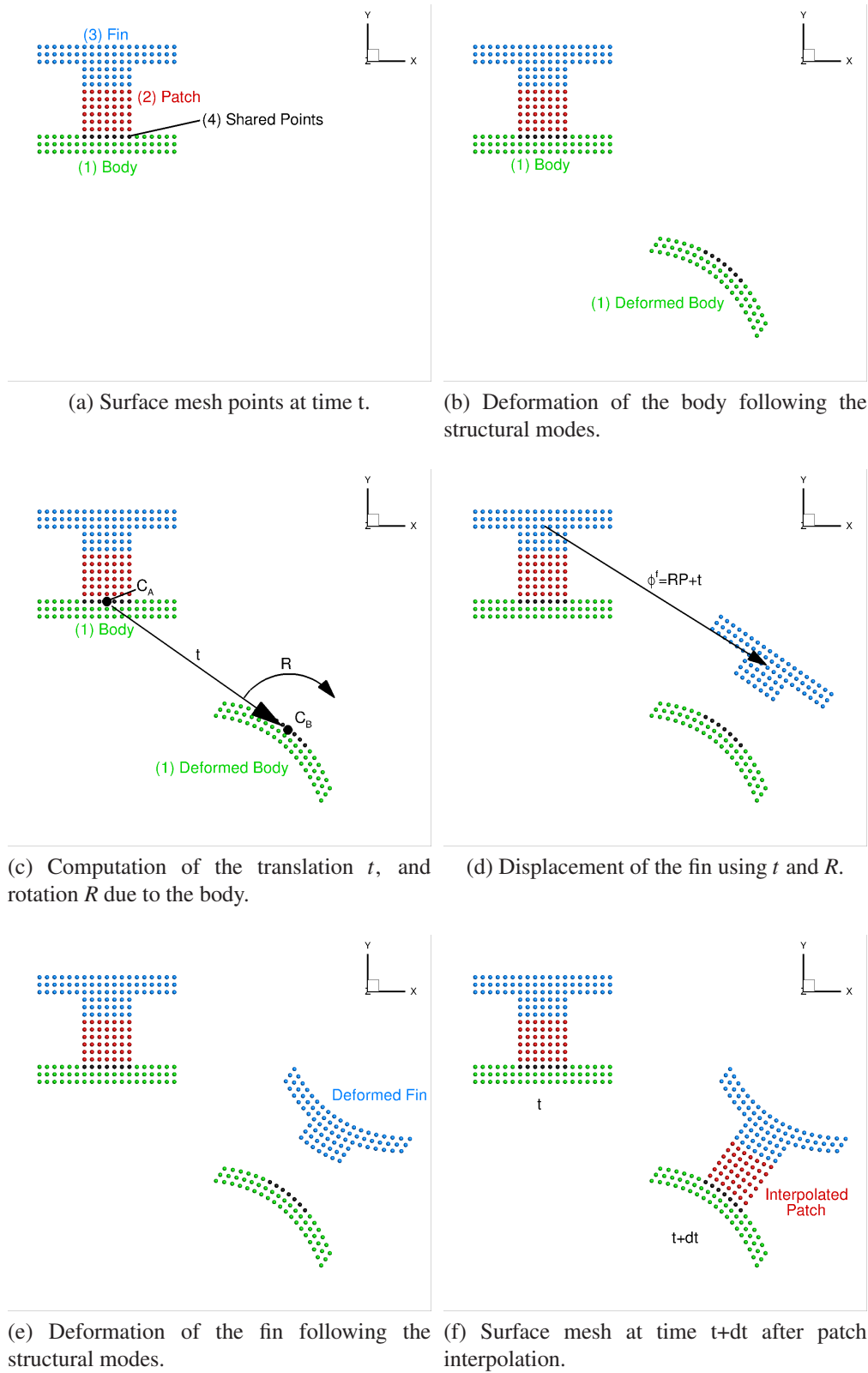


Figure 7.7: 2D example of surface mesh deformation with body and fin.

Finally, the computed displacement with equation 7.8 (Figure 7.7d) and the displacement due to the structural modes are applied to the fin (f) outside the patch (Figure 7.7e). The displacements of the patch points are interpolated using Inverse Distance Weighting (IDW) between the fins points that just moved, and the shared points imposed by the body position (Figure 7.7f). This interpolation uses the same method as described in the following section 7.1.5.

### 7.1.5 Volume Mesh Deformation

To adapt the volume mesh to the surface of the deformed solid, a mesh deformation algorithm has been implemented in HMB3, based on Inverse Distance Weighting (IDW) [149]. IDW interpolates the values at given points with a weighted average of the values available at a set of known points. The weight assigned to the value at a known point is proportional to the inverse of the distance between the known and the given point. Biava *et al.* [150] used this method to optimise rotor blade shapes in HMB3, and obtained good quality mesh after mesh deformations.

Given  $N$  samples  $\mathbf{u}_i = u(\mathbf{x}_i)$  for  $i = 1, 2, \dots, N$ , the interpolated value of the function  $\mathbf{u}$  at a point  $\mathbf{x}$  using IDW is given by:

$$\mathbf{u}(\mathbf{x}) = \begin{cases} \frac{\sum_{i=1}^N w_i(\mathbf{x}) \mathbf{u}_i}{\sum_{i=1}^N w_i(\mathbf{x})}, & \text{if } d(\mathbf{x}, \mathbf{x}_i) \neq 0 \text{ for all } i \\ \mathbf{u}_i, & \text{if } d(\mathbf{x}, \mathbf{x}_i) = 0 \text{ for some } i \end{cases} \quad (7.15)$$

where

$$w_i(\mathbf{x}) = \frac{1}{d(\mathbf{x}, \mathbf{x}_i)^p} \quad (7.16)$$

In the above equations,  $p$  is any positive real number (called the *power parameter*) and  $d(\mathbf{x}, \mathbf{y})$  is the Euclidean distance between  $\mathbf{x}$  and  $\mathbf{y}$  (but any other metric operator could be considered as well).

The method in its original form, becomes expensive as sample data sets get larger. An alternative formulation of the Shepard's method, which is better suited for large-scale problems, has been proposed by Renka [151] where the interpolated value is calculated using only the  $k$  nearest neighbours within an  $R$ -sphere ( $k$  and  $R$  are given, fixed, parameters) shown in green in figure 7.8. The weights are slightly modified in

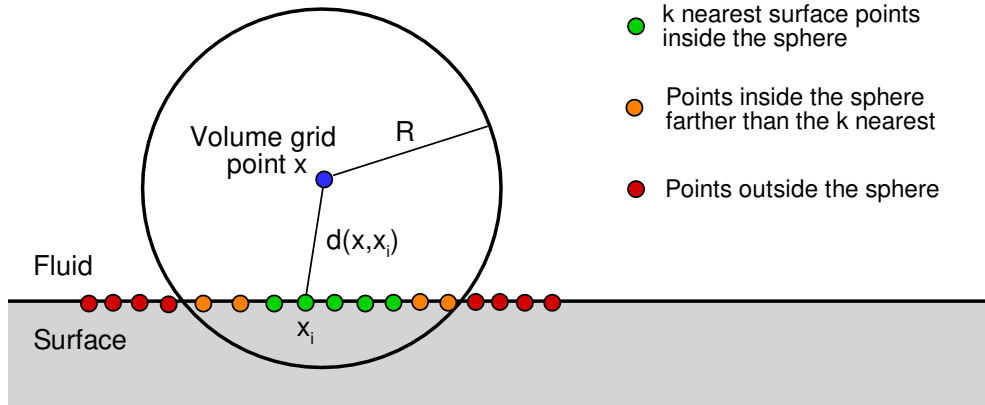


Figure 7.8: Selection of the points to interpolate from to compute the IDW weights.

this case:

$$w_i(\mathbf{x}) = \left( \frac{\max(0, R - d(\mathbf{x}, \mathbf{x}_i))}{Rd(\mathbf{x}, \mathbf{x}_i)} \right)^2, \quad i = 1, 2, \dots, k. \quad (7.17)$$

If this interpolation formula is combined with a fast spatial search structure for finding the  $k$  nearest points, it yields an efficient interpolation method suitable for large-scale problems<sup>[149]</sup>.

The modified IDW interpolation formula is used in HMB3 to implement mesh deformation in an efficient and robust way. The known displacements of points belonging to solid surfaces represent the sample data, while the displacements at all other points of the volume grid are computed using equation (7.15) with the weights of equation (7.17). For fast spatial search of the sample points, an Alternating Digital Tree (ADT) data structure<sup>[152]</sup> is used. A blending function is also applied to the interpolated displacements, so that they smoothly tend to zero as the distance from the deforming surface approaches  $R$ .

## 7.2 Results and Discussion

Simulations were carried out with the store at the carriage and at shear layer of the cavity without doors, and are summarised in table 7.2. At each store position, two computations were performed with rigid and elastic store body to determine if the fins are influenced by the body motion. In this section the carriage body modes were used since the store was fixed.

Figure 7.9 shows the sound pressure level (SPL) along the cavity ceiling mid-span with and without the store. In the following, the cavity modes are called M1 to

Name	Store position	Fins structure	Body structure	Travel Time
Carriage fins	Carriage	Elastic	Rigid	41.0
Carriage fins and body	Carriage	Elastic	Elastic	77.2
Shear layer fins	Shear layer	Elastic	Rigid	42.0
Shear layer fins and body	Shear layer	Elastic	Elastic	88.2

Table 7.2: Computed aeroelastic cases

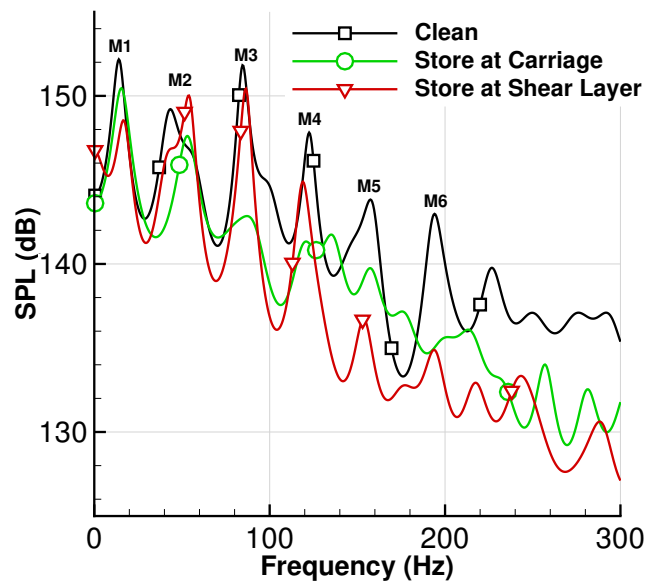


Figure 7.9: SPL along the cavity ceiling mid-span with aeroelastic store.

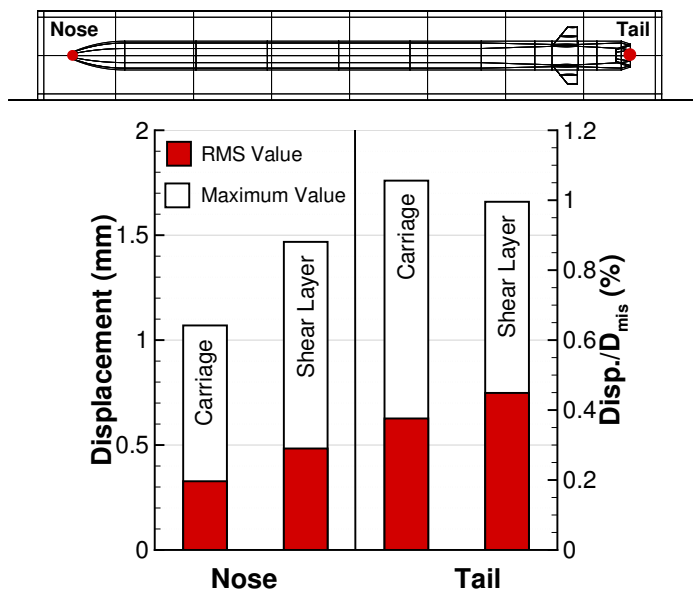


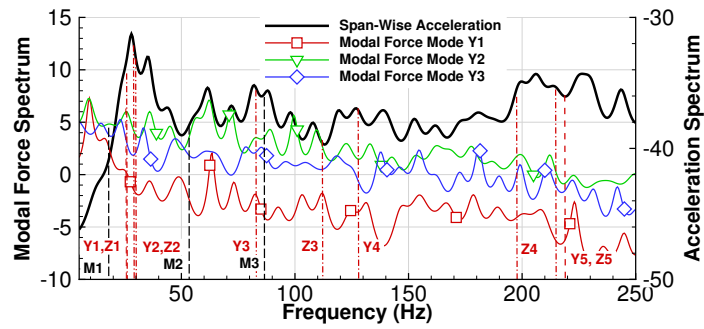
Figure 7.10: Deformations of the body at carriage and shear layer.

M6. The clean cavity presents strong resonance up to the sixth cavity mode. Adding the store at shear layer, reduces the broadband noise and the tonal amplitudes of modes 1, 4, 5 and 6. Moving the store at carriage, the noise decreases further with weaker tones. This is due to the blockage effect of the store that reduces the flow fluctuations inside the cavity.

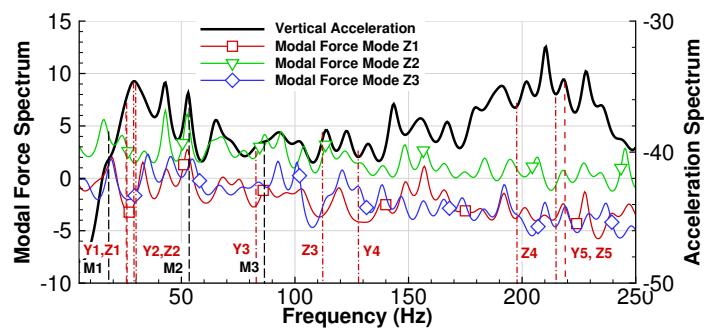
Figure 7.10 shows the RMS and maximum displacements of the store body nose and tail at carriage and shear layer. Overall, the tail vibrates at larger amplitude as most of the cavity flow unsteadiness occurs at the aft of the cavity. Moving from carriage to shear layer position, the RMS deformations increase by 40%, and the maximum deformations reach 1.8mm. This corresponds to about 1% of the store diameter.

The span-wise and vertical accelerations of the body tail are shown in figure 7.11 at carriage and at shear layer. They are respectively shown with the modal forces of the modes  $Y_i$  and  $Z_i$  contributing to the deformation along the Y, and Z axes. The modal forces of modes above Z3 are not shown as they drive negligible deformations. Between carriage and shear layer positions, the trends are similar, with an acceleration peak close to the structural modes Y1, Z1, Y2 and Z2, followed by a second weaker peak close to Z4, Y5, Z5. The body has a directional dependent response to the cavity flow. In the span-wise direction, the modal forces do not show strong peaks close to the cavity flow modes, and the body is only excited at its modal frequencies. On the other hand, the vertical modal forces exhibit peaks near the cavity modes. At carriage, the cavity modes M1 and M2 are visible in the modal forces and accelerations. At the shear layer position, there are stronger fluctuations, and all modal forces show peaks at the cavity modes M1 to M5, leading to significant acceleration peaks. The directionality of the acceleration is caused by the relatively symmetric cavity flow modes around the cavity mid-span, leading to weaker unsteady loads in the span-wise direction. When the store is at the shear layer, it is subjected to the strongest vertical loads due to the large differences between the cavity flow and the free-stream. The experiments in reference <sup>[40]</sup> show a similar behaviour with a smaller store model.

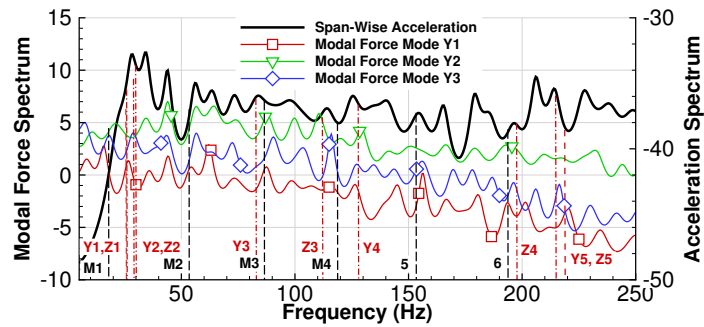
Figure 7.12 presents the RMS and maximum displacements of the trailing edge tips of the fins at carriage and shear layer. Here, the displacements are shown in a reference frame attached to the fin root, and moving with the store body (Figure 7.12a). The body elasticity has a small effect on the fins, because its deformations remain about 1% of the store diameter. However, fins 1 and 2 are close to the shear layer for both store positions, leading to similar RMS deformations of about 0.8mm. Moving closer



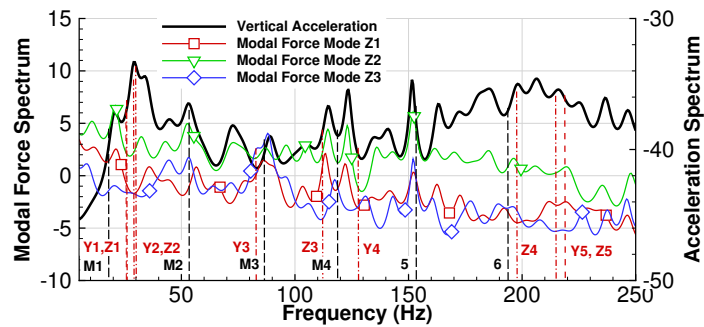
(a) Span-wise acceleration at carriage



(b) Vertical acceleration at carriage

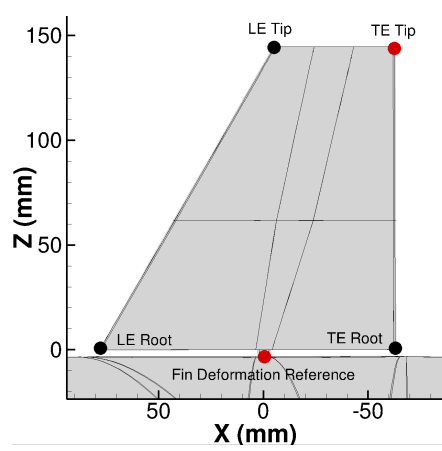


(c) Span-wise acceleration at shear layer

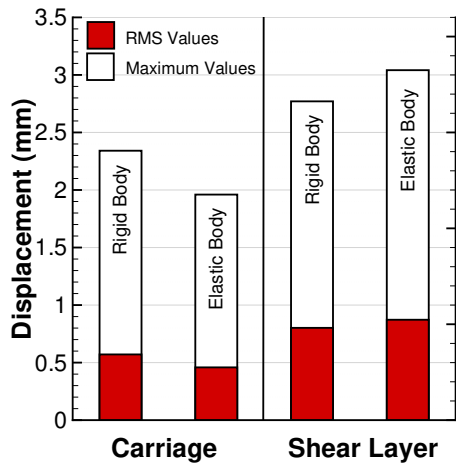


(d) Vertical acceleration at shear layer

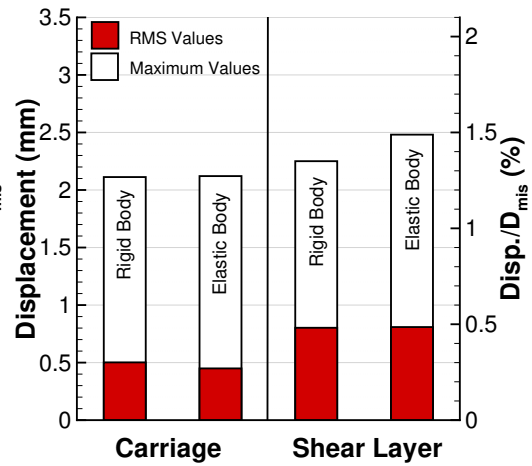
Figure 7.11: Spectrum of body modal forces, and tail acceleration.  $M_i$  are cavity modes.  $Y_l$  and  $Z_i$  are respectively vertical and span-wise body structural modes.



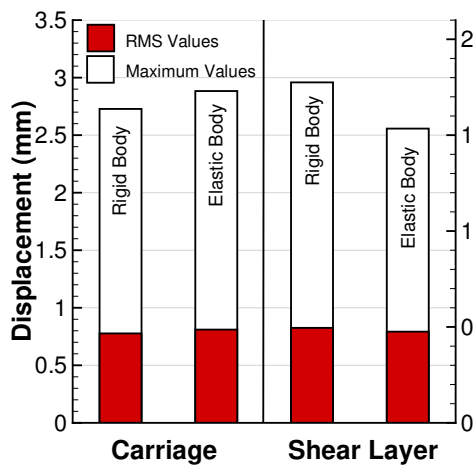
(a) Frame of reference



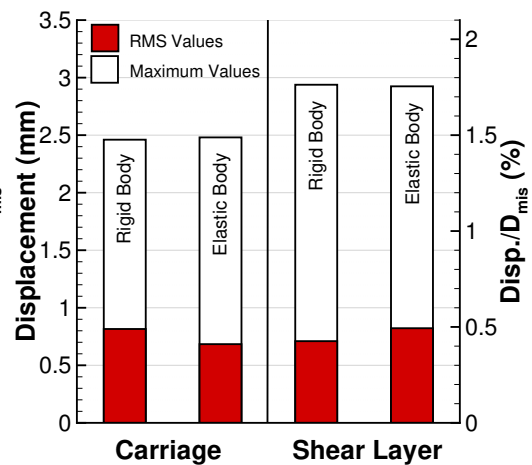
(b) Fin 3



(c) Fin 4



(d) Fin 2



(e) Fin 1

Figure 7.12: Deformations in the fin root reference frame, for the TE tip of the fins.

to the shear layer, fins 3 and 4 on the upper side of the store are subject to an increase of 60% of their RMS displacement from 0.5 to 0.8mm. The maximum deformations reach values of about 3mm. In the earth axis, the RMS and maximum displacements respectively reach values of 1.0mm and 3.5mm.

At the trailing edge tip of fin 4, the acceleration spectra are compared between the cases with rigid and elastic bodies, in figure 7.13. The fin accelerations show a peak at the two first structural modes. This supports that the body elasticity has a small effect on the fin deformations with no visible influence of the body acceleration.

The spectra of the modal forces of the four fins are shown in figures 7.14a and 7.14b with the store at carriage and shear layer. The modal forces of modes F3 and F4 are not shown here as they lead to negligible deformations. Overall, the cavity resonance had small footprint in the fins modal forces. This may be due to the small size of the fins compared to cavity flow resonance length scale of a cavity length. At carriage, fins 1 and 2, are closer to the shear layer than fins 3 and 4, and are exposed to stronger flow fluctuations. At the shear layer, where all the fins are exposed to the flow turbulence, they show similar modal forces. The response of the fins to the modal force shown in figures 7.14c and 7.14d, are also characterised by changes in the high frequency amplitudes regarding the store position. This shows that the fin deformations are mainly driven by the high frequency broadband noise, because their modal frequencies are far away from the cavity mode frequencies.

### 7.3 Chapter Summary

This chapter described the method and results for store aeroelasticity within the cavity flow. When the cavity flow was fully established, aeroelastic effects were present, but secondary for the case at hand. The structural excitation showed a directional dependence due to the span-wise symmetry of the geometry. The tonal fluctuations excited the body, while the fins were influenced by the broadband fluctuations. Overall, maximum store deformations were of about 2% of the store diameter. In case of matching between the cavity and the structural modes, the structural response seen in the present study can be amplified, and lead to much larger deformation, as seen in the experimental work of Wagner *et al.* <sup>[41]</sup>. This study should be carried out for every cases to ensure that strong interactions does not occur.

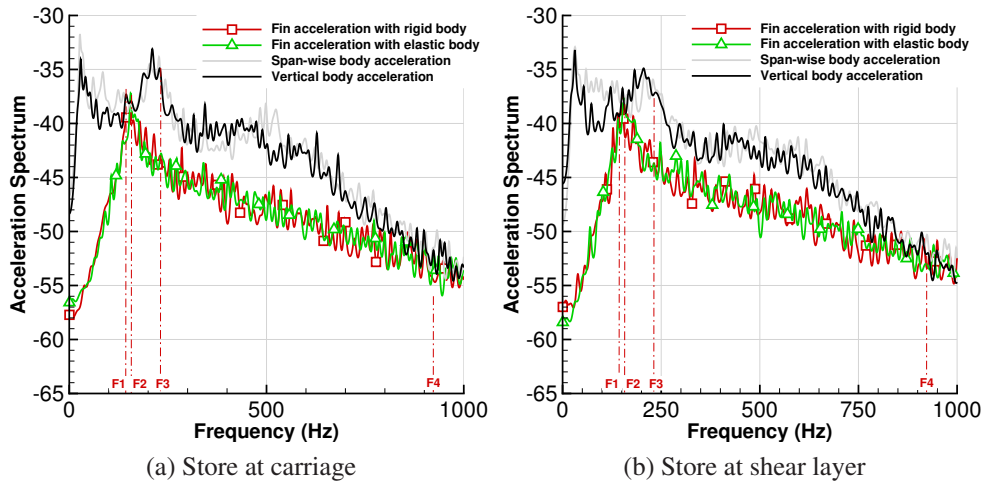


Figure 7.13: Spectra of fin 4 acceleration with and without body aeroelastics.

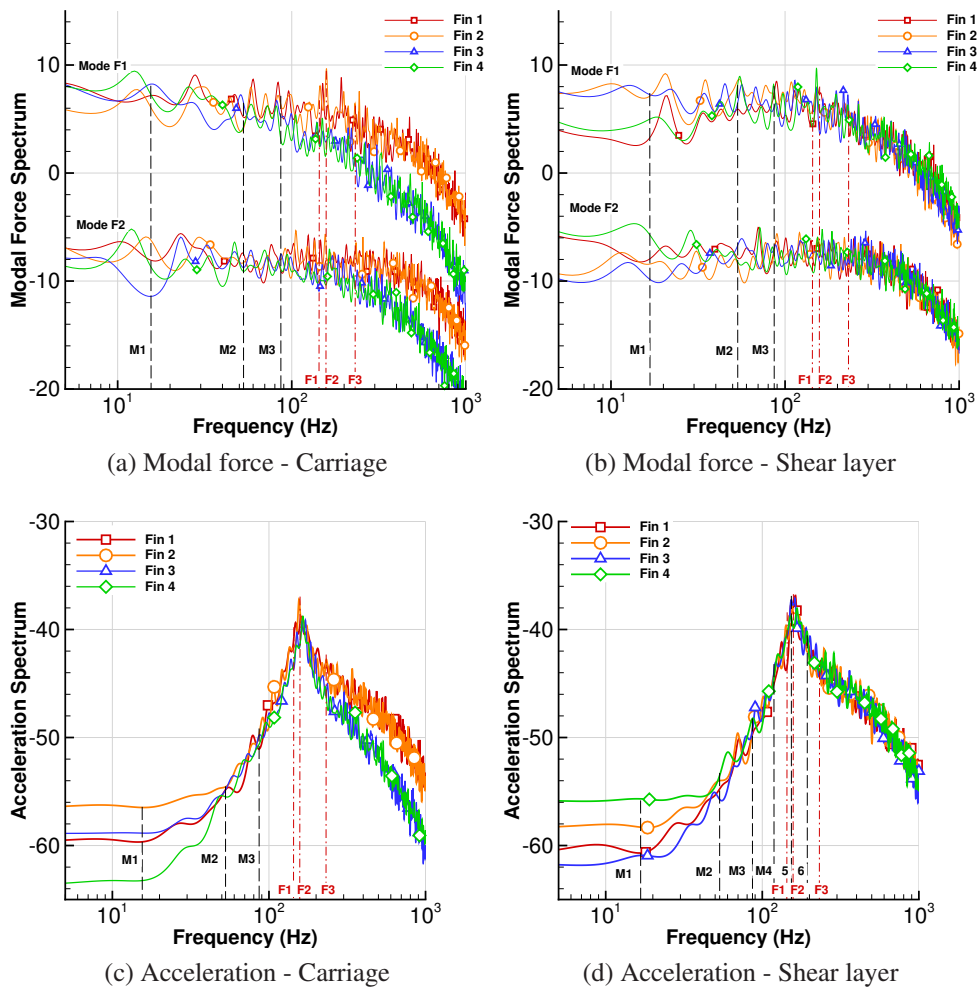


Figure 7.14: Spectra of fin modal forces, and acceleration at the trailing edge tip of the fin.  $M_i$  are cavity modes.  $F_i$  are fin structural modes.

# Chapter 8

## Simulations of Weapon Bay Doors

### Opening

This chapter describes simulations of the weapon bay doors operation. The doors were either fixed, or opened in a dynamic way. The flow evolution is analysed using flow visualisation, and point probes processed using signal analysis techniques.

Name	Angle (deg)	Door Velocity (deg/s)	Travel Time
Doors without Store			
Static 20deg	20	0	22
Static 45deg	45	0	20
Static 90deg	90	0	20
Static 110deg	110	0	38
Slow	0 → 110	110	40
Medium	0 → 110	220	82
Fast	0 → 110	440	40
Doors with Aeroelastic Store at Carriage			
Static & Store 20deg	20	0	20
Static & Store 45deg	45	0	22
Static & Store 90deg	90	0	19
Static & Store 110deg	110	0	19
Medium & Store	0 → 110	220	40

Table 8.1: Computed cases with doors

Comparisons are performed for different door opening speeds with and without store. Finally the aeroelastic deformation during this phase is also compared to the results of chapter 7. The computational plan is shown table 8.1.

## 8.1 Computations of Static Doors

Figure 8.1 shows the time-averaged Mach Number on a plane at 85% of the cavity length for the LD7 cavity with and without doors. Over the clean cavity, the shear layer deeps in, reaching large depths of penetration (Figure 8.1a), and creating large structures above the side walls. Adding doors at 110 degrees, the shear layer is lifted towards the outer cavity part (Figure 8.1b), reducing the Mach number inside the

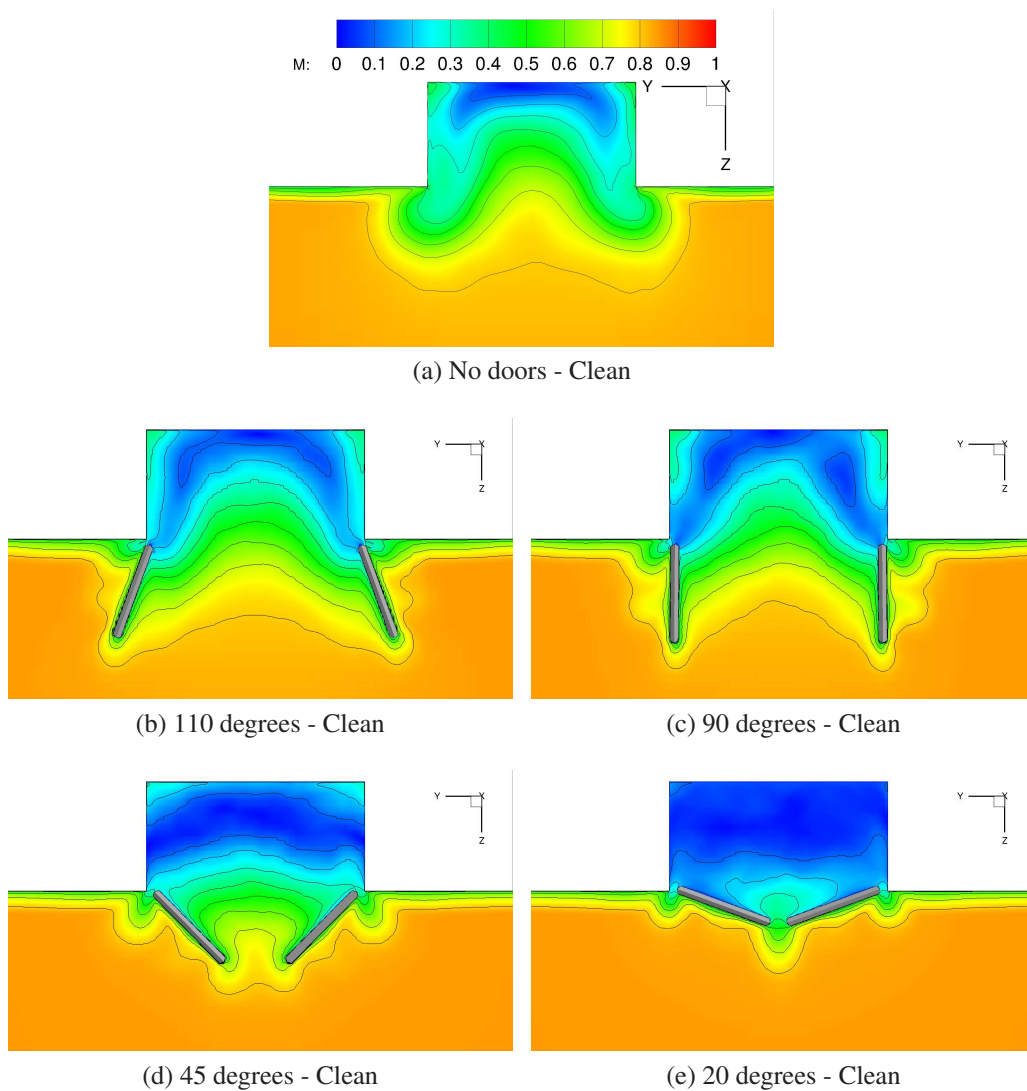


Figure 8.1: Time averaged Mach Number at  $X/L=0.85$  for the LD7 cavity.

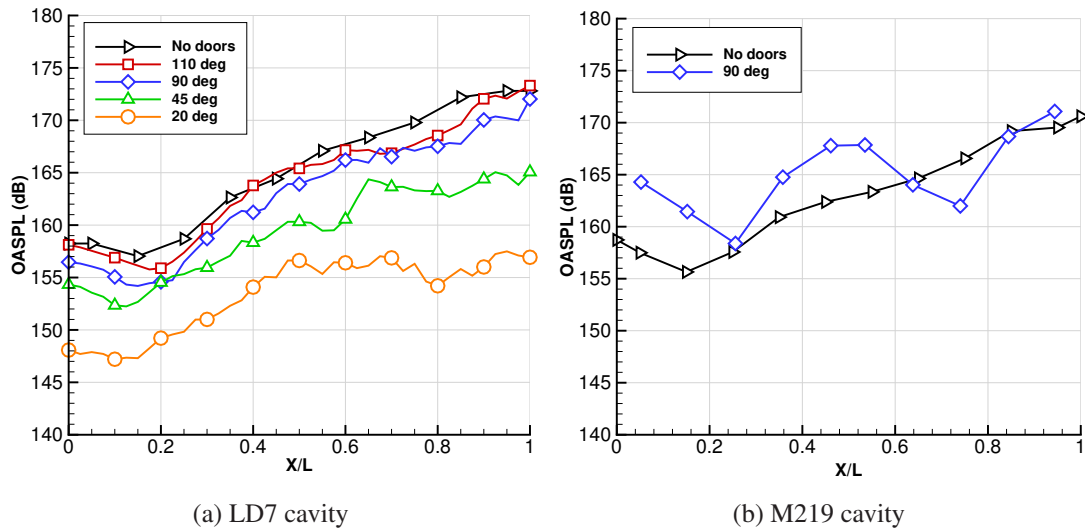


Figure 8.2: OASPL along the cavity ceiling mid-span.

cavity. Decreasing the door angle, a further reduction of the Mach number is seen, and the doors at 20 degrees show very slow flow inside the cavity (Figure 8.1e).

The blockage of the flow by the doors is also visible in the OASPL in figure 8.2a. The doors at 110 degrees have a small effect on the OASPL when compared to a cavity without doors. Reducing the door angle, a pacifying effect appears, leading to the reduction of the sound pressure level by up to 20dB at 20 degrees. The addition of the doors at 90 degrees on the M219 cavity, has dramatically different consequences, with a stronger second cavity mode, seen on the W shape of the OASPL (Figure 8.2b), and an overall noise increase. This difference is due to the geometry of the door leading edge, that is thicker for the M219 cavity. This leads to different flowfield over the cavity for the two cases. This is shown in figure 8.3 with bottom view of the RMS of longitudinal velocity at the middle section of the doors. The M219 door pushes the flow above the cavity (Figure 8.3a), while the LD7 door is thinner, and pushes less flow above the cavity (Figure 8.3b). This leads to more pronounced flow fluctuations for the M219 cavity.

Figure 8.4 shows the flow momentum of the time averaged flow for the LD7 and M219 cavities, with and without doors at 90 degrees computed using equation 2.38 over the cavity mid-span. The two cavities have similar shear layer patterns without doors, with a shear layer thickness of the same order of magnitude compared to the cavity depth on the second half of the cavity. Adding the doors, the M219 shear layer is lifted, and shows a dramatic reduction of its thickness compared to the LD7 cavity.

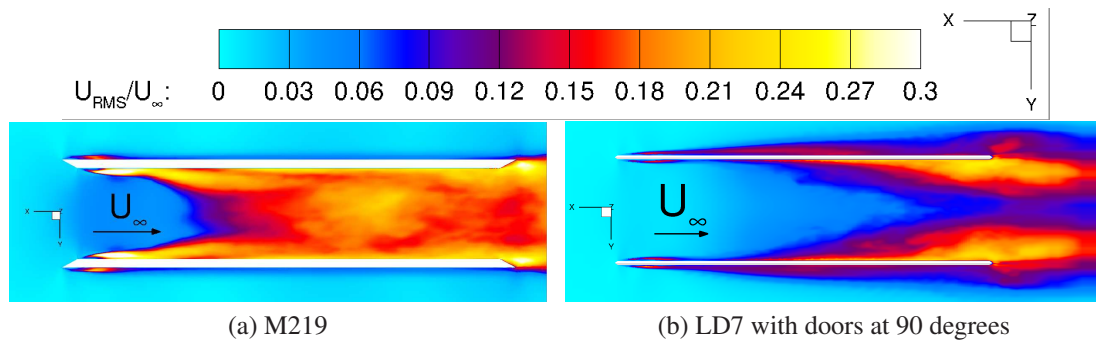
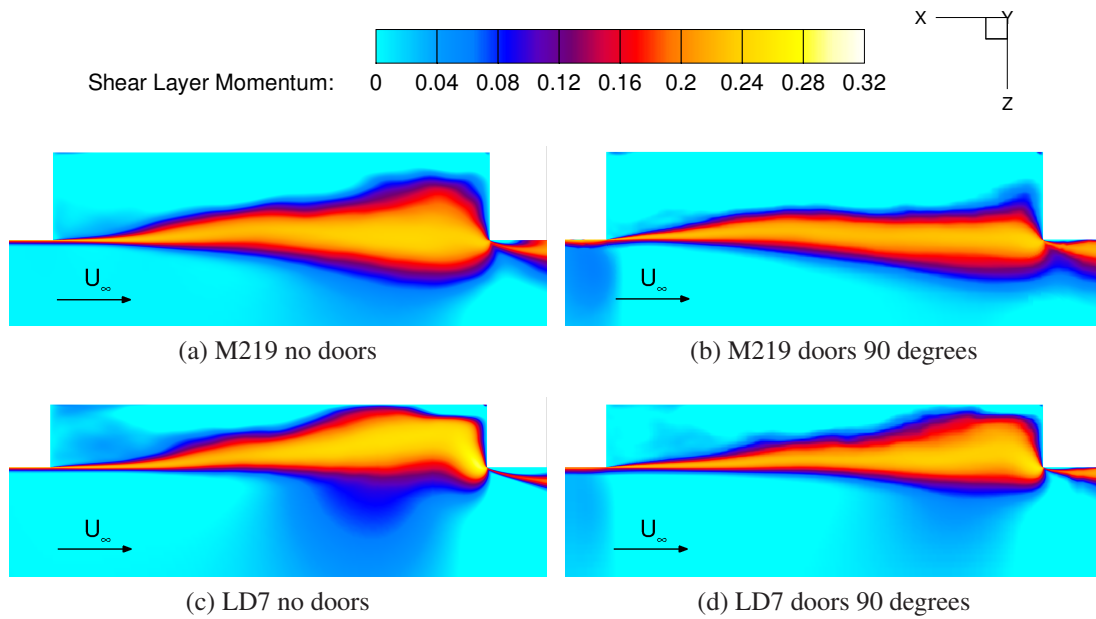
Figure 8.3: Time averaged  $U_{RMS}$  at the middle section of the doors.

Figure 8.4: Shear layer momentum of the time averaged flow on the cavity mid-span.

The smaller width of the M219 cavity enhances the effect of the doors, leading to larger changes at the mid-span. This shows that the doors, strongly affect the cavity flow.

## 8.2 Computations for Dynamic Door Opening

The flows for dynamic and static doors are compared in figure 8.5 using the Mach Number field, and LIC plots. The dynamic cases are time averaged over windows of 10 degrees centred in the investigated angle. The static cases are averaged over the total time signal available. Figure 8.6 shows the forces on the front, and aft walls. The signals of the dynamic cases are averaged around windows of 1.6 travel times. This window width filters the frequencies above 50Hz for a better readability of the plot.

The differences between min and max of the unfiltered signal during the same window are also computed. Again, for the static cases, the full time signal is used.

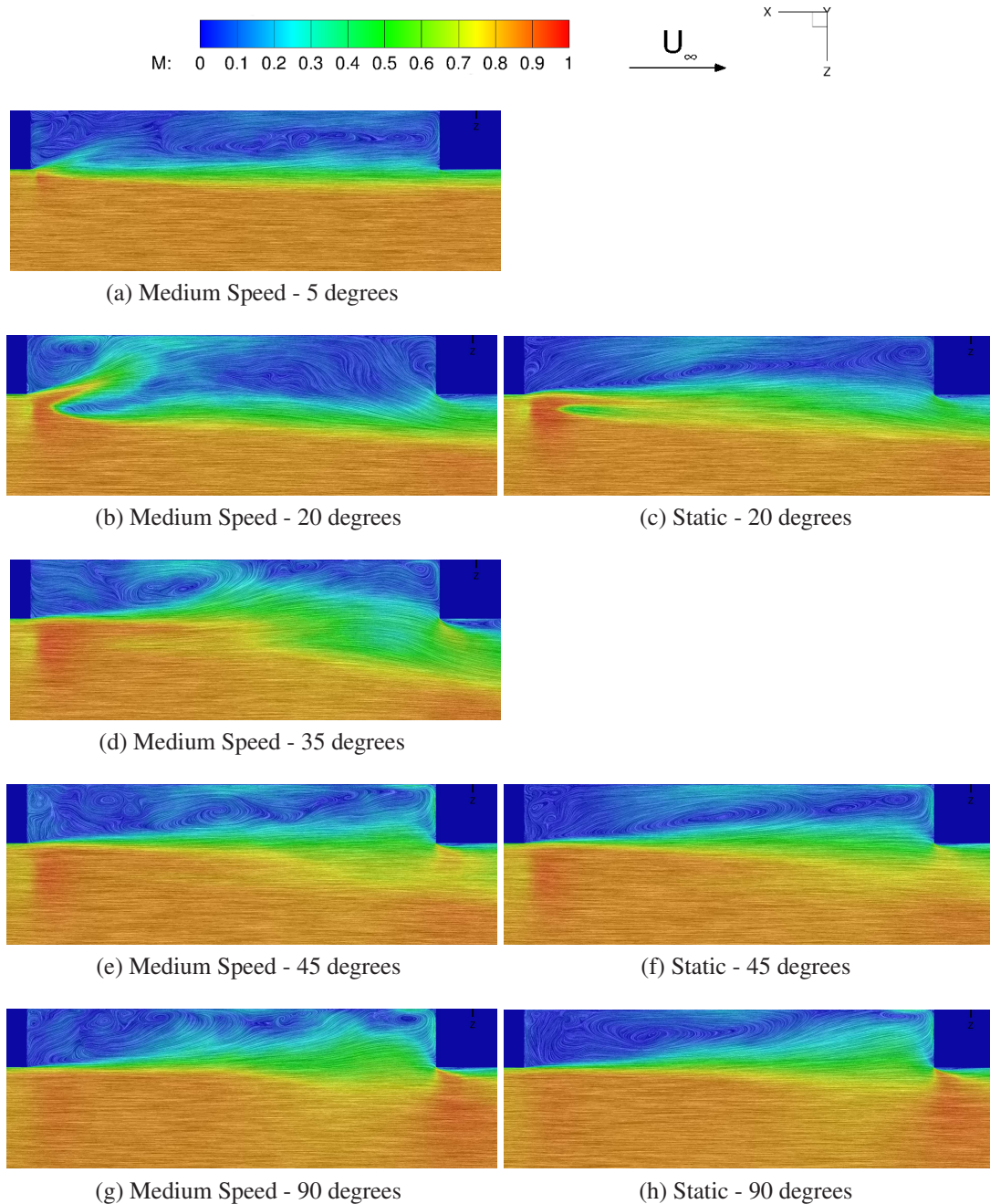


Figure 8.5: Mach Number and LICs between 5 and 90 degrees for dynamic and static cases. Plane at cavity mid-span

For the dynamic opening cases, three phases are identified. First, the cavity flow adopts the closed cavity topology, then it transitions to an open cavity topology, and finally the flow becomes fully established, as the two doors stop moving.

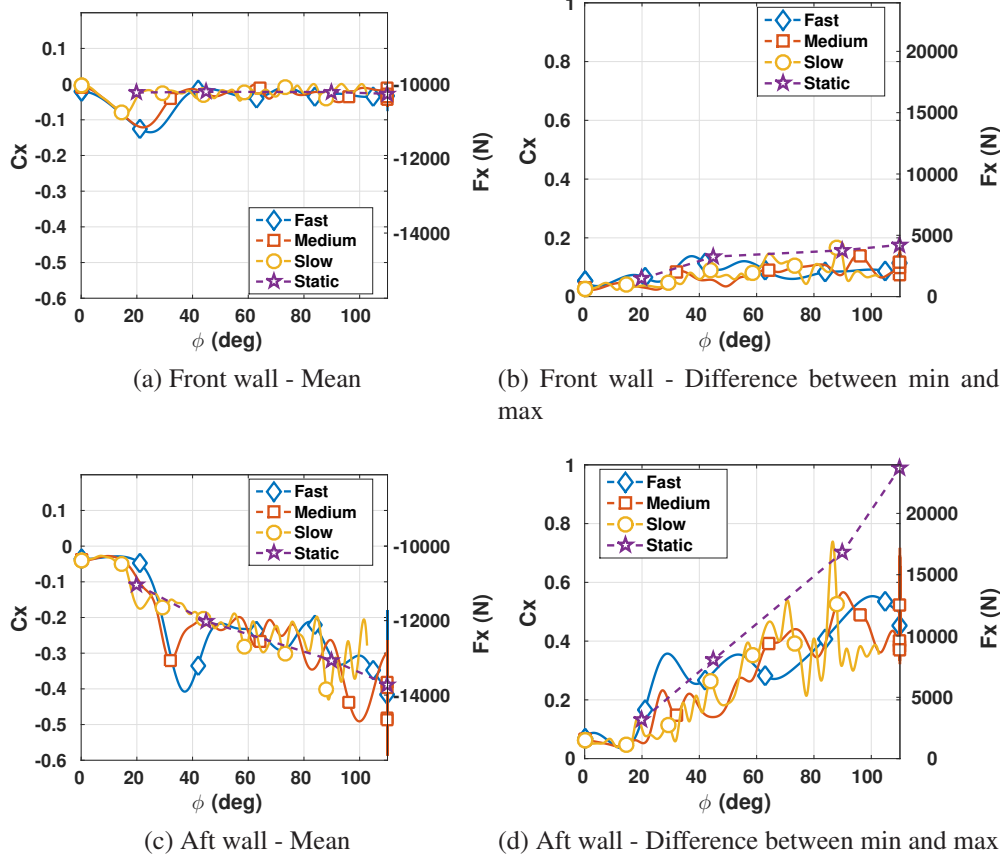


Figure 8.6: Force on the front and aft walls for static and dynamic doors.

With the doors closed, the Mach Number inside the cavity is small, and the pressure is ambient (Figure 8.5a), showing that the gap between the doors and the bay discussed in section 6.1, did not influence the flow. As soon as the doors open, the flow enters the cavity from the narrow gap between the doors and the cavity lips, creating a fast flow impacting the ceiling, and establishing a closed cavity flow (Figure 8.5b). The fast flow induces a vortex at the front of the cavity, decreasing the pressure, and increasing suction on the front wall (Figure 8.6a). This force is identical for all dynamic cases, driven by the jet flow. During this phase, the aft wall is subject to lower loads (Figure 8.6c).

The cavity flow then transitions to an open cavity <sup>[19]</sup>. The jet travels along the cavity ceiling, reaches the cavity aft, and detaches to hit the aft wall, creating a peak of loads (Figures 8.5d and 8.6c). This weakens the vortex near the front wall at different door angles according to the door velocity. The stronger front wall vortex is seen at 16, 23, and 25 degrees for the slow, medium, and fast doors (Figure 8.6a). The transition

ends when the dynamic cases reach the same level of loads as the static cases. The faster the door, the larger the loads, and the fluctuations during the transition phase (Figure 8.6d).

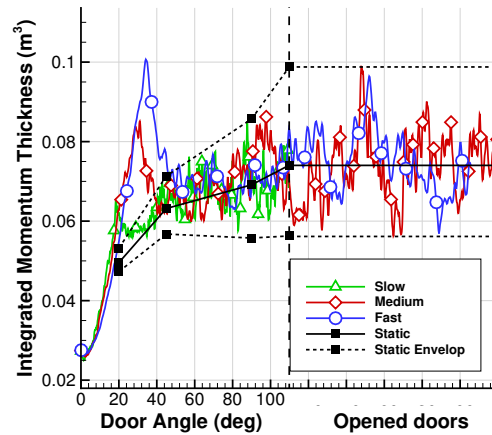


Figure 8.7: Shear layer momentum thickness  $\theta(x,y)$  integrated over the cavity opening. Fixed doors results are used for the static envelope.

Figure 8.7 shows the volume of the shear layer, computed as the integral of the shear layer thickness  $\theta(x,y)$  all over the cavity length and span. The static cases are drawn in black with their time averaged, minimum, and maximum values. The narrower door opening limits the flow development for this geometry, leading to smaller shear layer thickness and fluctuations of the shear layer. The dynamic cases show the footprint of the jet during the transitional phase, with a peak of the shear layer volume. Then, all the dynamic cases are within the envelope defined by the static cases showing that the door opening effect is important only for small door angle.

Figure 8.8 shows the pitching moment (Figures 8.8a to 8.8c) and the normal panel force (Figures 8.8d to 8.8f) on the starboard door, and the wall normal force on the ceiling (Figures 8.8g to 8.8i). The signal is averaged in windows of 1.6 travel times, and the coloured shaded envelope is the minimum and maximum of the signal within the same windows. This window width filters the frequencies above 50Hz for a better readability of the plot. The flow transition from open to closed topology, affects the weapon bay structures. Larger transient loads are observed when compared to the fully opened bay, especially for the faster case. The maximum pitching moment on the doors during the fast opening (Figure 8.8c) is about twice as large as for the fully open case.

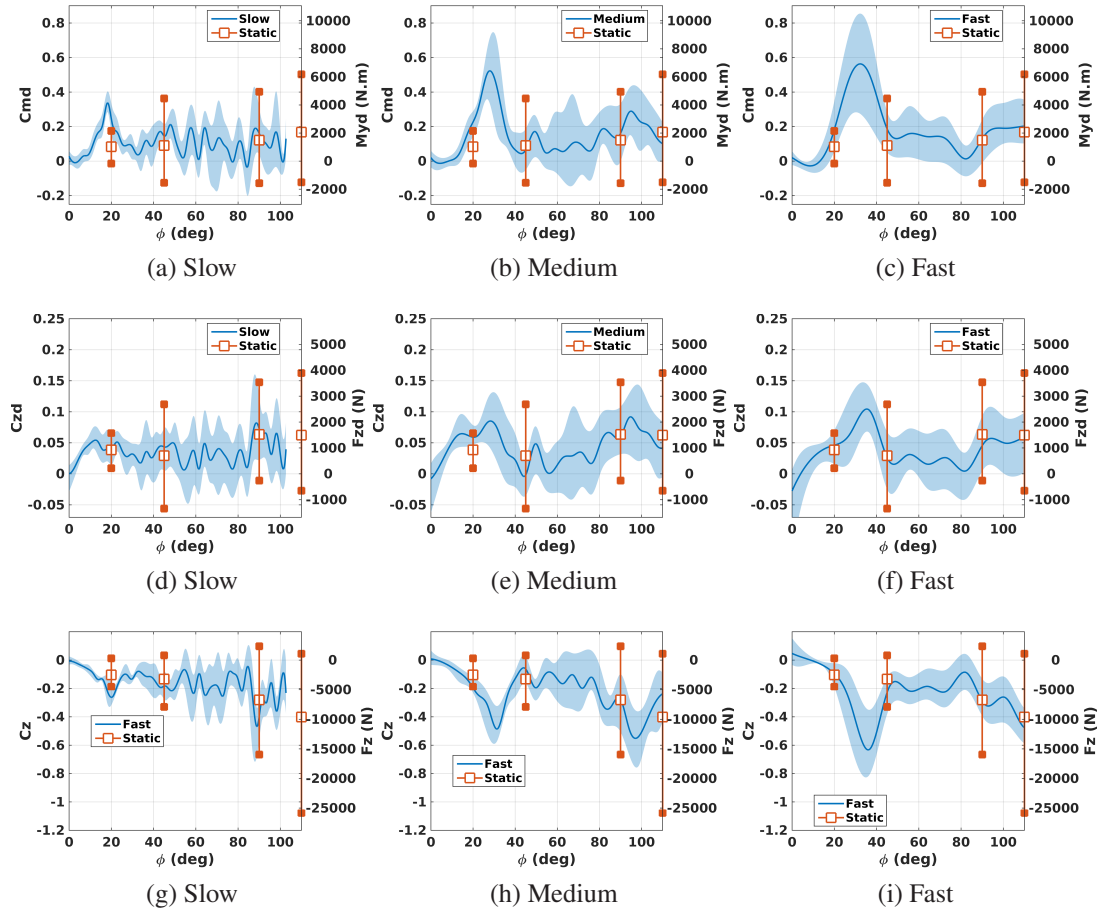


Figure 8.8: Loads on doors and cavity ceiling for dynamic and static cases.

### 8.3 Noise Field for Dynamic and Static Door Cases

Figure 8.9 shows the OASPL at the cavity mid-span for the medium door speed, and for the cases with static doors. For small door openings, the jet produces high levels of noise at the front of the cavity (Figure 8.9b), and makes the dynamic case noisier than the static case (Figure 8.9c). The flow transition is also very noisy (Figure 8.9d), and resembles the fully open door cavity (Figure 8.9i). For larger door angles, the door dynamics has minimal influence on the noise field, with two main sources of noise at the mid-length of the shear layer, and at the aft wall, characteristics of a strong second cavity mode.

The OASPL averaged along the ceiling mid-span ( $Z/D=-1$ ), as well as at the shear layer ( $Z/D=0$ ), and at  $Z/D=1$  are shown in figure 8.10, as functions of the door angle. At the ceiling, and outside the cavity, the dynamic cases show a peak of noise due to the flow transition. After the transition phase, for door angle larger than 40

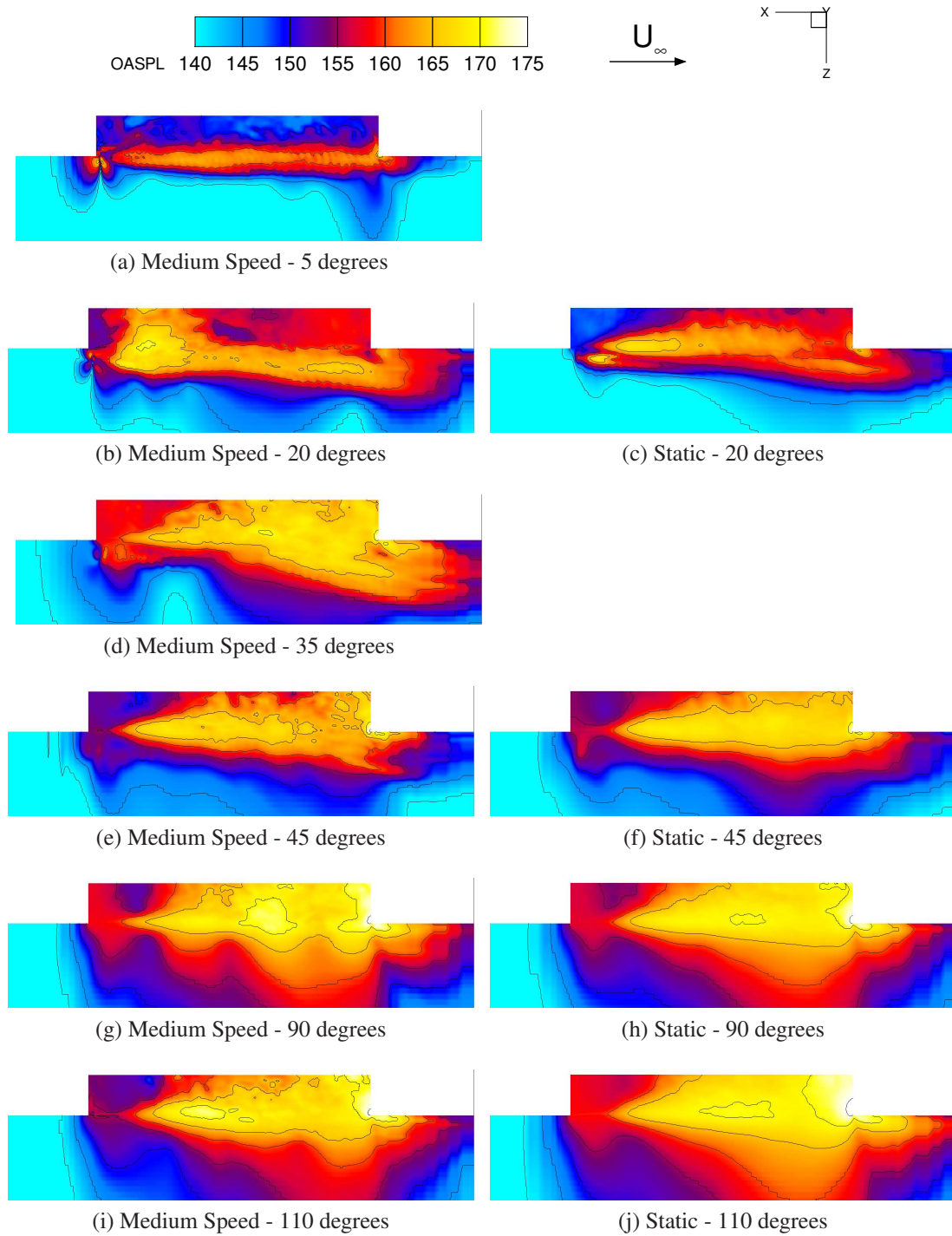


Figure 8.9: OASPL field during the doors opening between 5 and 110 degrees.

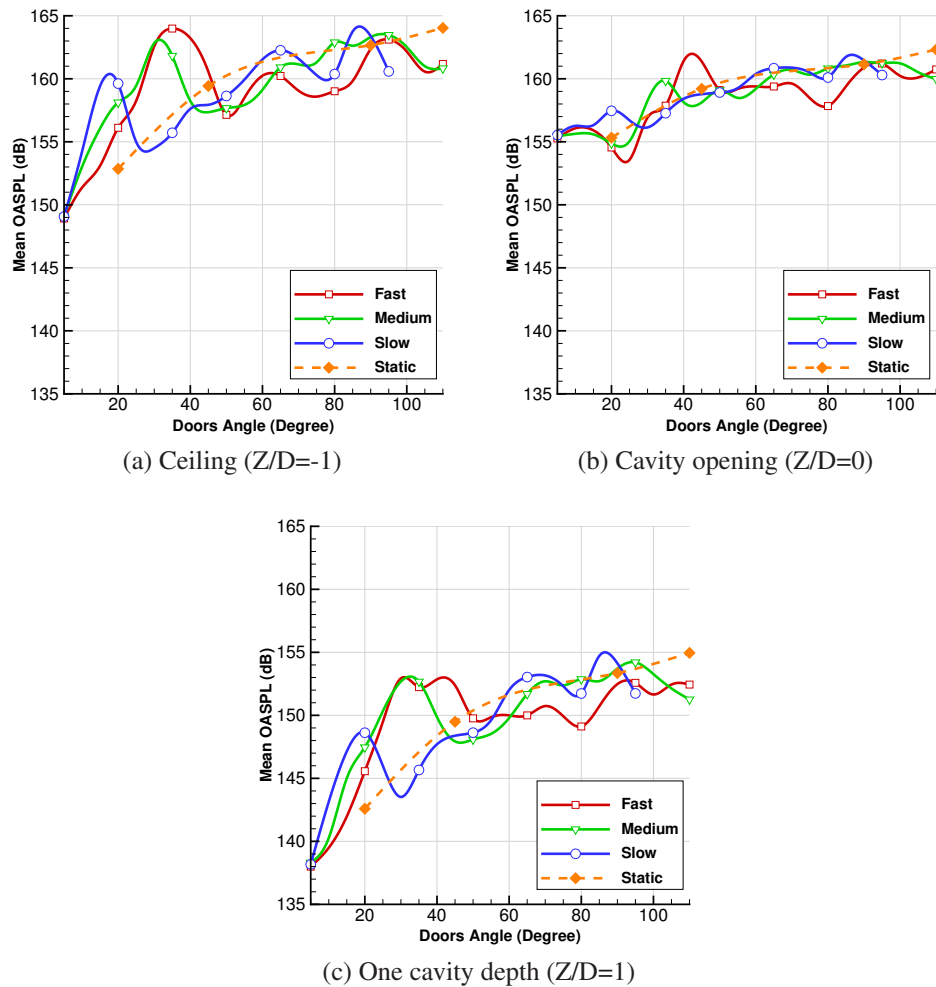


Figure 8.10: Averaged OASPL lines at the mid-span for fast, medium, slow, and static door cases.

degrees, the noise fields between static and dynamic openings are similar. The fast doors produce noise levels as loud as the fully open cavity during the transition. At the shear layer (Figure 8.10b), the noise is produced by the turbulent flow between the two doors for the smaller angles (Figure 8.9a). Then, the noise levels increase as the shear layer establishes towards the end of the transition phase (Figure 8.9e).

The cavity flow is very unsteady during the door opening, and spatio-temporal characterisation is needed to fully understand the flow. The pressure Banded Integrated Wavelet (BIW) envelope is shown for three door velocities in figure 8.11. The vertical axis is the time scaled by the door angle, and extends after the end of the opening. The horizontal axis represents the coordinate along the ceiling mid-span of the cavity. Three frequency bands of 4Hz centred on the cavity modes 1 to 3 are shown. During

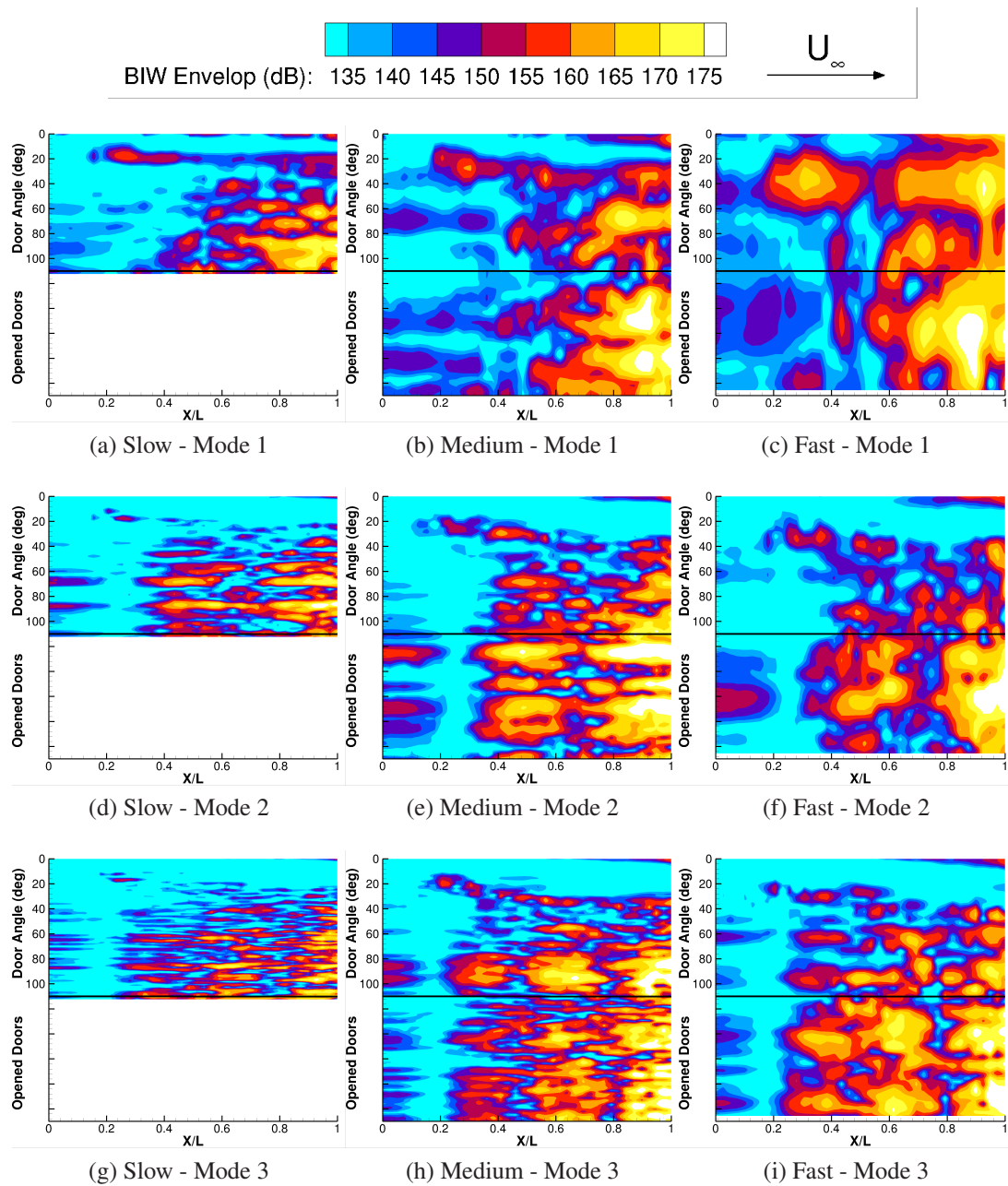


Figure 8.11: Pressure BIW envelope along the ceiling mid-span for dynamic opening and mode 1 to 3.

the cavity flow transition, the jet path is visible around a door angle of 20 degrees, interacting with the ceiling from 20% of the cavity length, and travelling towards the aft wall. After a door angle of 80 degrees, all cases look similar. After the flow transitioned to open cavity, the noise patterns, are characteristic of standing waves oscillations as described section 3.3.2, with nodes and antinodes of oscillation.

Figure 8.12 compares the SPL at  $X/L=0.95$  on the ceiling mid-span between

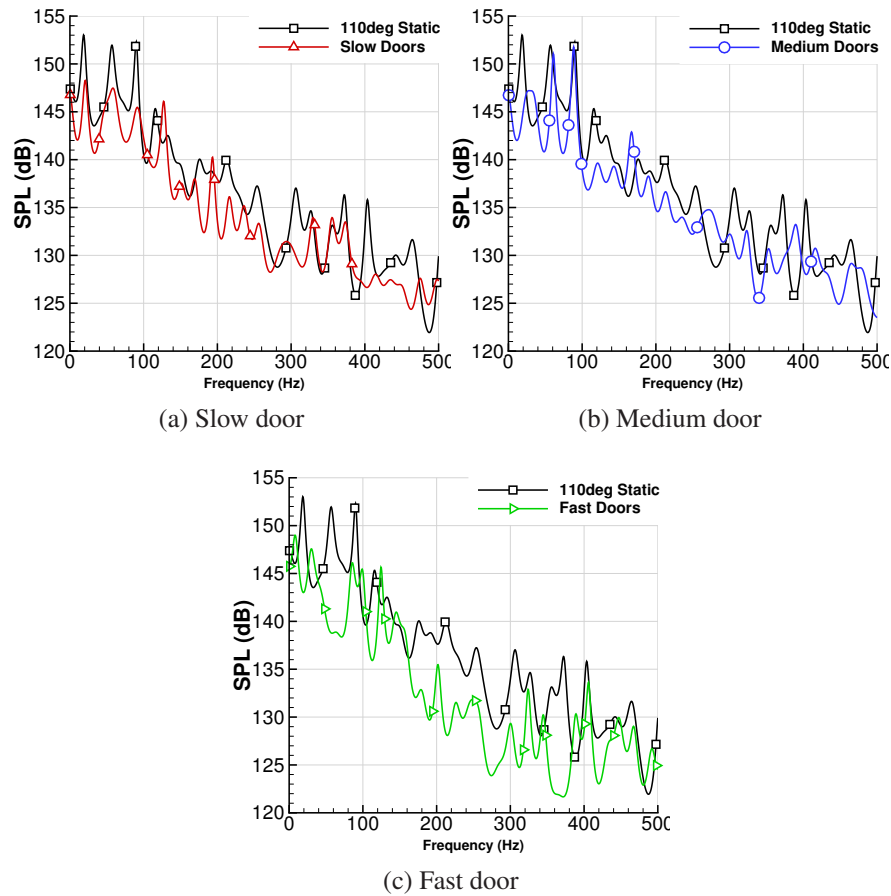


Figure 8.12: SPL at  $X/L=0.95$  of the ceiling mid-span for different door speed.

Case	Mode 1	Mode 2	Mode 3
Rossiter	23.7	55.2	86.8
Doors 110deg	19.1	57.6	89.7
Slow Doors	20.0	54.3	90.6
Medium Doors	19.5	60.2	88.0
Fast Doors	-	-	86.8

Table 8.2: Cavity mode frequency for dynamic and static doors in Hz.

static doors at 110 degrees, and dynamic door opening. The dynamic door signal is processed between angles of 45 and 110 degrees, after the cavity flow transition. The cavity with fully open doors is characterised by strong cavity modes (modes 1, 2 and 3 of table 8.2). During the slow and medium speed opening, those modes settle rapidly after the flow transition, and dominate the SPL. However, the broadband

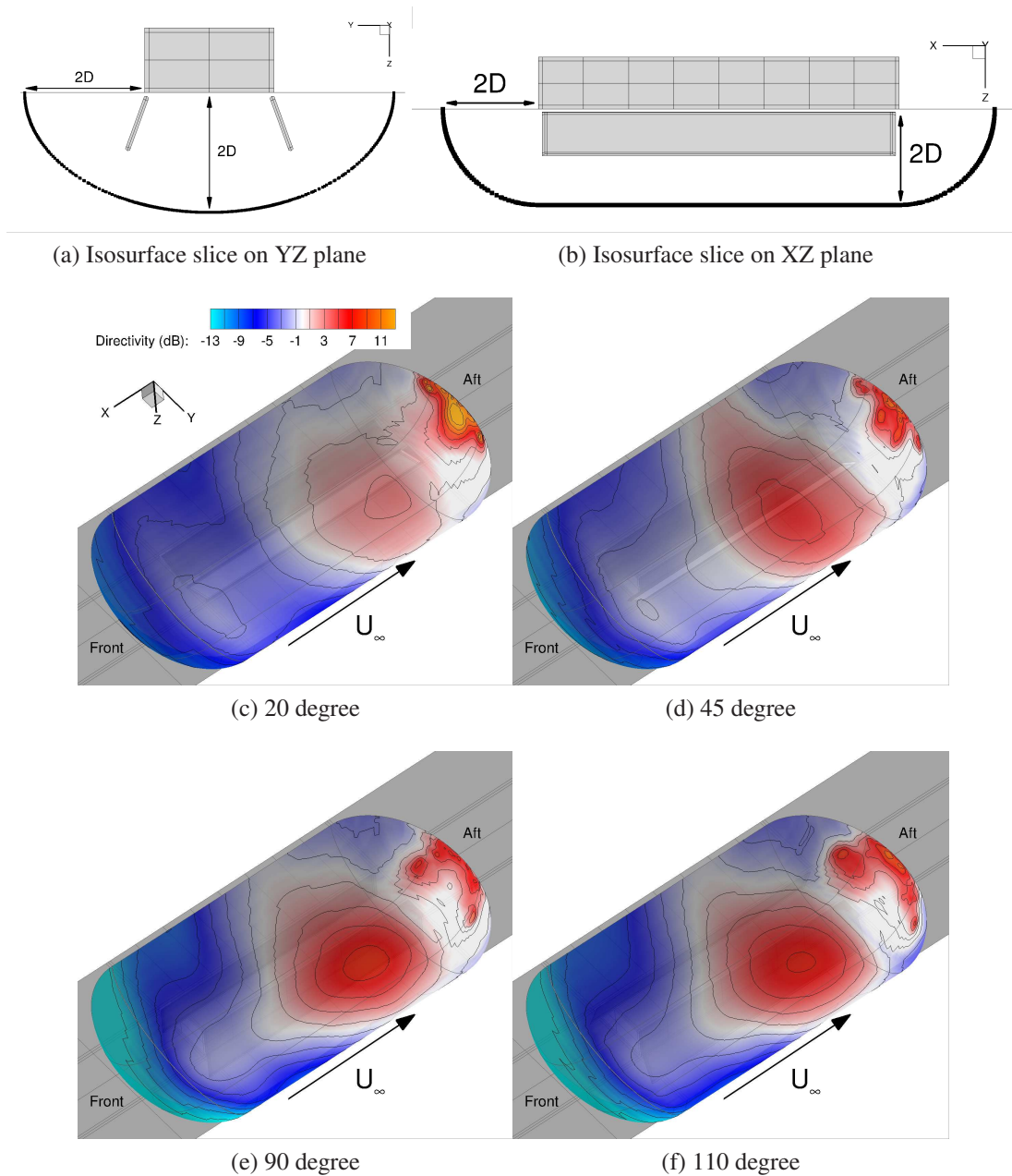


Figure 8.13: 3D Noise directivity for different fixed door angle. Iso-surface at 2 cavity depths from the shear layer.

noise is weaker than for the fully developed case. On the other hand, the fast opening does not allow enough time for the flow to develop, and only the third cavity mode is visible. The BIW envelope supports this conclusion with well established third mode oscillations (Figure 8.11i), while modes 1 and 2 respectively show tick, and W shape oscillations only after the end of the door opening. Table 8.2 shows the frequency of the three first cavity modes of those cases. The door dynamics has a milder effect on

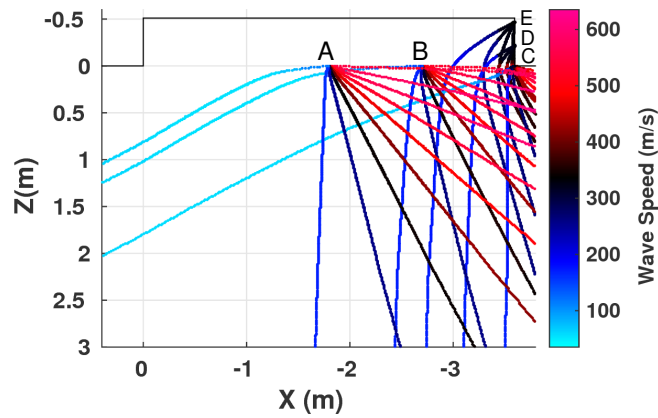


Figure 8.14: Noise propagation from the main sources of noise taking into account the flowfield with doors at 110 degrees. Five sources are shown at positions A,B,C,D,E.

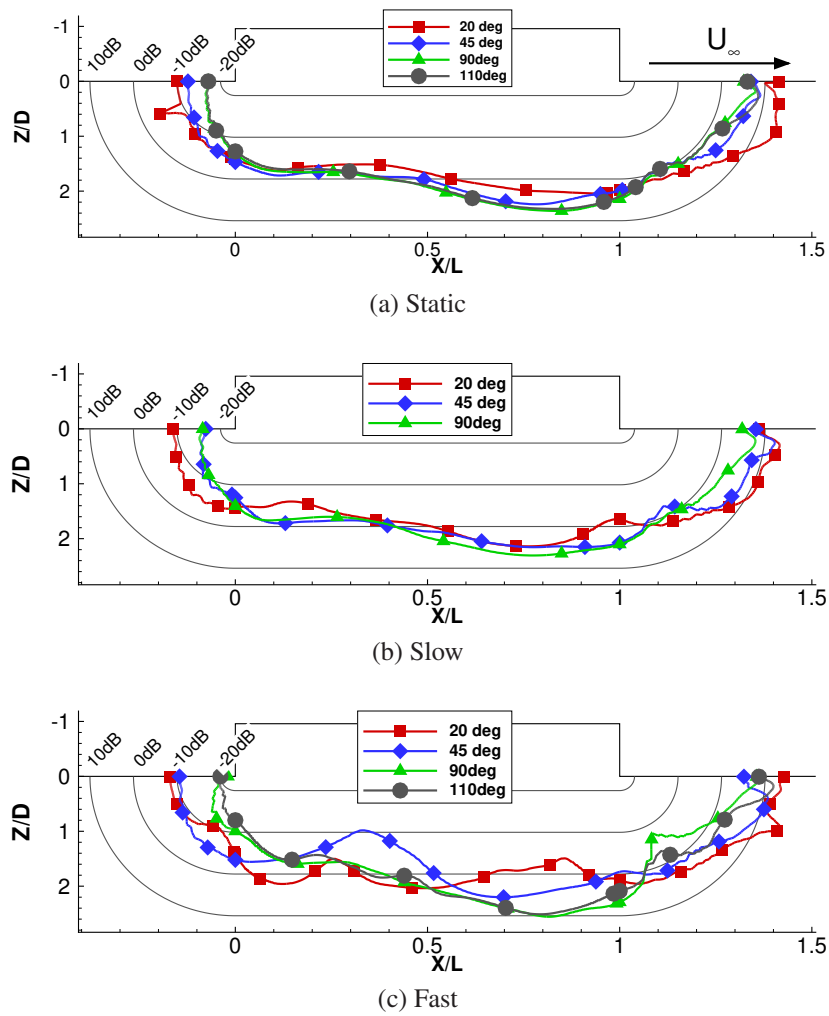


Figure 8.15: Noise directivity for different door angle and door velocity.

the modal frequencies, which lock rapidly to values close to the established cavity flow tone frequencies.

Figure 8.13 describes the noise directivity at the cavity near field for different fixed door angles. Equation 2.37 is used on every CFD points of an iso-surface two cavity depths away from the cavity opening (Figures 8.13a and 8.13b). The mesh at the near field has a maximum spacing  $dx$  of 2% of the cavity length, enough to capture frequencies up to  $f = c/10dx = 470Hz$  with 10 points per wave length. The noise is directed at the aft and above the cavity as indicated by the peak values of 10dB. This may be explained by the loud noise at the cavity aft, generated as the shear layer impacts the aft wall. Additionally, the noise propagation is influenced by the flow advection. This is visualised using a simple noise propagation model (Figure 8.14), where the speed of the pressure waves is the sum of the sound speed, and of the time averaged CFD flowfield velocity. Sources of noise are placed at 50%, 75% and 100%L of the shear layer and at 0%, 50%, and 100%D of the aft wall, and radiate uniformly around them. For most of the sources placed in the flow, the waves are influenced by the flow direction, either the free-stream, or the recirculation inside the cavity. As a result, most of the waves propagate downstream, and below the cavity in the Z direction.

Figure 8.15, shows iso-lines of acoustic directivity (Equation 2.37) at the mid-span of the cavity, and at different door angles for the static cases, as well as for the slow and fast dynamic door cases. The dynamic cases are averaged in a window of 10 degrees around the indicated angle. The shapes of the static, and slow door opening cases are similar past the 45 degrees door angle, as the cavity flow has time to establish. However, for the fast case, the shapes of the curves evolve, and fluctuate as the door opens.

## 8.4 Computations with Store at Carriage

The store is subject to the aerodynamics loads from the beginning of the door opening. This section presents results of computations including an aeroelastic store placed at carriage with doors. Static doors are held at 20, 45, 90 and 110 degrees, and are dynamically moving from 0 to 110 degrees at 220deg/s (Table 8.1). The computations are also compared with the results without store.

Figure 8.16 shows time averaged Mach number field and LIC at the cavity mid-

span for the dynamic opening with and without store. The dynamic cases are averaged over windows of 10 degrees centred in the investigated angle. The static cases are averaged over the total time signal available. The case without store shows the three steps during the cavity flow establishment as described in section 8.2. As soon, as the door opening begins, a jet appears between the doors and the cavity front lip (Figure 8.16a), producing disturbances at the cavity front. When reaching the ceiling, the flow resembles a closed cavity configuration (Figure 8.16c) but rapidly switches to a transitional flow (Figure 8.16e). Finally, the jet detaches from the ceiling, and an open

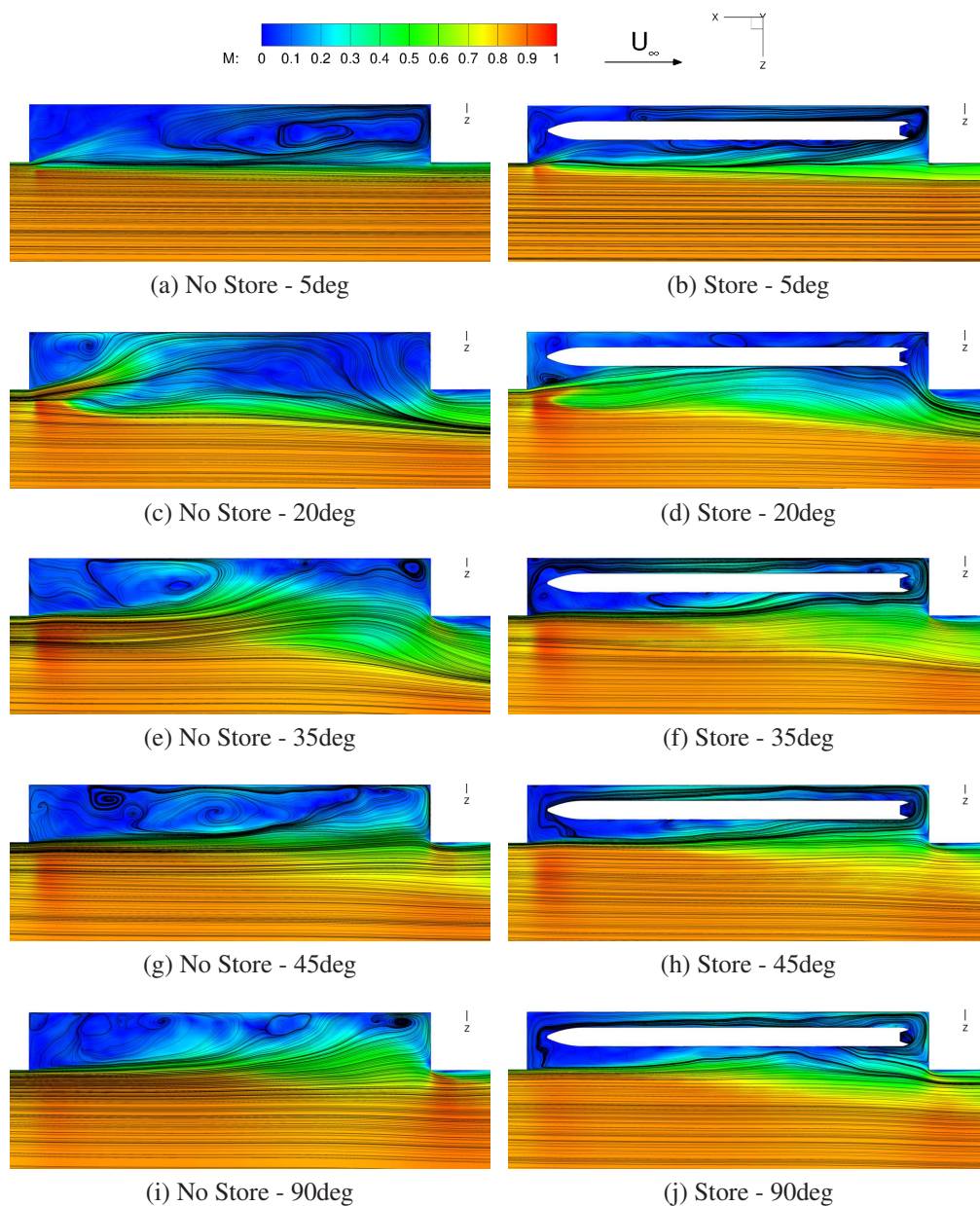


Figure 8.16: Mach number and LIC at mid-span during door opening.

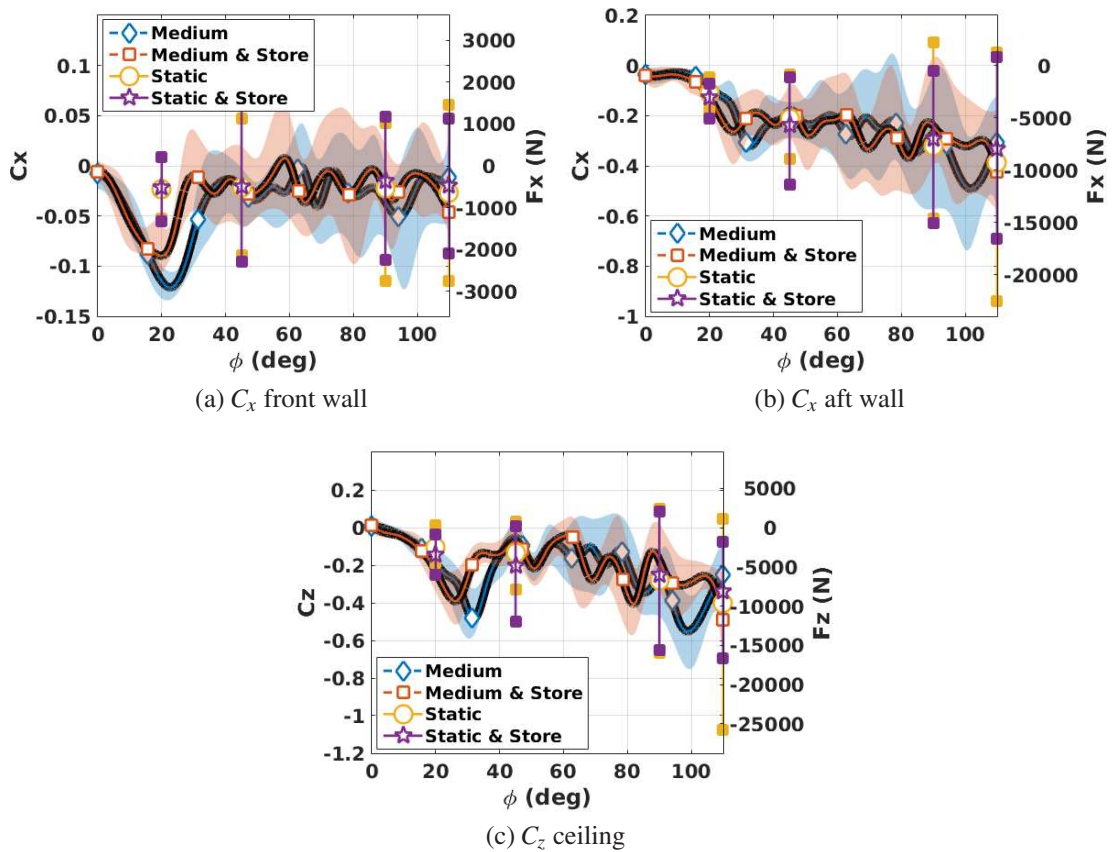


Figure 8.17: Force on the cavity walls during medium speed door opening.

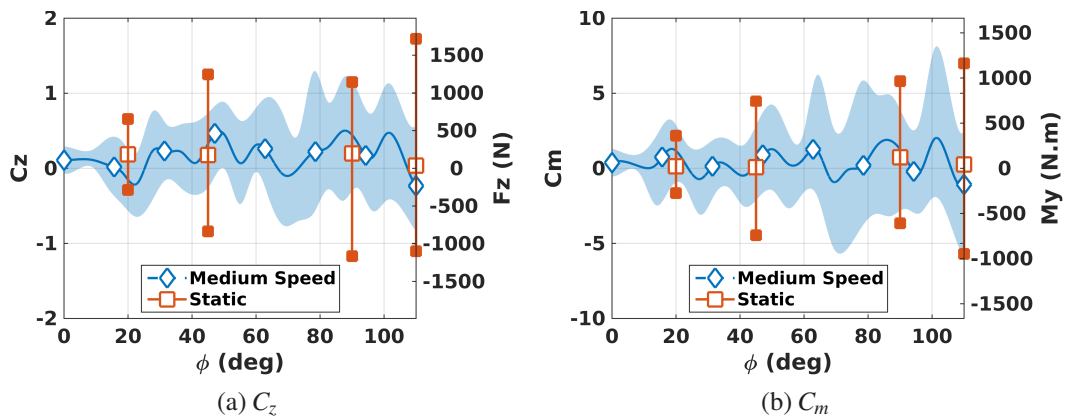


Figure 8.18: Force on the store during medium speed door opening.

cavity flow establishes with the shear layer spanning the cavity length (Figure 8.16g). With the store at carriage, the flow also goes through the closed, transitional, and open flow steps. However, the store shields a part of the cavity ceiling, and the jet hits the store while the flow evolves.

The loads on the cavity walls are presented in figure 8.17 for the cases with

and without store. The signals of the dynamic cases are averaged over windows of 1.6 travel times, and the min and max of the signal over the window are also computed and shown as shaded envelope. This window width filters the frequencies above 50Hz for better readability of the plot, and for the static cases, the full time signal is used. The dynamic case shows a peak around 20 degrees when the jet interacts with the cavity (Figure 8.16c), and the loads approach the static values when the open cavity flow is established. Adding the store at carriage, shields the cavity walls (Figure 8.16d), and alleviates peak loads due to the jet, while, after the flow transitions to an open configuration, the store does not influence the wall loads. The store loads (Figure 8.18) show small differences between static and dynamic cases during the transition at about 30 degrees opening as the jet affects only a small part of the store front. After transition (see figure 8.18 at  $\phi > 50$  degrees), the store load fluctuations increase reaching values

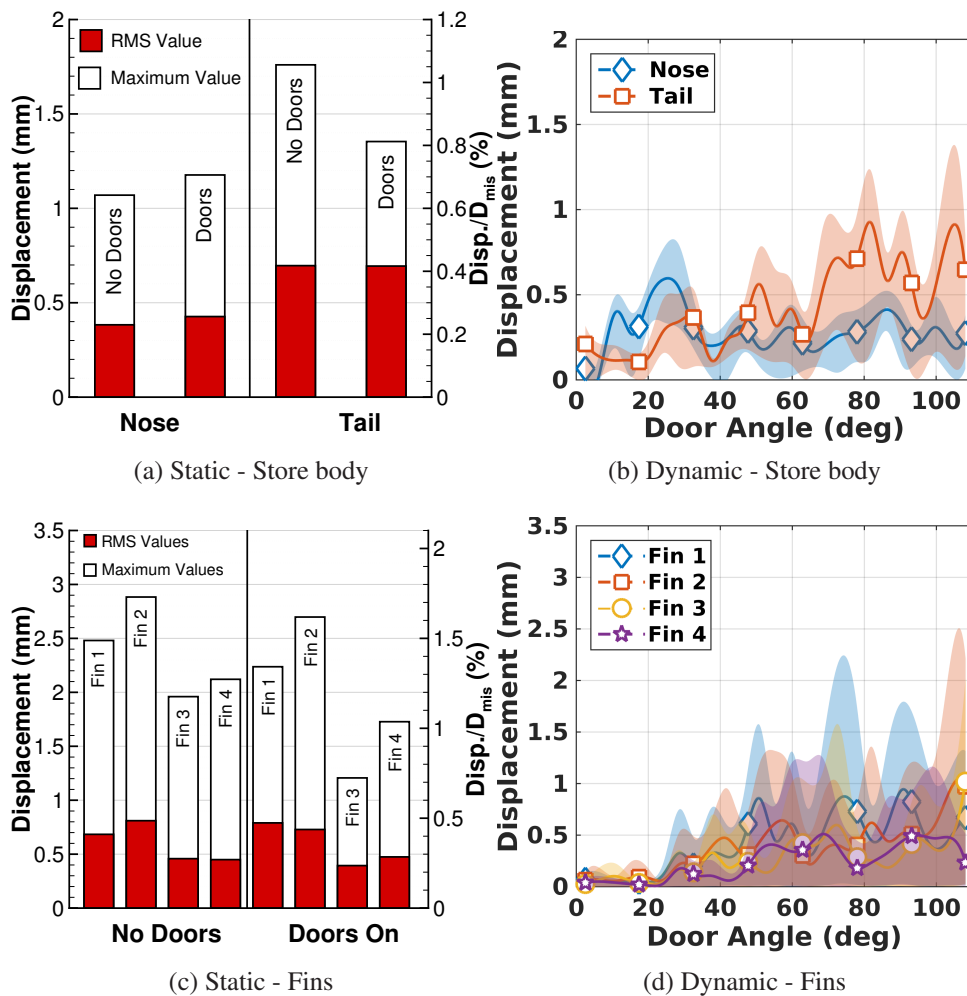


Figure 8.19: Deformation of the store during medium speed door opening.

close to one of the static door case as the flow develops.

In figure 8.19, the store deformations are shown for static door cases with and without doors (left column), and for dynamic cases with doors (right column). The RMS values are computed for the dynamic cases over windows of 1.6 travel times, and the envelope is represented in figure 8.17. Adding the fully opened doors to the cavity, the RMS displacements are unchanged (see red bars in figures 8.19a and 8.19c), because of a small effect of the doors at the mid-span of the cavity, as also shown in section 8.1. During the dynamic opening, the fin displacements are increasing with the door angle (Figure 8.19d), but not reaching larger values than the fully opened case. However, the body shows a different behaviour, with a peak deformation at the nose where the jet hits the store at about 20 degrees (Figure 8.19b), with larger RMS values compared to the static door cases. Nevertheless, the maximum values are smaller than for the static cases. The body tail behaves like the fins, because it is not directly impacted by the jet during transition.

## 8.5 Chapter Summary

This chapter presented simulations of a transonic weapon bay flow with doors either fixed, or opened in a dynamic way. The door opening evolved in three stages. First, a closed cavity flow was established, with the creation of a jet, impacting the bay ceiling, and producing large fluctuations inside it. Then, the flow became transitional, and the loads were amplified. The noise, as well as, the flow fluctuations, were also larger than for the fully established flow. The fastest door opening created the most unsteady flow of all cases during the opening phase. The flow during door opening may not influence the trajectory of a store released from the bay, as the flow has the time to reach a fully established state, before the release is initiated. In addition, the door opening is not a critical issue for the cavity/store structure, as the deformations are of the same order of as the one obtained from the fully established flow.

The doors used on the LD7 cavity had a pacifying effect on the cavity flow, while the M219 cavity doors, with a different design, amplified the cavity acoustics. This suggests that the door geometry can dramatically modify the cavity flow.

## Chapter 9

# Computation of Store Release from Weapon Bays

In this Chapter, scale-adaptive simulations are used to study store trajectory variability for releases from transonic weapon bays. The results of the simulations are treated as a statistical set and a metric is put forward to decide the minimum number of simulations necessary to establish the mean and the standard deviation of the releases. Averaging the results of all trajectories gives an overall understanding of the bay pressure field role on the store trajectories. Filtering the obtained trajectories provides insight in the flow frequencies affecting the forces acting on the store and its position during releases.

### 9.1 6DoF Method

The store motion during release was described using six rigid-body degrees of freedom (three body position coordinates and three body attitudes) and was strongly coupled with HMB3. This approach assumes that store release computations use the chimera method, so that a store has its own grid. The computed store position and attitude are applied at every instance in time to the store grid. Force and moment coefficients acting on the store, as obtained from HMB3, are applied into the translational and rotational

equations of motion <sup>[153]</sup> of a store in body axes:

$$\text{Longitudinal Acceleration: } \frac{du}{dt} = rv - qw - g \sin \theta (C_x q_s S) / m_s, \quad (9.1)$$

$$\text{Lateral Acceleration: } \frac{dv}{dt} = pw - ru + g \cos \theta \sin \phi (C_y q_s S) / m_s, \quad (9.2)$$

$$\text{Vertical Acceleration: } \frac{dw}{dt} = qu - pv + g \cos \theta \cos \phi (C_z q_s S) / m_s, \quad (9.3)$$

$$\text{Roll Acceleration: } \frac{dp}{dt} = C_l (q_s S d_{ref} / I_x) + qr [(I_y I_z) / I_x], \quad (9.4)$$

$$\text{Pitch Acceleration: } \frac{dq}{dt} = C_m (q_s S d / I_y) + pr [(I_z I_x) / I_y], \quad (9.5)$$

$$\text{Yaw Acceleration: } \frac{dr}{dt} = C_n (q_s S d / I_z) + pq [(I_x I_y) / I_z]. \quad (9.6)$$

In the above,  $m_s$  is the mass of the store and  $q_s$  is the free-stream dynamic pressure.  $u$ ,  $v$  and  $w$  are the velocity components of the store.  $p$ ,  $q$  and  $r$  are the roll, pitch and yaw rates, respectively, of the store.  $\phi$ ,  $\theta$  and  $\psi$  are the roll, pitch and yaw angle, respectively, of the store.  $C_x$ ,  $C_y$  and  $C_z$  are the axial, side and normal force coefficients, respectively, and  $C_l$ ,  $C_m$  and  $C_n$  are the rolling, pitching and yawing moment coefficients, respectively, acting on the store.  $C_m$  is positive nose up.  $d_{ref}$  is the store reference diameter and  $S$  its base area.  $I_x$ ,  $I_y$ ,  $I_z$  are the moments of inertia of the store about the X, Y and Z axis respectively. As the store used in this project is symmetric about the  $X_b - Y_b$  plane, the off-diagonal products of inertia terms, are ignored.

The equations for the angular velocities <sup>[153]</sup> in terms of the Euler angles are then:

$$\frac{d\psi}{dt} = (q \sin \phi + r \cos \phi) / \cos \theta, \quad (9.7)$$

$$\frac{d\theta}{dt} = q \cos \phi - r \sin \phi, \quad (9.8)$$

$$\frac{d\phi}{dt} = p + \left( \frac{d\psi}{dt} \right) \cdot \sin \theta \quad (9.9)$$

The translational components are calculated in the earth axis system attached to the cavity and the angular components are calculated using the Euler angles. The integration of the equations of motion are done with the Runge-Kutta method of order 4 (RK4).

## 9.2 Validation of the 6DoF Method

### 9.2.1 External Store Release

The following section presents validation of the 6DoF method in HMB3 for the widely used, wind tunnel test conducted at the Arnold Engineering Development Center (AEDC) [154]. Several studies have utilised this test case, using structured [155, 156, 157, 158], unstructured [159, 160, 161, 162, 163, 164] and meshless solvers [165], for validation purposes. The test provided pressure data for a geometrically simple and rigid wing and store, as well as the store trajectory. The AEDC 4-Foot Transonic Aerodynamic Wind Tunnel (4T) was used for the test together with its captive trajectory support system to simulate the motion of the store and the Mach number was 0.95.

#### Model Geometry and Release Conditions

The computational model was based on the wind tunnel geometry as reported in [154] (Figure 9.1). The properties of the store and ejectors are summarised in table 9.1. While the wind tunnel test consisted of a wing, pylon and store configuration, the pylon was omitted from the computational model to simplify the overset mesh in the region where the pylon and the store are almost in contact. Nevertheless, good agreement was found in the loads between experiments and CFD. The wind tunnel test model was of 5% scale of a generic full-scale wing/pylon/store.

#### Decoupled Analysis

Prior to running a fully coupled trajectory computation in HMB3, a decoupled approach was taken to compare the wind tunnel trajectory to that obtained from the 6DoF method in HMB3. Force and moment coefficients from the wind tunnel data were used as input. In this way the 6DoF method is tested without the expense of

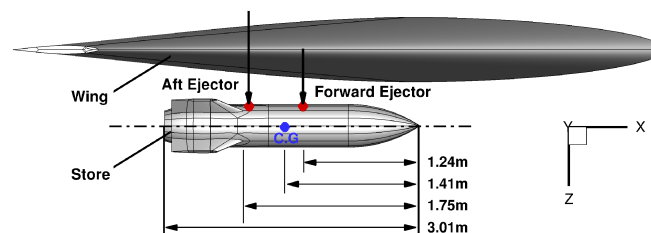


Figure 9.1: Wing store configuration and ejector position.

Characteristics	
Weight	8896.4 <i>N</i>
Centre of Gravity	1.41 <i>m</i> (aft of store nose)
Roll Inertia ( $I_x$ )	27.12 <i>kg.m</i> <sup>2</sup>
Pitch Inertia ( $I_y$ )	488.1 <i>kg.m</i> <sup>2</sup>
Yaw Inertia ( $I_z$ )	488.1 <i>kg.m</i> <sup>2</sup>
Forward Ejector Location	1.24 <i>m</i> (aft of store nose)
Forward Ejector Force	10675.7 <i>N</i>
Aft Ejector Location	1.75 <i>m</i> (aft of store nose)
Aft Ejector Force	42702.9 <i>N</i>
Ejector Stroke Length	0.1 <i>m</i>

Table 9.1: Full-scale store and ejector characteristics<sup>[154]</sup>.

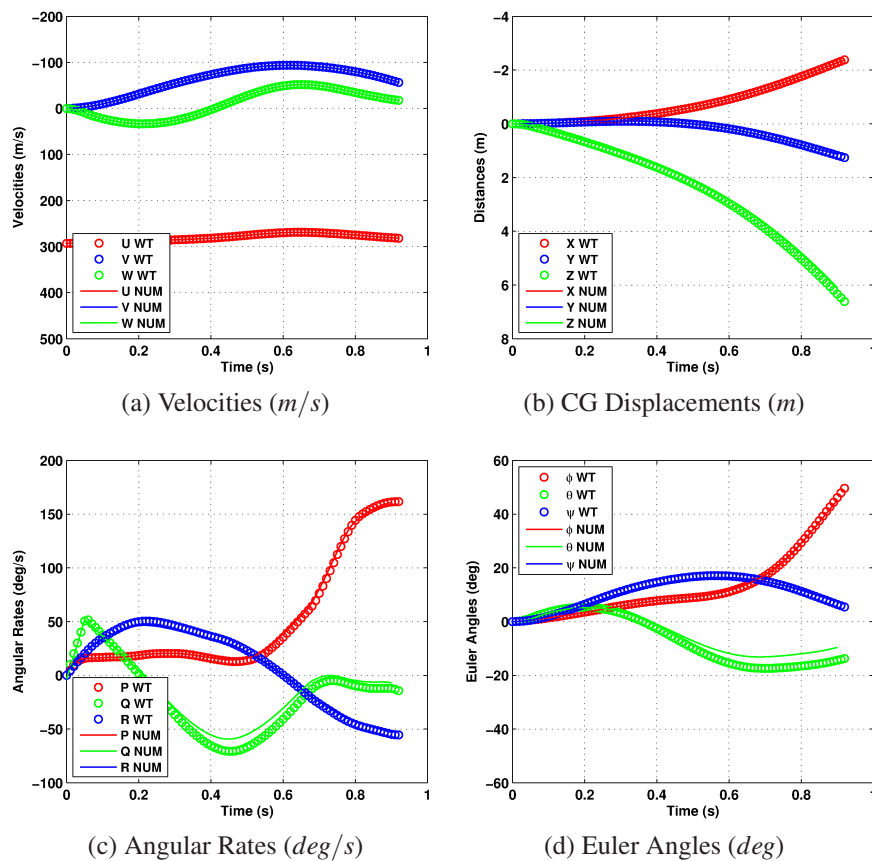


Figure 9.2: Comparison of trajectories from a decoupled approach and wind tunnel data<sup>[154]</sup>. WT : Wind tunnel. NUM : Decoupled simulation.

computing the flow at every instance in time.

Figure 9.2 shows a comparison of the wind tunnel trajectory to the trajectory computed by the 6DoF method in HMB3 through the decoupled approach, for the full available signal length of 0.92s. WT is the wind tunnel data, and NUM the decoupled results from HMB3. Velocity components and CG displacements agreed well with the wind tunnel data, however small differences can be seen in the pitch and yaw rates and hence the pitch and yaw angles. The initial part of the trajectory, controlled by the ejector forces compared closely to wind tunnel data, however, after about 0.3s the pitch and yaw rate started to drift away from wind tunnel data. This behaviour over time, especially in pitch rate and attitude, was also reported in previous studies<sup>[155, 161, 162]</sup>.

### Store Loads and Trajectory

Computations were run at a Mach number of 0.95 and Reynolds number of  $1.0 \times 10^6$  (based on the root chord of the wing). The store release computation, solving Euler's equations of motion, was initiated from a solution around the store at carriage position, after the flow was fully developed. The store loads obtained through HMB3 agreed with the wind tunnel data. Figure 9.3 shows the trajectory of the store starting from the carriage position at time  $t = 0.0s$  with a time step of 0.1s computed with HMB. The trajectory visualised here shows the store having an initial nose-up pitching moment as expected from the difference in force between the forward and aft ejectors. The store recovers from the pitch, and is seen to have a growing positive yawing moment over time.

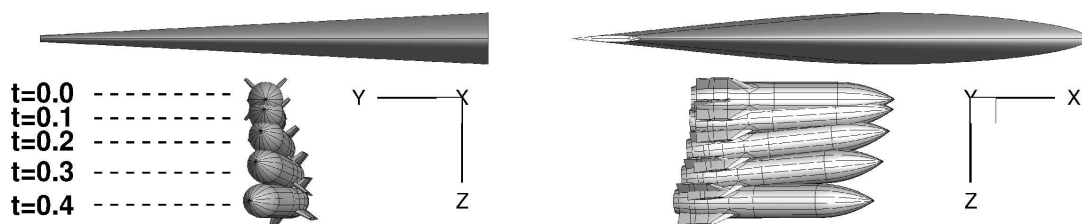


Figure 9.3: Store trajectory released from the wing at different time instances.

Figure 9.4 presents a comparison of the trajectory computed using HMB3 and the wind tunnel data. The forces, velocities, displacements, moments, angular rate and Euler angles, in the missile axes, were compared for 0.4s of the simulation. It is apparent that the force coefficients, velocity and location of the CG closely matched the wind tunnel data. The store moved slightly rearward and inboard as it moved further

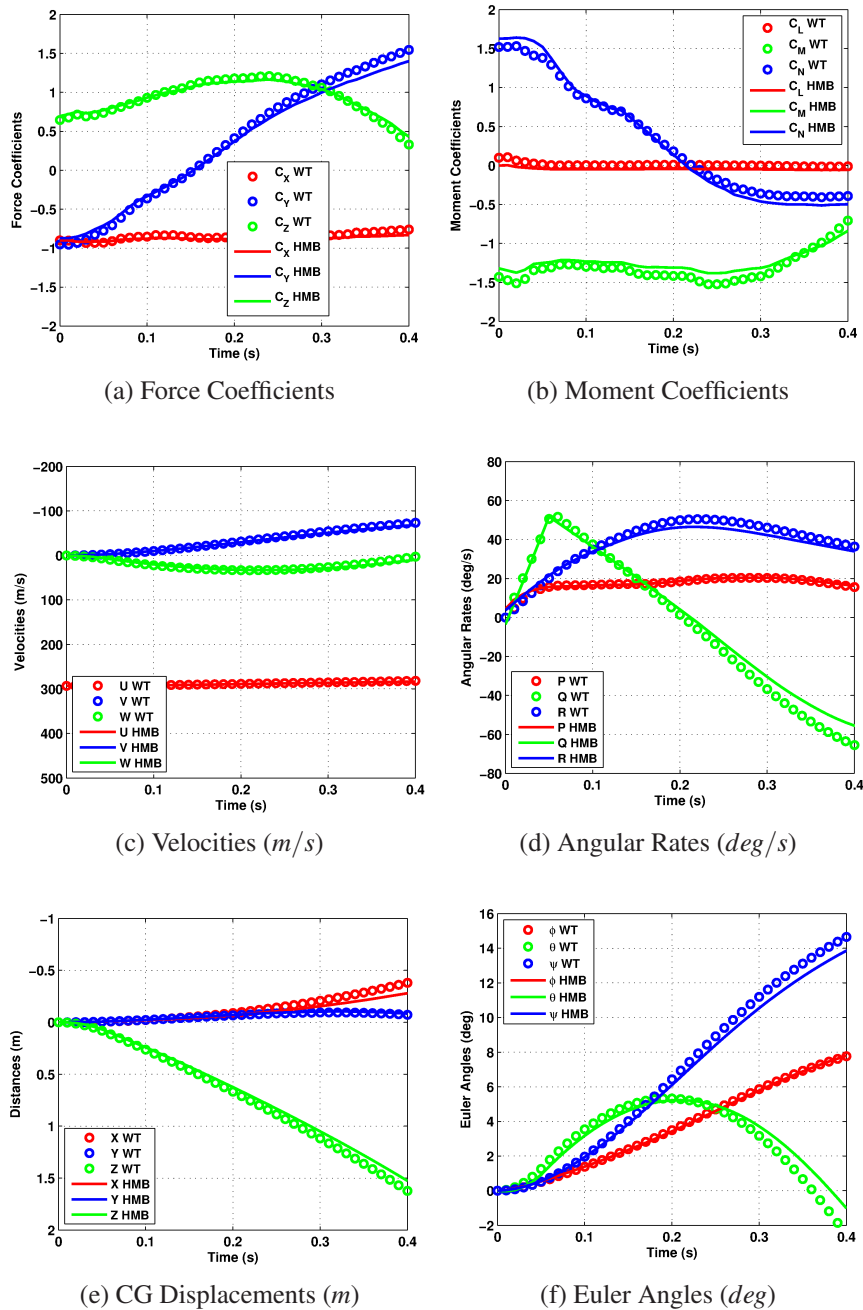


Figure 9.4: Trajectories comparison between HMB3 and wind tunnel data<sup>[154]</sup>. WT: Wind tunnel.

away from the wing. Small discrepancies were seen in the moment coefficients that were carried into the angular rates and Euler angles.

Initially, there was a slight underprediction of the rolling moment and overprediction of the pitching and yawing moment coefficients. The initial overprediction in the pitching moment coefficient did not affect the initial part of the trajectory in terms of gravity center location or pitch attitude as the ejector and gravity forces dominated the aerodynamic forces and moments in that direction. Nevertheless, aerodynamic forces remained important after the stroke due to the large pitch angle, and the presence of the wing that influences the pressure field around the store..

The effect of the ejectors is seen clearly in the pitch rate that grows positively for the initial 0.5 seconds of the release. Once the ejector stroke ended, the aerodynamic pitching moment on the store began to reduce. The pitch and yaw curves showed a slight divergence from the wind tunnel data after about 0.3 seconds of the release. This divergence over time was not only observed in the original study by Fox<sup>[154]</sup>, but in other studies<sup>[155, 161, 162]</sup> as well.

### 9.2.2 Internal Store Release

This section presents additional validation of the employed CFD method for a store released from a weapon bay. The experiments performed at the Arnold Engineering Development Center (AEDC) <sup>[50]</sup>, and described in section 1.1.4 are at conditions closer to the present store release computations, and have thus been selected for validation.

The Mach number was 0.95, and the cavity was assumed to fly at altitude of 6096m. The Captive Trajectory System (CTS) was used. Using the standard atmosphere, the flight conditions were equivalent to a temperature of -24.6deg, a static pressure of 46619 Pa, and a density of 0.65 kg/m<sup>3</sup>. The full scale cavity was 4.57m long, 1.02m wide with L/D of 4.5. The employed store was 2.87m long, with four fins and canards in a cross configuration <sup>[50]</sup>. The store had five degrees of freedom with rolling disabled due to the employed CTS. At carriage, the store CG was at half cavity depth. After an ejector stroke, the store was released with a full size downward velocity of 9.14m/s, and a pitch, nose-down velocity of 57deg/s. The store release characteristics are summarised in table 9.2. The wind tunnel Reynolds number based on the scaled cavity length of 0.46m was  $3.75 \cdot 10^6$ .

Characteristics	
Weight	88.5 kg
Centre of Gravity	1.5 m (aft of store nose)
Pitch Inertia ( $I_y$ )	61.8 kg.m <sup>2</sup>
Yaw Inertia ( $I_z$ )	61.8 kg.m <sup>2</sup>
Stroke Length	0.2 m
Stroke Velocity	9.14 m/s
Initial Pitch rate	57.3 deg/s

Table 9.2: Full-scale store and ejector characteristics<sup>[50]</sup>.

ID	Stroke Start Time	
	Travel Time	Time (ms)
CFD 2000	20	30
CFD 2200	22	33
CFD 2400	24	37
CFD 2600	26	40

Table 9.3: List of computations carried out to validate internal store release.

Four releases are performed at different times from the beginning of the computation (Table 9.3), and the results are shown in figure 9.6 between HMB using

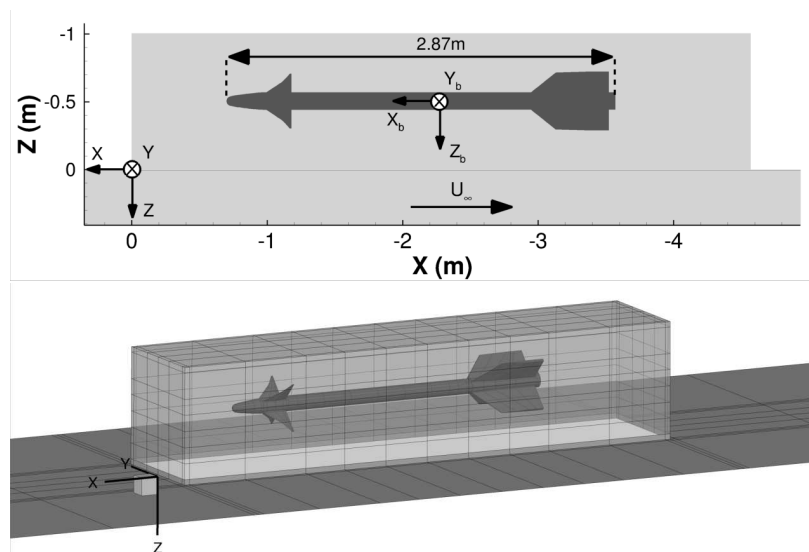


Figure 9.5: Geometry, cavity axis, and store at carriage position.

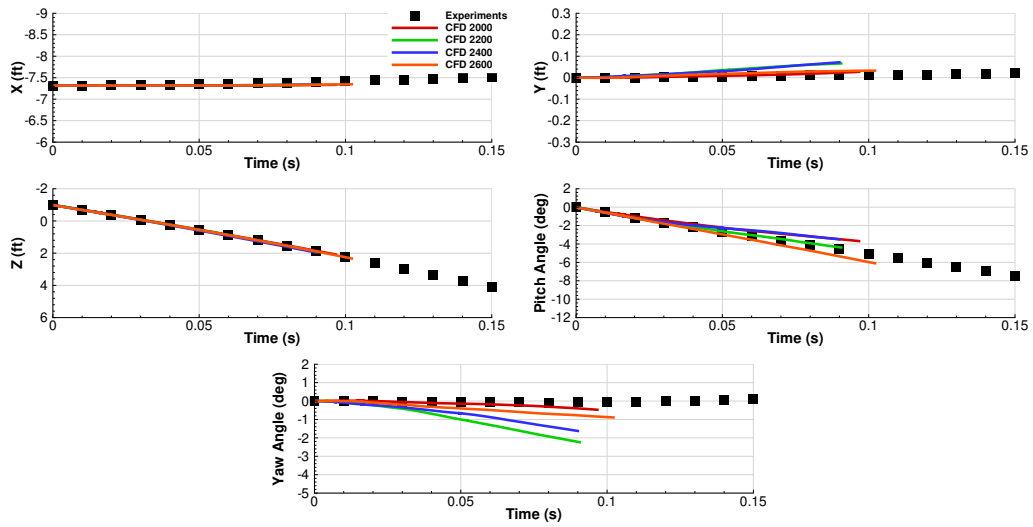


Figure 9.6: Store position during release simulation using HMB3.

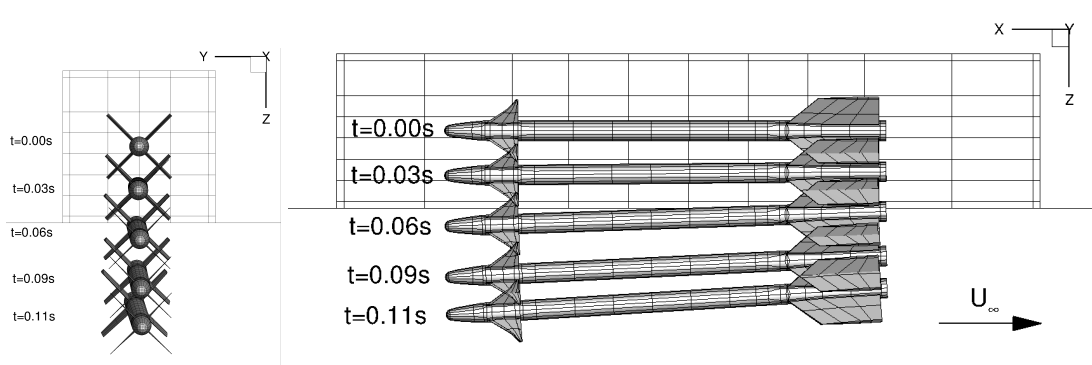


Figure 9.7: Sequence of separating store CFD 2400 computed with the coupled 6DoF and HMB3.

SAS, and experiments [50]. The displacements in the stream-wise, and span-wise directions are small, and less than two centimeters. The vertical displacement is mainly driven by gravity, and ejection characteristics, and no significant variability is seen in the computations for it. However, the store attitudes, show large variability in pitch and yaw, as also seen in reference [62]. After few releases, both numerical results from HMB3, and Kim *et al.* [62] look similar in terms of variability.

Figure 9.7 shows a side, and a front view of the store at multiple times during the release CFD 2400. The store reaches rapidly a large pitch angle that helps the safe release of the store. Figure 9.8 shows the separating store at selected time steps for one of the releases. The results are very similar in terms of store position.

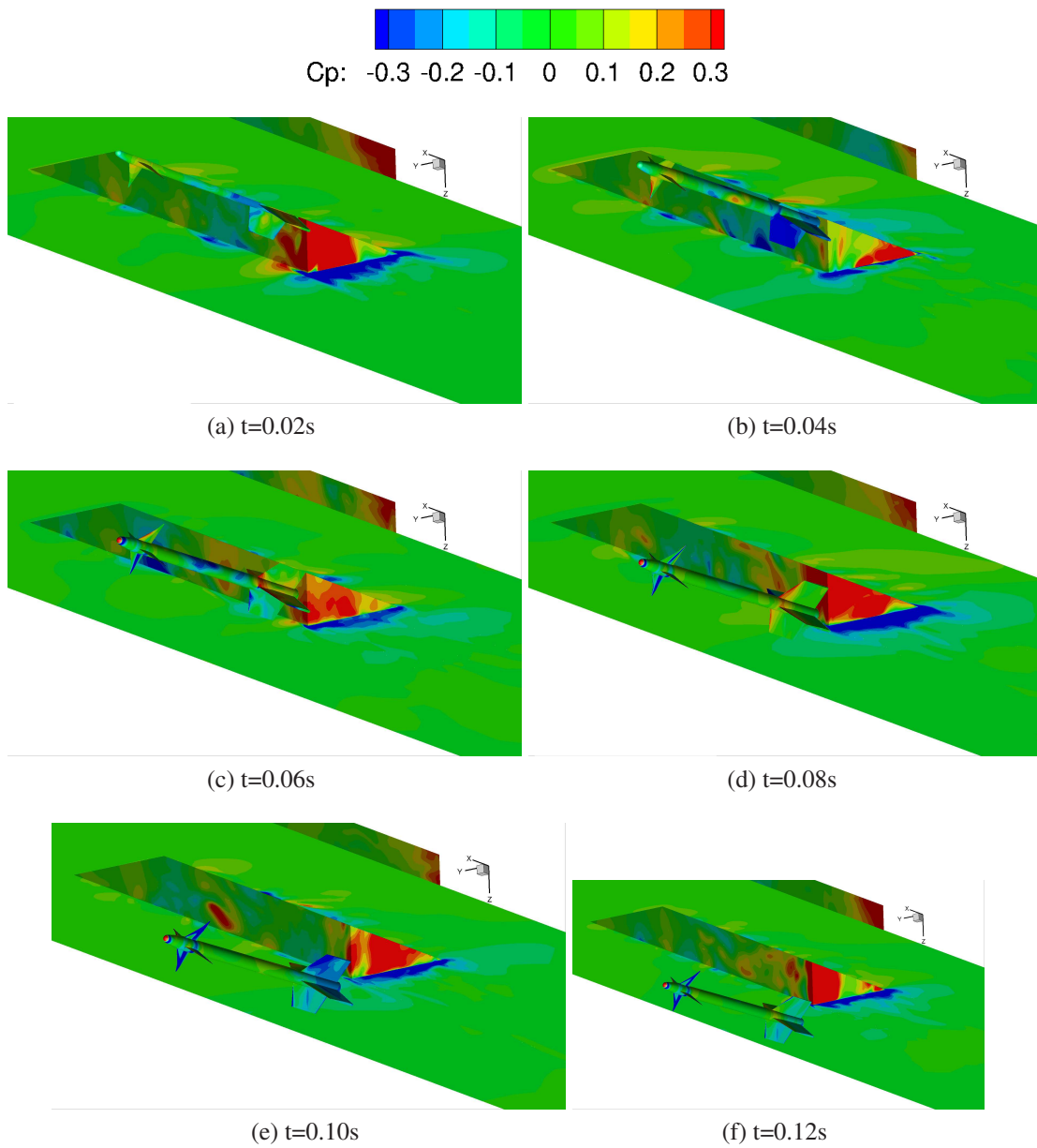


Figure 9.8: Sequence of separating store computed with HMB3

### 9.3 Computational Model for Store Release

The store release includes three phases. At *carriage* ( $Z/D=-0.5$ ), the store is fixed while the flow is allowed to develop. Then, during the *stroke phase*, the store is pushed towards the cavity opening. During this phase, a vertical velocity of 5m/s is imposed on the store, with other degrees of freedom set to zero. This phase ends when the stroke length is reached. The full stroke is half a cavity depth (0.257m). In addition, a half stroke is also used (0.129m). Finally the store is free to move under the aerodynamic forces. Twenty computations are carried out, 5 applying a full stroke (FS) length and 15 applying a half stroke (HS) length, at different release times. The aircraft is supposed

ID	Stroke Start Travel Time / Time (ms)	Stroke Length (m)
FS2000	20 / 13	0.257
FS2400	24 / 62	0.257
FS2600	26 / 87	0.257
FS3000	30 / 137	0.257
FS3400	34 / 187	0.257
HS2000	20 / 13	0.129
HS2200	22 / 37	0.129
HS2400	24 / 63	0.129
HS2600	26 / 87	0.129
HS2800	28 / 113	0.129
HS3000	30 / 137	0.129
HS3200	32 / 162	0.129
HS3400	34 / 189	0.129
HS3600	36 / 212	0.129
HS3800	38 / 238	0.129
HS4000	40 / 263	0.129
HS4200	42 / 289	0.129
HS4600	46 / 339	0.129
HS5000	50 / 390	0.129
HS5400	54 / 440	0.129

Table 9.4: List of computations carried out to demonstrate the trajectory variability.

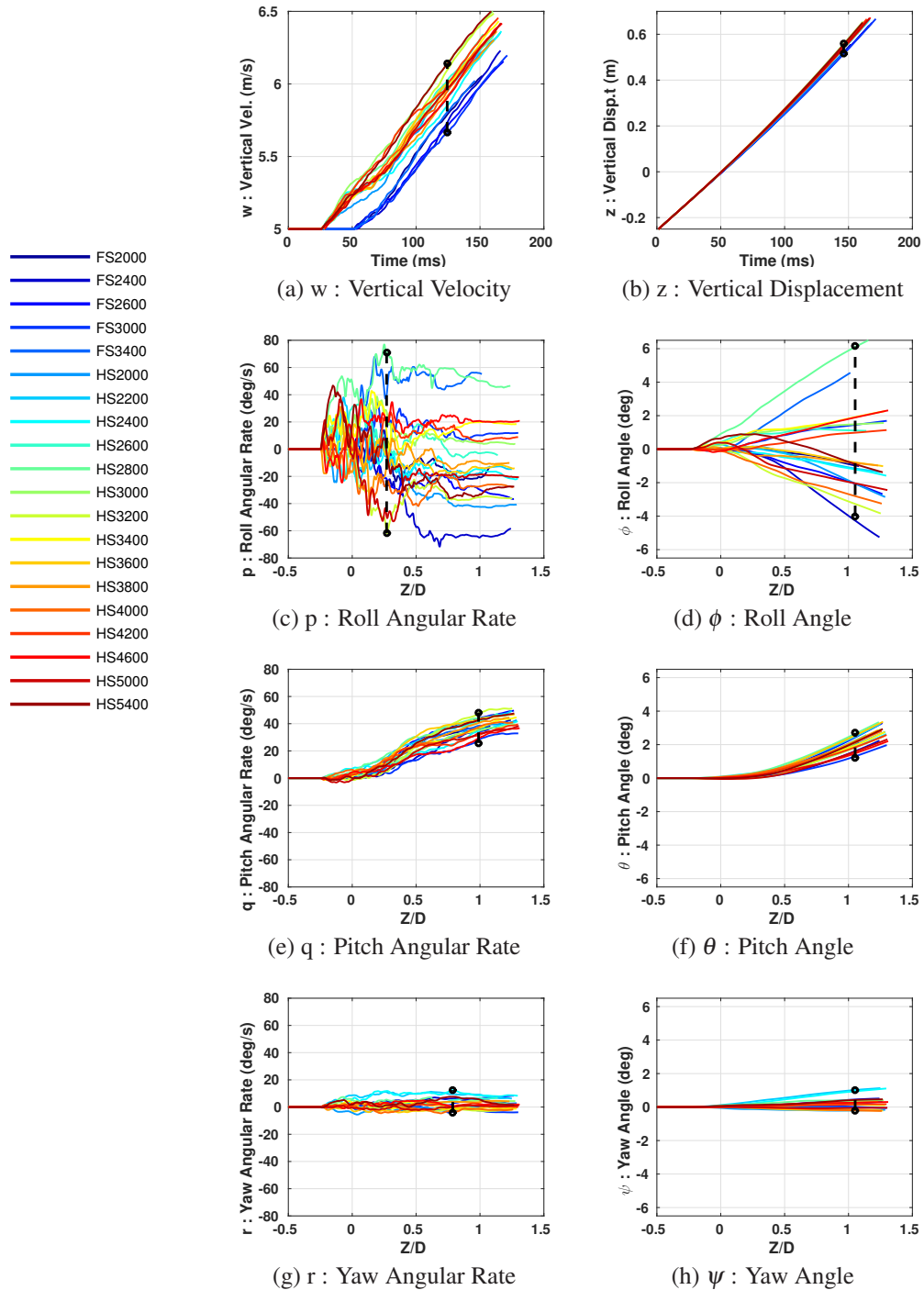


Figure 9.9: Trajectory of full and half stroke cases. Vertical dashed bars denote  $W_e$ .

to fly at an altitude of 1000m, and the atmospheric conditions were computed using the standard atmosphere. The computations are summarised table 9.4.

## 9.4 Results and Discussion

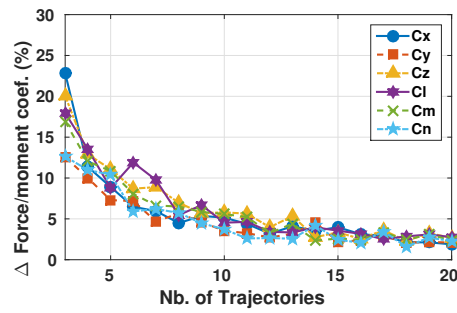
### 9.4.1 Statistical Analysis of the Trajectories

Figures 9.9a and 9.9b present the vertical velocity  $w$ , and the displacement  $Z$  for the full and half stroke releases, as functions of time. The variability is negligible, of the order of 5cm, and the vertical displacement  $Z$  appears to be mainly driven by gravity. For a better reading, the trajectories are shown as function of  $Z/D$  in the following. The longitudinal and the span-wise amplitudes of displacement, not shown in the figures, are of the order of 1 cm, and are also negligible compared to the vertical displacement. The store angles shown in figure 9.9 have broader variability, with the roll angle varying between -5 and 6 degrees, the pitch between 2 and 4 degrees, and the yaw between -1 and 1 degrees at one cavity depth away from the cavity opening ( $Z/D=1$ ). The roll rate reaches peak values (up to 80deg/s), and the curves have more frequency content compared to the pitch and yaw angles.

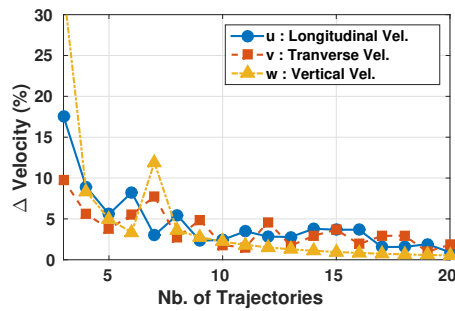
Amongst other possible criteria, statistical convergence is tested here using the maximum of the normalised difference between the average of  $n+1$ , and  $n$  trajectories:

$$\Delta_{\mu} = \frac{\max|\mu(t, n+1) - \mu(t, n)|}{W_e} \quad (9.10)$$

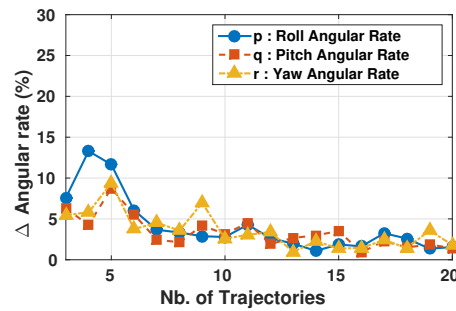
with  $\mu(t, n)$  the average of  $n$  trajectories, where  $t$  covers the complete time of simulation. The envelope of the trajectory is defined as the maximum difference between minimum, and maximum over all releases and all store vertical positions.  $W_e$  is the largest envelope width over all positions, and indicated by dashed lines in figures 9.9 and 9.12. Figure 9.10 shows the convergence of the proposed metric for all store releases in a random order. A trajectory component is considered as converged if the difference ( $\Delta_{\mu}$ ) between two consecutive averages is less than 5%. As can be seen in figure 9.10, the averages substantially fluctuate with less than 10 drops due to the flow variability. For example, the roll angle may even change sign for two consecutive releases. In the case the statistics are not convincing, we decided to investigate the order of the trajectories. The result is that given enough releases, the actual order is not relevant, because the envelope of the trajectories is established, and the mean



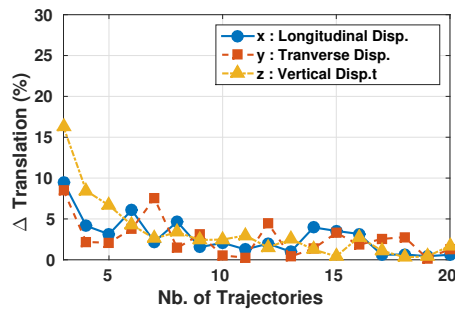
(a) Forces and Moments



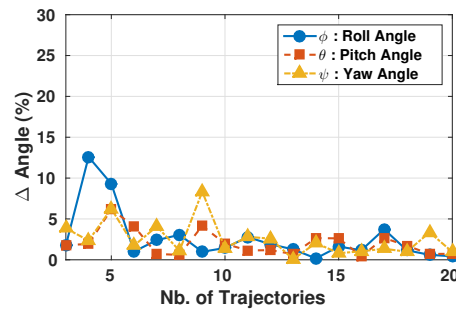
(b) Velocity



(c) Angle Rate



(d) Translation



(e) Angle

Figure 9.10: Convergence of the averaged trajectory.

values are not affected by adding samples. This is exactly the same as the averaging process in turbulence where any random fluctuation converge to a mean value as the number of sample increase [166]. Despite the speed of SAS, it is still difficult for an engineer to compute enough trajectories to reach the convergence point. To minimise this effect,  $\Delta_{\mu}$  was computed for 100,000 random permutations of the 20 trajectories. For each permutation, the number of releases required to converge the statistics was computed, and the cumulative plot in figure 9.11a indicates the number of converged permutations with respect to the number of releases included in the mean. For the store at hand, 17 trajectories were necessary mainly due to variability in roll associated with its low roll inertia.

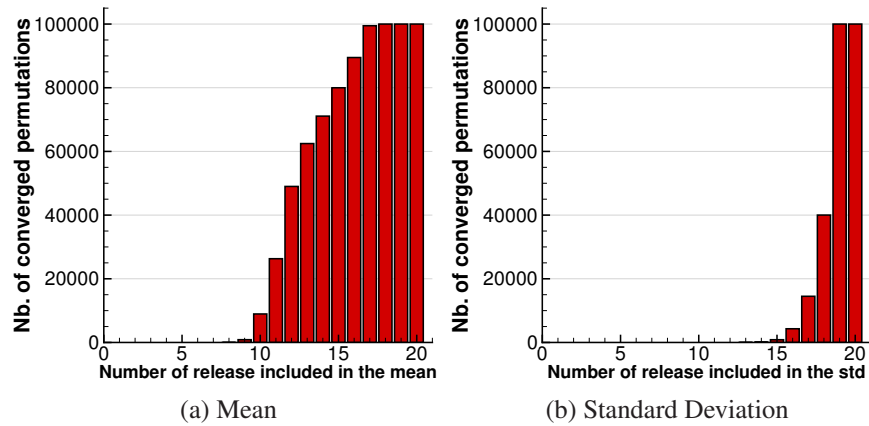


Figure 9.11: Number of converged release permutations as function of the number of releases used for the statistics.

A similar metric is defined for the standard deviation  $\sigma$ :

$$\Delta\sigma = \frac{\max|\sigma(t, n + 1) - \sigma(t, n)|}{W_e} \tag{9.11}$$

The number of converged permutations under 5% as function of the number of releases included in the standard deviation is shown figure 9.11b for 100,000 permutations.

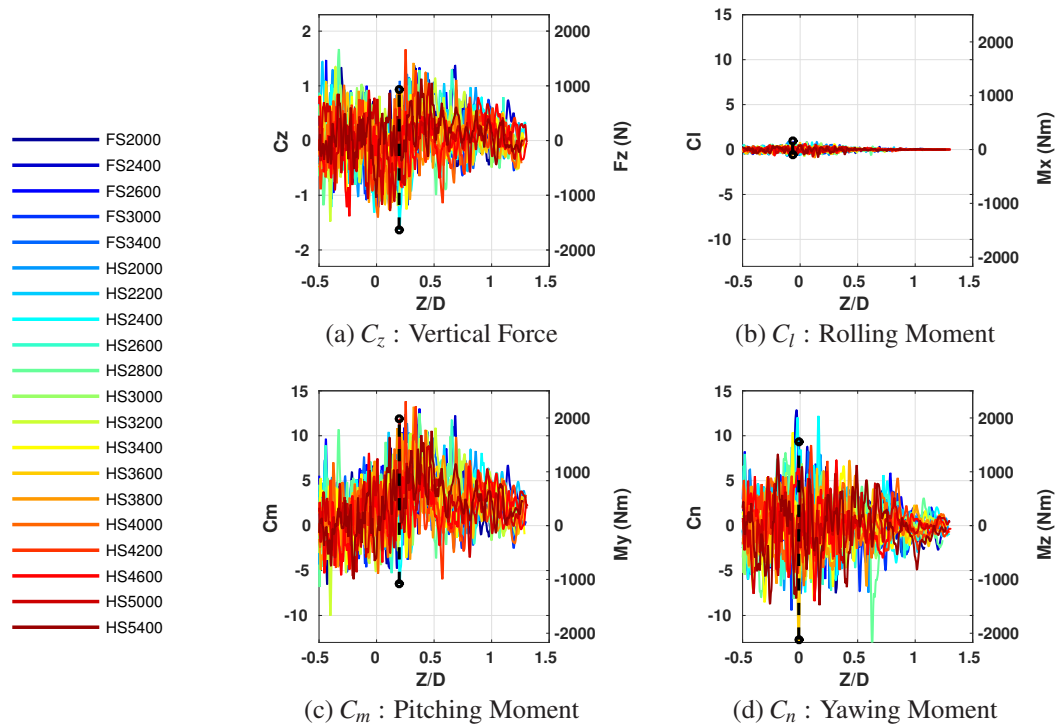


Figure 9.12: Force and moment coefficients during full and half stroke releases. Vertical dashed bars denote  $W_e$ .

The standard deviation requires 19 releases to converge. This is more than the mean because the standard deviation is more sensitive to the large variability in roll.

Figure 9.12 shows the forces driving the trajectories. The curves appear to be very noisy. The largest variability is seen for the roll angle that is sensitive to high flow frequencies, due to the roll inertia being two orders of magnitude smaller than the inertias in pitch and yaw.

### 9.4.2 Mean Flow

Taking all the trajectories with full and half stroke, an averaged trajectory was constructed, considering all times of the simulations from stroke initiation until a common point in time  $t = 12$  travel times, corresponding to the shortest of the simulated trajectories (FS3400). Figure 9.13 shows the average trajectory in continuous lines, and the standard deviation in dashed lines, for the vertical store displacement, and all store rotations. The vertical velocity did not increase linearly during the release, as a strong normal aerodynamic force is present when the store interacts with the shear layer at  $Z/D = 0.2$ . The averaged pitch angle grows with the distance from the cavity, and the pitching moment reaches a peak at  $Z/D = 0.35$ .

Figures 9.14a and 9.14b show the distributions of vertical force  $C_z$  and pitching moment  $C_m$  coefficients along the store length, averaged over all releases. The loads were integrated on the store body and fins, in sections of 3.5% of the store length, and the vertical axis represents the store CG position for each instance in time of the release. The two main sources of loads are localised where the flow encounters the store nose, and fins. The  $C_p$  distribution averaged over all releases is also shown at the mid-span plane of the cavity (Figures 9.14c to 9.14f). The averaged results are shown for four bands: for the store inside the cavity ( $-0.40 < Z/D < -0.30$ ), at the shear layer ( $0.00 < Z/D < 0.10$ ), at the peak of pitching moment  $C_m$  ( $0.35 < Z/D < 0.45$ ) and far from the cavity ( $0.90 < Z/D < 1.00$ ).

Inside the cavity (Figure 9.14c), a small pressure gradient between the upper and lower surfaces of the store, explains the small averaged loads at this position, and the small differences between full and half stroke releases. When the store crosses the bay opening (Figure 9.14d), it is at the interface between the cavity and the free-stream conditions, leading to a strong average pressure gradient at its mid length. A further contribution to the aerodynamic normal force is due to the impact of the shear layer on

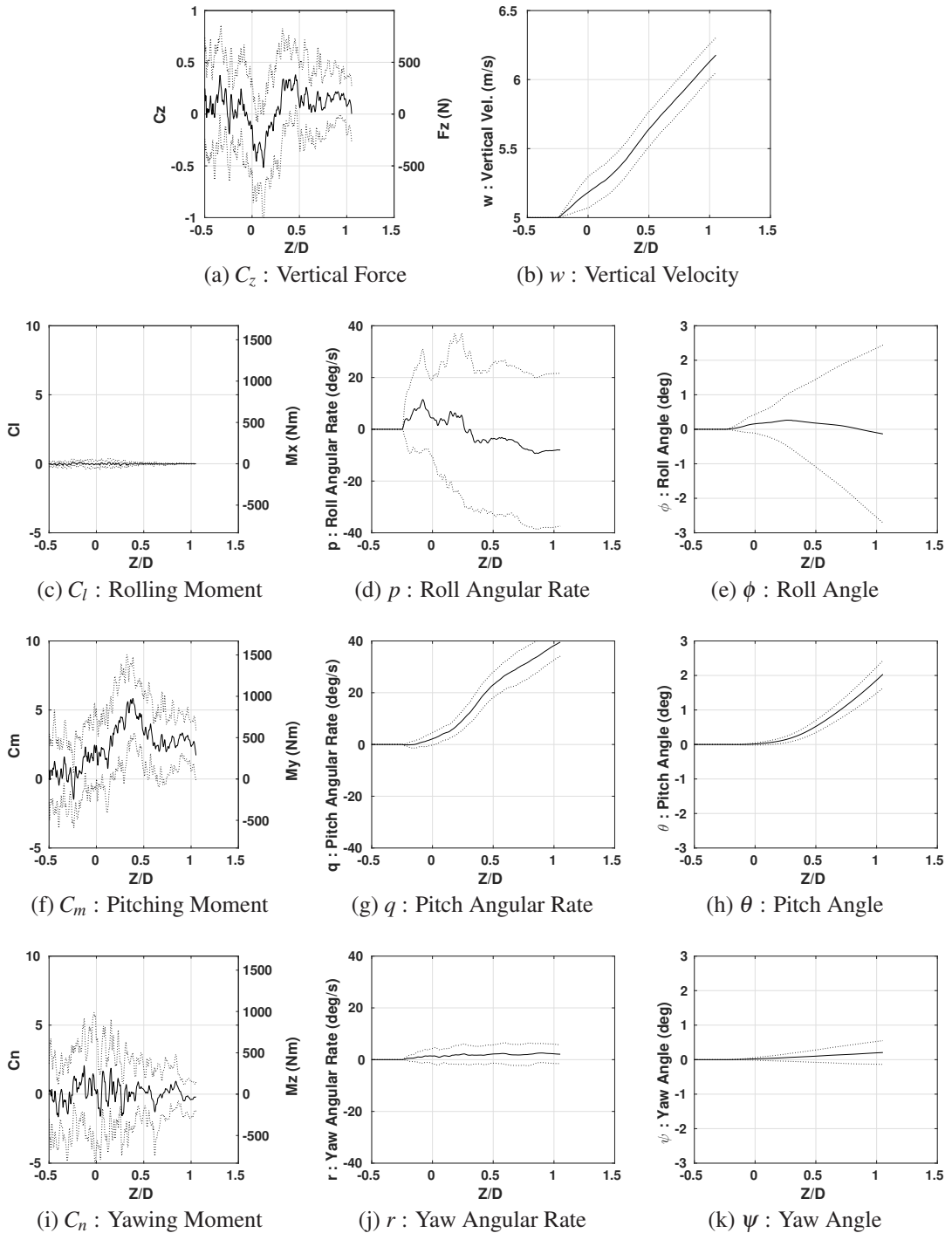


Figure 9.13: Averaged and standard deviation of translations and rotations with half and full stroke releases.

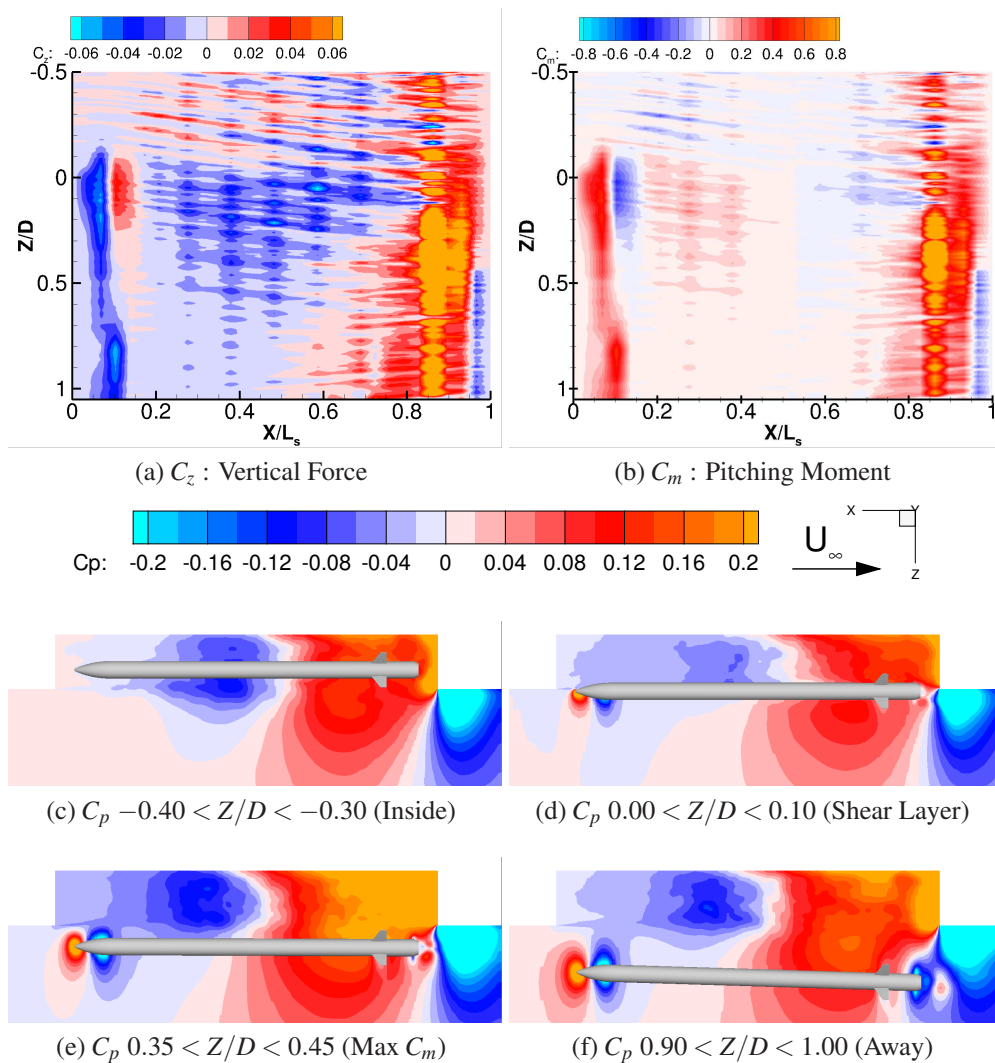


Figure 9.14: Averaged store loads, and pressure coefficient at cavity mid-span.

the store nose. Nevertheless, the effects of the ejector push and gravity dominate. Away from the cavity, at the peak of pitching moment (Figure 9.14e), there is a large increase of the pressure at the aft cavity wall, leading to an increase of the vertical force on the fins, and to the peak of pitching moment. The free-stream impacting on the pitched store nose, also contributes to the larger pitching moment at this position. Going further away (Figure 9.14f), the pressure gradients due to the cavity flow decrease, and the loads at the store nose and the fins dominate.

Using equation 2.38, the flow momentum is shown in figure 9.15 averaged over all releases at the previous store positions, inside the cavity, at shear layer, at the peak of pitching moment, and far from the cavity. As the store travels towards the far-field, the shear layer is deflected towards the cavity by the store, more than for the clean

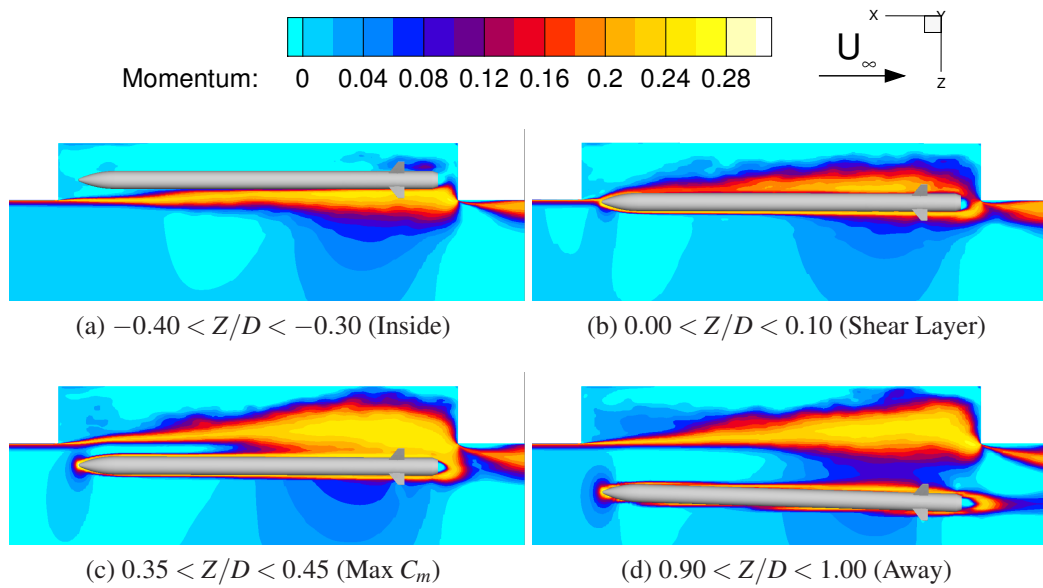


Figure 9.15: Flow momentum at the cavity mid-span.

cavity case. This results in a pressure peak at the aft wall, leading to the peak of pitching moment (Figure 9.15c). Away from the cavity, the store effect reduces, and the shear layer resembles that of a clean cavity flow.

### 9.4.3 Filtered Loads

The store forces are decomposed in pressure and viscous contributions for release HS2600 (Figure 9.16). All trajectory components are driven by the pressure forces, and only the drag force ( $C_x$ ) noticeably depends on viscosity. Store angles not shown here are also driven by pressure forces. The load fluctuations driving the trajectory variability are very noisy, and difficult to interpret (Figure 9.17). To determine the frequency bands that drive the trajectories, a low pass Butterworth filter of 4th order is applied to the signals, minimising the band overlapping, and signal distortion <sup>[167]</sup>. The Butterworth filter has some advantages in processing noisy signals removing the highest frequencies without affecting the main tones at lower frequencies <sup>[167]</sup>. In the following, trajectories computed with unfiltered loads are denoted as “original”, in contrast to the “filtered” ones. For each trajectory, the Minimum Frequency required to Reconstruct the Trajectory (MFRT) is found by limiting the error between the original and the filtered signals, to 0.05 degrees in angle, and 1 mm in translation over the complete trajectory. This is done by scanning the signals in steps of 3Hz, from 3 to 300Hz and applying filtering. Figure 9.17 shows pitch moment, and store pitch angle

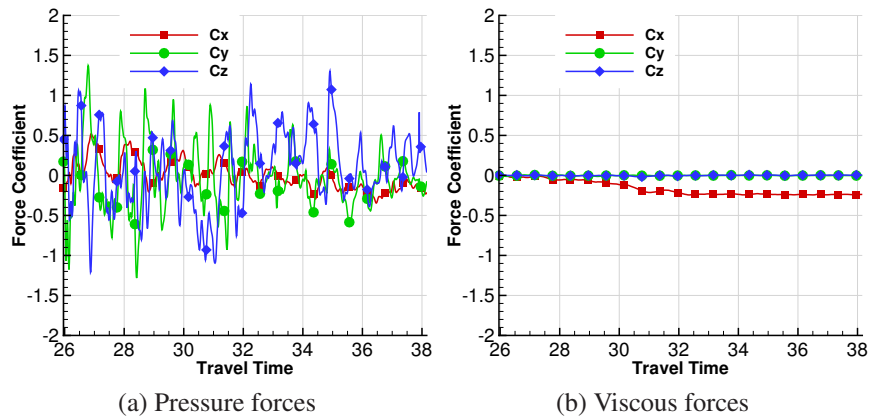


Figure 9.16: Decomposition of the HS2600 store forces in pressure and viscous components.

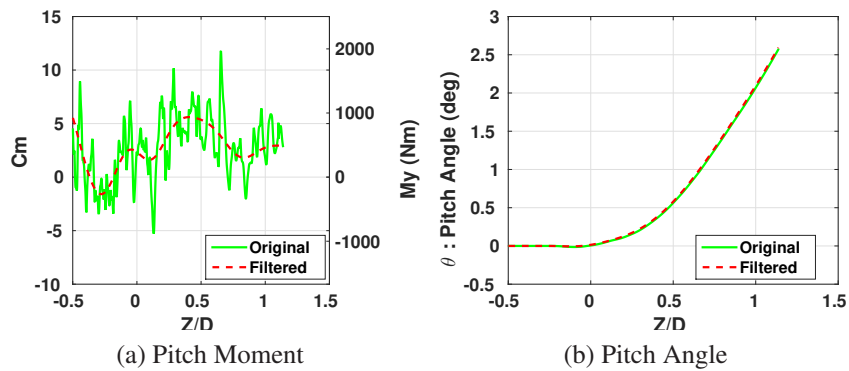


Figure 9.17: Original and filtered pitch for the case HS2600.

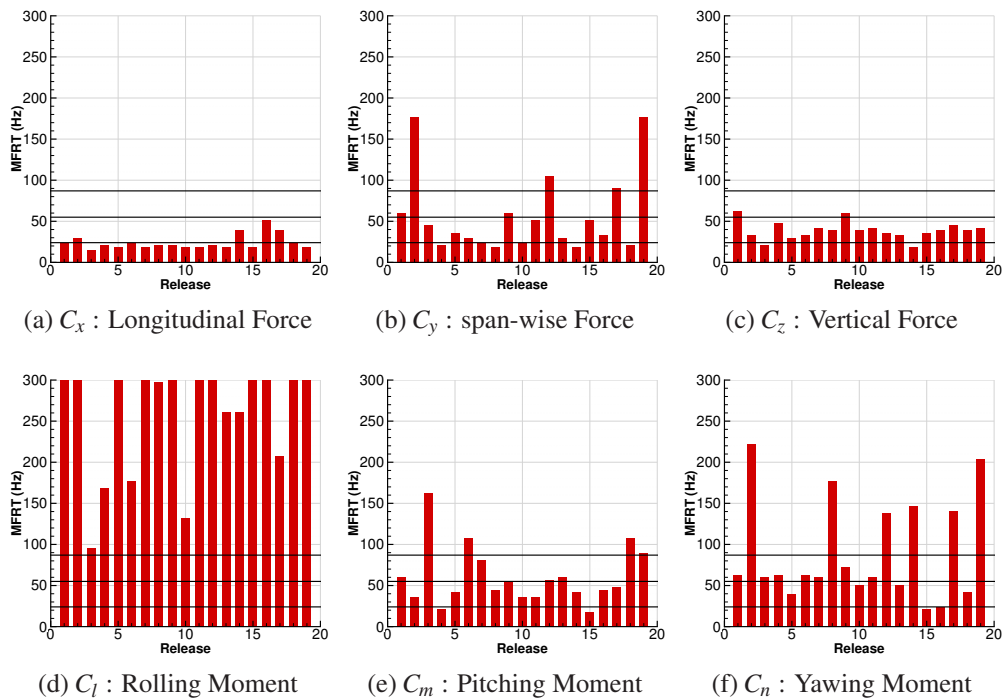


Figure 9.18: MFRT for the different releases and force/moment coefficients. The horizontal lines represent the cavity tones 1, 2 and 3.

from trajectory HS2600. The filtering dramatically reduces the spectral content of the moment signal. However, the filtered pitch angle matches perfectly the original signal.

Figure 9.18 summarises the MFRT frequencies for the different computed cases. The black lines correspond to the frequencies of the cavity modes. As can be seen, different trajectory parameters are driven by different frequency ranges. The longitudinal displacement is dictated by  $C_x$ , which is sensitive to frequencies below the first cavity mode (24Hz). The span-wise and vertical displacements are dictated by  $C_y$ , and  $C_z$  respectively, and are driven by frequencies below cavity mode 2 (55Hz), with some limited influence of frequencies up to 170Hz in the span-wise direction. The pitch and yaw angles are on average, influenced by frequencies below the third cavity mode(87Hz), and in some cases by frequencies up to 200Hz. Finally, the roll angle is sensitive to frequencies even above 300Hz.

Figure 9.19 shows the filtered loads for the different releases.  $C_x$  (Figure 9.19a) only depends on the store position, meaning that the longitudinal displacement is driven by the mean flow. The filtered  $C_y$ ,  $C_l$  and  $C_n$  fluctuate around zero, and are influenced by local asymmetries of flow inside the bay. The filtered  $C_z$  and  $C_m$  (Figures 9.19e and 9.19d) significantly fluctuate around the averaged release, and show the largest excursions from it.

The store loads fluctuate under the action of three main pressure contributions. First, the tonal fluctuations caused by standing wave oscillations (typical in cavity flows, see section 3.5), lead to variability due to the time of release <sup>[52]</sup>. In addition, turbulence also increases variability, mainly for the roll angle. Finally, the store/shear layer interaction differs depending on the store trajectory history and the instantaneous flowfield. This interaction, and the associated trajectory variability, can be captured only if the loads are fully coupled with the flowfield, which means that coupled CFD/6DoF calculations are needed.

#### 9.4.4 Releases with Aeroelasticity

This section goes further into the realism of the simulation, adding the aeroelasticity to the complete store. The following computations do not include bay doors.

### Store Release Process

This set of calculations includes only half-stroke releases. At carriage, and during the stroke phase, the store is fixed to an ejection system that is not included in the CFD geometry. In addition, carriage modes are used for the store aeroelasticity (See section 7.1.1). At the end of the stroke, the store detaches from the ejection mechanism. To ensure continuity of the computation, the carriage modes are still active with their forces  $f_m^s(t)$  set to zero to stop their excitation. At the same time, the free air structural modes are activated. Figure 9.20 shows the deformations at the body tail due to both sets of modes during the release HS10000. Computations carried out for different release times are shown here, and are summarised in table 9.5.

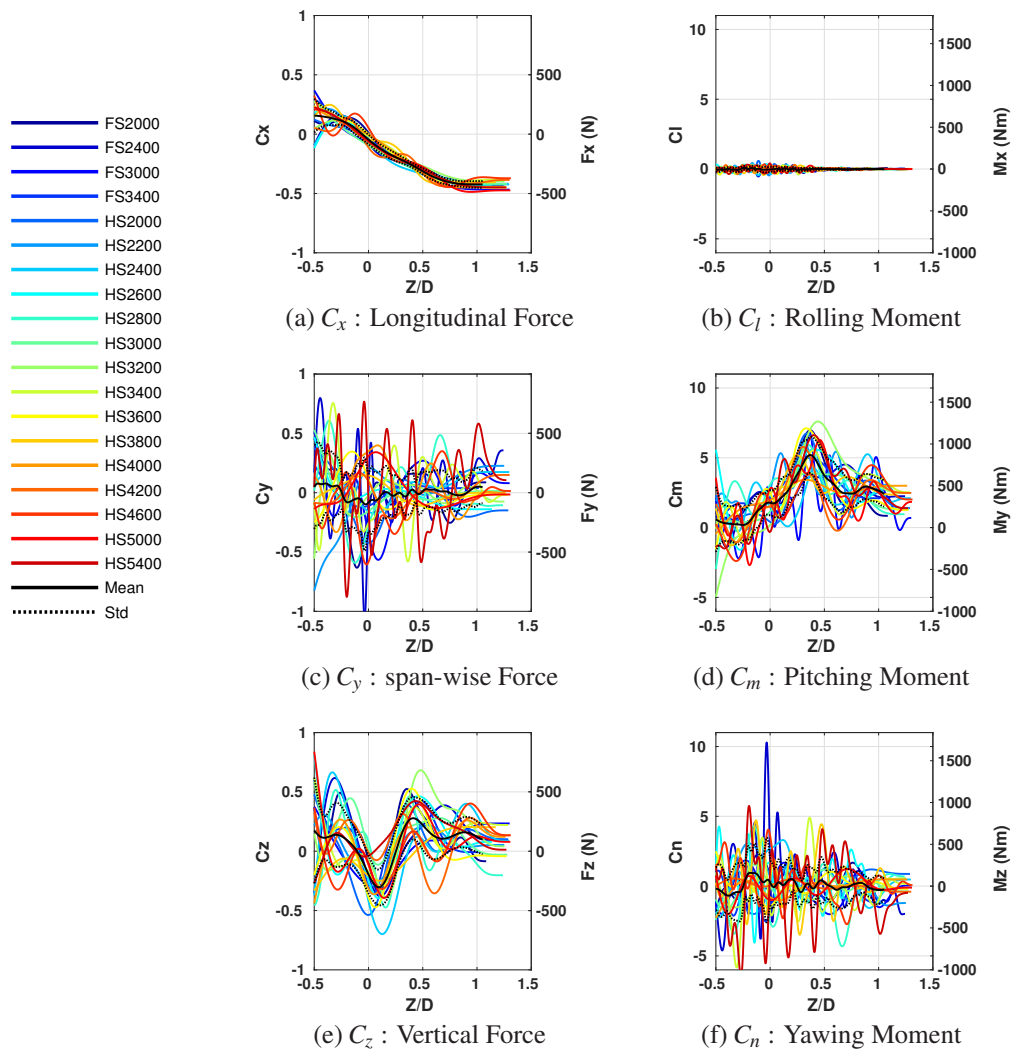


Figure 9.19: Filtered force and moment during full and half stroke releases.

ID	Stroke Start	
	Travel Time	Time (s)
HS9300	93	0.93
HS9600	96	0.99
HS9900	99	1.00
HS10000	100	1.02
HS10200	102	1.04
HS10500	105	1.08
HS11100	111	1.16
HS11400	114	1.19
HS11700	117	1.23
HS13800	138	1.49
HS14000	140	1.52
HS14200	142	1.54
HS16300	163	1.81
HS16500	165	1.83
HS16700	167	1.86

Table 9.5: List of carried elastic releases.

## Results and Discussion

Figure 9.21a shows the number of converged permutations as function of the number of releases included in the mean, with a criteria of 5% using equation 9.10. The statistics

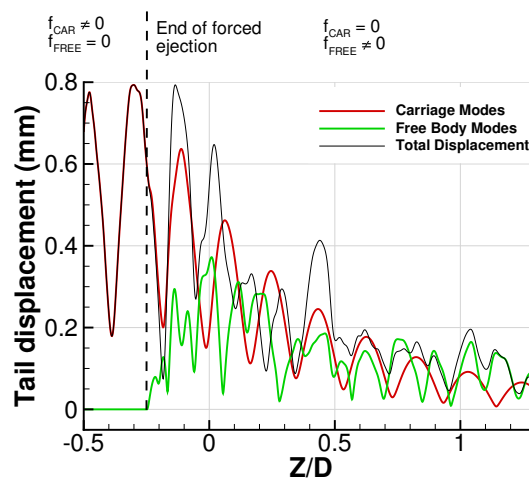


Figure 9.20: Tail displacement due to the carriage, and the free flight structural modes during store release HS10000.

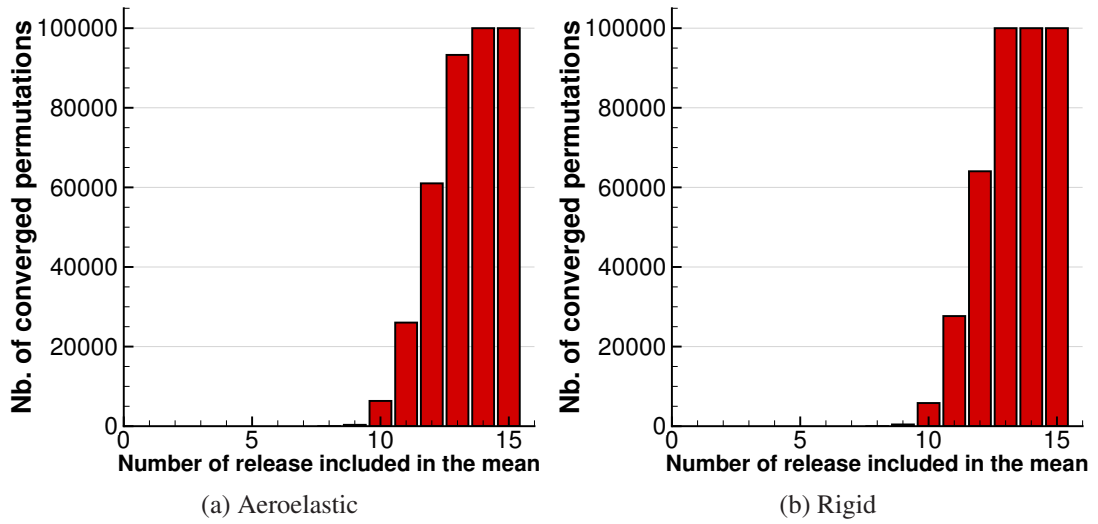


Figure 9.21: Converged release permutations number in function of the number of releases.

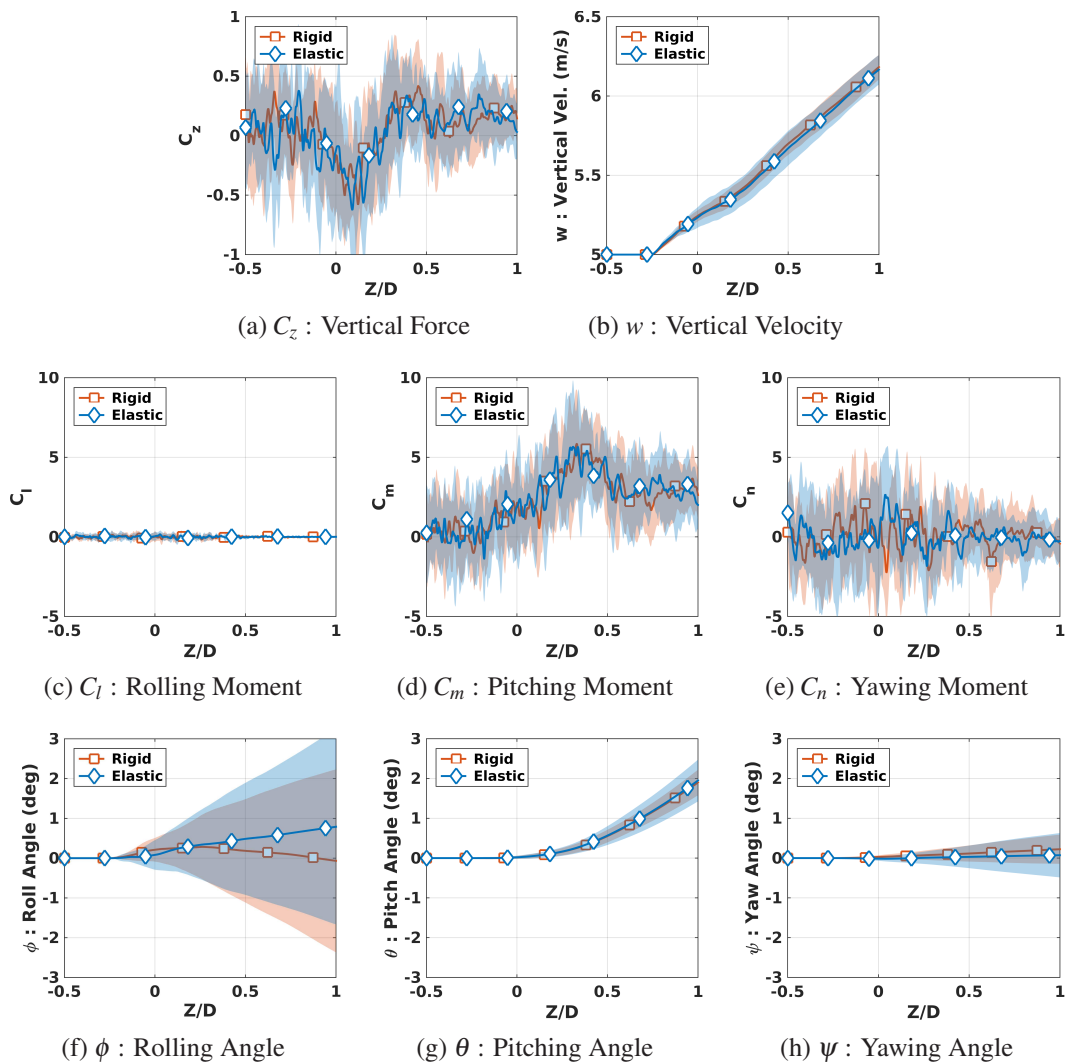


Figure 9.22: Average and standard deviation of store trajectory during release.

always converge after 13 releases. Consequently, this average is seen as converged for this case, and the results can now be used to compute a mean flow. Aeroelastic results are compared to the 15 rigid store cases with half-stroke from section 9.4.1. Figure 9.21b shows the convergence for the rigid half-stroke cases, and there is small differences with the elastic cases. Here the number of releases to converge is smaller than for section 9.4.1, as full-stroke releases are subject to a slightly smaller vertical velocity due to the shorter time for gravity to accelerate the store.

Figure 9.22 shows the store trajectory for elastic and rigid releases. The average over all releases is shown as solid lines, and the standard deviation as shaded area. Overall, the averaged loads are unchanged by the store aeroelasticity because the deformations are not large enough to lead to any significant flow modification. The variability in roll is evident in the results of figure 9.22, and the difference between rigid and elastic cases are more pronounced. To reduce this difference, further releases are required, as this component is driven by small turbulent structures. The amplitude of the roll angle variability is, however, of similar size.

The store deformations are shown in figure 9.23 for the body and the trailing edge tip of the fins during the aeroelastic release. The average over all releases is shown as solid lines, and the standard deviation as shaded area. As the store clears the cavity, its tail leaves the influence of the cavity flow fluctuations at the cavity aft, and its structural deformations become smaller. On the other hand, the store nose reaches a peak of deformation when it interacts with the shear layer at  $Z/D=0.2$ . Further away from the cavity, the store reaches the free-stream, and the deformations are getting closer to zero.

The fins behave differently during the release. Fins 1 and 2 are subject to larger deformations when the store is inside the cavity, as they are directly exposed to the turbulent shear layer. Moving outside the cavity, the fins rapidly leave the high pressure fluctuations, and their deformations become smaller. Fins 3 and 4 present a peak of deformation when the store is around  $Z/D=0.4$ . At this point, the fins are in contact with the turbulent shear layer which is more active than for the fully established cavity flow, due to the interaction between the store nose and the shear layer as shown in section 9.4.2.

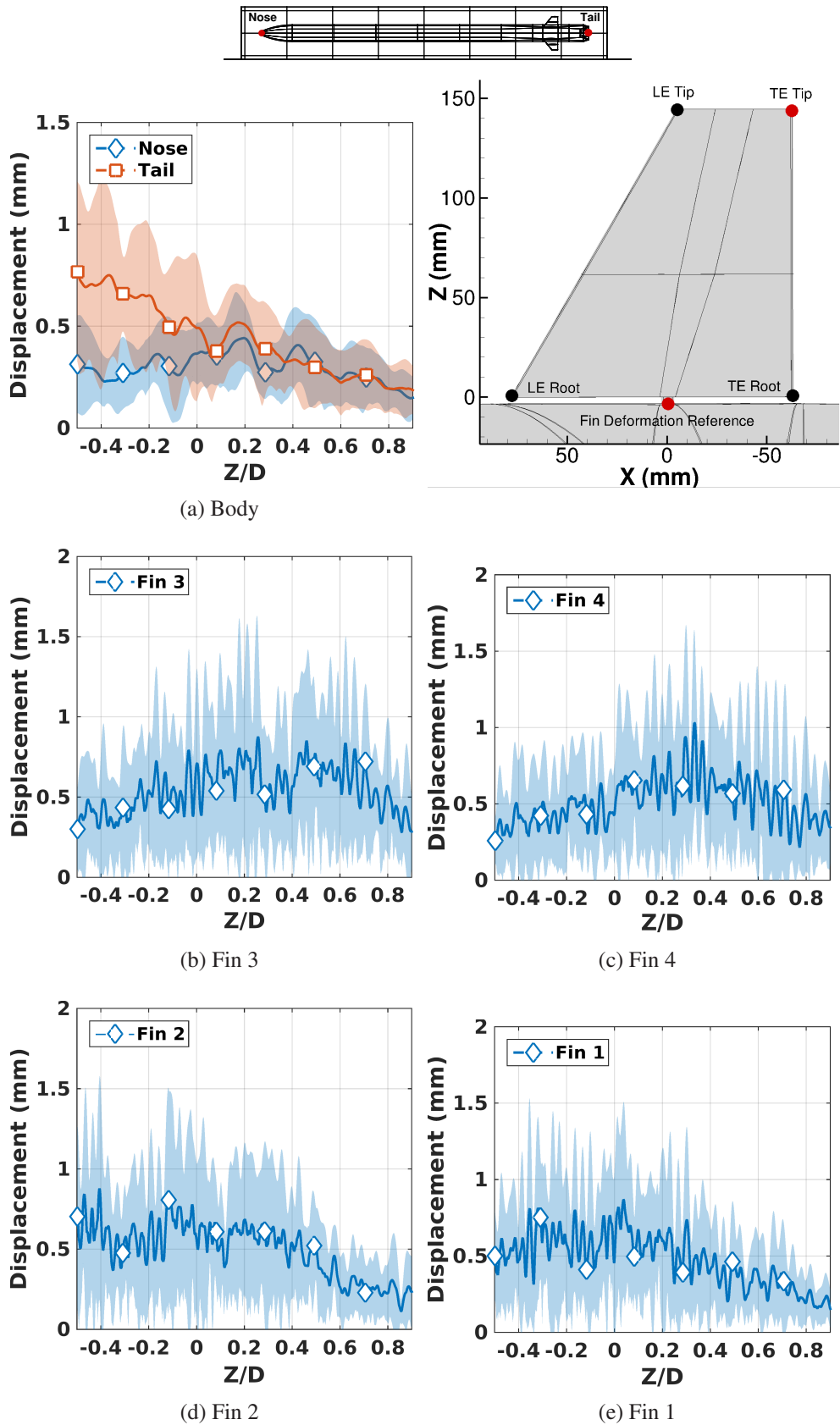


Figure 9.23: Average and standard deviation of store deformations during release. Fins deformations are shown at the tip of the fin trailing edge.

### 9.4.5 Aeroelastic Store Releases with Static Doors

This section describes the most realistic release configuration, where the store is aeroelastic, and the doors are present and open at 110 degrees. The aeroelastic model including carriage, and free flight modes is the same as used in section 9.4.4, and only half stroke releases are simulated. Fifteen releases were computed at different stroke start times, and are summarised table 9.6.

ID	Stroke Start	
	Travel Time	Time (s)
DHS3180	32	0.16
DHS3300	33	0.18
DHS3730	37	0.23
DHS3900	39	0.25
DHS4100	41	0.28
DHS4300	43	0.30
DHS4520	45	0.33
DHS4700	47	0.35
DHS4900	49	0.38
DHS5100	51	0.40
DHS5930	59	0.51
DHS6100	61	0.53
DHS6300	63	0.55
DHS6500	65	0.58
DHS6700	67	0.60

Table 9.6: List of carried elastic releases with doors.

Figure 9.24 shows the number of converged permutations as a function of the number of releases included in the mean, with a criterion of 5% using equation 9.10. This is the same criterion as for the case of releases with aeroelasticity, and no doors. The statistics always converge after 13 releases. Consequently, this average is seen as converged for this case, and the results can now be used to compute a mean flow and make comparisons between doors and no door cases.

Figure 9.25 shows the trajectory of the aeroelastic store for the doors, and no doors cases, averaged from all available releases. Also, the standard deviation is shown

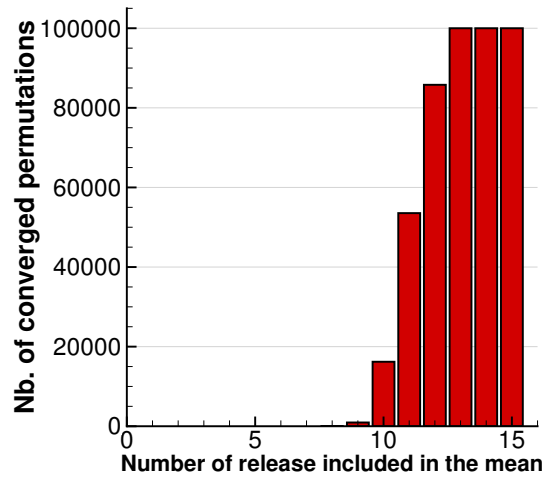


Figure 9.24: Number of converged release permutations in function of the number of releases in the statistics. (5% criterium, store aeroelasticity and doors included)

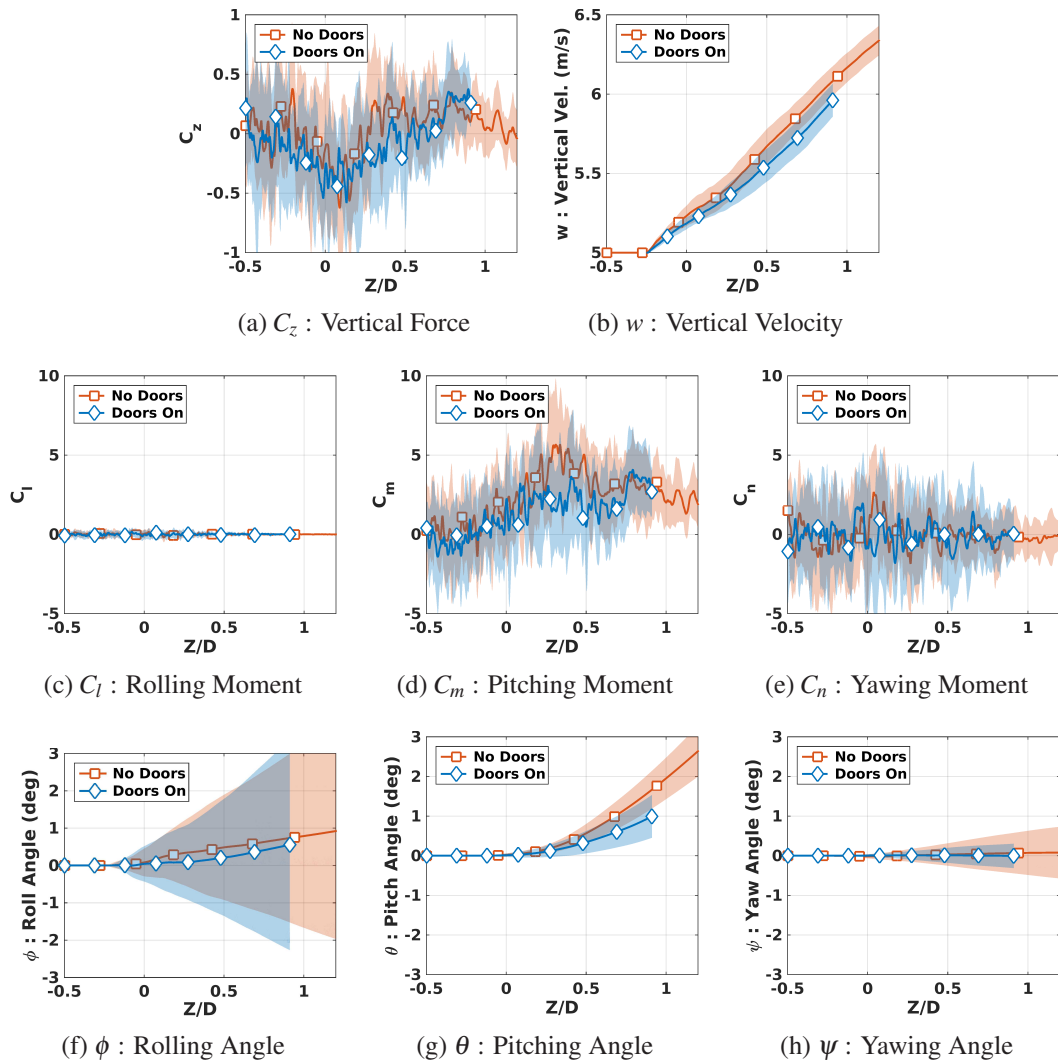


Figure 9.25: Average and standard deviation of store trajectory during aeroelastic releases with and without doors.

as shaded area. The vertical velocity, and the pitch angle are slightly smaller with the doors, while all other components are very similar.

Figure 9.26 shows the the  $C_p$  at the mid-span of the cavity averaged from all available releases without and with doors (respectively left and right columns). The addition of the doors leads to visible changes to the pressure field. Overall, the pressure at the front of the cavity decreases adding the doors. As a consequence, the vertical pressure gradient inside the cavity gets stronger (Figures 9.26e and 9.26f), and increases the vertical force pushing the store inside the cavity, when the store is close to the shear layer (Figure 9.25a). The pitch angle is smaller with the doors, because of a weaker pressure rise at the aft wall, when the store interacts with the shear layer at the peak of pitching moment. This is visible on figures 9.26i to 9.26l with a smaller high pressure zone with the doors on.

Figure 9.27 shows the deformation of the store on the body, and the fins at the tip of their tailing edge. The average computed using all the available releases is shown in solid lines, and the standard deviation is shown as shaded area. Differences between the two cases appear when the store travels outside of the cavity. The nose and the tail are subject to twice larger deformation for  $Z/D > 0.4$ , and the standard deviation is also wider adding the doors. The fins are also subject to larger vibrations outside the cavity with doors, both in amplitude and mean value, mainly visible for fin 4. This is due to the doors that channel the pressure fluctuations outside the cavity, as can be seen in figure 9.28, that shows the OASPL at  $X/L=0.85$ , for different store positions. On the other hand, the doors pacify the noise field on the side of the cavity. Further realism could be achieved adding aeroelasticity to the doors, which vibrations may change the noise directivity.

This study shows that important features like doors should be modelled, to correctly capture the complete store interaction with the cavity flow. Even if the doors held at 110 degrees lead to small changes in terms of pressure, and noise field at the mid-span of the cavity, it was enough to make visible changes to the pitch angle and vertical velocity.

HMB can simulate the complete weapon bay operation in a single computation. The doors opening with aeroelastic store (Simulation Medium & Store of table 8.1), and the aeroelastic store release DHS5930 (Table 9.6) were included in the same computation. The stroke was activated as soon as the doors reached the fully open position. Figure 9.29 shows  $C_p$  field over the surfaces during the complete operation.

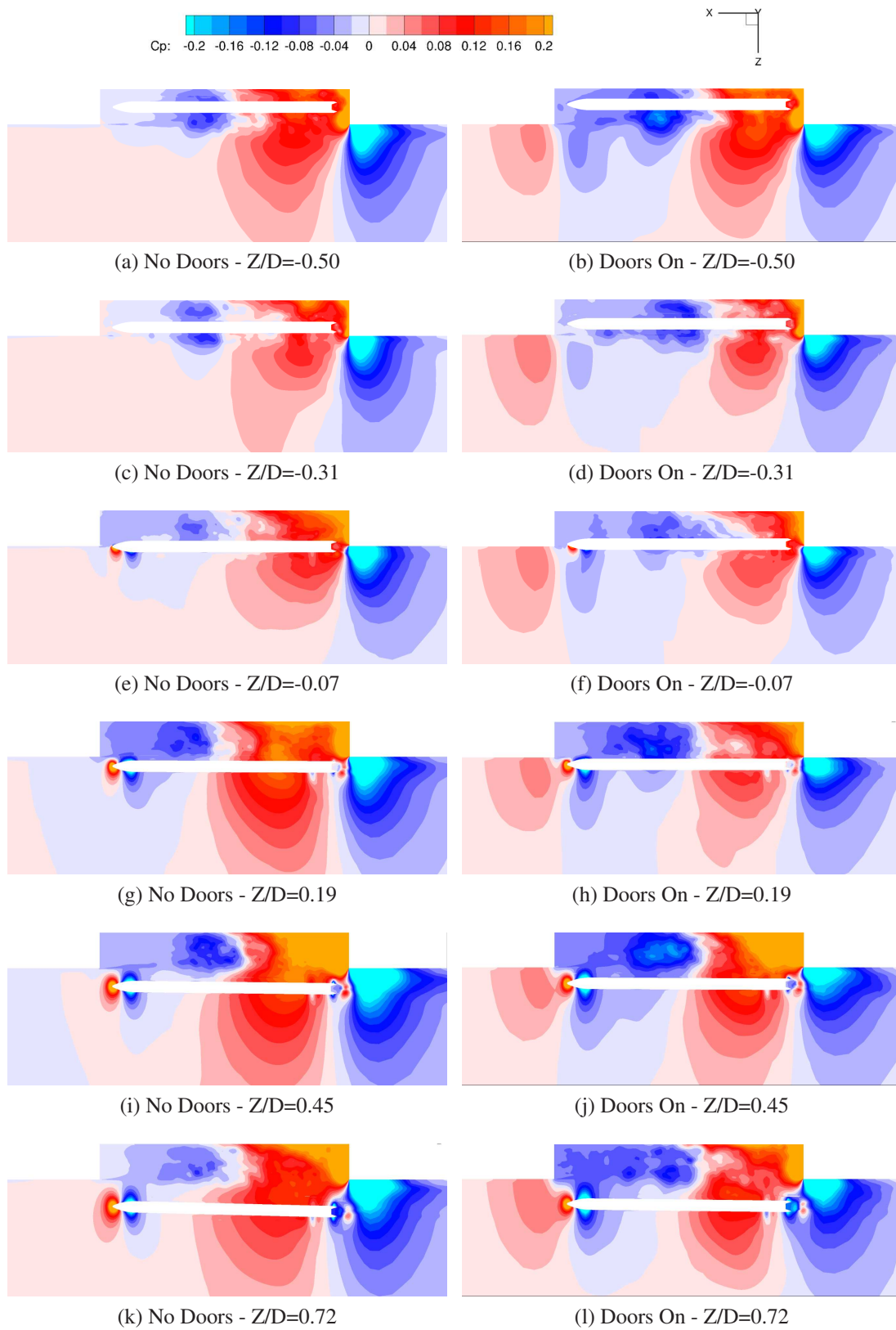


Figure 9.26:  $C_p$  field at the mid-span of the cavity during releases with and without doors averaged from all available releases.

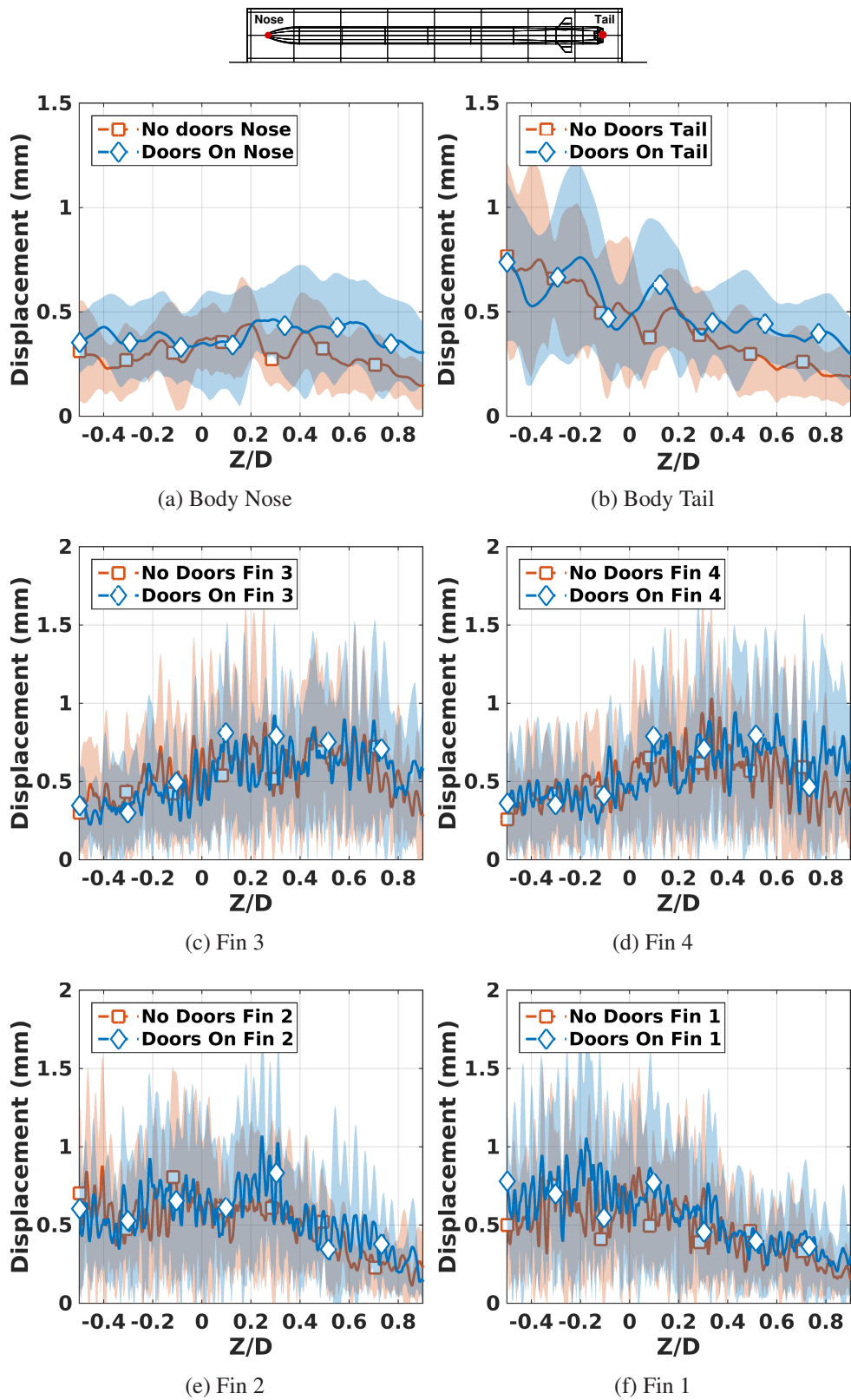


Figure 9.27: Average and standard deviation of store deformations during release with and without doors. Fins deformations are shown at the tip of the fin trailing edge.

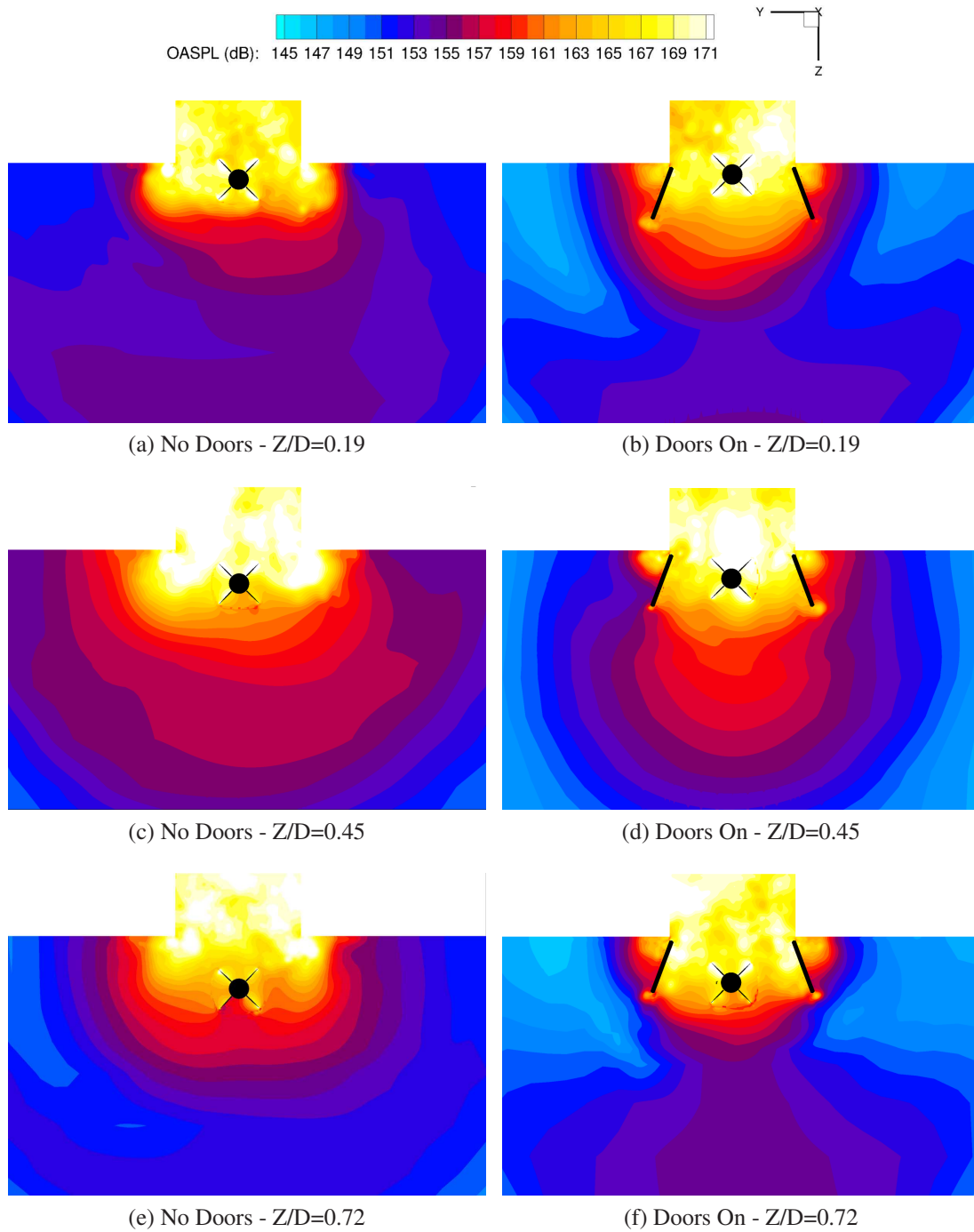


Figure 9.28: OASPL field at  $X/L=0.85$  during releases with and without doors averaged using all available releases.

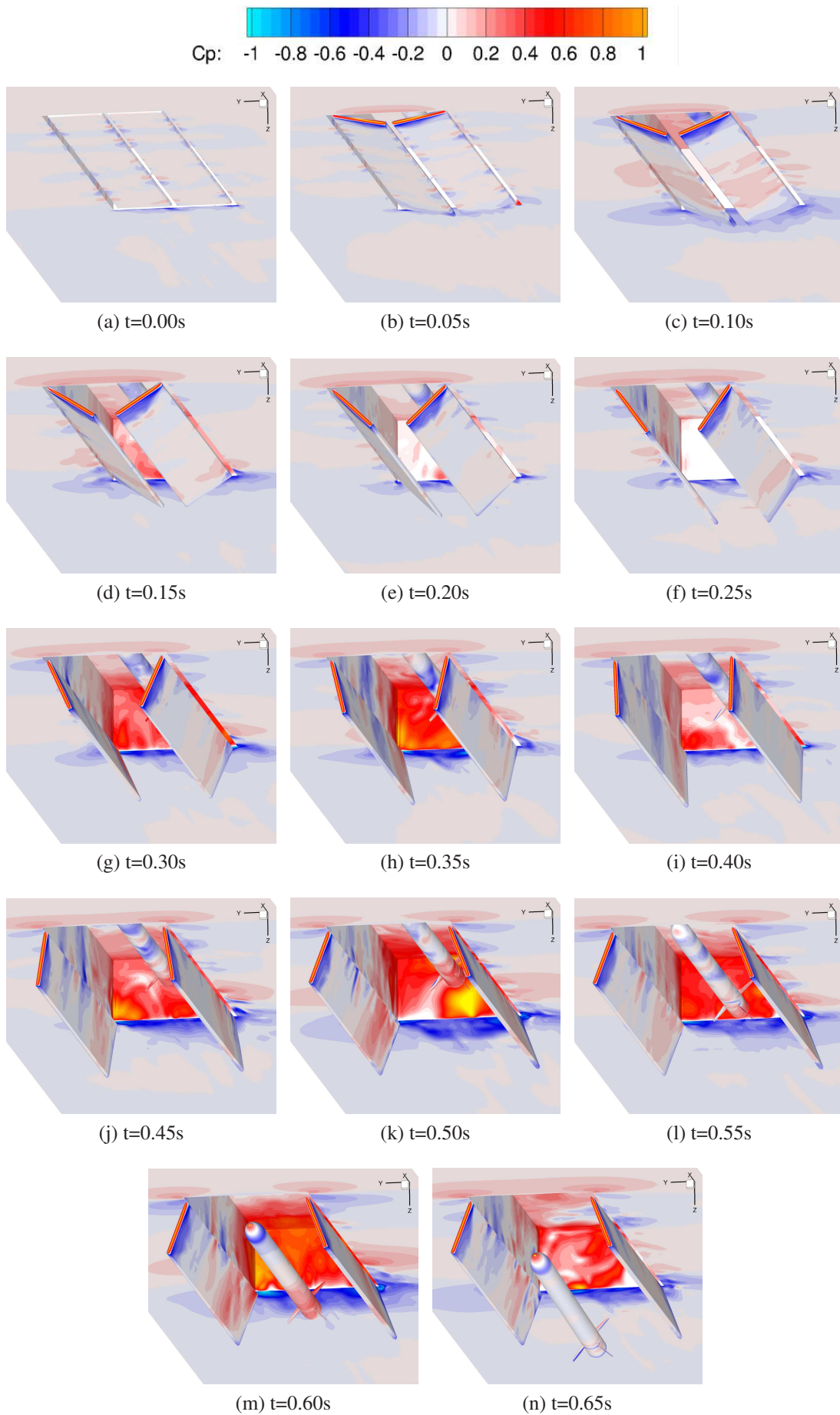


Figure 9.29: Snapshots of the weapon bay operation computed using HMB.  $C_p$  field over the surfaces.

### 9.4.6 Influence of the Store Properties on the Release Trajectory

The employed store is relatively heavy, and the stroke velocity is high, leading to low translational variability. To be closer to a configuration where the store do not properly clear the cavity, releases with modified properties are also simulated. Table 9.7 summarises the cases with different stroke velocities, store weight, CG position, and inertia. Each configuration is computed once, and compared to the baseline configuration without doors, and without aeroelasticity, HS2600.

ID	Stroke		Store		
	Length (m)	Velocity (m/s)	Mass (kg)	CG Pos (% $L_s$ )	Inertia
Baseline C0	D/4	5.0	$m_s$	50	$I_x, I_y, I_z$
HS2600 C1	D/4	2.5	$m_s$	50	$I_x, I_y, I_z$
HS2600 C2	D/4	5.0	$m_s$	50	$I_x, \frac{2I_y}{3}, \frac{2I_z}{3}$
HS2600 C3	D/4	5.0	$m_s$	40	$I_x, I_y, I_z$
HS2600 C4	D/4	1.0	$m_s$	40	$I_x, I_y, I_z$
HS2600 C5	D/3	1.0	$\frac{m_s}{3}$	40	$I_x, I_y, I_z$

Table 9.7: List of computations carried out to study the effect of store parameter on the trajectory. Parameters in red are changed compared to the baseline.

Figures 9.30 and 9.31, respectively, show the trajectories in terms of translation, and rotation. In addition, figure 9.32 shows the store loads about the CG. For a better reading of the plots, the load signals are averaged in 15 windows distributed between the beginning of the stroke and the last timestep of each simulation.

The release C1 has a reduced stroke velocity to 2.5m/s. This increases the store residence time inside the cavity, and its exposure to the unsteady cavity flow. Nevertheless, the store displacements remain small in the stream-wise and span-wise directions due to the large store mass (Figures 9.30b and 9.30d). Also, the vertical displacement (Figure 9.30f) remains driven by gravity, and the store clears the cavity. The store rotations were also small, and of the order of few degrees. Nevertheless, the pitch and yaw angles increased by about a degree (Figures 9.31d and 9.31f) with respect to the baseline store.

Release C2 has reduced pitching and yawing inertias. Overall, this configuration was similar to the baseline, and the store cleared the cavity.

Release C3 had the CG placed at 40% of the store length. The translation is

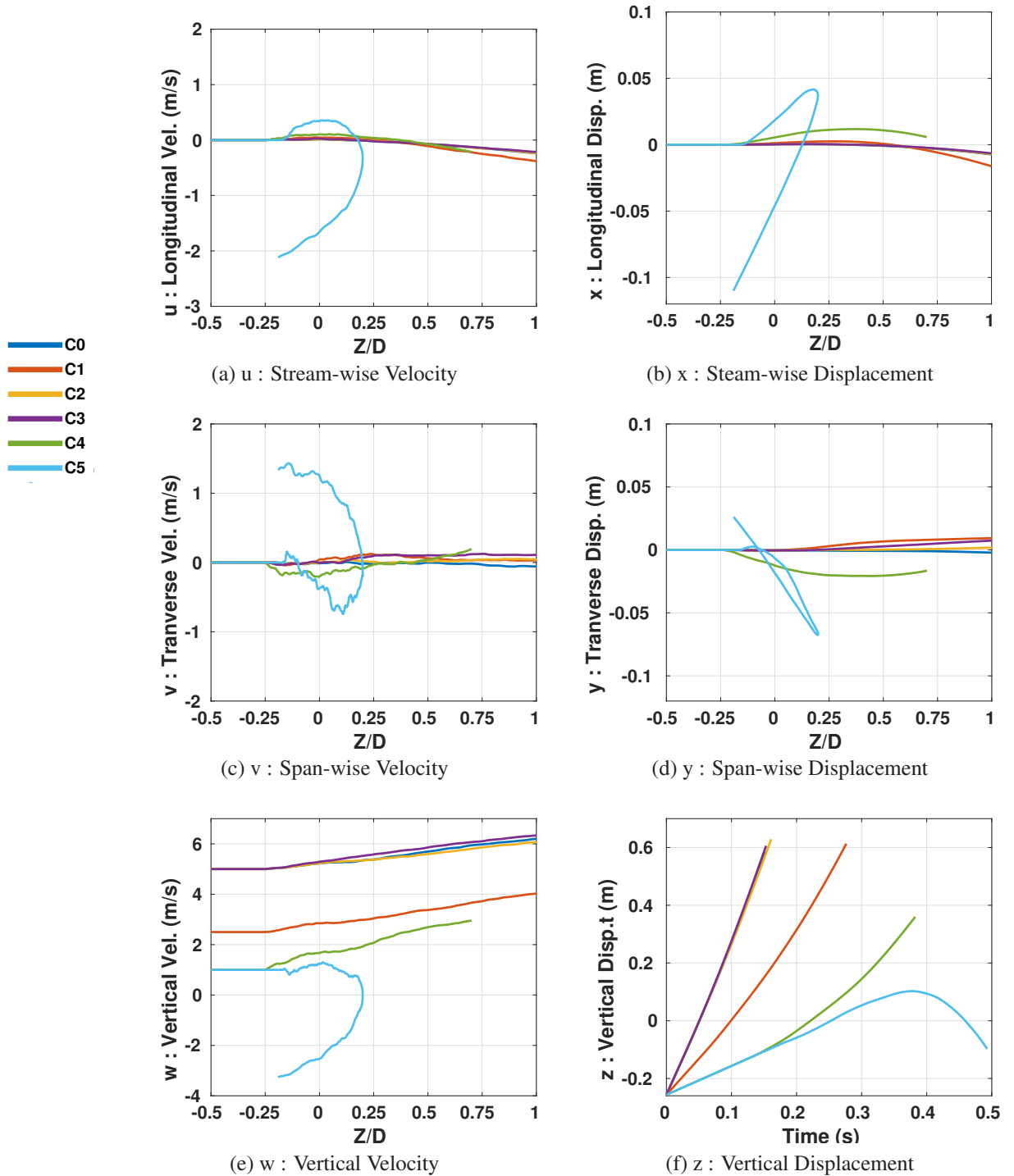


Figure 9.30: Store displacements for different store configurations.

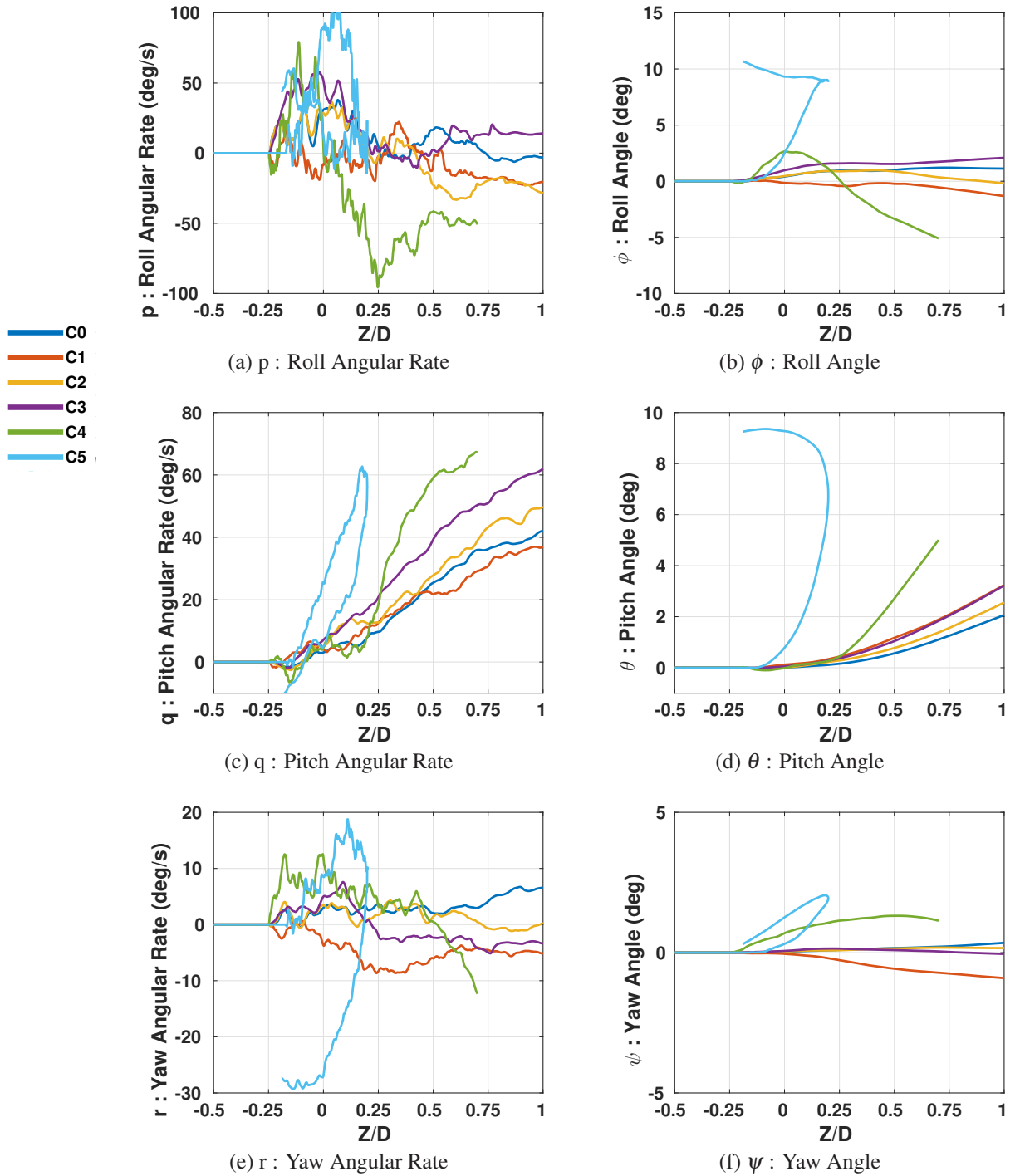


Figure 9.31: Store attitude for different store configurations.

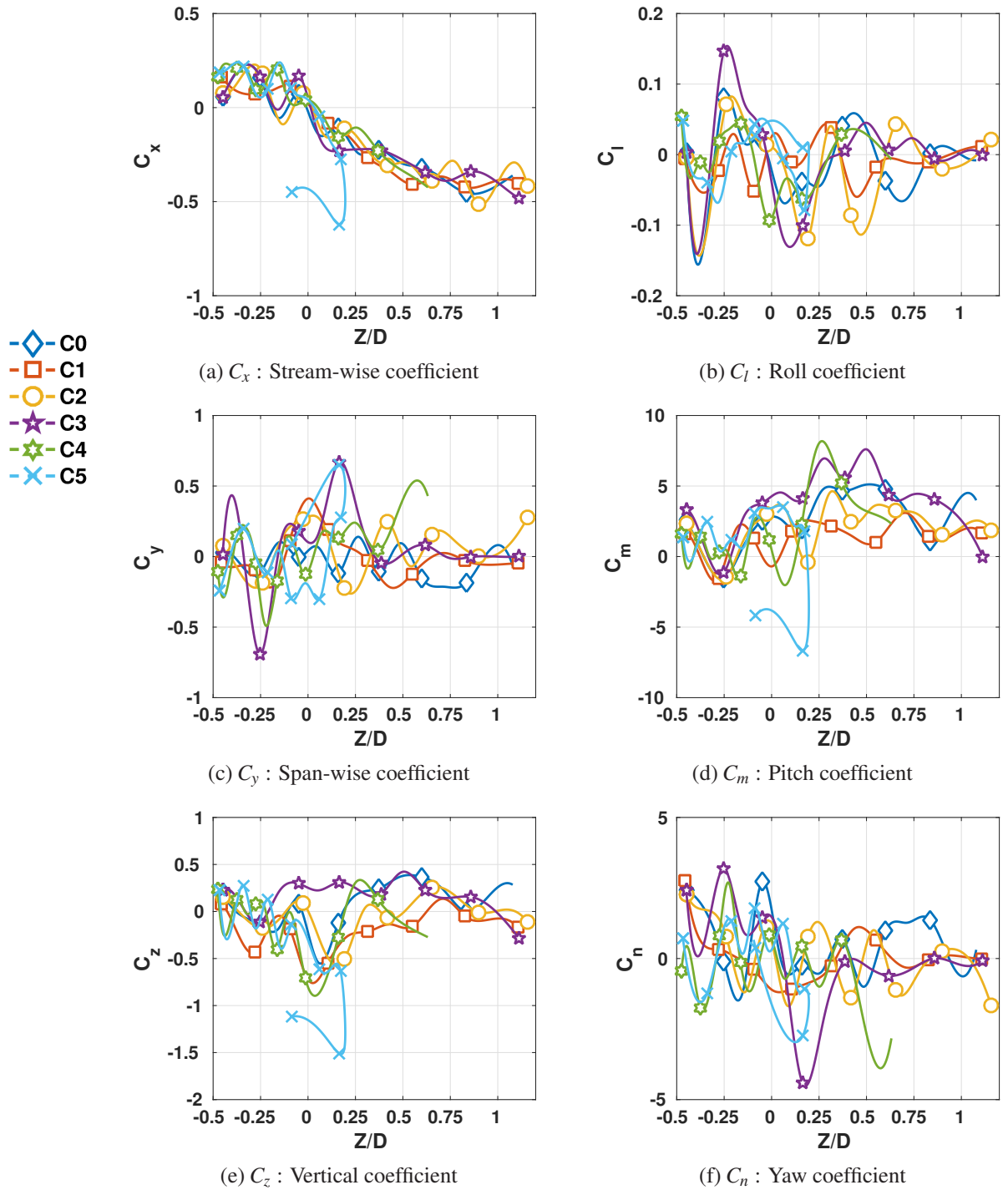


Figure 9.32: Pressure coefficients on the store for different store configurations.

similar to the baseline. However, the pitch angle is larger (Figure 9.31d), reaching values close to configuration C1. This is due to the CG moved towards the front. This increases the pitching moment (Figure 9.32d) caused by large vertical forces on the tail, as shown in section 9.4.2. This store also clears the cavity.

Release C4 reduced the stroke velocity of C3 to 1m/s. This may occur if there is a failure of the ejector release unit (ERU). This configuration shows large differences compared to the baseline. As for C1, the store remains longer in the cavity, and moves upstream (Figure 9.30b) due to the stream-wise pressure gradient inside the cavity (Figure 9.32a). With the store reaching the free-stream, the stream-wise velocity changes sign, and the store moves towards the cavity aft wall. The span-wise displacement is also larger (Figure 9.30d), reaching 2cm outside the cavity. However, the store clears the cavity and the trajectory remains driven by gravity. At  $Z/D=0.7$ , the pitch angle is five times larger than the baseline (Figure 9.31d), because of the longer exposure to the peak of pitching moment at about  $Z/D=0.30$  (Figure 9.32d).

A large pitching angle could lead to an unsafe store release. Figure 9.33 shows the loads on the isolated store at a free-stream at Mach of 0.85. The computations were performed using unsteady SAS, and the results were averaged in time. Increasing the pitch angle, the vertical force increases, pushing the store upward. Reaching a pitching angle of 6 degrees, the force is strong enough to lift the store of mass  $m_s$ . Releases C1 to C4, did not reached this point so they cleared the cavity. The accuracy of full scale store simulation at high attitude is important to obtain reliable results for unusual store trajectories. The appendix A shows that stores with more features, as wings, and strakes is a challenge for turbulence modelling, and their integration using CFD to a weapon bay, may be more difficult than the present case.

Release C5, had a store mass  $m_s/3$ , and the stroke is released from a quarter of a cavity depth, to a third. This stroke length is chosen to restrict the exposure of the store to the positive vertical force, that helps the store clearance, when the store is inside the cavity (Figure 9.32e). The release shows dramatic differences with the baseline as shown figures 9.34 and 9.35 as functions of time. The store translation is larger, reaching values above 8cm at  $t=0.38s$  both in stream-wise and span-wise directions (Figure 9.34c). This is due to the reduced mass, that makes the store more affected by the flow. This may be unsafe, as the spacing between stores and cavity walls can be a few centimeters only for smaller bays. The angles are also very large, reaching 10 degrees in roll and pitch, and 2 degrees in yaw (Figure 9.34d). The large pitch angle

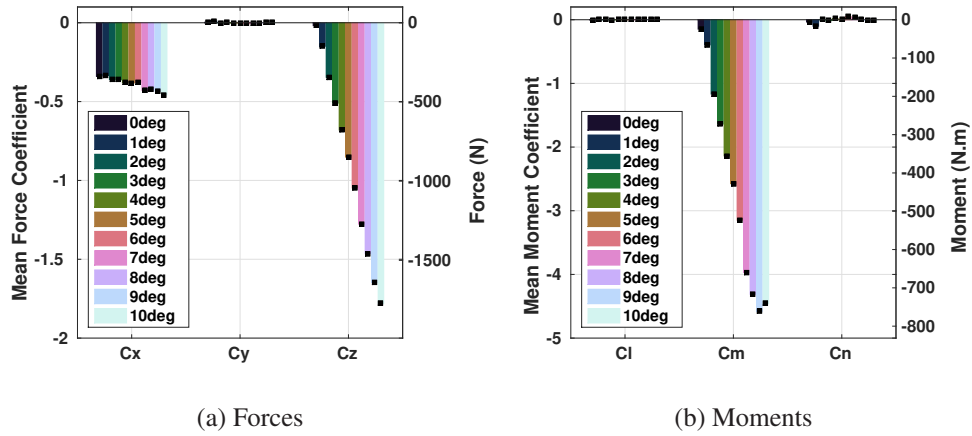


Figure 9.33: Loads on the isolated store in free-stream at Mach 0.85.

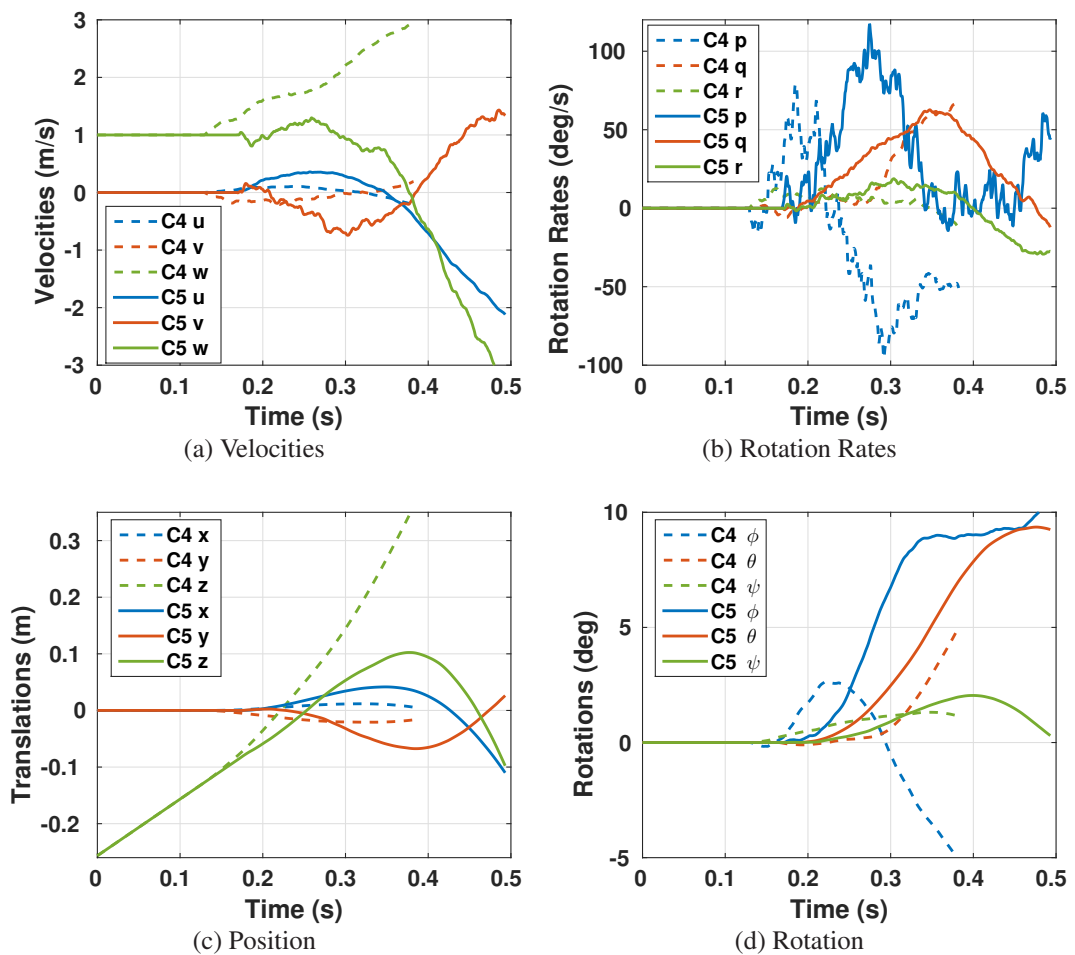
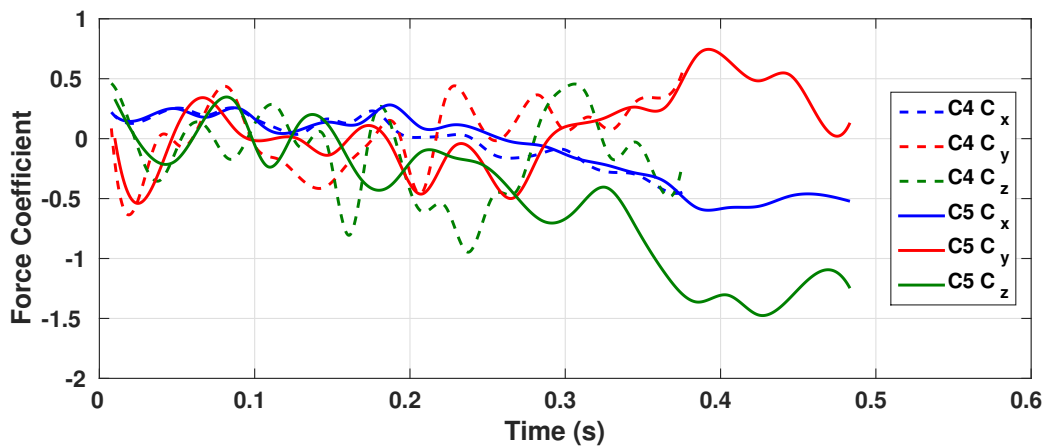


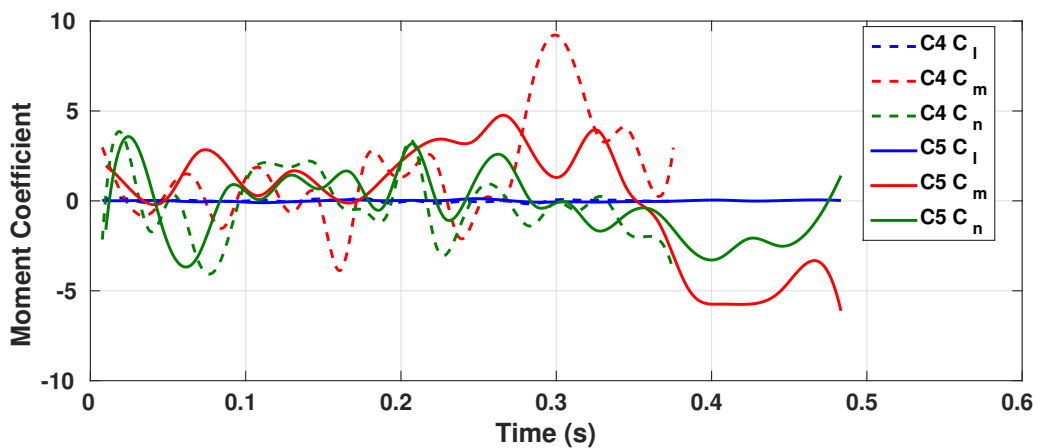
Figure 9.34: Store trajectory during releases C4 and C5 in function of time.

of release C5 compared to C4, is due to the stronger, and positive pitching moment of C5 up to  $t=0.35$  (Figure 9.35b). Because of the large pitch angle, the vertical force lifts the store (Figure 9.35a), and takes it back in the direction of the cavity from  $t=0.38$ s (Figure 9.34c). With the increasing drag force, as the store goes out from the cavity, the store also moves towards the cavity aft wall.

The Mach number at the mid-span of the cavity, and at 85% of the cavity length are shown in figures 9.36 and 9.37 for release C5. The plots also show the  $C_p$  on the store, and snapshots are shown at every 0.05s. When the store is inside the bay (Figures 9.36a to 9.36e), it shows small rotations, and its motion is close to a translation along the vertical axis. As soon as the store nose interacts with the coherent shear layer at  $t=0.25$ s (Figure 9.36f), the pitch rate shows a strong increase (Figure 9.35b). This is due to the low vertical velocity of C5, in comparison to C4, towards  $Z/D=0$  (Figure



(a) Force Coefficients



(b) Moment Coefficients

Figure 9.35: Store forces during releases C4 and C5 in function of time.

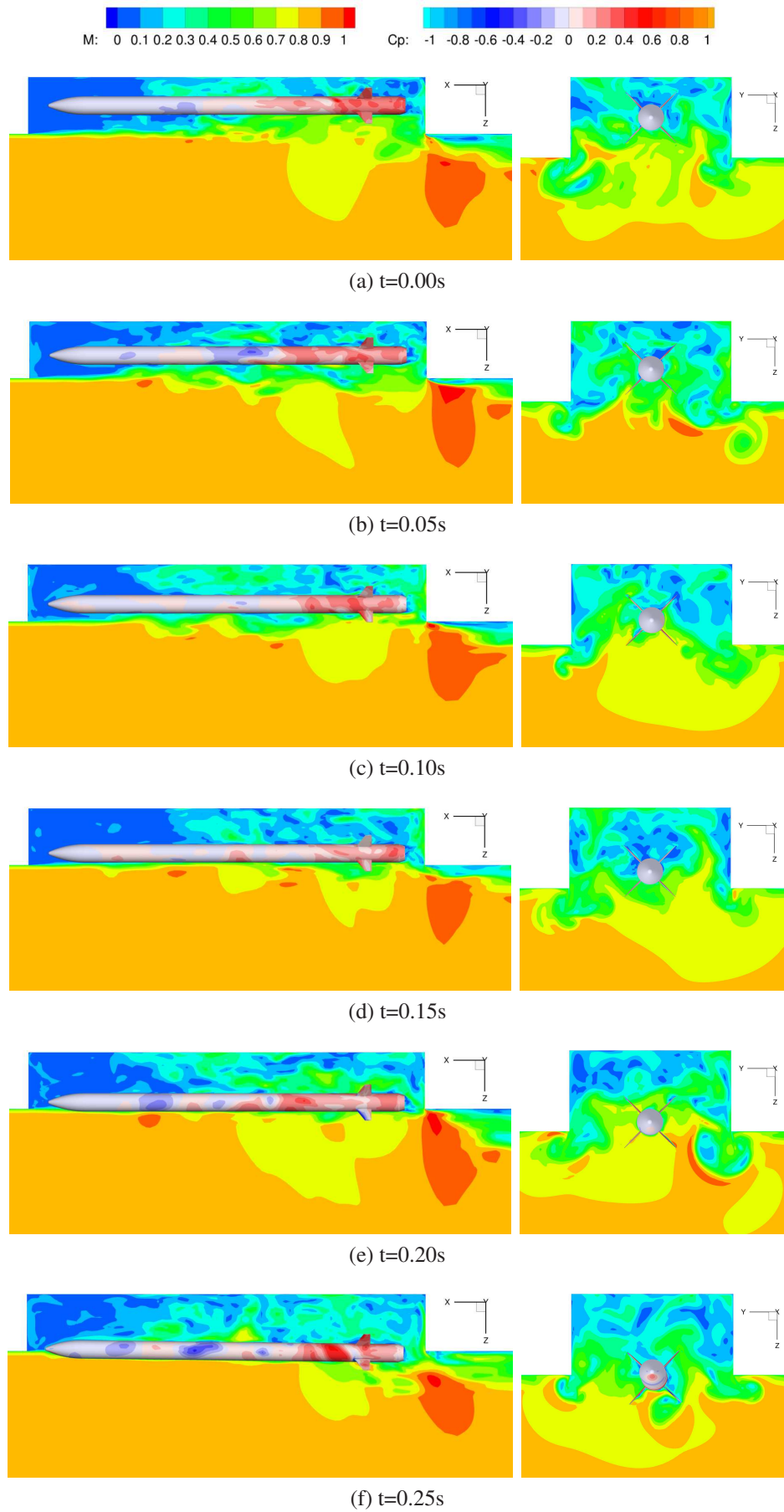
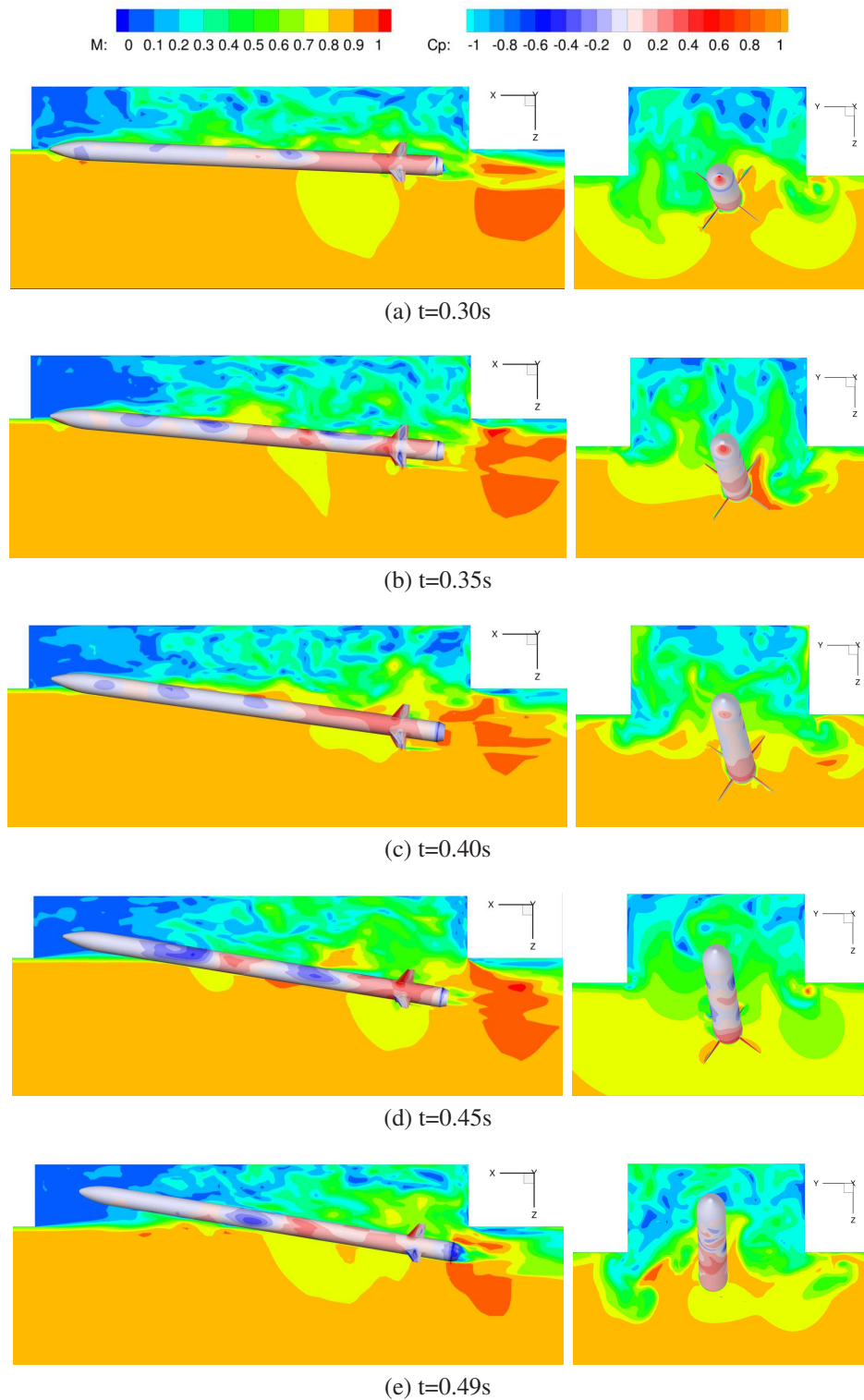


Figure 9.36: Instantaneous Mach number and  $C_p$  on the store during the release C5.

Figure 9.37: Instantaneous Mach number and  $C_p$  on the store during the release C5.

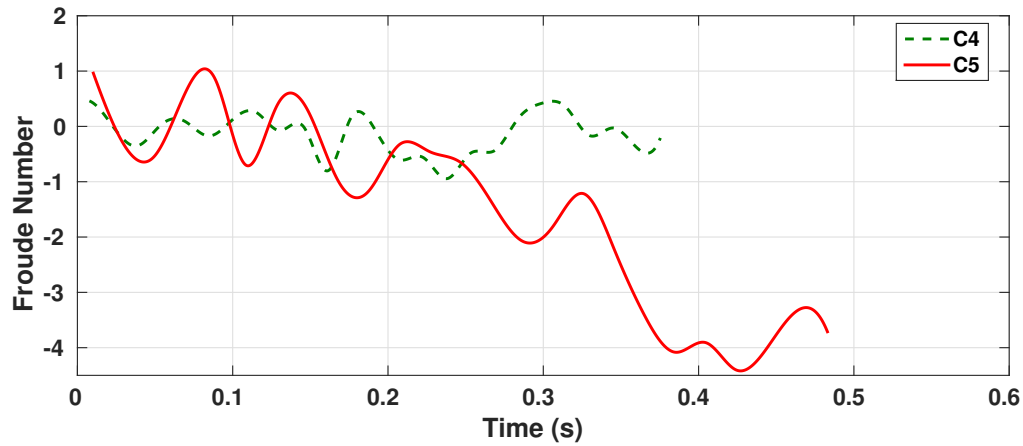


Figure 9.38: Froude number during releases C4 and C5.

9.34a), leading to a longer exposure of the nose to the shear layer. As can be seen between  $t=0.25s$  (Figure 9.36f), and  $t=0.35s$  (Figure 9.37b), the shear layer pushes the store nose back inside the cavity, while the tail continues to fall under gravity. This leads to a large pitch angle, and aerodynamics becomes stronger than gravity. This is shown with the Froude number (Figure 9.38), ratio between the aerodynamic, and the gravity forces on the vertical direction:

$$Fr = \frac{F_z}{m_s \cdot g} \quad (9.12)$$

The Froude number is three time larger during C5 than C4, due to the lighter store C5. After  $t=0.26s$ , the pitch angle is larger than 2 degrees, and the Froude number is below -1, showing that the store is pushed upwards.

The simulation shows that the prediction of unusual store release can be made with HMB3, but only if the CFD is strongly coupled with 6DoF, to fully capture the interaction between the cavity flow and the store.

## 9.5 Chapter Summary

Scale-Adaptive Simulations of stores released from weapon bays show that it is possible to numerically estimate store trajectory variability. A statistical metric was proposed to identify the minimum number of simulations necessary for capturing the mean and standard deviation of the trajectories. For the store at hand, 17 trajectories were necessary mainly due to the strong variability in roll associated with the low roll inertia. Using the averaged flow data, the trajectory phases were identified and the role

---

of the pressure field inside the cavity was clarified. Then, filtering of the simulation results, revealed that only the roll angle was driven by the finest fluctuations in the flowfield while the vertical displacement of the store was driven by the ejection velocity and gravity. This is reinforced by the relatively low pitch angle of the store during the release, leading to a reduced effect of the aerodynamic lift generated. This was the first time that aeroelastic effects were quantified for releases. During store release, the store trajectory variability remained using an aeroelastic store, but the aeroelasticity was secondary for the case at hand, with cavity flow effects dominating the release. A parametric study shown that CFD captures the physics that could lead to unusual store releases, and that the interaction between the shear layer and the store is critical for light stores. The present results suggest that the proposed method is efficient and can be used for initial investigations of store clearance before flight testing.

# Chapter 10

## Conclusions

This thesis presented methods to model cavity flows. Also, HMB3 was shown to be a tool able to compute the complete weapon bay operation, thanks to the developments carried out during this thesis. The simulations of weapon bay door opening, store release, and store aeroelasticity, lead to the conclusions, and future work of the following sections.

### 10.1 Conclusions from Current Work

The flow present in weapon bays is very complex, and its simulation requires accurate predictions of a large range of time scales. The flow is non periodic, and never repeats in the same way, making it difficult to measure, and simulate. SAS turbulence simulation was in good agreement with experiments, for averaged and unsteady values. Furthermore, SAS is very efficient compared to DES, and LES, producing similar results with a timestep ten times larger. Nevertheless, SAS requires grids as fine as for DES, and LES. This makes possible the simulation of cavity flow for engineering applications, and more than 1800 cavity travel times were computed for this thesis.

Beamforming was applied using CFD simulations to provide microphone signals. This method proved capable to capture the noise field around the cavity using a limited number of probes, using the mean CFD flow-field to compute the noise propagation. This technique could be used in wind tunnels, coupling microphone array measurement, and PIV data. The method provided meaningful results using an array at appropriate position, density, shape, and size. As a result, further cavity flows physics, and more data could be obtained for CFD validation.

To further understand the mechanism driving the tonal and broadband fluctuation inside cavity flows, the cavity dynamics was modelled as a standing wave resonator, influenced by the shear layer flow. For the first time, the tonal dynamics of the cavity flow was fully represented by a model with the standing wave oscillations and their modulation. This suggests that the generation mechanism of cavity noise proposed by Rossiter is not the main mechanism driving cavity flows. In addition, the results shown that the time averaged flow-field drives the tonal frequencies, while the flow-field fluctuations drive their amplitude and feed the broadband noise.

A large number of computations were carried out for different configurations of cavity, store, and doors, with and without store aeroelasticity. The door opening evolved in three stages. First, a closed cavity flow was established, with the creation of a jet impacting the bay ceiling and producing large fluctuations inside it. After, the flow became transitional and the loads were amplified. The faster door opening, created the most unsteady flow of all cases during the opening phase. For medium and slow door opening speeds that can be encountered on real aircraft, the door opening did not lead to larger flow fluctuations and store deformation, compared to the fully established cavity flow. This phase have to be taken into account for the store/weapon bay integration, only for very fast door opening.

The simulations of store release from weapon bays have shown that it is possible to numerically estimate store trajectory variability. A statistical metric was proposed to identify the minimum number of simulations necessary for capturing the mean and standard deviation of the trajectories. For the store at hand, 17 trajectories were necessary mainly due to the strong variability in roll associated with the low roll inertia. Using the averaged flow data, the trajectory phases were identified and the role of the pressure field inside the cavity was clarified. Then, filtering of the simulation results, revealed that only the roll angle was driven by the finest fluctuations in the flowfield while the vertical displacement of the store was driven by the ejection velocity and gravity. Adding doors to the clean cavity, channelled the pressure fluctuations, increasing the store deformation outside the cavity. Also, small changes of the mean pressure field at the mid-span of the cavity, influenced the store trajectory with doors. This study shows that the interaction of the store with the cavity flow is critical for store trajectory variability, and that all weapon bay features, like the doors, have to be included in the geometry to obtain meaningful statistics. As a consequence, methods with a strong coupling between CFD, 6DoF, and aeroelasticity are preferable.

A study on the store release parameters, shown that CFD captures the physics that could lead to unusual store releases. If a store is released with a small stroke velocity, the coherent shear layer that interacts with the nose, keeps the store nose inside the cavity, while the tail continues to fall. Consequently, the pitch angle increases, and the free-stream tends to push the store inside the cavity. This interaction is critical for light stores that can be pushed upwards for a small pitch angle. The present results suggest that the proposed method is efficient, and can be used for initial investigations of store clearance before flight testing.

Aeroelastic effects were present during door opening and store release. The structural excitation showed a directional dependence due to the span-wise symmetry of the geometry. The tonal fluctuations excited the body, while the fins were influenced by the broadband fluctuations. Over the weapon bay operation, maximum store deformations were of about 2% of the store diameter. This may trigger some fatigue, mainly for stores staying in the cavity after repeated door operations. This was the first time that aeroelastic effects were quantified for releases. The store trajectory variability remained using an aeroelastic store, but the aeroelasticity was secondary for the case at hand.

## 10.2 Future Work

This thesis sets the basis of a framework including CFD, aeroelasticity, and flight mechanics for store release simulation. Nevertheless, the presented cases are limited to ideal cavities and flat plate doors. The strong influence of the weapon bay components on the release characteristics, like the doors, shows that future work must use geometries as realistic as possible. However, to build a structured mesh inside a realistic cavity can be an arduous task, and the computation of weapon bays with unstructured, hybrid, and meshless methods have to be investigated to reduce the density of points. In addition, future simulations should include the complete aircraft geometry to take into account the non uniformity of the boundary layer across the weapon bays. The relative direction of the free-stream is also important to take into account as it may change the behavior of the cavity flow, and the store trajectory characteristics. Recommendations on the aircraft attitude when releasing a store from a weapon bay could be found for safer operation. Finally, store release and aeroelastics should be computed for other subsonic and supersonic Mach numbers to

further validate the method.

The better understanding of the resonance of the cavity flow, and of store release mechanism should be used to improve, and design new weapon bay flow control solutions. With current tools, the test of any flow control solution in a fast way for cavity resonance, store aeroelasticity, and store trajectory is in reach.

A missing key for further CFD developments is the availability of experimental data. Future work must also focus on experiments of cavity flows to generate more data for CFD validation. For aeroelasticity, acceleration measurements, both on the store, and the cavity walls are required to validate the aeroelasticity method. More importantly, releases of full scale stores must be performed in free flight. This avoids scaling effects, and the loss in the flow/store interactions due to CTS techniques. Also, the releases have to be repeated, and the required number of releases should be determined using a metric as proposed in this thesis.

# Appendix A

## Flowfield Around an Isolated Store at High Pitch Angle

The pitch angle is a parameter that matters when it comes to predict unusual store releases (Section 9.4.6). For this reason, the flowfield around a store at high pitch angle is computed here. The store model, was provided by MBDA UK. Ltd. <sup>[168]</sup>. The case was computed with different turbulence models, and grids, to determine if there is mesh convergence. Also, the physics of the flowfield is described.

### A.1 Geometry and Conditions

The store was 3.45m long, with four strakes, and fins, in a cross configuration (Figure A.1). The store was assumed flying at International Standard Atmosphere (ISA) and sea level conditions at a Mach number 1.4, and Reynolds number  $Re_{L_s}$  based on the store length of 110 million. The pitch angle was 15 degrees, and there was a small roll angle of 2.5 degrees. There is no experimental data available for comparison.

### A.2 Computational Mesh

The chimera method is used to overlap a store mesh fitted over a Cartesian background mesh. Five grid densities were tested, and are summarised table A.1 for the different mesh components. Figures A.2, and A.3 show slices through the different grids, and the mesh volume. The simulations are performed for steady  $k-\omega$  -SST (Section 2.3.3), steady  $k-\omega$  -SST  $P_k$  Limiter <sup>[169]</sup>, steady EARSM <sup>[112, 170]</sup>, and for unsteady SAS

(Section 2.3.4) turbulence models. Table A.1 summarises the computed cases. The non dimensional timestep was the same for all grids, and was 0.01 using unsteady SAS. This resolution is the same used for cavities.

	Number of Grid Points			Turbulence Models			
	Total	Store	Background	$k-\omega$ -SST	$k-\omega$ -SST $P_k$ Limiter	EARSM	SAS
Coarse	18.9	14.5	4.4	X	X	-	X
Medium	32.8	28.4	4.4	X	X	X	X
Fine	55.8	43.1	12.7	X	X	X	X
Very Fine	104.5	64.0	40.4	X	X	X	X
Extra Fine	203.8	133.1	70.7	-	-	X	X

Table A.1: Grid density and simulated cases. Performed simulations are marked with X.

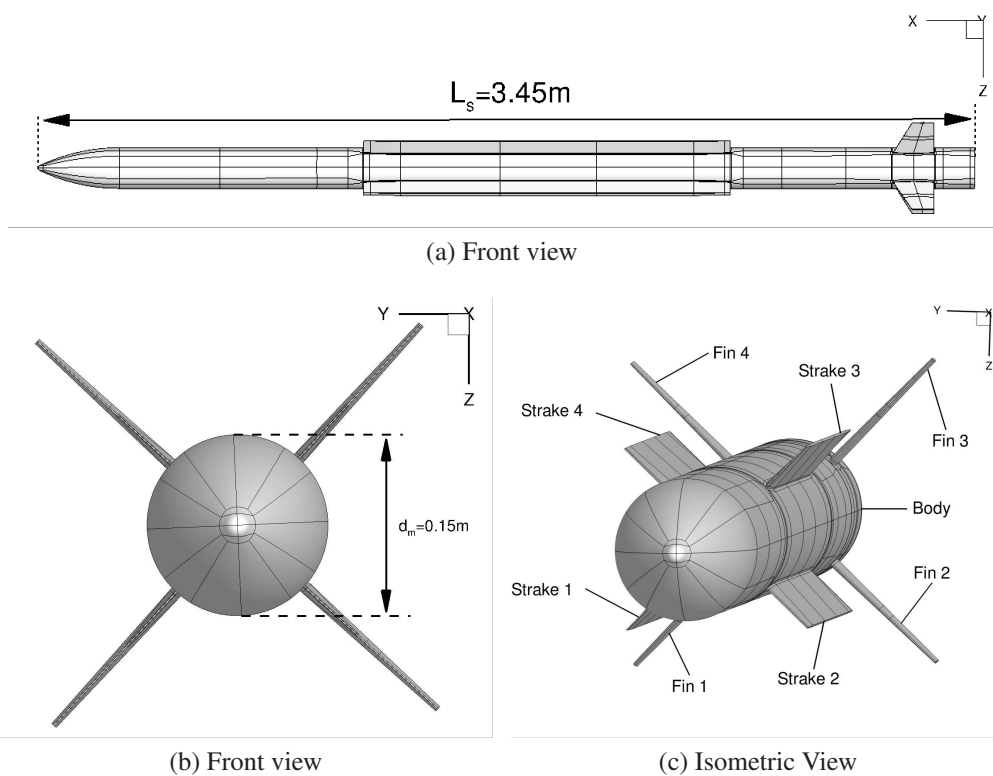


Figure A.1: Store geometry.

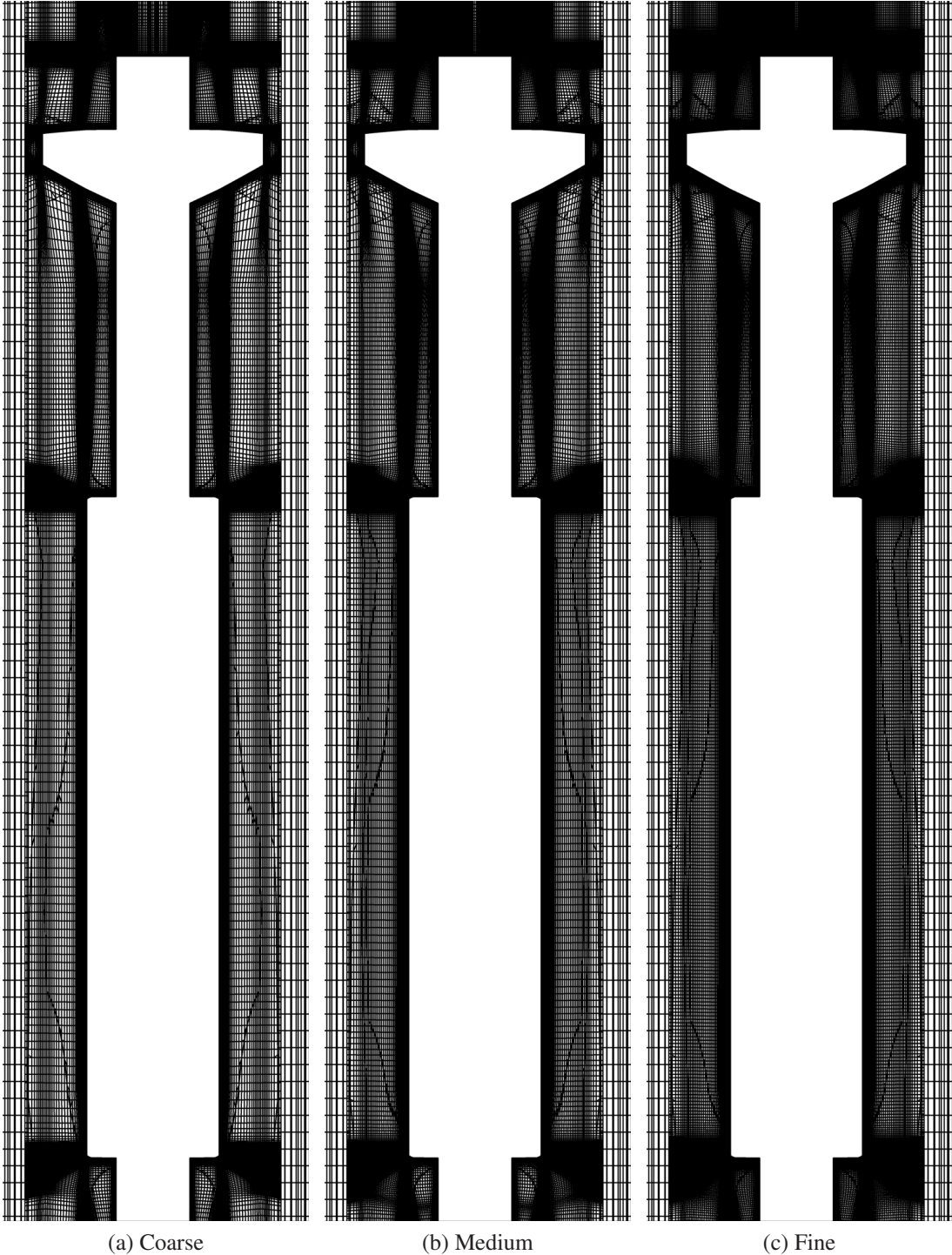


Figure A.2: Grid slice at the fins.

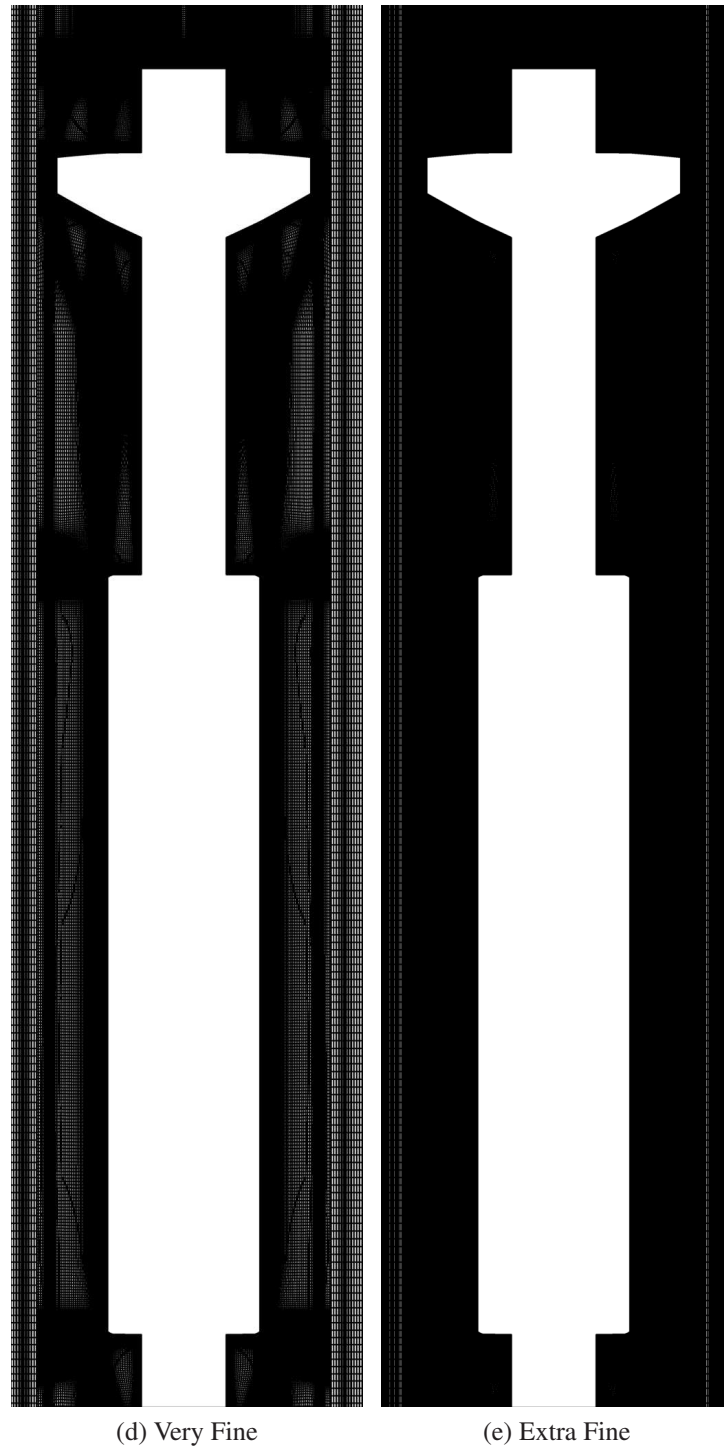
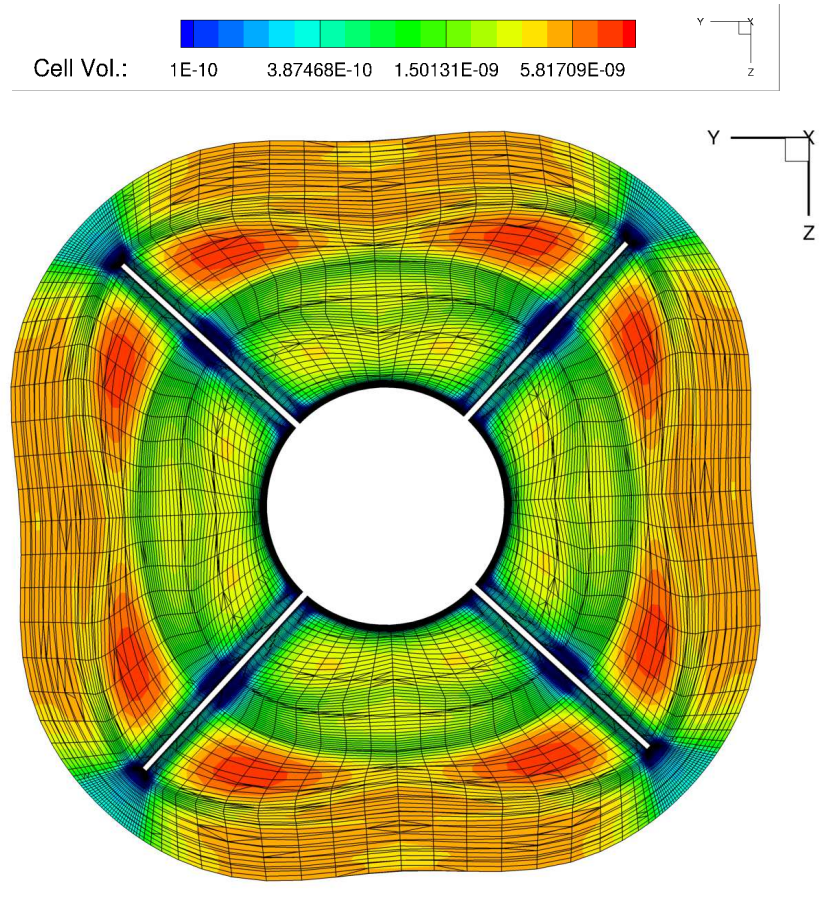
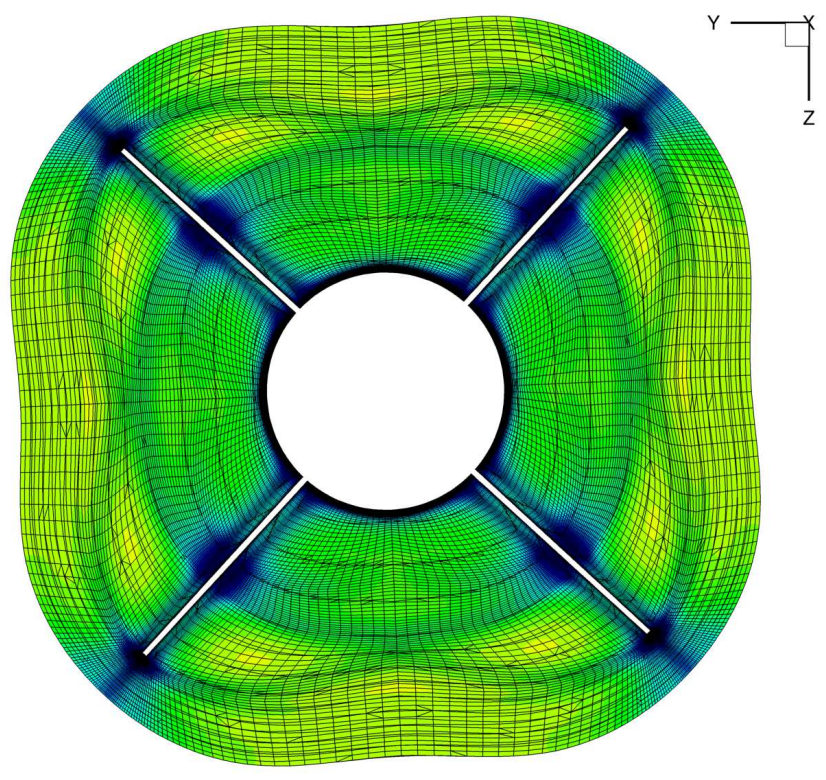


Figure A.2: Grid slice at the fins.

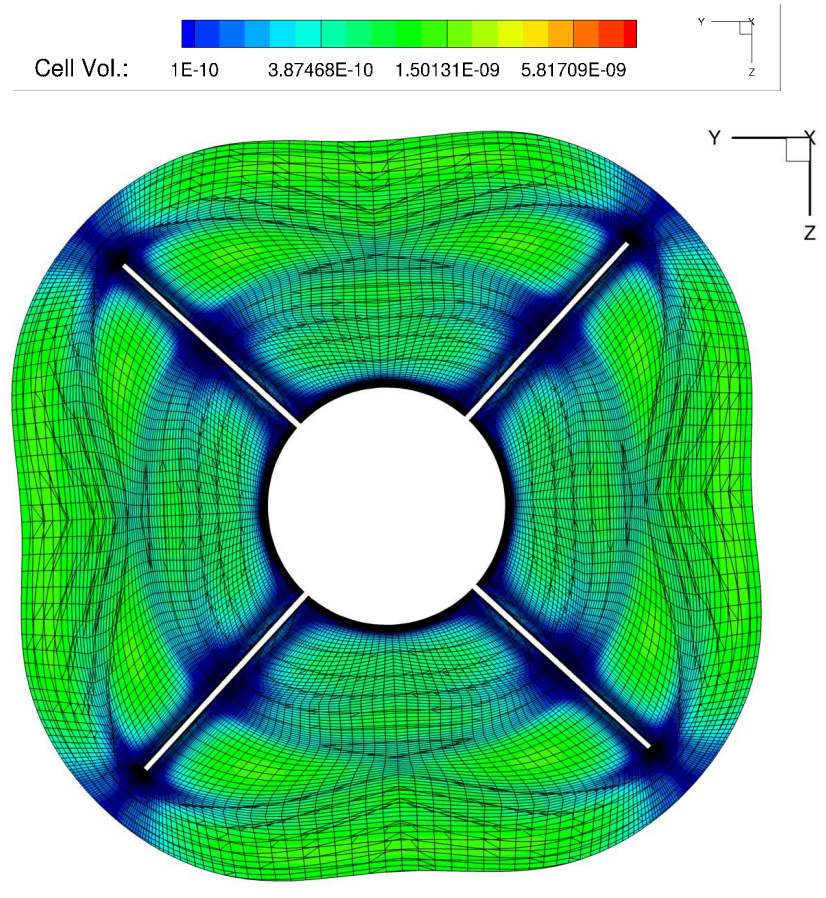


(a) Coarse

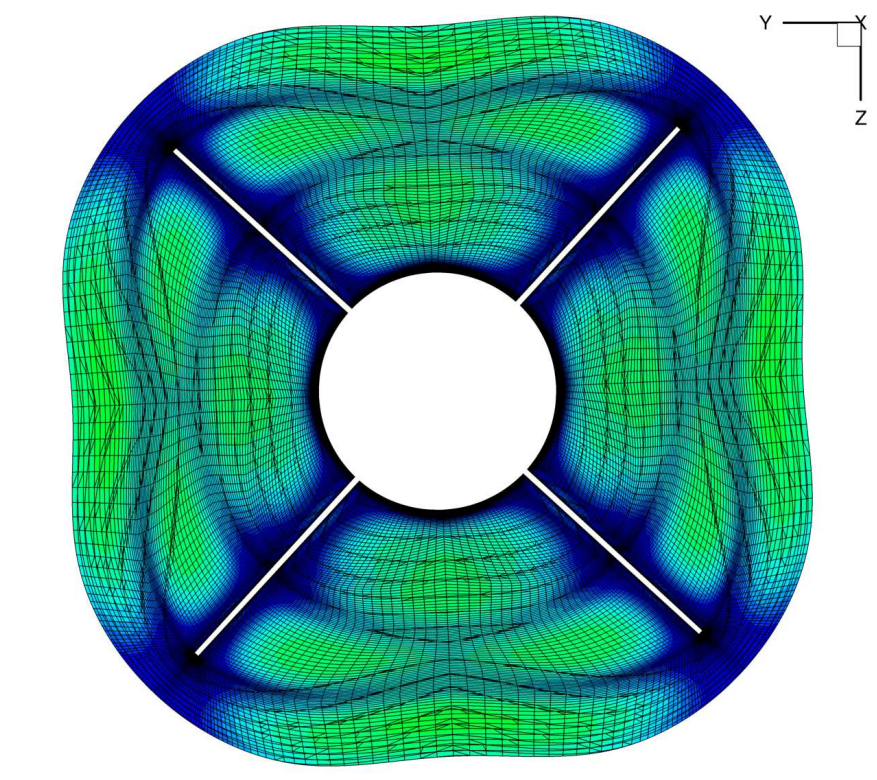


(b) Medium

Figure A.3: Grid slice at the fins.



(c) Fine



(d) Very Fine

Figure A.3: Grid slice at the fins.

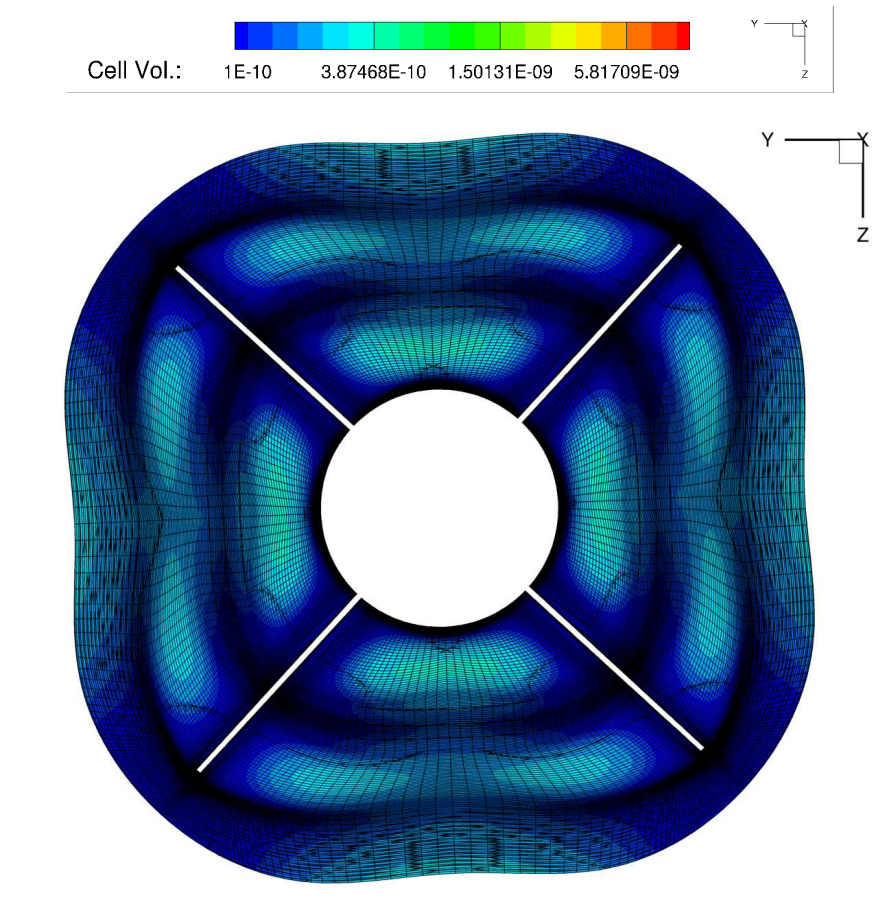


Figure A.3: Grid slice at the fins.

### A.3 Flowfield Visualisation and Flow Physics

This section presents the flowfield obtained using different turbulence models. Figures A.4 to A.5 show the total pressure  $P_t = P_s + \rho \cdot U^2/2$  over sectional planes along the store length for the very fine grid. Each turbulence model gave a different result, showing very different vortical content.  $k-\omega$ -SST, and  $k-\omega$ -SST with  $P_k$  Limiter are very dissipative, and few vortical structures appear in the flowfield. Figure A.6 compares store loads between  $k-\omega$ -SST, and the EARSM turbulence models on the coarse grid, for pitch angle between 0 and 15 degrees, and for a roll angle of 2.5 degrees. Overall, the models agree for pitch angles less than 5 degrees. On the other hand, the  $k-\omega$ -SST behaves erratically at high alpha. Using the  $P_k$  Limiter slightly decreases the dissipation in the flow, and the vortical structures become stronger (Figure A.4). However, the flowfield remains similar to the  $k-\omega$ -SST results, and the flow configuration is different to the predictions of EARSM and SAS (Figure A.5)

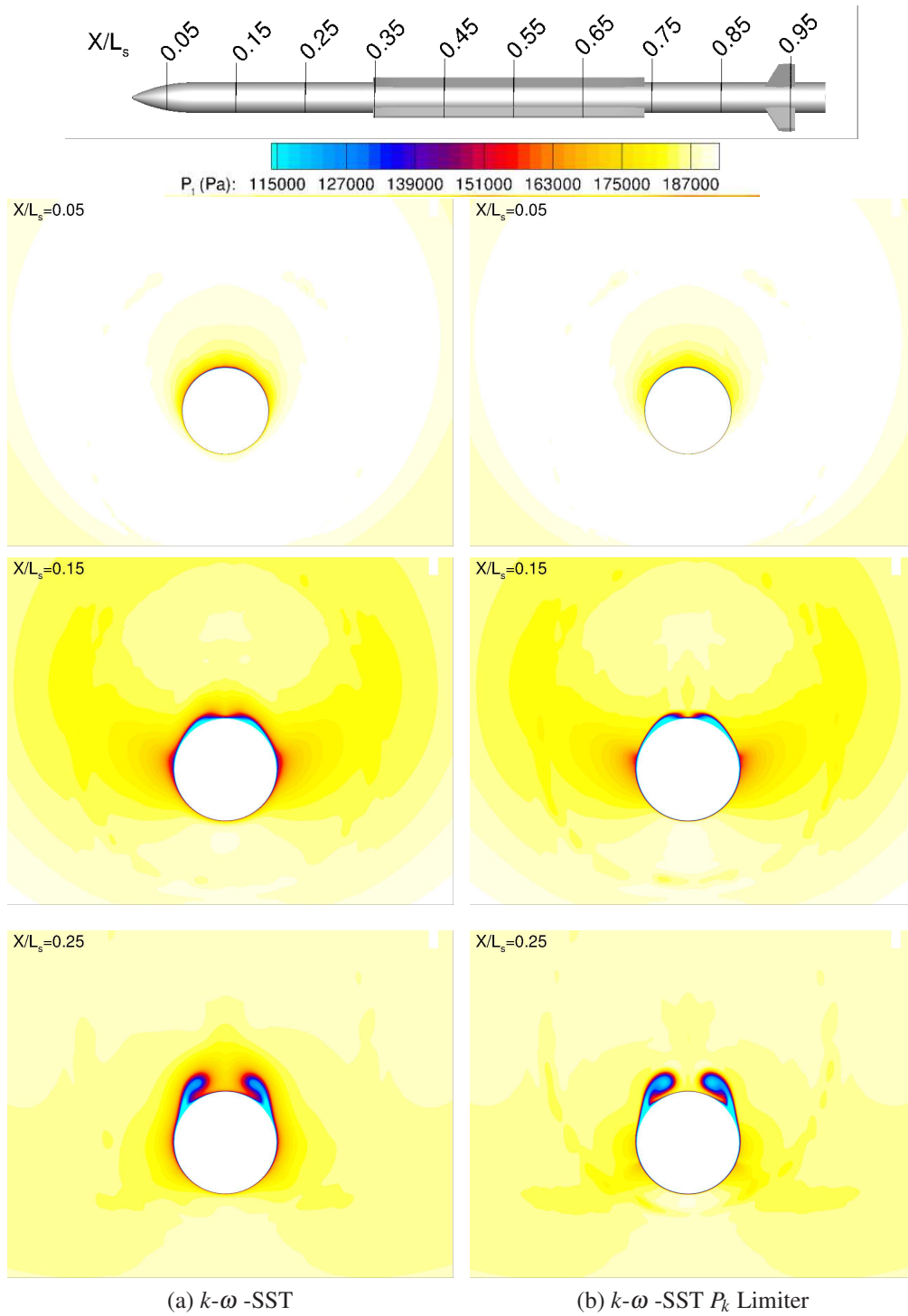


Figure A.4: Total pressure along the store length using  $k-\omega$ -SST (Left) and  $k-\omega$ -SST  $P_k$  Limiter (Right). Results on very fine grid.

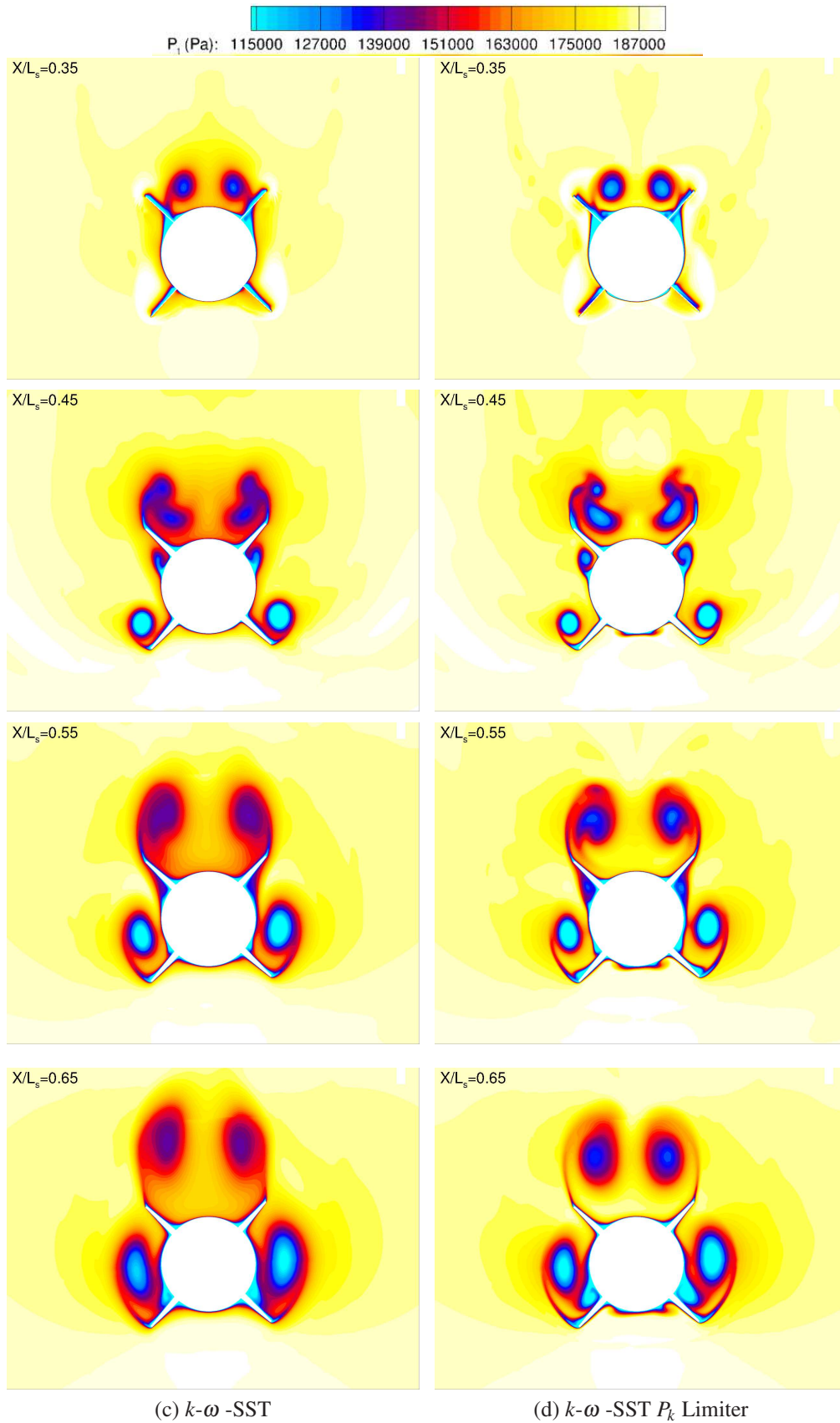


Figure A.4: Total pressure along the store length using  $k-\omega$  -SST (Left) and  $k-\omega$  -SST  $P_k$  Limiter (Right). Results on very fine grid.

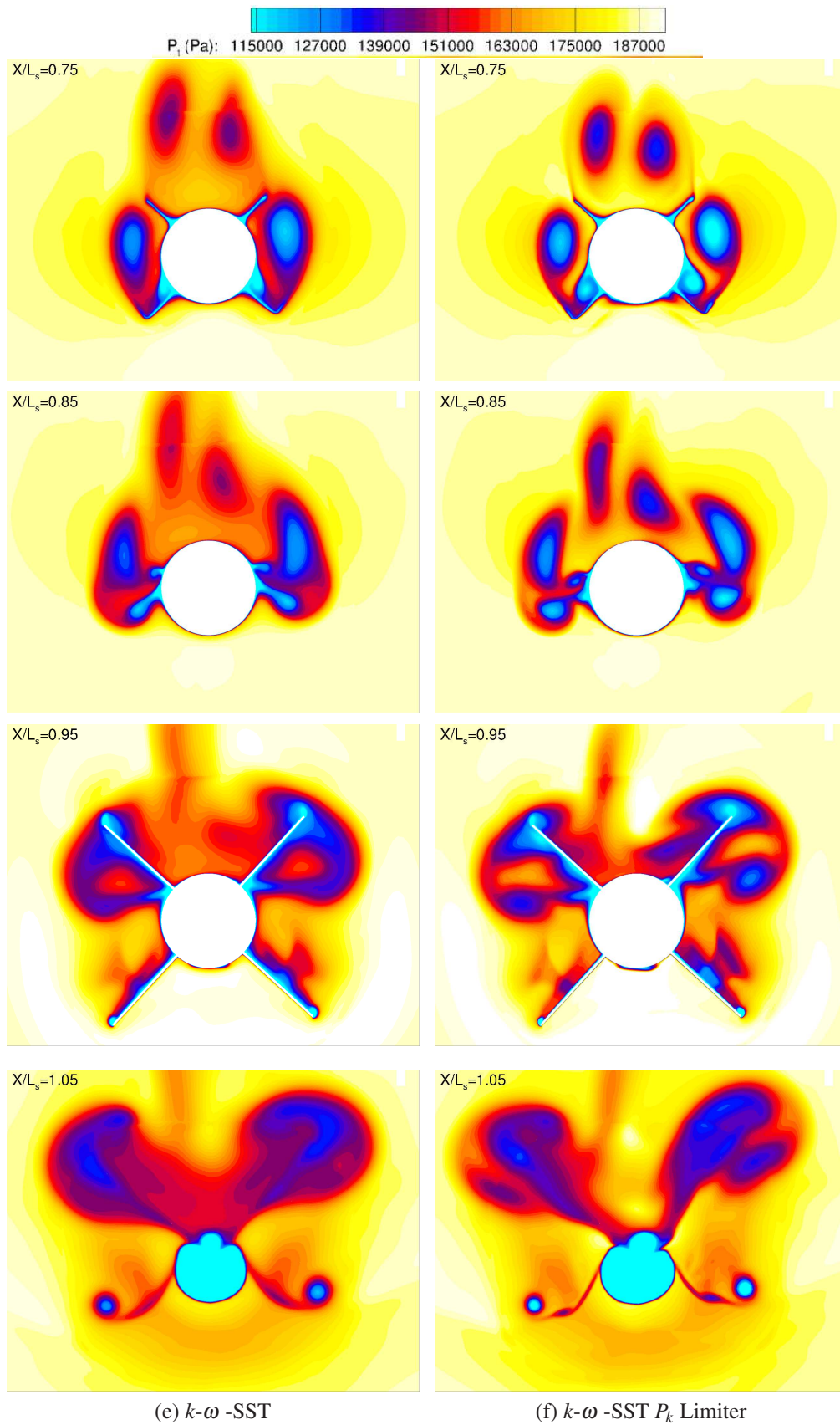


Figure A.4: Total pressure along the store length using  $k-\omega$ -SST (Left) and  $k-\omega$ -SST  $P_k$  Limiter (Right). Results on very fine grid.

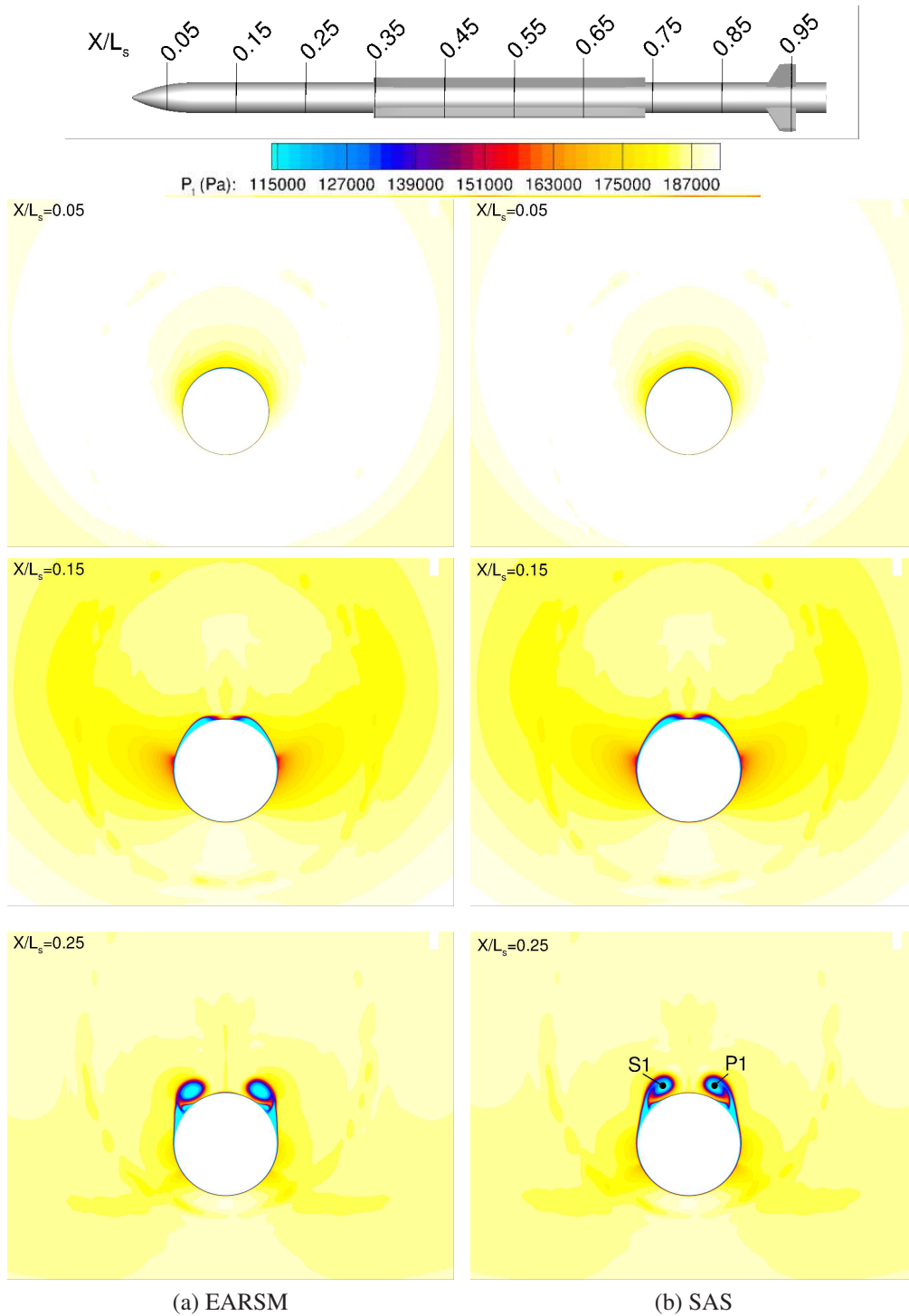


Figure A.5: Total pressure along the store length using EARSIM (Left) and SAS (Right). Results on very fine grid.

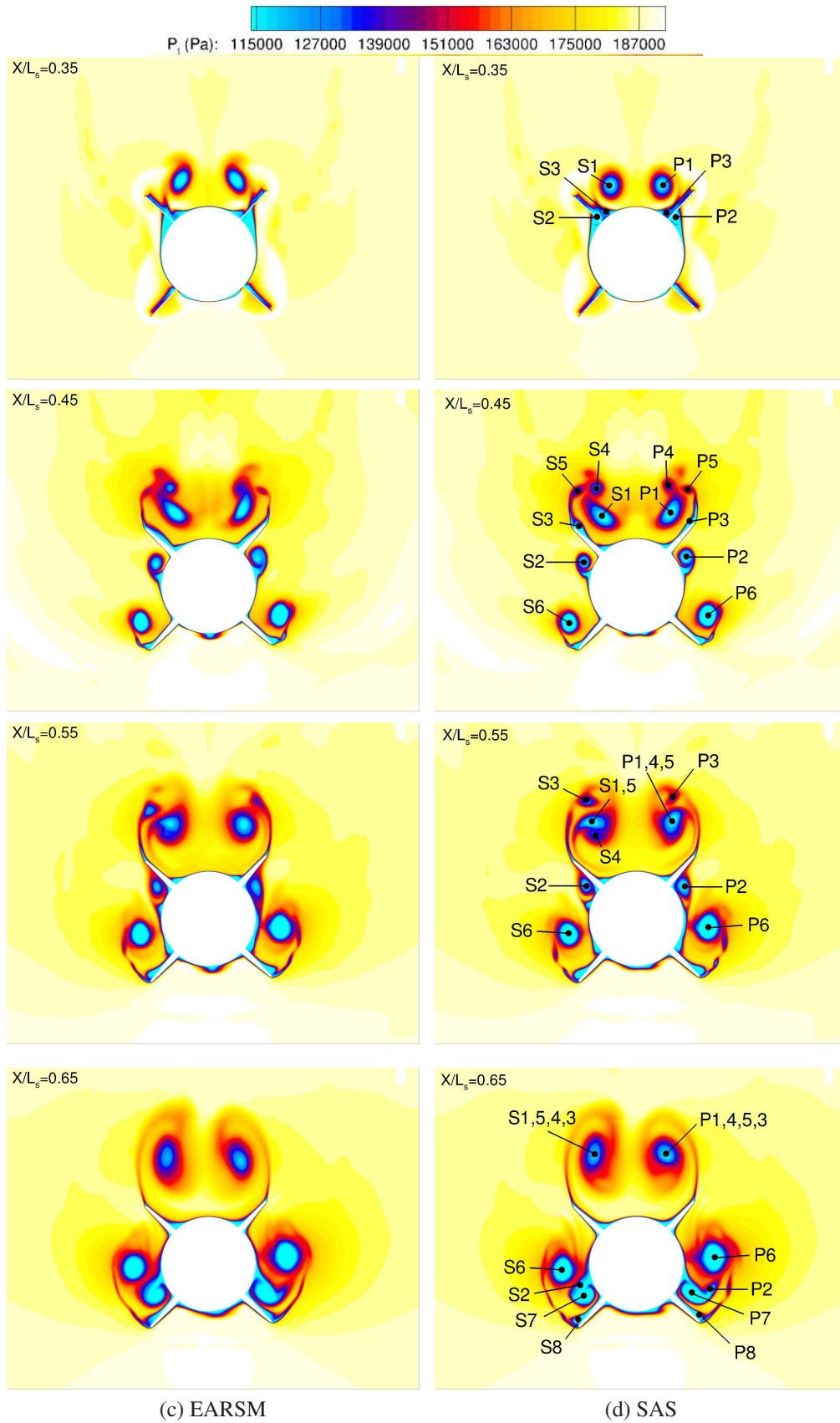


Figure A.5: Total pressure along the store length using EARSIM (Left) and SAS (Right). Results on very fine grid.

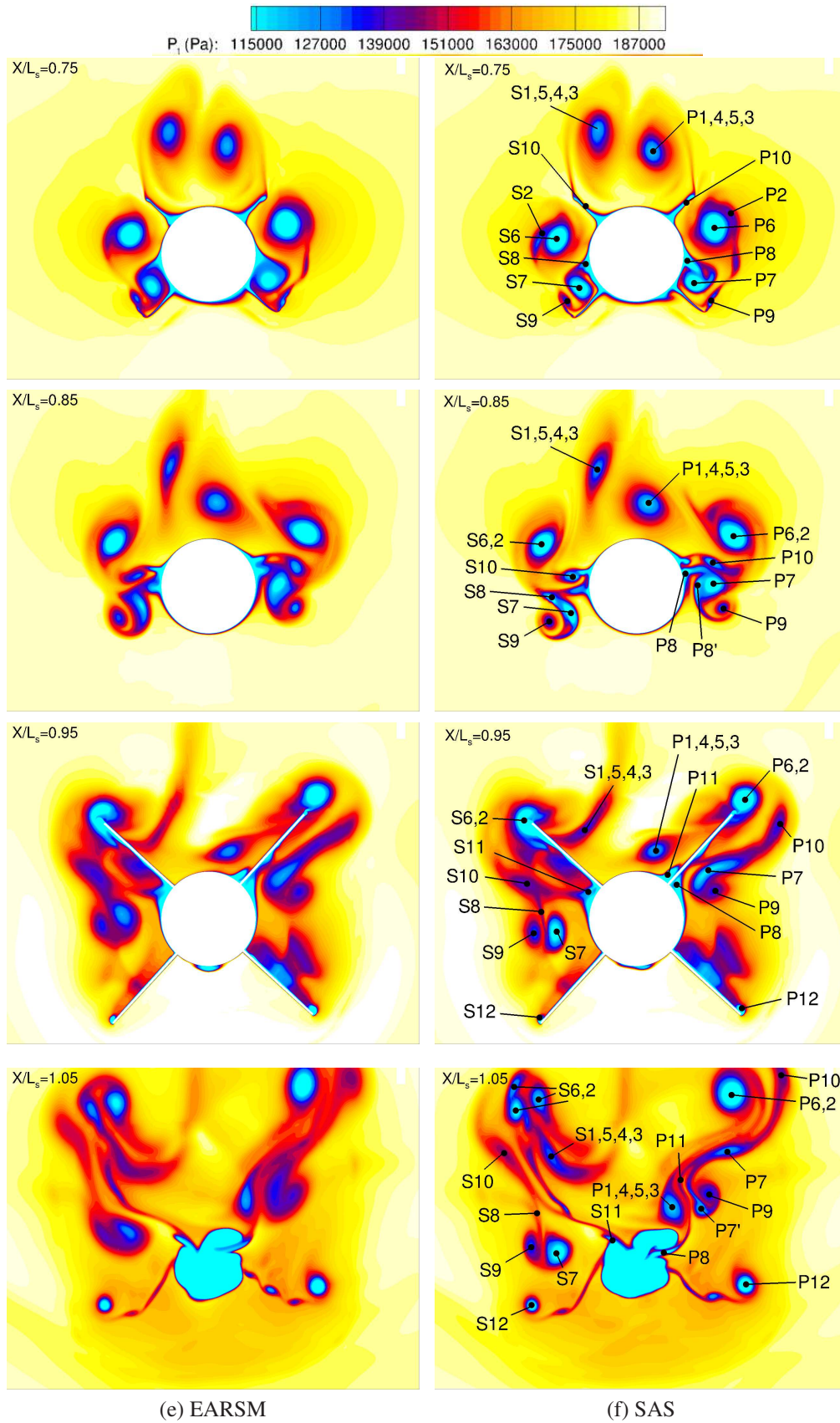


Figure A.5: Total pressure along the store length using EARSIM (Left) and SAS (Right). Results on very fine grid.

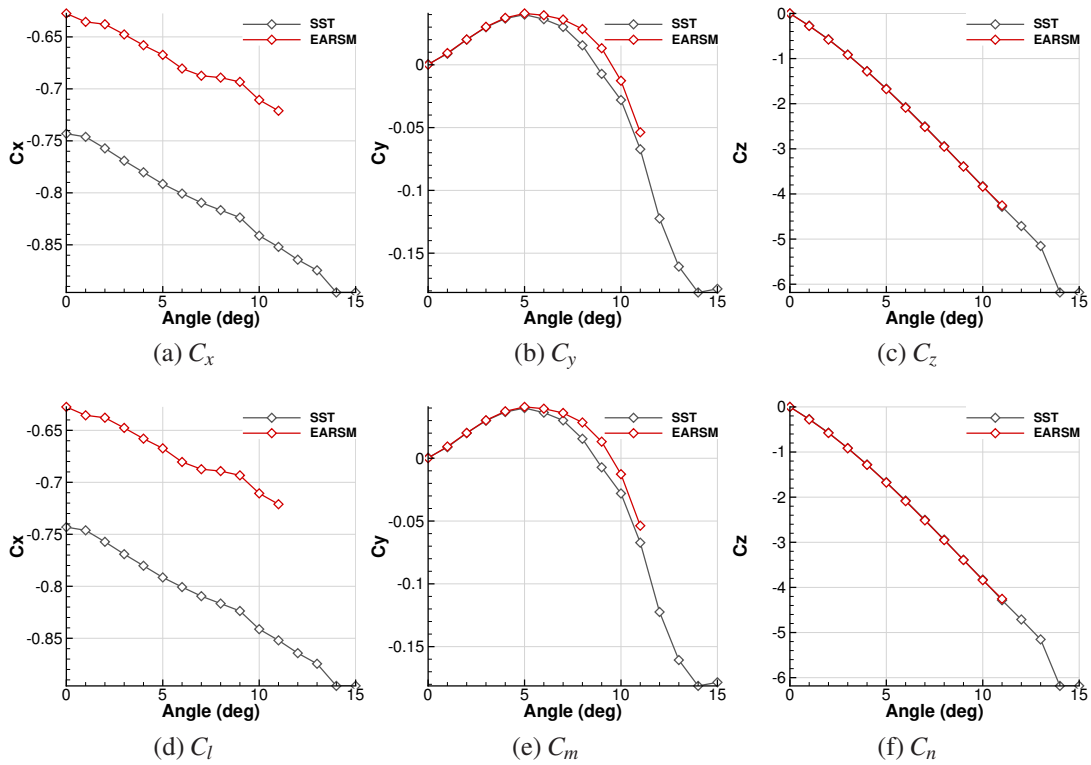


Figure A.6: Load polar for pitch between 0 and 15 degrees on the coarse grid. Results obtained using steady state CFD and RANS equations.

The EARSM, and SAS models (Figure A.5) show a large number of structures shed from the store body, strakes, and fins. SAS is less dissipative, and the vortices are stronger than for the EARSM model. The port, and starboard side vortices are highlighted on the figures for the SAS simulation, and are respectively called Px, and Sx. First, two vortices S1, and P1 appear at the starboard and port side of the store due to the high pitch angle at about  $X/L_s = 0.20$  (Figure A.5). At the leading edge of the strakes ( $X/L_s = 0.35$ ), P2, P3, S2 and S3 are generated by the junctions between the body, and the strakes at the upper side of the store. Then, at  $X/L_s = 0.45$ , P4, P5, S4 and S5 are shed from the upper side strakes, and rotate around P1, and S1. At the same time, S3, and P3 move towards the tip of the strakes under the influence of S1, and P1. S2, and P2 detach from the body, and S6, and P6 are shed from the strakes of the pressure side of the store. Farther, at  $X/L_s = 0.55$ , S1 merges with S4, and S5, while P1 merges with P4, and P5. At the same time S3, and P3 rotate around the strong merged vortices. On the pressure side, S6, and P6 move upwards, and begin to influence the position of S2, and P2. At  $X/L_s = 0.65$ , two strong vortices S1 and P2 remain above the store, having merged with all other shed vortices from the upper

side. At the pressure side, S2, and P2 rotate around S6 and P6, and move downwards. At the same time, S6 and P6 generate the vortices S7, and P7 at the junction between strakes of the pressure side of the store, and the body. Also, the pressure side strakes shed the vortices S8 and P8. At  $X/L_s = 0.75$ , the flow reaches the trailing edge of the strakes, and their boundary layers feed the structures S9, S10, P9, and P10. The two vortices S1, and P1, lose their symmetry, and P1 moves below S1. At the pressure side, S6, and P6 continue to move upwards, and merge with S2, and P2. Under the influence of S7, and P7, the vortices S8, and P8, move upwards. Between the strakes, and the fins ( $X/L_s = 0.85$ ), the flow is complex with strong interaction between a large number of vortices. P1 continues to move downwards, and interacts with P6, while S1 and S6 remain away one from the other. On the port side, P7, P8', and P10, become very close, and interact with P9. On the starboard side, S7, and S8 get closer, and interact with S9, while S10 stays away from this group. Then, at  $X/L_s = 0.95$ , this complex flow hits the fins, contributing significantly to the store loads. S6, and P6 are still strong, and hit the tips of the fins, leading to large changes in the loads, for a small change of their position and strength. The comparison with the EARSM pressure field, shows differences in the strength, and position of the vortices. This increases along the store length due to the differences in the dissipation of the models. Nevertheless, it is not possible to determine what solution is closer to the reality, as no experimental data is available.

## A.4 Mesh Convergence

This section investigates the mesh convergence of the flowfield, and store loads.

The total pressure field for EARSM (Figure A.7) and SAS (Figure A.8) turbulence models, are shown for different grid densities, at cross sections close to the fins. The coarse grid shows to a large dissipation (Figures A.8f), and a small number of vortices present in the SAS solution. Also, the EARSM turbulence model did not converged due the coarseness of the grid. Medium, fine, and very fine grids, lead to similar results, with small changes at  $X/L_s = 0.95$ . The EARSM shows a weaker vortex S1, and a stronger vortex P10 going from the fine (Figure A.7f) to the very fine grid (Figure A.7g). The SAS shows a stronger vortex P10, and the vortices S7, S8 and S10 move together going from the fine (Figure A.8h) to the very fine grid (Figure A.8i).

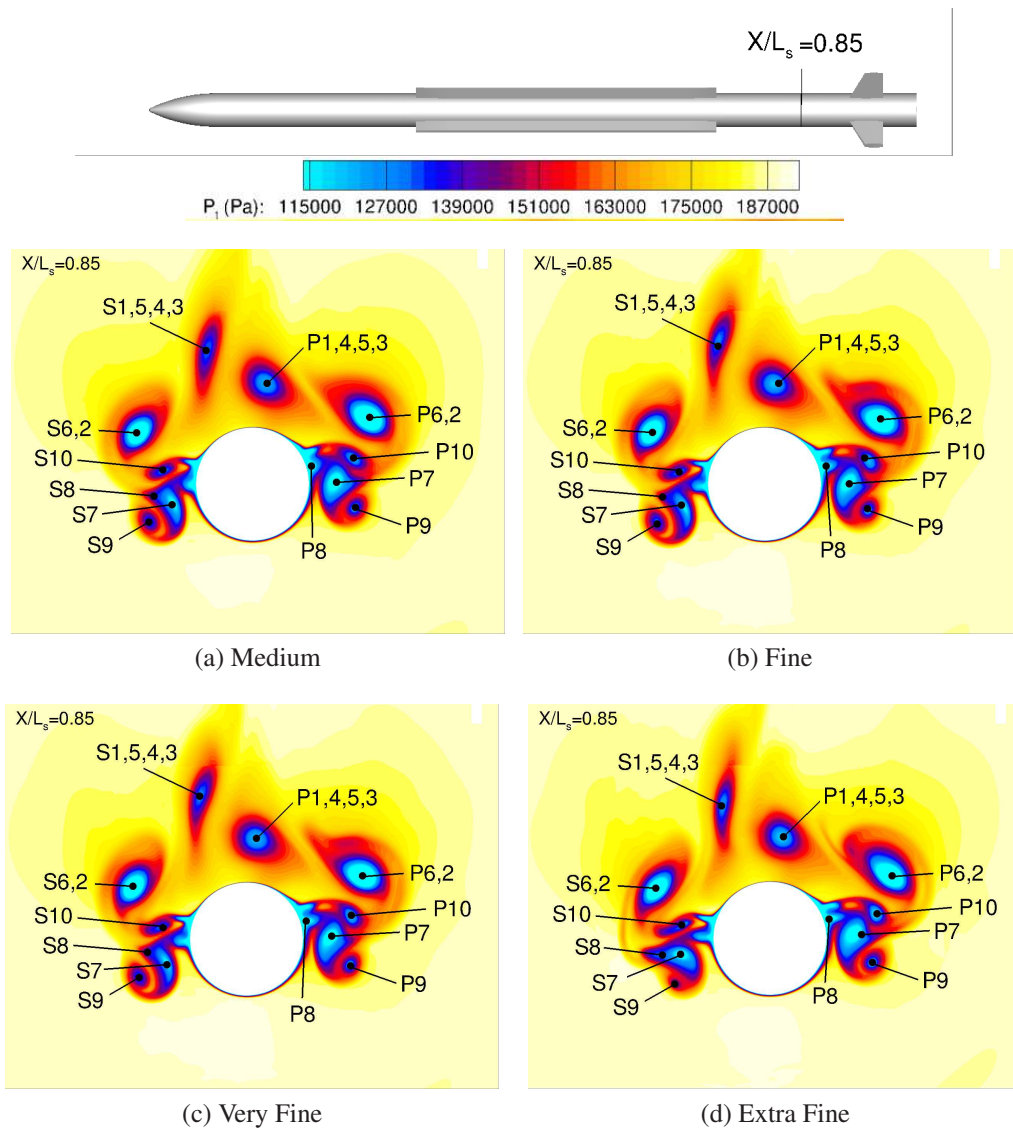


Figure A.7: Total pressure at  $X/L_s = 0.85$  for different grid densities, and for the EARSM turbulence model.

The passage from the very fine, to the extra fine grid, leads to larger changes for both models. At  $X/L_s = 0.85$ , vortex S9 is predicted weaker (Figures A.7d and A.8e), and its interaction with S7, and S8 changes. As a consequence, the flowfield at  $X/L_s = 0.95$  looks different, and the vortices S7, S8, S9, and S10 are distributed differently in space (Figures A.7h and A.8j). Also, vortex S6 hits the fin in a different way. This also may be the consequence of the better definition of the shocks produced by the fins on the extra fine grid, that influences the vortex positions.

A small change on the position, or the strength of a vortex, changes the way it interacts with his neighbours, and this has dramatic consequences on the downstream

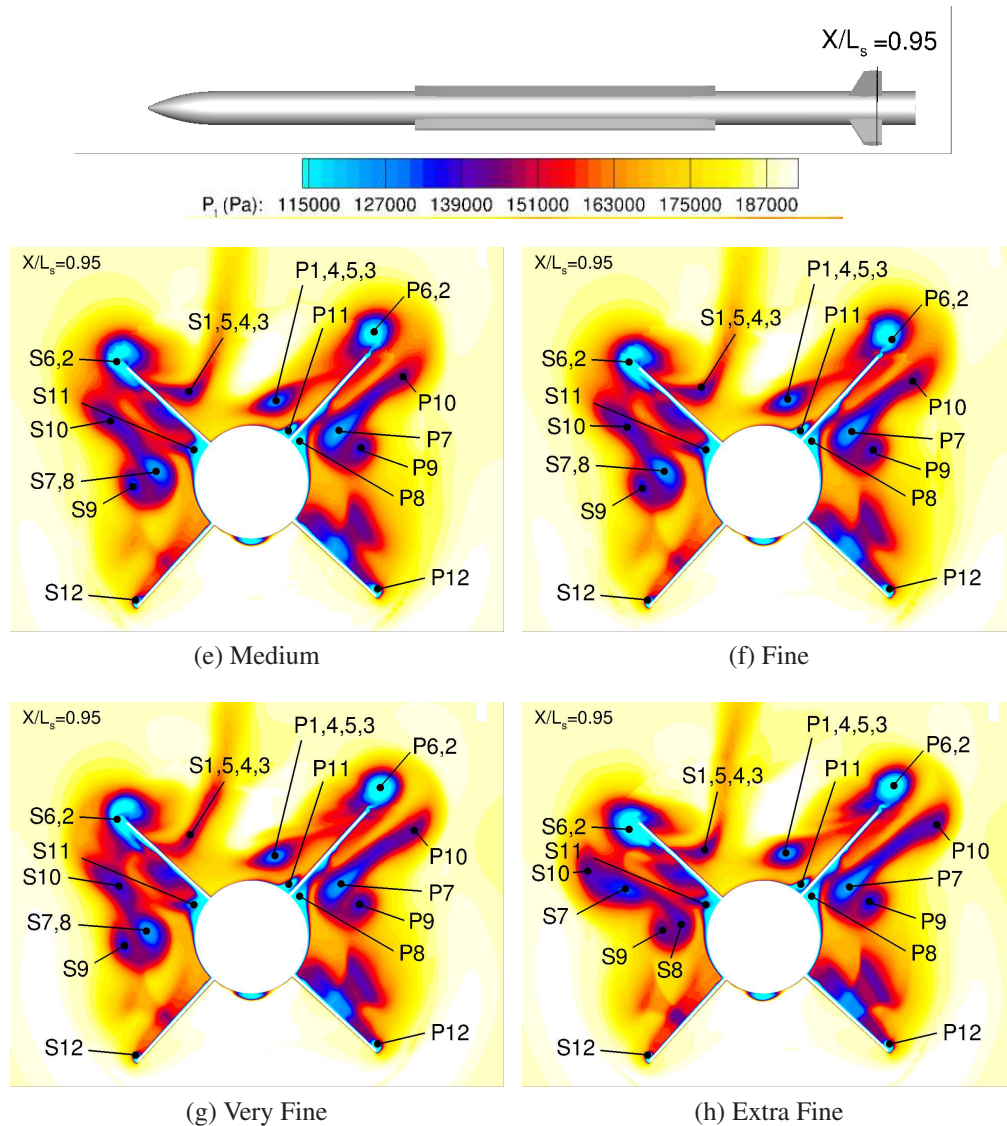


Figure A.7: Total pressure at  $X/L_s = 0.95$  for different grid densities, and for the EARSM turbulence model

flow in a cascade fashion.

Figure A.9 shows the loads on the store for the different grids. The forces are slightly influenced by the grids, and both models give the same values. However, the moments change with the grid, and the models gave different values. Figure A.10 shows a convergence plot with the load difference between each grid, and the extra fine grid. Overall, the moments are subject to larger changes than the forces, and the yaw, and pitch moments show the largest changes. The rolling angle shows smaller changes, but a change of 0.1 in roll moment leads to large changes in roll angle due to small store inertia about that axis.

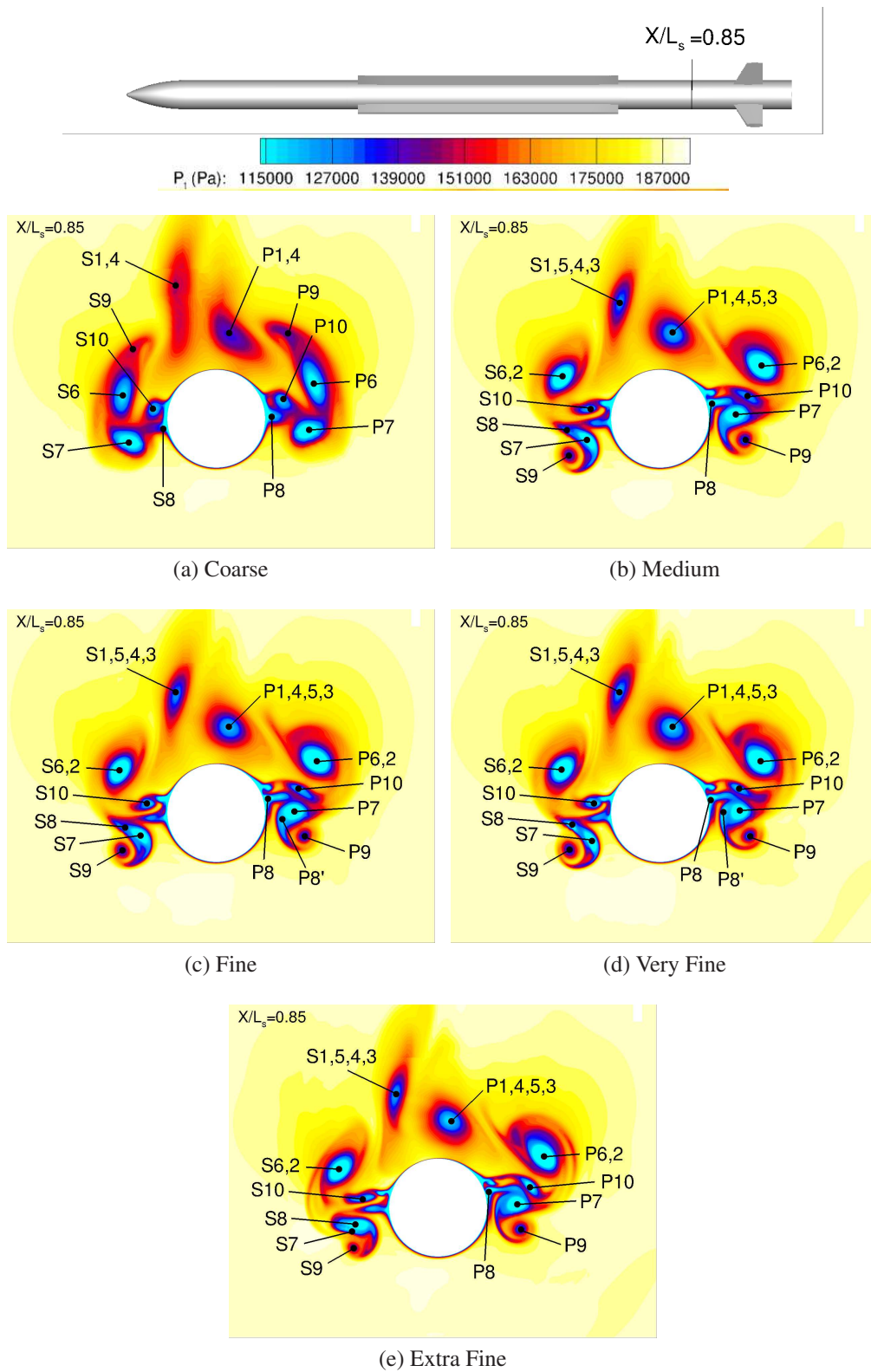


Figure A.8: Total pressure at  $X/L_s = 0.85$  for different grid densities, and for the SAS turbulence model.

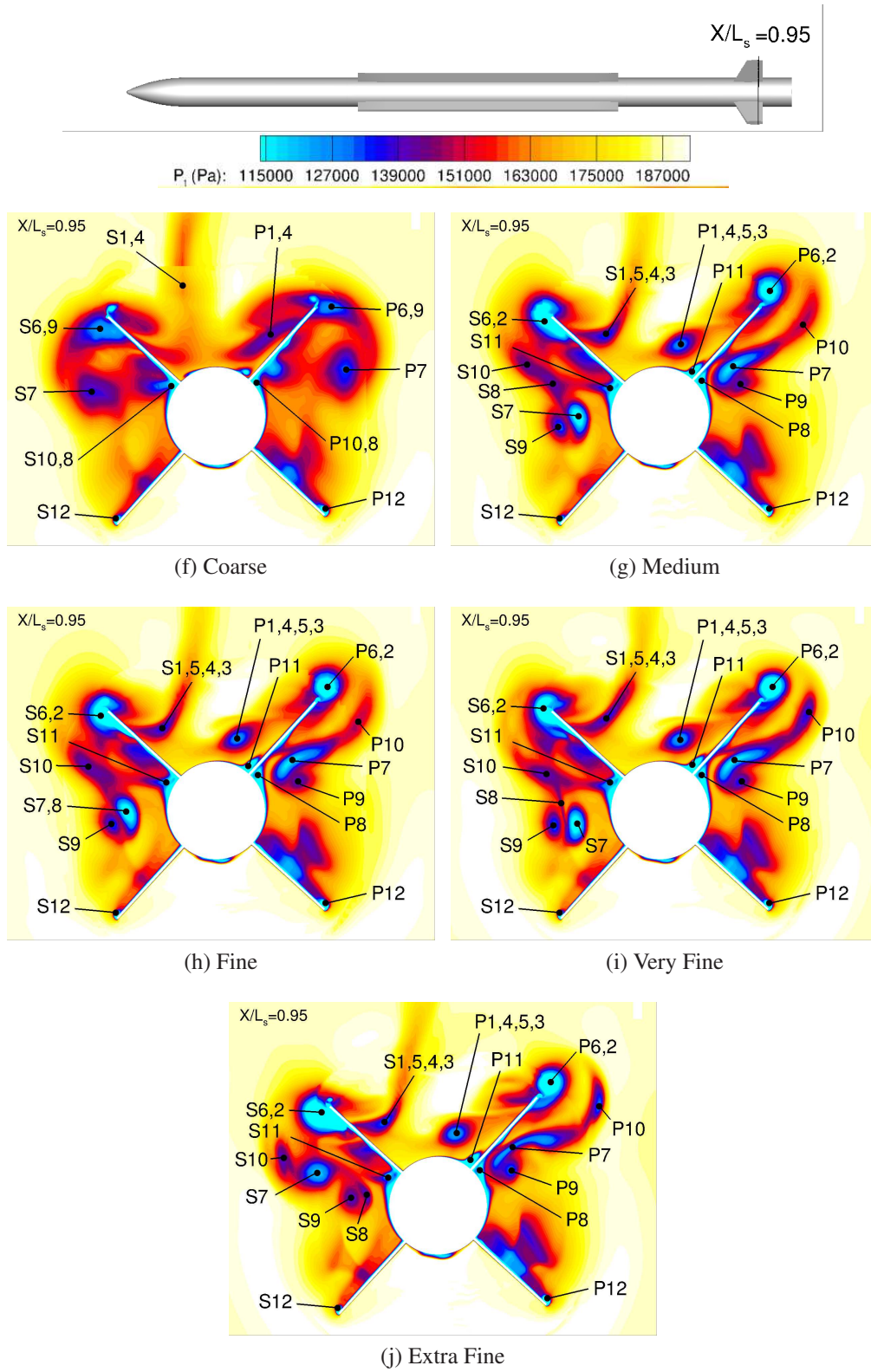


Figure A.8: Total pressure at  $X/L_s = 0.95$  for different grid densities, and for the SAS turbulence model.

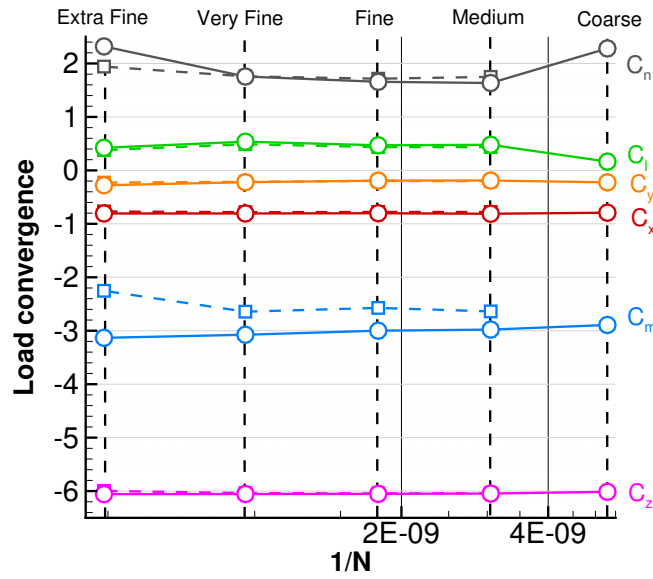


Figure A.9: Load on the store using EARSM (Dashed lines, square) , and SAS (Continuous lines, circle) turbulence models.

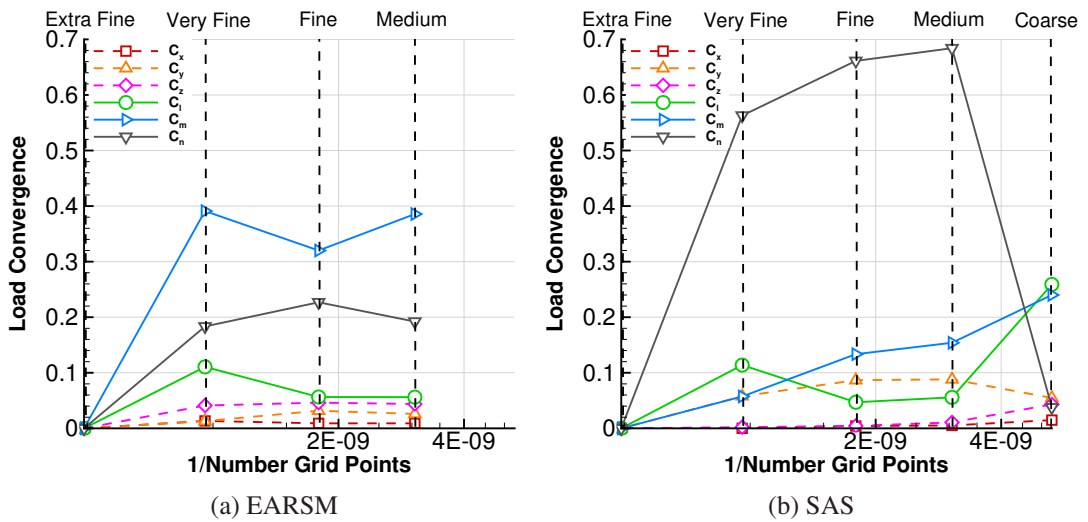


Figure A.10: Load convergence using EARSM, and SAS turbulence models.

Figure A.11 shows the convergence plot for each component of the store. Overall, the fins, and the body lead to the larger load deviation as function of the grid size. On the other hand, the loads on the strakes appear grid converged between the medium, and the extra fine grid. This is due to the differences in the development of the vortices, that influences the pressure field at the back of the store. As a consequence, the pitching, and the yawing moments are subject to large changes. The rolling moment is also influenced by the position of the vortices S2, and P6, very close to the fins tip. The larger changes in loads, from the very fine, to the extra fine grids, correspond to

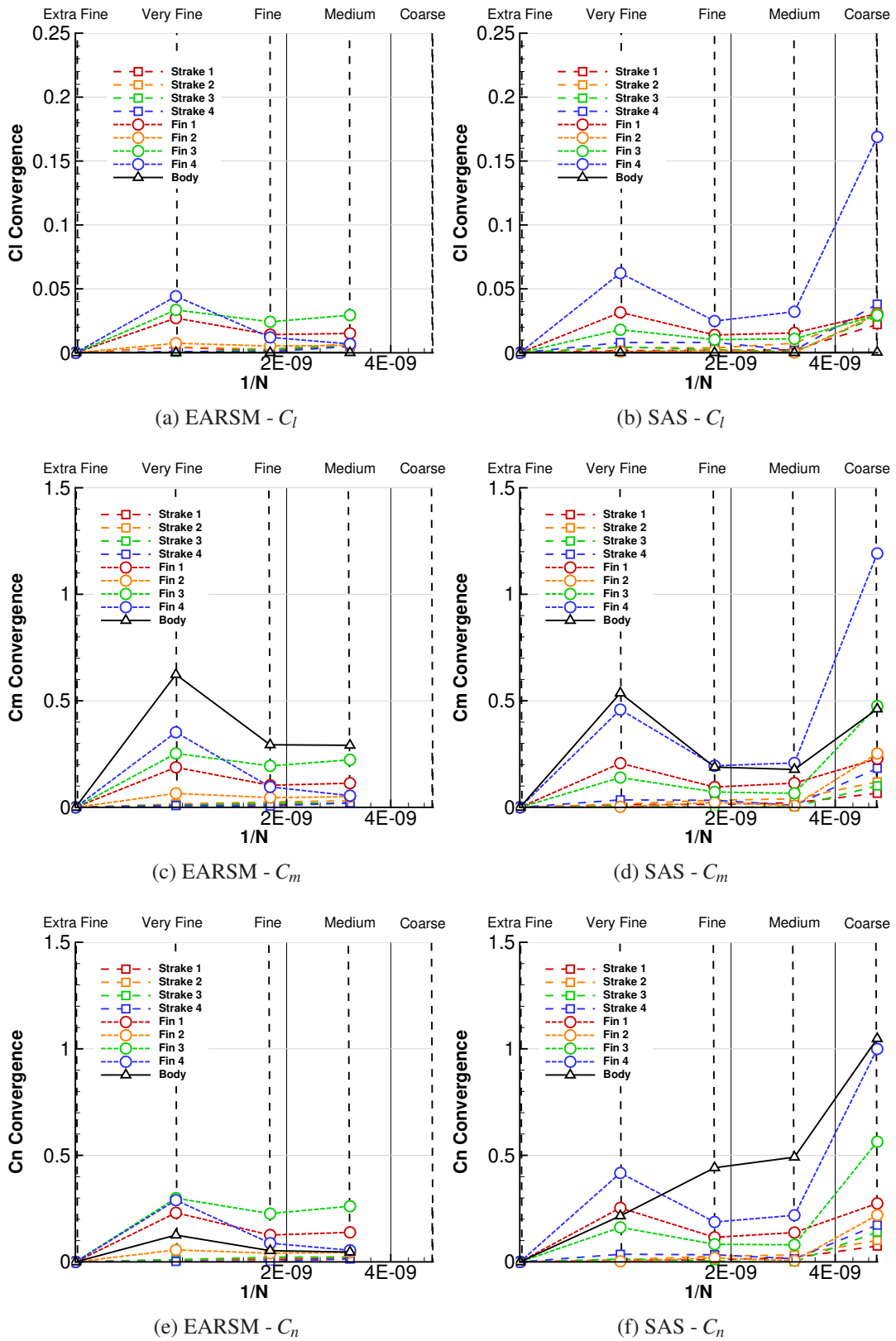


Figure A.11: Load convergence using EARSM, and SAS turbulence models.

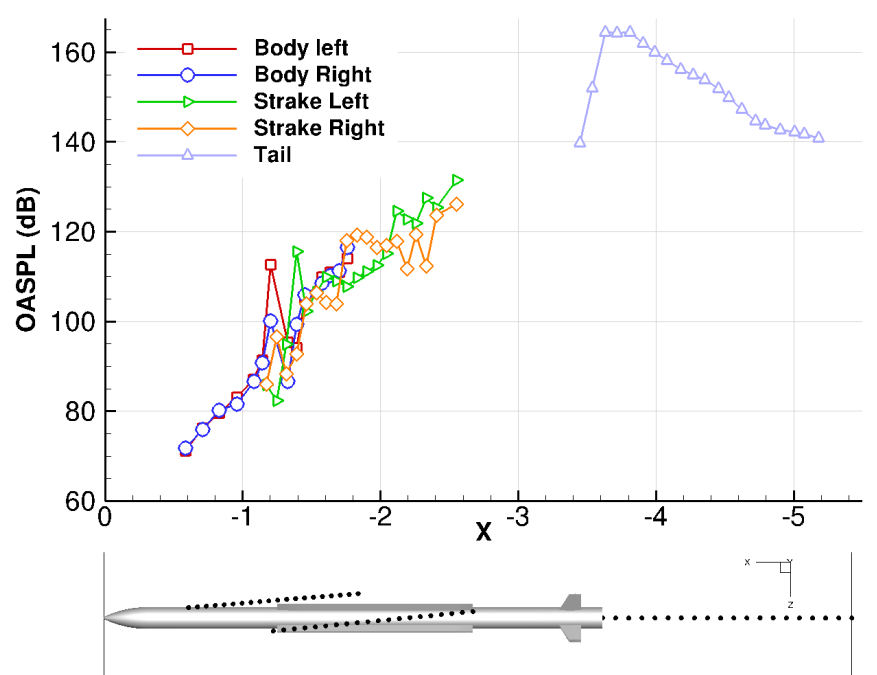


Figure A.12: OASPL along the path of the main vortices, and at the wake. Result scaled for ISA sea level. SAS on very fine grid.

the most significant change in the flowfield as seen figures A.7 and A.8. Also, fins 3 and 4, on the upper side of the store lead to larger changes in the loads than fins 1 and 2, as they are located in the more complex flow shed from the body and the strakes.

Figure A.12 shows the OASPL along the path of the vortices shed from the strake, and along the store wake. The probes were placed in the very fine grid computed with SAS. Along the store length, more and more pressure fluctuations develop, as the consequence of the presence of numerous vortices. This indicates that steady computation of this flow, may be not accurate, and not fully capture the vortex interactions.

To improve the results, further computations are required. Finer meshes may lead to mesh convergence for the moments. Also, the timestep was kept constant, while the grid was finer. The effect of the timestep on the SAS results have to be quantified, to verify if further unsteadiness is captured. In addition, high order models may improve the results, reducing the dissipation on the coarser grids.

## A.5 Summary of Work

As is the case for cavity flows, simulation of turbulence is very important for a store at high  $\alpha$ . The development of vortical structures around it are influenced by small changes in the flowfield due to the grids, and the turbulence models. As a consequence, in a cascade effect, downstream vortices change position, and strength, leading to a different flow at the back of the store. This flow cannot be simulated with RANS models that dissipate too much the vortices. SAS gave the best results, with the smaller dissipation of the vortical structures. In addition, fine grids are required to capture the smaller vortices, and the strong shocks that influence the evolution of the vortices. Due to the high Reynolds number, experiments are difficult to perform, and CFD simulations is the preferred way to handle this flow. However, to further understand this flow, an effort is required to obtain experimental data to validate the present results. CFD studies of the effect of the employed timestep for unsteady computations are also needed.

# Appendix B

## Proper Orthogonal Decomposition for Engineering Applications

This section presents the Proper Orthogonal Decomposition (POD) technique to compress output files from HMB3. This was used to easily share data with MBDA UK Ltd. With the present technique it is possible to share a complete flowfield in time and space using a file lighter than 100MB.

### B.1 POD Principle

The Proper Orthogonal Decomposition (POD) is a mathematical technique used in applications such as image processing, signal analysis and data compression<sup>[171]</sup>. It aims to obtain low-dimensional approximations of high-dimensional processes, therefore eliminating information which has little impact on the overall process. It was first introduced in the context of fluid mechanics and turbulence by Lumley<sup>[172]</sup> to decompose the flow into modes. These modes identify the large coherent structures which contribute to the flow.

The principle behind POD is that any function can be written as a linear combination of a finite set of functions, termed basis functions. Any set of functions or vectors,  $f_0, f_1, \dots, f_n$  are linearly independent if they satisfy the following equation:

$$\alpha_0 f_0 + \alpha_1 f_1 + \dots + \alpha_n f_n \neq 0 \quad (\text{B.1})$$

where the coefficients  $\alpha_0, \alpha_1, \dots, \alpha_n$  are constants and non-zero. If a vector space  $V$ , can be described by a subset of vectors  $v_0, v_1, \dots, v_n$ , then these form a basis set if they

are linearly independent and they can be written in a linear combination of the form:

$$V = \alpha_0 v_0 + \alpha_1 v_1 + \dots + \alpha_n v_n \quad (\text{B.2})$$

The set of basis vectors can also be an orthonormal basis set if the inner product of  $v_i$  and  $v_j$  is zero, where  $i \neq j$ . Also, they are required to have a length of 1 (i.e the inner product of  $v_i$  and  $v_i$  is 1).

Three different methods fall under the generalised term of Proper Orthogonal Decomposition: Karhunen-Loeve Decomposition (KLD), Principal Component Analysis (PCA) and Singular Value Decomposition (SVD). However, in the context of turbulence and fluid mechanics, if the acronym POD is used, it generally refers to KLD.

In practice, the POD generation takes as input  $N$  snapshots of the flowfield  $u(x,t)$ , and generates a mean flow  $\Phi_0(x)$ , and  $N$  modes  $\Phi_i(x)$ . Then, each timestep can be reconstructed using the linear combination of the modes:

$$u(x,t) = \sum_{i=0}^{i=N} a_i(t) \Phi_i(x) \quad (\text{B.3})$$

Each mode contains a different level of energy, and the linear combination of the most energetic POD modes is enough to capture the total flowfield energy. Figure B.1 shows the energy contained in the flow reconstruction as function of the number of modes included. Over the 200 modes generated, only 125 are required to capture 90% of the energy. To discard all the modes above this limit saves 38% of disk space. For

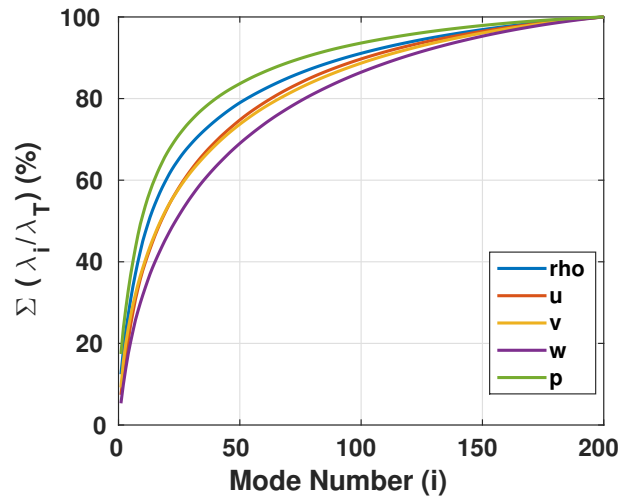


Figure B.1: Cumulative energy contained in the POD modes.

larger data sets, the saving can be more than 50%. Figure B.2 shows an example of POD modes of a cavity flowfield. The first modes contain a large part of the flowfield energy, and show the largest structures. On the other hand, the latest modes describe the smaller details of the flowfield, and contain a small amount of flowfield energy.

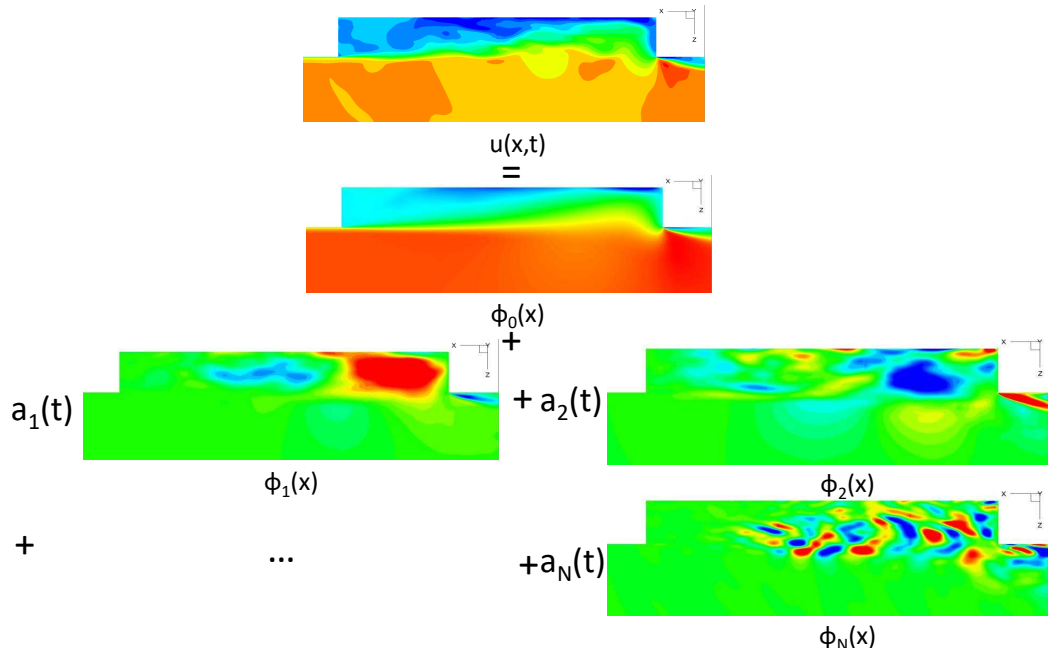
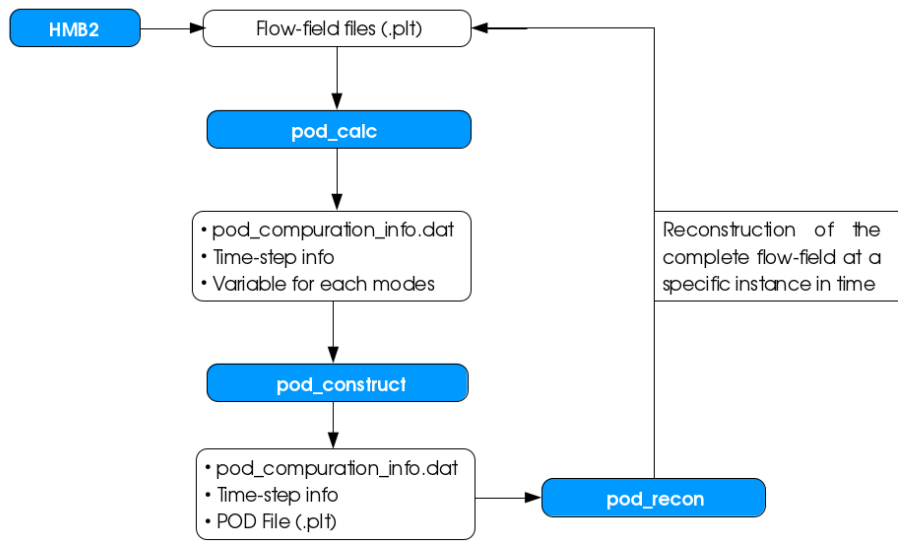


Figure B.2: Example of POD modes for a cavity flowfield.

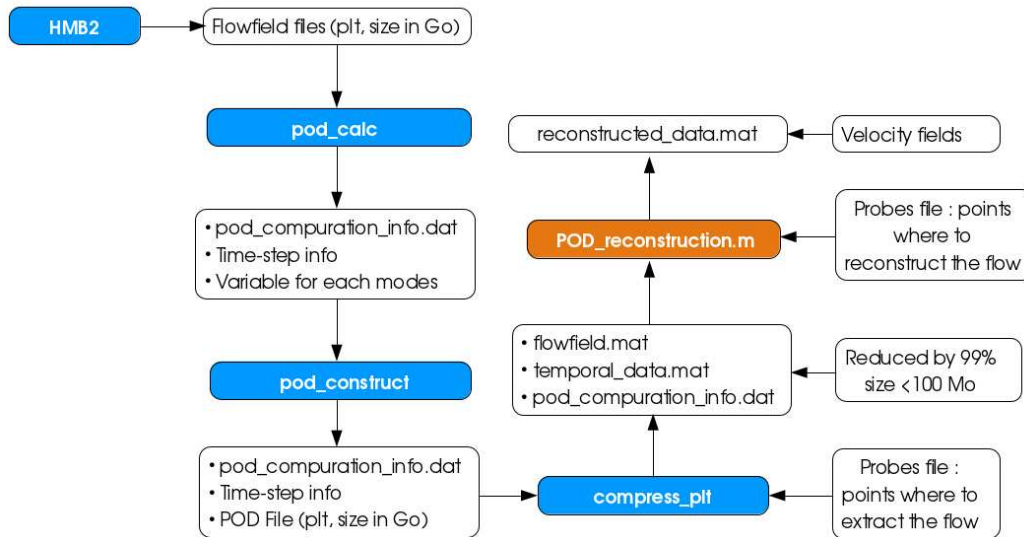
## B.2 Modified POD Process

Figure B.3 presents process flow diagrams of the original POD process in C (See TN10-014, June 2010), and the modified POD reconstruction processes including MATLAB routines. The decomposition in POD modes is the same for both methods. Flowfield outputs from the HMB flow solver, are obtained at regular intervals in time, usually over a time period equal to 10% of a travel time. Then, routines in C (*pod\_calc* and *pod\_construct*) are used to extract flow variables, and temporal information from the individual flowfield output files.

In the original C process, POD was performed on five primitive variables:  $\rho$ ,  $u$ ,  $v$ ,  $w$ , and  $p$ . The flow-field reconstruction, for a specific instance in time, was obtained using the *pod\_reconstruct* routine. This reconstructs all the flowfield variables on the CFD mesh, resulting in a file with the same size as the original flowfield file (approx. 2.5Go for 35 million grid points). Note that this is for one instance in time, and



(a) Original C POD process



(b) C and MATLAB POD process

Figure B.3: POD generation and reconstruction processes. Go : gigaoctet, Mo : megaoctet.

the reconstruction procedure has to be repeated, producing additional files, if other instances in time are required.

Velocity information inside, and immediately outside the cavity is useful for grid data analysis, where the aerodynamic loads of a store can be determined from the local velocity components and look-up tables. The modified POD reconstruction process uses a routine called *compress\_plt*, that uses an input file, (eg. *probes.plt*), generally containing a relatively coarse distribution of points around the cavity, to store the modes. *compress\_plt* produces two files, *flowfield.mat* and *temporal\_data.mat*,

that have a combined size in the range of 50MB for 15000 grid points. In the examples given in this report, the reduction of the data set size is more than 99%. These files are used by MATLAB functions to reconstruct velocities using the Nearest Neighbour (NN), or the Moving Least Square (MLS) interpolation methods of the POD modes. The reconstruction can be done for any time within the signal used to construct the POD modes.

## B.3 Creation of the MATLAB Input Files

To create the inputs files for MATLAB reconstruction, three type of files are required. *name.podmode.mmmmm.plt* contains the flowfield corresponding to each mode  $m$  on the CFD grid.

*name.VT podmode.mmmmm.dat* contains the coefficients  $a_m(t, v)$  to reconstruct the original flow by linear combination. *pod\_computation\_info.dat* contains information about the POD computation.

A Tecplot binary file called *probes.plt* has to be generated containing all the non-dimensional coordinates (all dimensions are scaled with the cavity length) of the points where the flow is to be extracted at.

### B.3.1 Process of MATLAB File Generation

The script *make\_matlab\_pod.sh* automatically creates MATLAB inputs.

The script is launched with the following command from the case folder containing the inputs files:

```
./make_matlab_pod.sh <filename_root> <nb_modes> <probes> <xyz_file>
<nb_x_divisions> optional: <nb_procs>
```

The number of modes to take into account may be less than the available number of modes. This could result in even smaller files. *probes* is the path to the Tecplot probes file discussed above. *xyz\_file* is the path to the Tecplot file containing the spacial coordinates of the POD modes if they are stored separately. *nb\_x\_divisions* is a parameter to increase the execution speed of the compression. A value of 10 is enough for the MATLAB POD generation. A folder called *matlab\_pod* containing *flowfield.mat*, *temporal\_data.mat* and *pod\_computation\_info.dat* is then created.

The data in *flowfield.mat* is written as a 2-dimensional array and if loaded using the command line prompt it contains:

```
flowfield: [Lx6 double]
```

```
L : number of probe points x number of samples
```

```
The second index will always have 6 values (x, y, z, u, v and w)
```

The data in *temporal\_data.mat* is written as a 3-dimensional array and if loaded using the command line prompt it contains:

```
t_data: [Tx4xM double]
```

```
T : Number of timestep
```

```
The second index will always have 4 values (step, a(u,m), a(v,m)
and a(w,m))
```

```
M : Number of modes
```

## B.4 Running a Reconstruction with MATLAB

The POD program reconstructs velocity variables at specific points in the flow domain, and for user-specified signal length, sampling frequency and number of samples. A *probes.dat* file has to be created by the user containing the x, y and z coordinates of every point where the user would like the velocity variables to be reconstructed at. The non-dimensional coordinates (all dimensions are scaled with the cavity length) in this file are written in three columns while each point is represented by a row in the following format:

```
0.0100 0.0000 -0.1000
```

```
0.0200 0.0000 -0.1000
```

```
0.0300 0.0000 -0.1000
```

```
0.0400 0.0000 -0.1000
```

```
0.0500 0.0000 -0.1000
```

### B.4.1 GUI Execution

Executing the *POD\_Reconstruction.m* file brings up the user interface shown in figure B.4.

First, in the POD case frame, the path to the directory containing the input files has to be entered. The path to the probe file is relative to the directory provided. Then

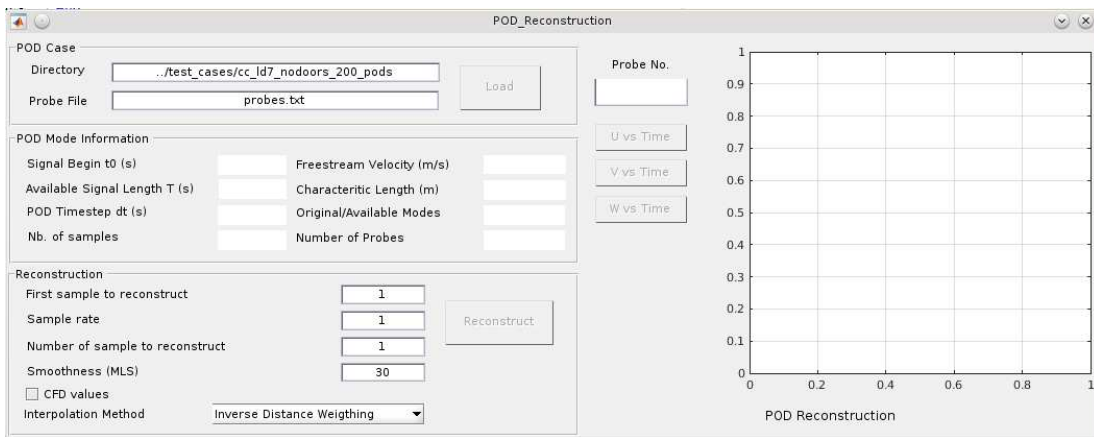


Figure B.4: POD Reconstruction GUI.

it is possible to click on "Load". The "POD Mode Information" part is automatically filled, giving information about the case. The length of the cavity can be changed to scale the results.

Next, for the flow reconstruction, the user has to specify the first sample to reconstruct from, the sample rate, the number of samples to reconstruct and the smoothness for the MLS method. By default, all available modes are used for the reconstruction. If the check box *CFD value* is checked, scaled values are given, else dimensional values with  $L$  and  $U_\infty$  are given. There is also the option between Nearest Neighbour, and Moving Least Square methods. Once the reconstruction information is specified by the user, the "Reconstruct" button has to be clicked; this begins the reconstruction process and the progress is shown in the MATLAB command window. As soon as the reconstruction is complete a MATLAB binary file named *reconstructed\_data.mat* will be saved in the current test case folder.

The right part of the window can plot the  $u$ ,  $v$  and  $w$  velocities for all probes once the computation is over. The user must enter the probe id and to click on the desired component.

### B.4.2 Batch Execution

If the reconstruction has to be automated it is also possible to run the program in batch mode with the file *run\_reconstruction.m*. The parameters are the followings:

<i>directory</i>	Case folder
<i>probe_file</i>	File containing point where to interpolate flow, relative to directory
<i>first_timestep</i>	First timestep to reconstruct
<i>no_of_samples</i>	Number of timesteps to reconstruct
<i>unsteady_step_rate</i>	Rate between two timesteps to reconstruct
<i>freestream_velocity</i>	Freestream Velocity (m/s)
<i>characteristic_length</i>	Characteristic Length (m)
<i>interp_method</i>	Spatial interpolation. 0 for NN; 1 for MLS
<i>smoothness</i>	Only for MLS, a value close to 1 will smooth the result

To obtain CFD unscaled values *freestream\_velocity* and *characteristic\_length* have to be set to 1.

### B.4.3 Output

The output file can be loaded from the MATLAB command window using the *load* command:

```
load ../test_cases/cc_ld7_nodoors_100_pods/recon_data.mat
```

Data in *recon\_data.mat* is written as a 3 arrays and when loaded from the command line contains:

velocity: [Px3xS double] : The velocity components.

P: number of probe points

The second index will always have 3 values (u, v and w)

S: number of samples

coords: [Px3 double] : The reconstruction points coordinates.

P: number of probe points

The second index will always have 3 values (x, y and z)

time: [S double] : The time signal.

S: number of samples

### B.4.4 Interpolation parameters

The nearest neighbour method has no parameter, the value at a probe is taken from the nearest grid point.

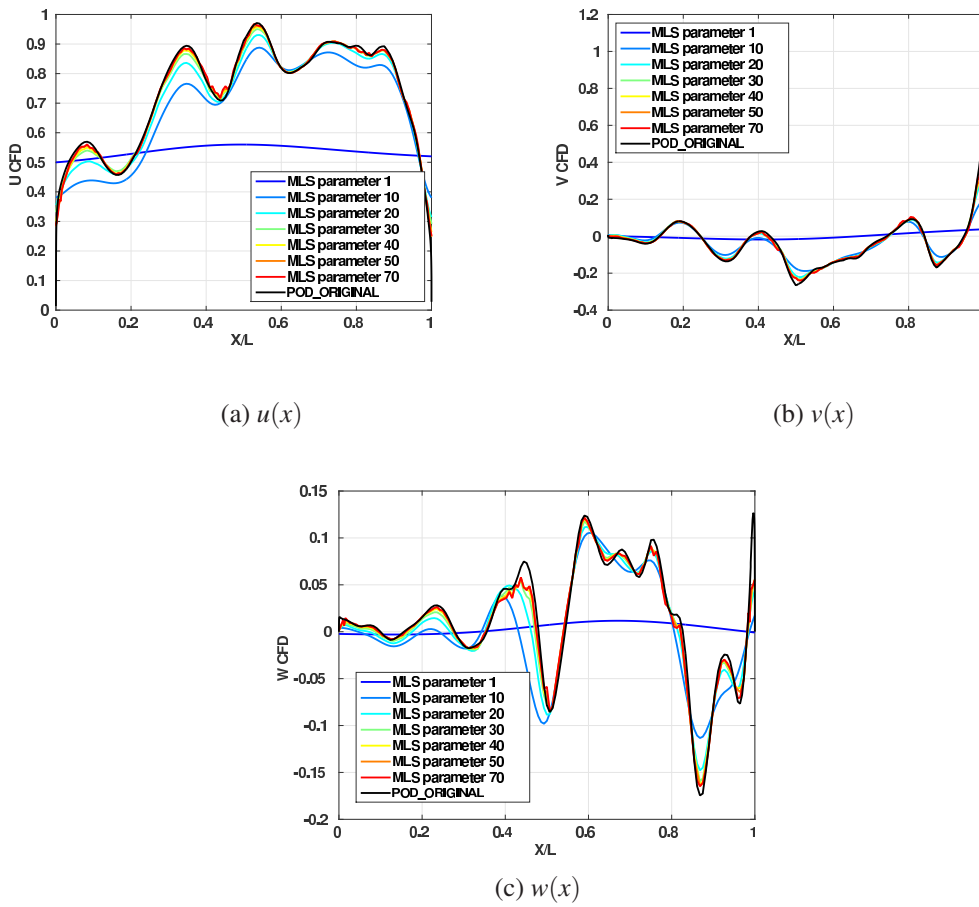


Figure B.5: Influence of the smoothing parameter on the velocity interpolation at  $y = 0$ ,  $z = 0$ . Comparison with the POD\_ORIGINAL reconstruction.

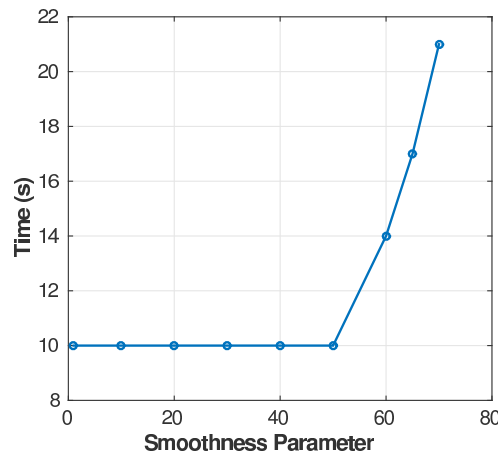


Figure B.6: Reconstruction time with MLS in function of the smoothness parameter.

The moving least square method has a smoothness parameter. This value is higher than 1. Decreasing this value will smooth the result. Increasing this value

on a fine grid will converge the interpolation result towards the original flowfield values (Figure B.5). Figure B.6 shows the MLS reconstruction time as function of the smoothness parameter. After a smoothness of 50, the reconstruction time increases when the smoothness parameter increases. A balance has to be found between accurate reconstructions, and short reconstruction time.

## B.5 Test Case : Clean Cavity Without Doors

This section presents reconstruction results for an idealised cavity of non-dimensional length of 1.00 (along x-axis), depth of 0.14 (along y-axis), and width of 0.29 (along z-axis). The cavity  $L/D$  is 7, and  $W/D$  is 2. The leading edge of the cavity is at  $X/L = 0.0$  and extends to  $X/L = 1.0$ . The shear layer is located at  $Y/L = 0.0$ , and the cavity ceiling at  $Y/L = -0.14$ . The mid-span of the cavity is positioned at  $Z/L = 0.0$  and extends to positive and negative  $Z$  by 0.14.

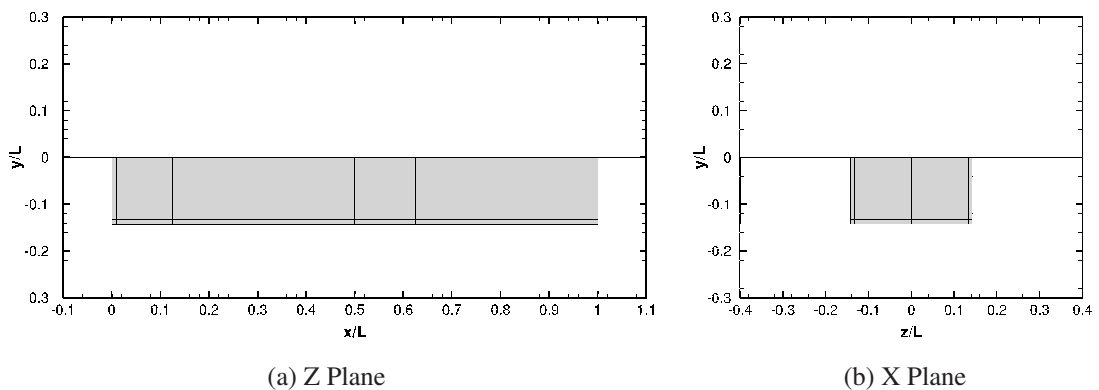


Figure B.7: Geometry of a clean cavity without doors.

### B.5.1 Reconstruction grids

A coarse distribution of points, at which mode information was stored, was defined in the cavity region, and immediately outside. Most of the points are in the shear layer, characterised by large velocity gradients. The grids cover the surfaces to capture the zero velocity on the solids. In the following, five different grids are used to reconstruct the flowfield. POD\_ORIGINAL is the original CFD grid of 7.1 million of points. POD\_VERY\_FINE (Figure B.11) is a grid of 41604 points, POD\_FINE (Figure B.10)

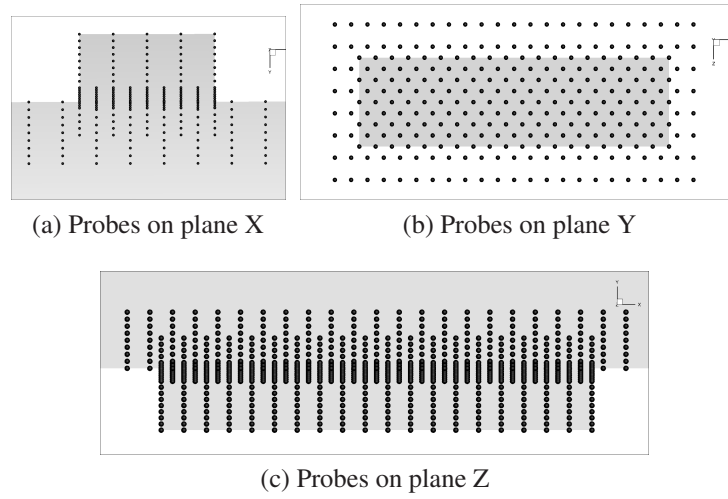


Figure B.8: POD\_COARSE distribution of points around the cavity region.

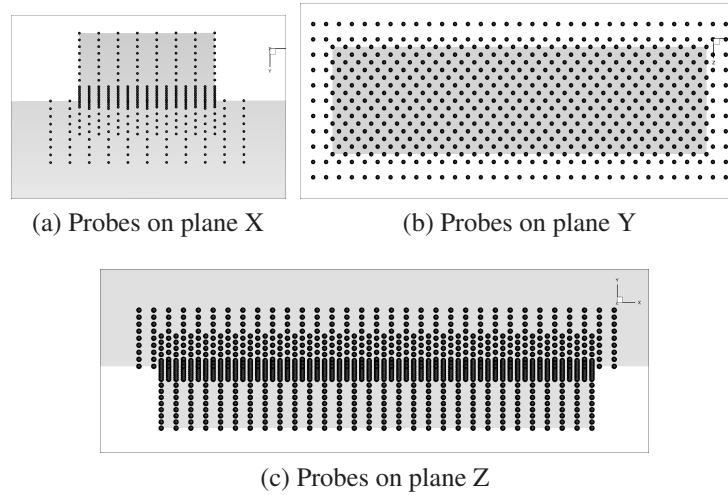


Figure B.9: POD\_MEDIUM distribution of points around the cavity region.

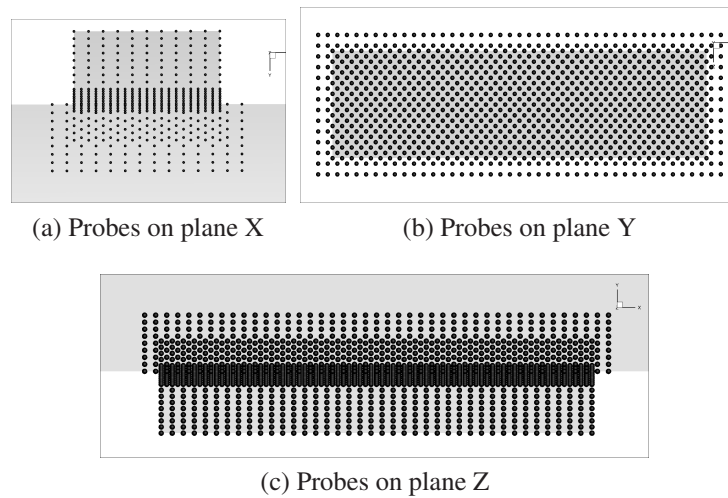


Figure B.10: POD\_FINE distribution of points around the cavity region.

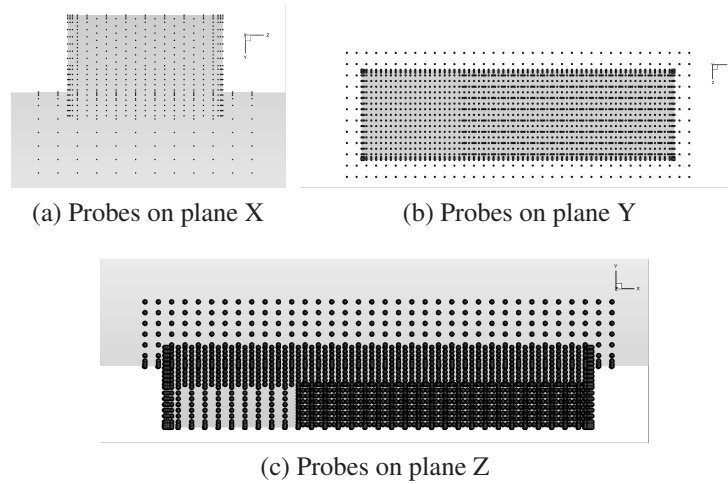


Figure B.11: POD\_VERY\_FINE distribution of points around the cavity region.

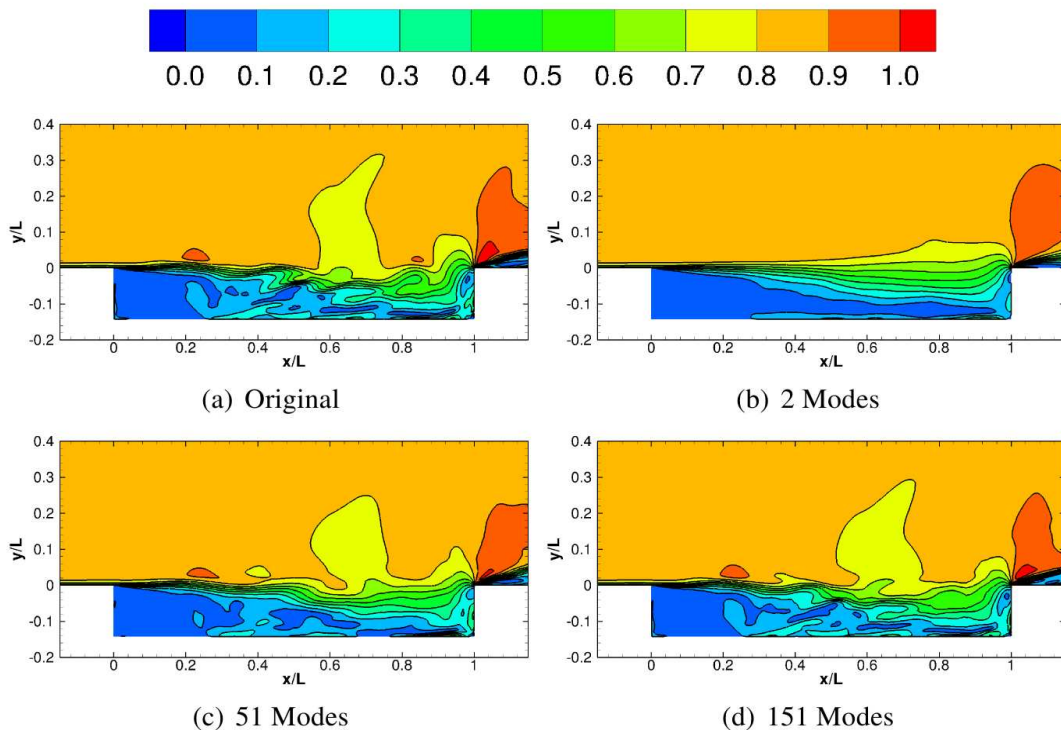


Figure B.12: POD\_ORIGINAL Reconstruction of Mach number at centerline

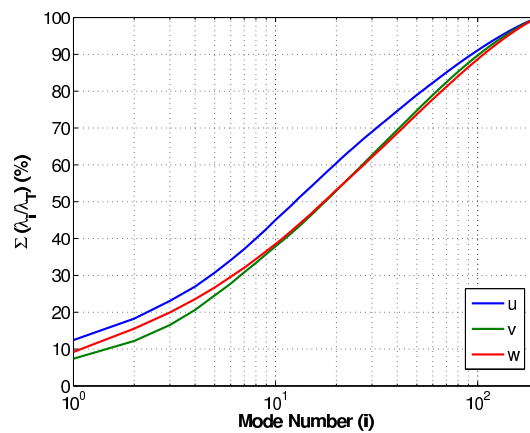


Figure B.13: Energy of the POD reconstruction, as a function of the number of modes.

is a grid of 20758 points, POD\_MEDIUM (Figure B.9) is a grid of 11537 points and POD\_COARSE (Figure B.8) contains 5016 points.

### B.5.2 Reconstruction

The first parameter to select is the number of POD modes to include in the reconstruction. The reconstruction POD\_ORIGINAL shows that 151 modes gives a flowfield that contains more than 95% of the energy (Figures B.12 and B.13). All following reconstructions are performed with 151 modes.

Figures B.14 and B.15 show a good agreement between POD\_ORIGINAL, and POD\_COARSE reconstructions using the MLS interpolation. Most of the discrepancies are located near high velocities gradients in the shear layer. The

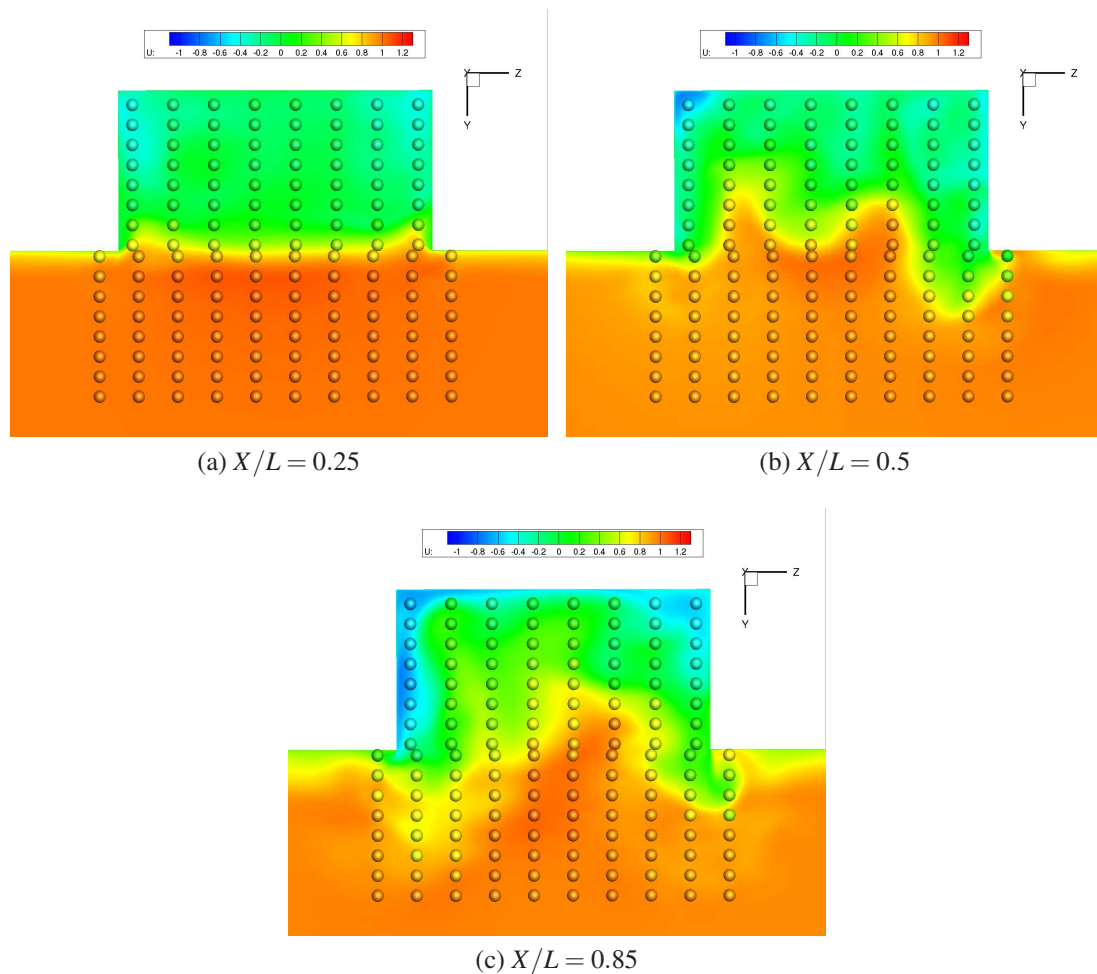
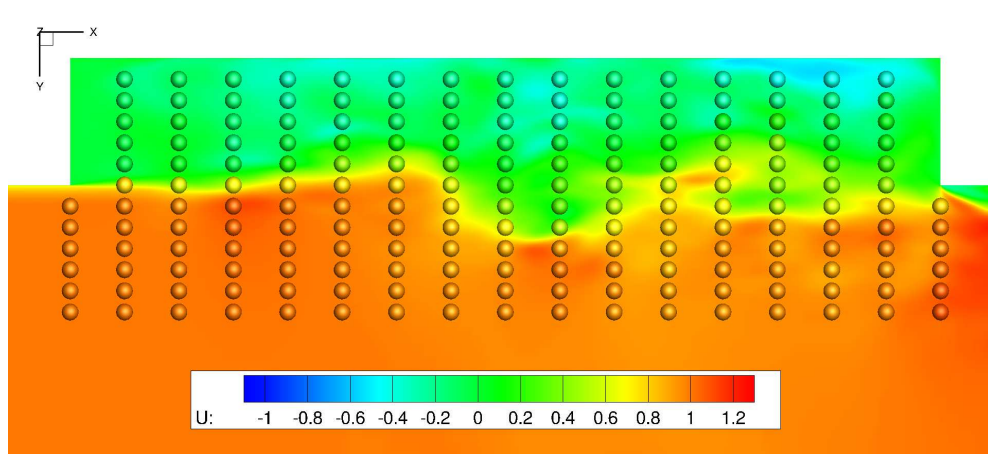
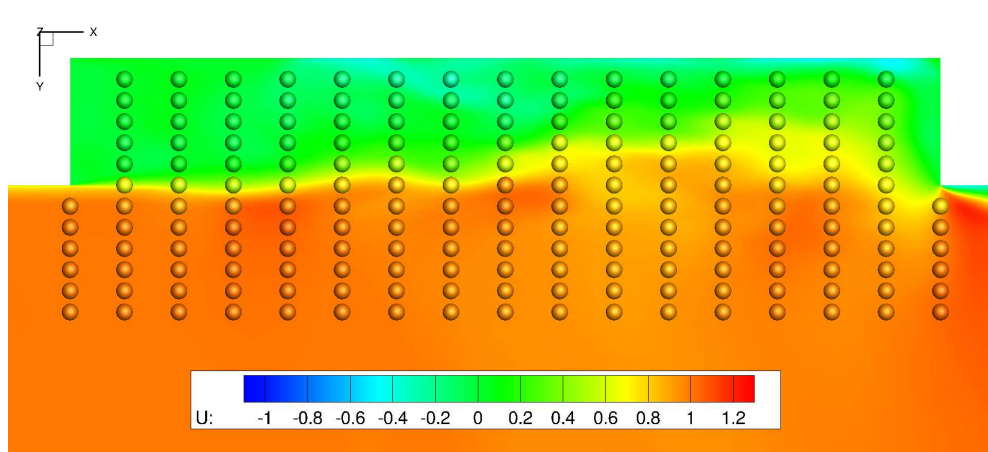


Figure B.14: Reconstructions POD\_COARSE (Spheres) and POD\_ORIGINAL (Background color) at the same CFD time of 80 with 151 modes. Reconstruction at the front, middle, and rear end of the cavity.

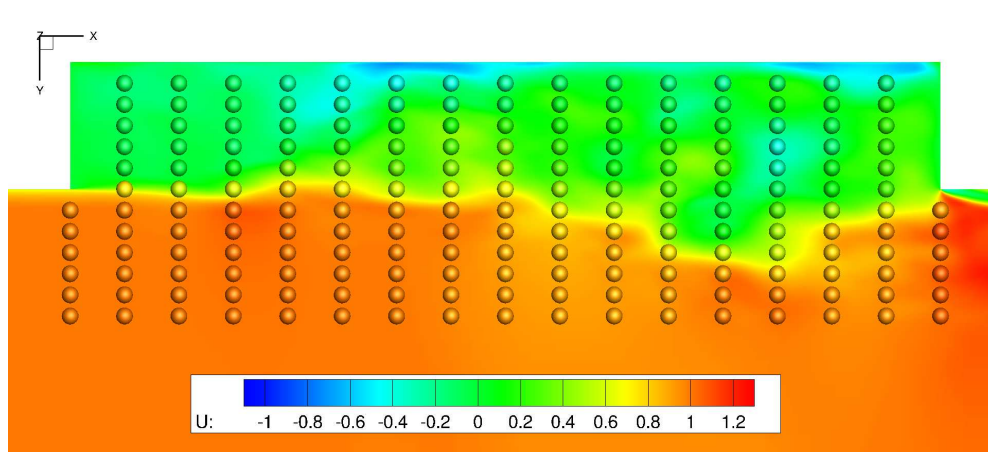
coarseness of the extraction grid only preserve the smoothest gradient of the flowfield.



(a)  $Z/L = 0.1071$



(b)  $Z/L = 0.0$



(c)  $Z/L = -0.1071$

Figure B.15: Reconstructions POD\_COARSE (Spheres) and POD\_ORIGINAL (Background color) at the same CFD time of 80 with 151 modes. Reconstruction at the cavity mid-span, port, and starboard side.

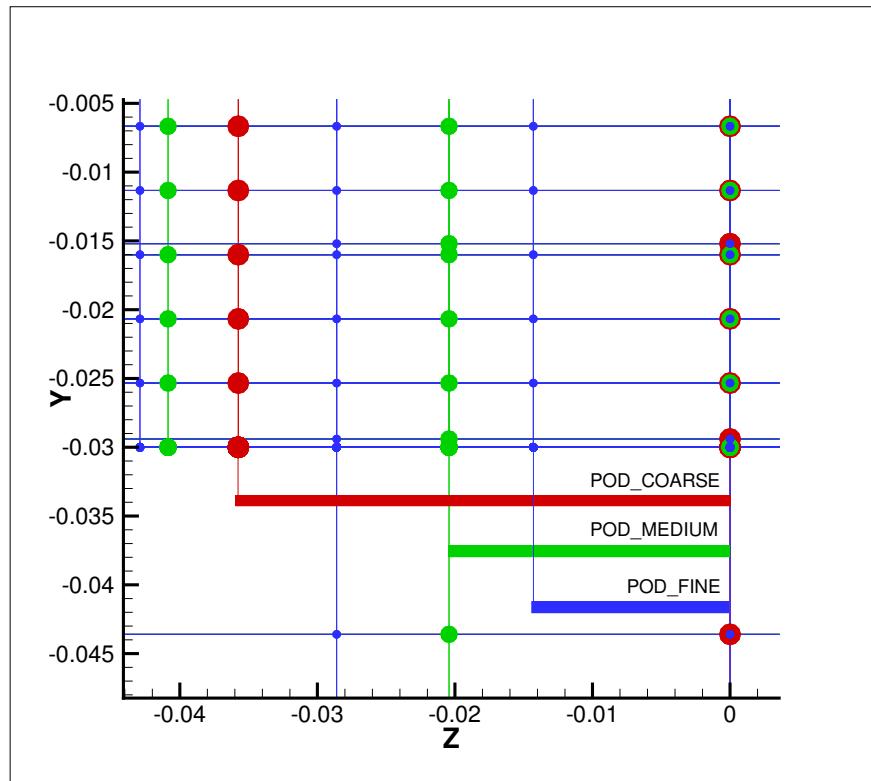


Figure B.16: Minimum distance between points in the coarse, medium and fine grids on the plane facing the flow ( $X=\text{constant}$ ).

Figure B.16 shows the spacing between the grid points for the coarse, medium and fine MATLAB reconstruction data sets at mid-length of the shear layer. The minimum distances between two points are respectively for GRID\_COARSE, GRID\_MEDIUM and GRID\_FINE, 0.036, 0.02 and 0.015 cavity length. To check the accuracy of the interpolation methods, the reconstructions are performed both close, and far away from the data points.

The time required to reconstruct the flowfield, and the size of the files are summarised in table B.1. The reduction of the file size is up to 99.96% for the POD\_COARSE case. Multiple test cases were performed with different numbers of probes, and samples to reconstruct. Overall, the reconstruction of less than a thousand points is done in less than few minutes. Also the nearest neighbour interpolation is faster, but is less accurate than the MLS method. A reconstruction of 324.000 points for 201 time steps was performed using MLS interpolation, and needs few hours to be complete.

Figure B.17 shows the reconstruction of the time signal  $u(t)$  at two probes placed at the shear layer mid-span. It is the most difficult part of the flow to reconstruct due to

	<b>COARSE</b>	<b>MEDIUM</b>	<b>FINE</b>	<b>VERY_FINE</b>
Nb. Grid Points	5016	11537	20758	41604
File Weight (Mb)	17	39	71	142
Weight reduction (%)	99,96	99,91	99,80	99.70
Mean recon. error (%)	19	13	9	6
<b>Reconstruction Time - 1000 Probes, 1 Sample (s)</b>				
NN	1	1	1	3
MLS	5	8	12	23
<b>Reconstruction Time - 1000 Probes, 201 Samples (s)</b>				
NN	14	33	60	91
MLS	34	69	117	214
<b>Reconstruction Time - 3 Probes, 201 Samples (s)</b>				
NN	14	25	44	90
MLS	14	25	44	118
<b>Reconstruction Time - 324.000 Probes, 201 Samples (h)</b>				
MLS	2.7	4.2	7.2	12.4

Table B.1: Time needed for the MATLAB POD reconstruction

the large velocity gradients. The results are compared between POD\_ORIGINAL, and MATLAB reconstructions using nearest neighbour (NN), inverse distance weighting (IDW), and moving least square (MLS) methods. The IDW is shown here, but not included in the final version of the code due to a lack of efficiency against the MLS method. There is a fair agreement between all reconstructions and POD\_ORIGINAL, for all interpolation methods used. All the details of the signal, including the high frequency are well captured.

The velocity field is reconstructed far from the data set grids, at Z positions of 0.017, 0.01 and 0.007 for POD\_COARSE, POD\_MEDIUM and POD\_FINE (figure B.18). In this case, POD\_COARSE shows discrepancies as it cannot capture the strong span-wise gradient within the cells. However, POD\_MEDIUM and POD\_FINE show better agreement. The accuracy of the reconstruction depends on the probe positions. The closer the probe to the data points, the better the result. For each flow, a balance has

to be found between a large file that provides an accurate reconstruction, and a small file that will not necessarily give accurate reconstruction with any of the methods. The moving least square method gave the most accurate temporal reconstructions over the computational domain.

Figures B.19, B.20 and B.21 show the spatial reconstruction of the velocity components along the shear layer. Each reconstruction is performed at points close, and far from the data set points. The flow is reconstructed on 194 points along  $x$ , corresponding to the CFD points. The accuracy depends on the grid density, and the probe position. Reconstructions using inverse distance weighting, are subject to spacial oscillations (Figure B.19d). Figure B.22 shows a simple example of inverse distance weighting over a 1D domain. The contribution of each grid point to the interpolation is shown as thin curves, and the interpolated function is the sum of them, and shown as a thick curve. The oscillations are caused by the weight function, that leads to higher or lower values between the grid points, by addition of the lobes around each points. In addition, the oscillation wavelength becomes larger for increasing spacing between grid points.

The distribution of the points also influences the accuracy of the reconstruction. A coarse grid does not accurately capture the details of the velocity gradients. As a consequence, POD\_COARSE at  $z=0.02$  shows large oscillation with all methods (Figure B.19b). The flowfield is reconstructed on a line alternatively closer to  $z=0.0$ , and  $z=0.036$ , and there is a large gradient between those planes (Figure B.23). As a consequence, the reconstructed value oscillate between the values of those planes.

The nearest neighbour method gives a fair estimation of the velocities close to the grids points for POD\_FINE. In all other cases, far from the grids points, or with a coarser mesh, this method is not accurate. The inverse distance weighting method has better performances than NN, but is subject to oscillations around the expected value. The moving least square method generates the most accurate reconstruction for all grids within minutes.

In conclusion, to obtain accurate reconstructions, the values from a large POD data set have to be extracted on a well-chosen grid. All zones with large gradient as the shear layer and the walls must be meshed with a higher density than other smoother parts. The reconstructions have to be performed as close as possible to the grid points. Finally, the combination of the POD\_FINE grid, with the Moving Least Square method gave the best accuracy with respect to the computational time.

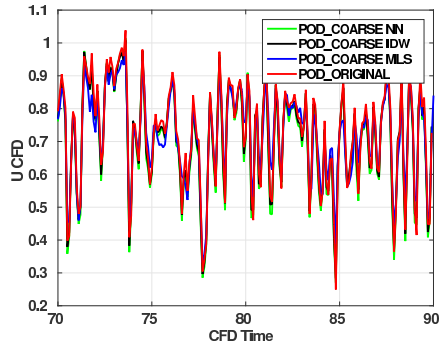
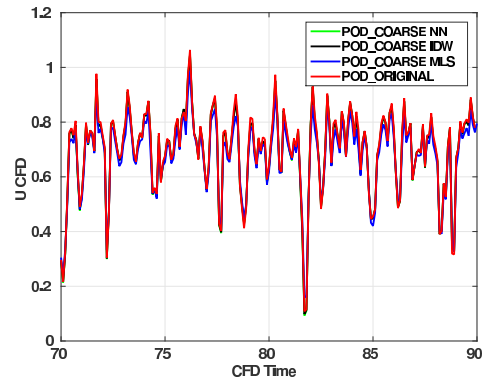
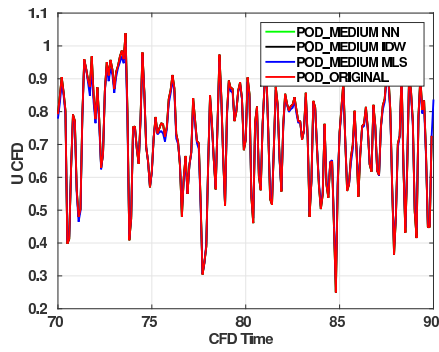
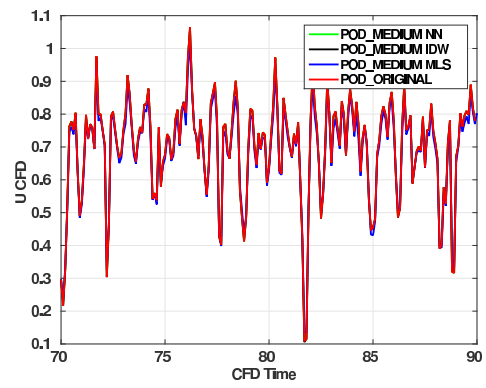
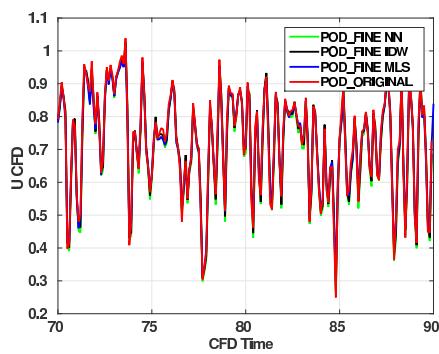
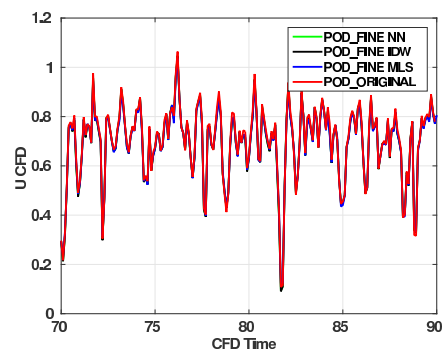
(a)  $x/L = 0.43$ (b)  $x/L = 0.95$ (c)  $x/L = 0.43$ (d)  $x/L = 0.95$ (e)  $x/L = 0.43$ (f)  $x/L = 0.95$ 

Figure B.17: Temporal reconstructions of  $u(t)$  at two probes at the mid-span of the shear layer using POD\_COARSE (a-b), POD\_MEDIUM (c-d) and POD\_FINE (e-f).

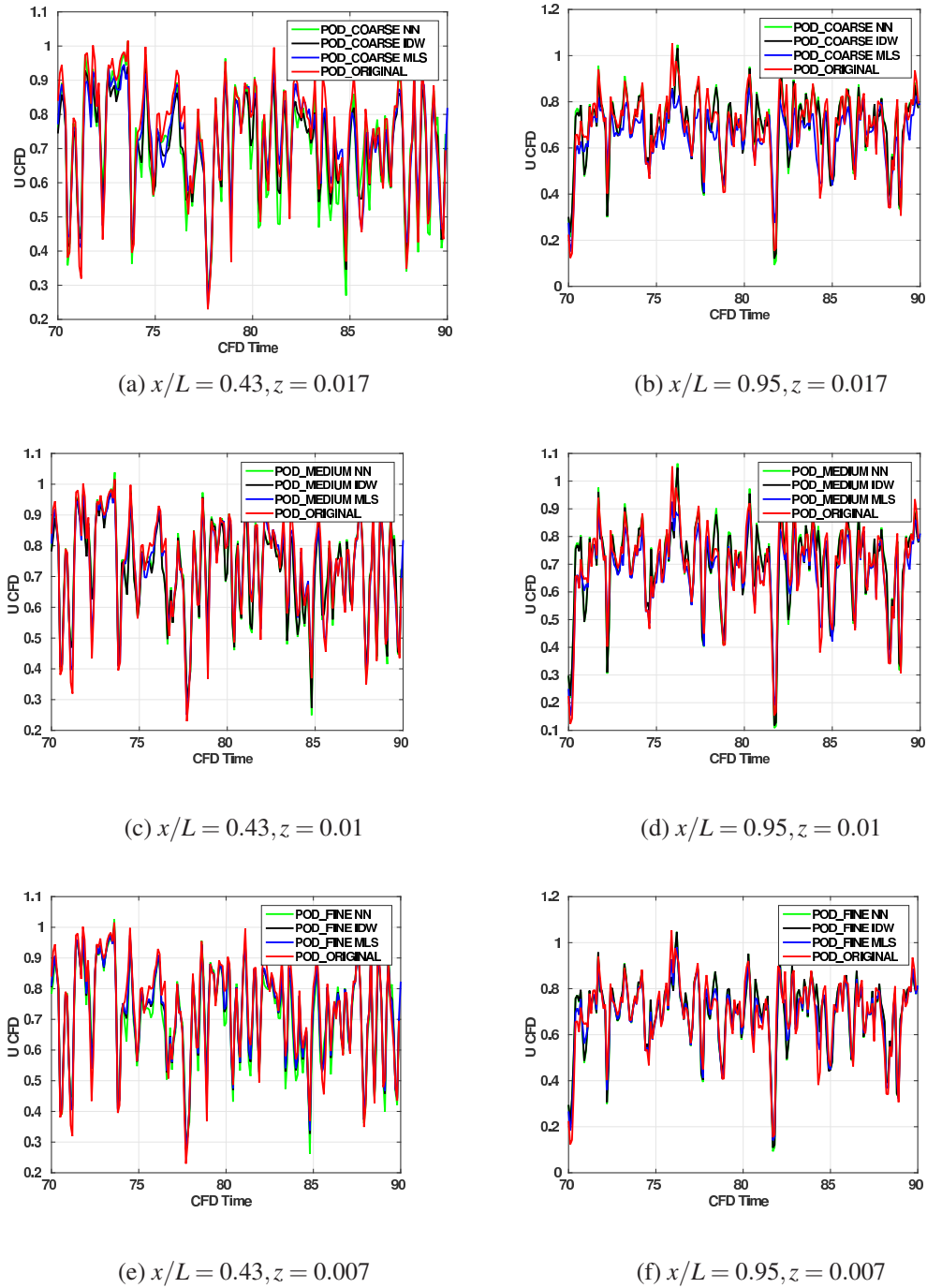
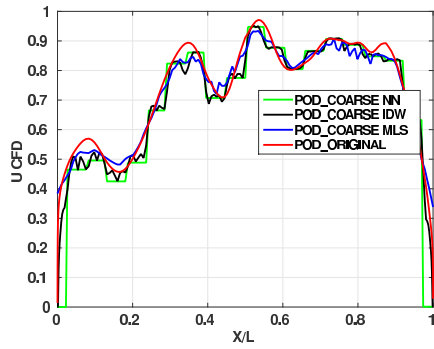
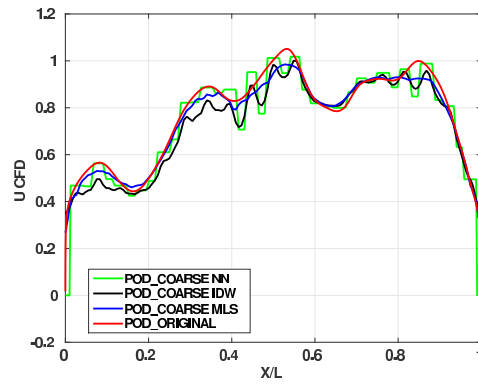


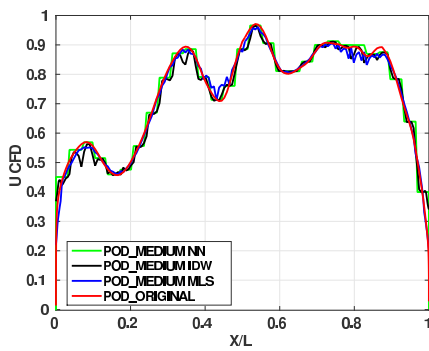
Figure B.18: Temporal reconstructions of  $u(t)$  at two probes at the shear layer using POD\_COARSE (a-b), POD\_MEDIUM (c-d) and POD\_FINE (e-f).



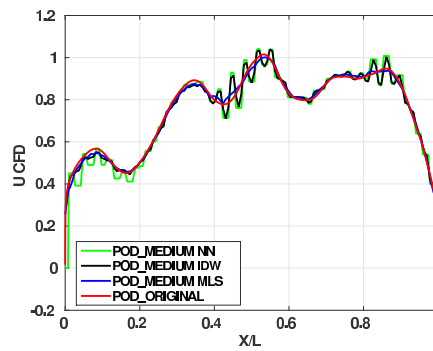
(a) POD\_COARSE at  $z=0.0$



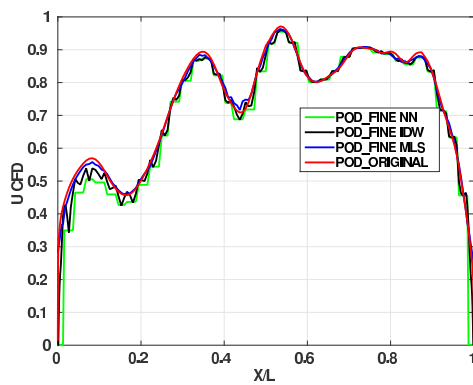
(b) POD\_COARSE at  $z=0.02$



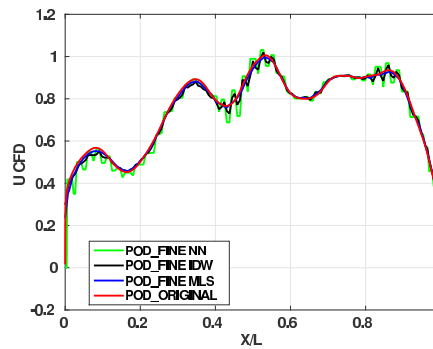
(c) POD\_MEDIUM at  $z=0.0$



(d) POD\_MEDIUM at  $z=0.01$

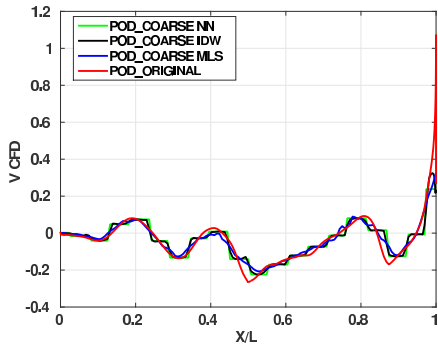


(e) POD\_FINE at  $z=0.0$

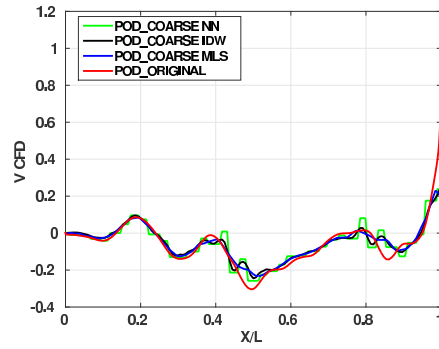


(f) POD\_FINE at  $z=0.008$

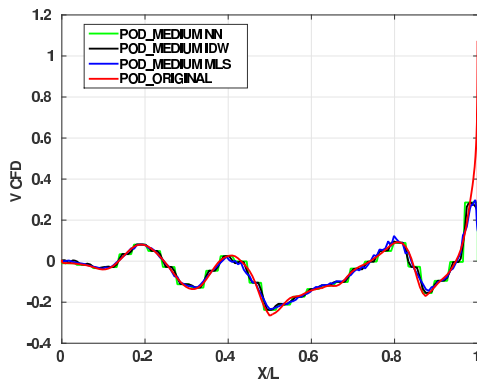
Figure B.19: Spatial reconstructions of  $u(x)$  at shear layer.



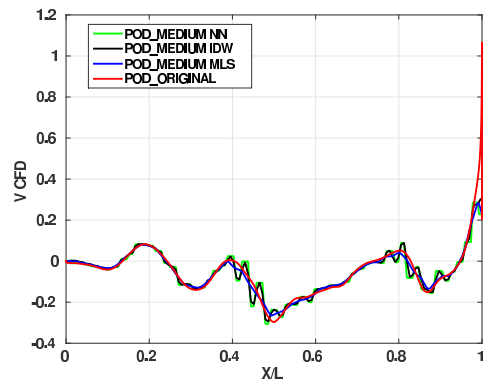
(a) POD\_COARSE at  $z=0.0$



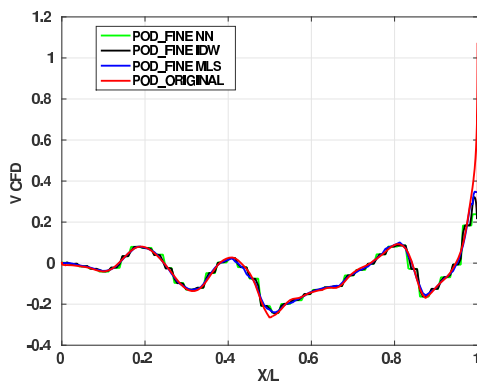
(b) POD\_COARSE at  $z=0.02$



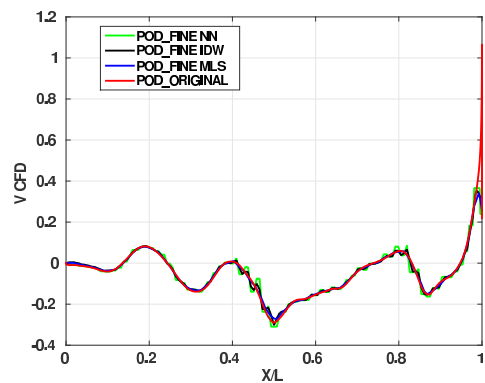
(c) POD\_MEDIUM at  $z=0.0$



(d) POD\_MEDIUM at  $z=0.01$

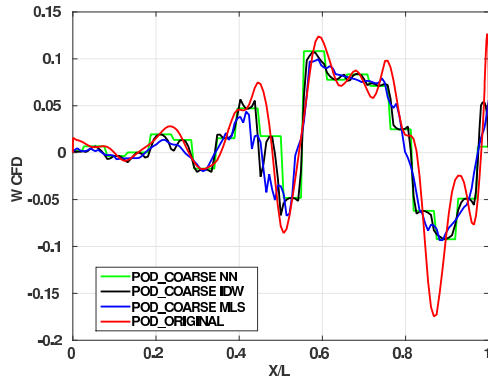


(e) POD\_FINE at  $z=0.0$

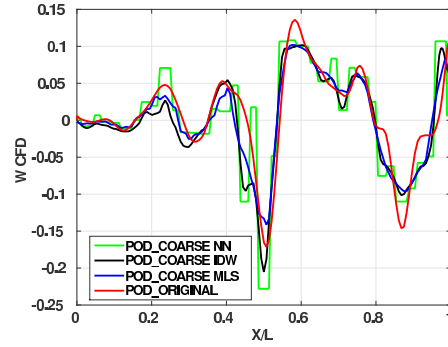


(f) POD\_FINE at  $z=0.008$

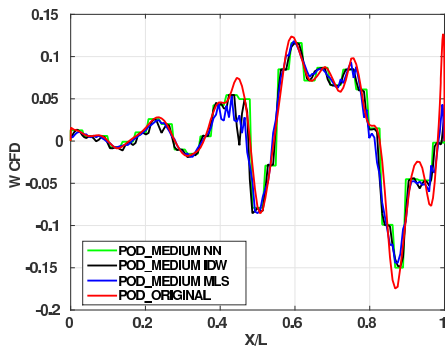
Figure B.20: Spatial reconstructions of  $v(x)$  at shear layer.



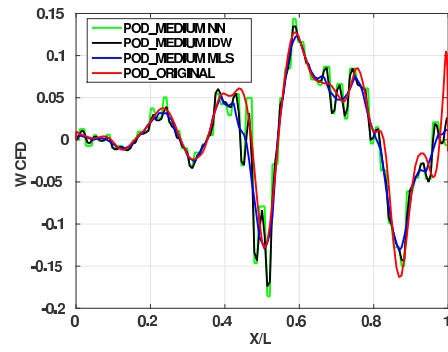
(a) POD\_COARSE at  $z=0.0$



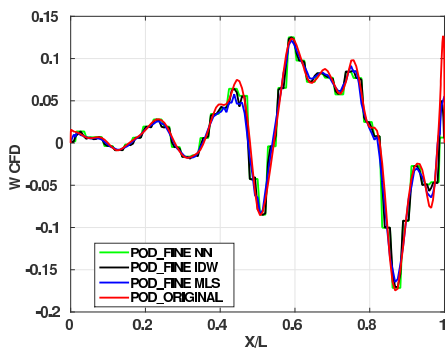
(b) POD\_COARSE at  $z=0.02$



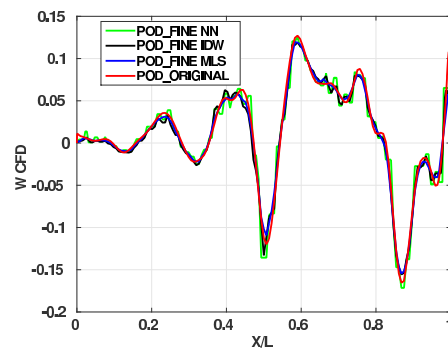
(c) POD\_MEDIUM at  $z=0.0$



(d) POD\_MEDIUM at  $z=0.01$



(e) POD\_FINE at  $z=0.0$



(f) POD\_FINE at  $z=0.008$

Figure B.21: Spatial reconstructions of  $w(x)$  at shear layer.

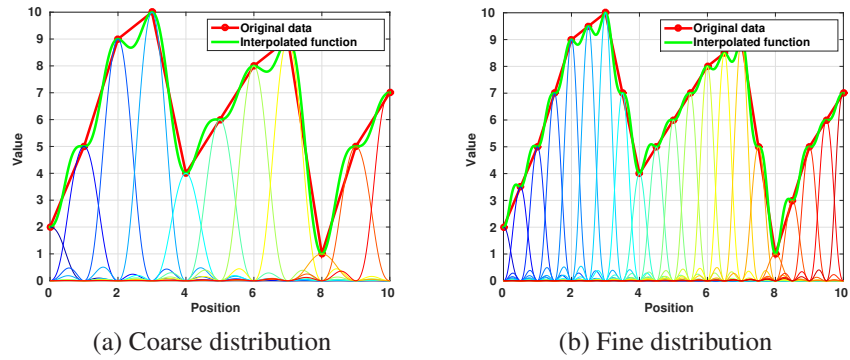


Figure B.22: 1D example of the effect of the point density of the Inverse Distance Weighting interpolation.

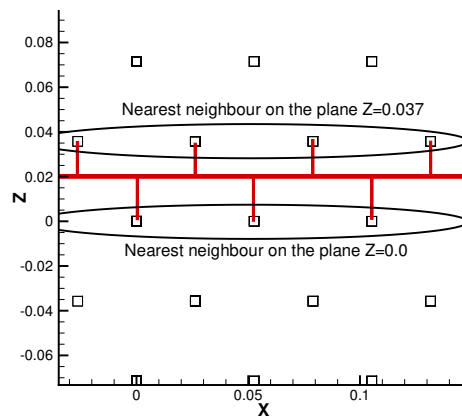


Figure B.23: Position of the reconstruction axis in the POD\_COARSE case. The closer value is alternating between  $z=0.0$  and  $z=0.037$ .

# Appendix C

## Post-processing Codes

### C.1 Beamforming

The beamformer was written in Matlab, and is composed of 5 functions. *beamforming.m* reads three inputs files, containing the probe positions, the microphone signals, and the flowfield around the scanned zone. Then, *beamforming\_function.m* computes the scanned grid, and the distances between the microphones and the scan grid with the function *compute\_distances.m*. After, it computes the beamforming output using *BF3D\_function.m*, and *compute\_fft.m*. At the end, *beamforming\_function.m* writes a Tecplot file of the beamforming output on the scan grid. The theory and the results are presented chapter 4 of the thesis.

#### LISTING : beamforming.m

```
1 %% =====
2 % BEAM FORMER – Giulia Chirico – Gaetan Loupy
3 %% =====
4 % This script implements the conventional beamformer algorithm ,
5 % the MUSIC technique in the case of a 3D array of microphones .
6 % The program takes in input position and signal of a sensor array
7 % and gives as output the noise map on the scan domain .
8 % -----
9 % The notation used here is the one used by Simley in his thesis
10 % "Development of an Acoustic Array for Wind Turbine Aeroacoustic Noise
11 % Analysis" from which this script is derived . In particular , a short
12 % description of the two algorithms used here can be found in Chapter 2
13 % and a MATLAB code is also included in the Appendix A for reference .
14 %% =====
15
16 function [] = beamforming ()
17
```

```

18 % Output file name
19 outfile = 'beamformed_data';
20
21 %% -----
22 % Signal Input Data
23 %% -----
24
25 % microphone positions in the sensor array (x,y,z)
26 sens_array = 'microphones_pos.dat';
27 % signal from each microphone (format file: time, p_microphone 1, ...,
    p_microphone n)
28 signal = 'microphones.dat';
29 % The last signal_length steps will be taken
30 signal_length = 147455;
31 % Activate a hamming windowing for the fft computation (For short signals)
32 windowing = 0;
33
34 % scan domain (position in the absolute reference system non scaled)
35 x = [-0.50,0.50]; % xlim
36 y = [ 0.00,1.00]; % ylim
37 z = [-0.50,0.50]; % zlim
38 nx = 60; % number of x points
39 ny = 60; % number of y points
40 nz = 60; % number of z points
41
42 %% -----
43 % Dimensionalisation
44 %% -----
45
46 % Dimensionalisation pressure and time signals, lengths
47 rhos=1.11; % Static density kg/m3
48 U0=0.00; % Satic velocity m/s
49 Ps=1.00; % P=Pfile*Ps, 1.0 for no diemntionalisation (ex: rhos*U0*U0)
50 L=1.00; % Factor to go to dimentional lengths (ex: 3.594)
51 td=1.00; % time=tfile*td, 1.0 for no dimentionalisation (ex: L/U0)
52
53 %% -----
54 % Distances computation
55 %% -----
56
57 % Velocity file (x,y,z,u,v,w) cfd values, 'none' for no velocity
58 flow_file='none';
59 % Load the distances, 'none' for calculation of distances
60 distance_file='none';
61 % Grid points in x,y,z to store velocity
62 nbptsvel=[20,40,10];
63 % Convergence factor, the lower the faster and less stable
64 Vconv=2.0;
65 % Maximum iteration
66 max_try=40;
67 % Tolerance trajectory to microphone distance

```

```

68     tolerance=0.005;
69     % Save the distances result
70     save_dist=0;
71
72     %% -----
73     % Beamforming Parameters
74     %% -----
75
76     % Beamforming algorithm choice:
77     % 0 = conventional beamforming (see pages 23–25 of Simley thesis),
78     % 1 = MUSIC algorithm (see pages 41–45 of Simley thesis)
79     beamf = 1;
80
81     % Beamforming algorithm parameters:
82     diagelim = 1;          % diagonal elimination (see pages 37–38 of Simley thesis)
83     N_sources = 2;        % number of sources for MUSIC algorithm
84
85     % lower and upper frequencies of the band to be analyzed
86     freq_min = [1800];
87     freq_max = [1800]; % Hz
88
89     % speed of sound
90     sound_speed = 335.3101807;
91
92     %% -----
93     % Run Beamforming
94     %% -----
95     % Point to script folder
96     addpath( '/home/cfd/gloupy/PROJECT/utilities/postprocessing_scripts/beamforming' );
97     beamforming_function( outfile , sens_array , signal , signal_length , x , y , z , nx , ny , nz , U0 , Ps
98         , L , td , flow_file , nbptsvel , Vconv , max_try , tolerance , save_dist , distance_file ,
99         , beamf , diagelim , N_sources , freq_min , freq_max , sound_speed , windowing )
100 end

```

### LISTING : beamforming function.m

```

1  %% =====
2  % BEAM FORMER – Giulia Chirico – Gaetan Loupy
3  %% =====
4  % This script implements the conventional beamformer algorithm ,
5  % the MUSIC technique in the case of a 3D array of microphones .
6  % The program takes in input position and signal of a sensor array
7  % and gives as output the noise map on the scan domain .
8  % -----
9  % The notation used here is the one used by Simley in his thesis
10 % "Development of an Acoustic Array for Wind Turbine Aeroacoustic Noise
11 % Analysis" from which this script is derived. In particular , a short
12 % description of the two algorithms used here can be found in Chapter 2
13 % and a MATLAB code is also included in the Appendix A for reference ..
14 %% =====
15 %% Grid generation
16 function [] = beamforming_function( outfile , mic , signal , x , y , z , nx , ny , nz , U0 , Ps , L , td ,
    flow_file , blkx , blkz , blkz , nbptsvelx , nbptsvely , nbptsvelz , Vconv , max_try , tolerance ,

```

```

save_dist , distance_file , beamf , diagelim , N_sources , freq_min , freq_max , sound_speed ,
windowing , reference , B1 , B2)
17 close all
18
19 % Load microphone position
20 mic = load(mic);
21 % number of microphones in the array
22 Nmic = size(mic,1);
23 %-----
24 % time vector and pressure signal data extraction
25 %-----
26
27 signal = load(signal);
28 time = signal(:,1)*td;
29 dtd=time(1,2)-time(1,1); % Timestep
30 f_samp = 1/dtd; % sampling frequency
31 ym = signal(:,2:end)*Ps; % dimensions = [nsensors , sig_len]
32 clear signal
33 % Withdraw the mean from the pressure signals
34 for s=1:Nmic
35     ym(s,:)=ym(s,:)-mean(ym(s,:));
36 end
37
38 %-----
39 % Create grid
40 %-----
41 [grid , nxf , nyf , nzf]=compute_grid(x , y , z , nx , ny , nz);
42 grid=grid*L;
43 mic = mic*L;
44 num_points=nxf*nyf*nzf;
45 save('grid.dat' , 'grid' , '-ascii');
46 %-----
47 % Frequency Domain Beamforming
48 %-----
49 tic
50
51 % Distance computation
52 if strcmp(distance_file , 'none')==1
53     % Compute the distances
54     [dist_g , coef_probe]=compute_distances(L , blkx , blk_y , blk_z , nbptsvelx , nbptsvely ,
55         nbptsvelz , grid , sound_speed , U0 , mic , flow_file , Vconv , max_try , tolerance);
56     if save_dist==1
57         save(strcat(outfile , '_dist.mat') , 'dist_g' , 'coef_probe');
58         display('Distances saved in dist.mat');
59     end
60 else
61     % Load the distances
62     load(distance_file);
63     if save_dist==1
64         save(strcat(outfile , '_dist.mat') , 'dist_g' , 'coef_probe');
65         display('Distances saved in dist.mat');

```

```

65         end
66     end
67
68     dist_mic=dist_g(:,1);
69     % Difference of positions
70     dist=bsxfun(@minus,dist_mic,dist_g)';
71     clear dist_mic sens_array
72
73     % Compute the fft of the signals
74     [fft_signal,freq]=compute_fft(ym,f_samp,windowing);
75     clear ym
76
77     % Find the closet points to the reference points
78     % Scale reference
79     reference=reference*L;
80     probe2ref = bsxfun(@plus,sum(grid.^2,2),sum(reference.^2,2)') - 2*(grid*reference
81         ');
82
83     [~,closest]=min(probe2ref);
84
85     %%
86     display('Running Beamforming...');
87     Power_detected=zeros(num_points,length(freq_min));
88
89     % Number of frequencies
90     nfreq=length(freq_min);
91
92     for k = 1 : nfreq
93         freq_min_int = freq_min(k);
94         freq_max_int = freq_max(k);
95         Power_detected(:,k)=BF3D_function(Nmic,sound_speed,freq_min_int,freq_max_int,
96             beamf,diagelim,N_sources,dist,nxf,nyf,nzf,fft_signal,freq,1,coef_probe);
97
98         % Find the peak location
99         [~,loc_found] = max(Power_detected(:,k));
100        fprintf(1,'Source at x = %f, y = %f, z = %f \n',grid(loc_found,1),grid(
101            loc_found,2),grid(loc_found,3));
102
103        % Convert to dB
104        Power_detected(:,k)=20*log10(Power_detected(:,k).^2/2e-5);
105
106        % Scale the values
107        A1=Power_detected(closest(1),k);
108        A2=Power_detected(closest(2),k);
109        %Power_detected(:,k)=B1(k)+(B2(k)-B1(k))*(Power_detected(:,k)-A1)/(A2-A1);
110    end
111
112    toc
113
114    % Open output file
115    name=strcat(outfile, '.tec');
116    tec_output=fopen(name,'w');

```

```

113     fprintf(tec_output, 'TITLE      = "Beamforming"\n');
114     fprintf(tec_output, 'VARIABLES = "X" "Y" "Z" "Pow"\n');
115
116     for k = 1 : length(freq_min)
117         fprintf(tec_output, 'ZONE T="Beamforming f=%0.2f-%0.2fHz"\n', freq_min(k),
118             freq_max(k));
119         fprintf(tec_output, 'STRANDID=0, SOLUTIONTIME=0\n');
120         fprintf(tec_output, 'I=%d, J=%d, K=%d, ZONETYPE=Ordered\n', nxf, nyf, nzf);
121         fprintf(tec_output, 'DATAPACKING=POINT\n');
122         fprintf(tec_output, 'DT=(DOUBLE DOUBLE DOUBLE DOUBLE)\n');
123
124         for i=1:num_points
125             fprintf(tec_output, '%e %e %e %e\n', grid(i,1), grid(i,2), grid(i,3),
126                 Power_detected(i,k));
127         end
128     end
129     fclose(tec_output);
130     command=strcat({'preplot '}, name);
131     system(command{1});
132     delete(name)
133
134 end
135
136 %% Grid generation
137 function [grid, nxf, nyf, nzf] = compute_grid(x, y, z, nx, ny, nz)
138
139 % The data must be interpolated in a meshgrid
140 % Number of blocks in x,y,z
141 nbx=numel(x)-1;
142 nby=numel(y)-1;
143 nbz=numel(z)-1;
144
145 % Vectors to define the grid
146 % X
147 vecx=x(1);
148 for xg=1:nbx
149     vecx=[vecx, x(xg):(x(xg+1)-x(xg))/nx(xg):x(xg+1)];
150 end
151 % Y
152 vecy=y(1);
153 for yg=1:nby
154     vecy=[vecy, y(yg):(y(yg+1)-y(yg))/ny(yg):y(yg+1)];
155 end
156 % Z
157 vecz=z(1);
158 for zg=1:nbz
159     vecz=[vecz, z(zg):(z(zg+1)-z(zg))/nz(zg):z(zg+1)];
160 end
161
162 % Keep unique points
163 vecx=unique(vecx);

```

```

162     vecy=unique( vecy );
163     vecz=unique( vecz );
164
165     % Grid size
166     nxf = numel( vecx );
167     nyf = numel( vecy );
168     nzf = numel( vecz );
169
170     % Generate grid
171     [X,Y,Z] = meshgrid( vecx , vecy , vecz );
172
173     grid=zeros( nxf*nyf*nzf ,3 );
174
175     indice=0;
176     % loop over number of points
177     for k=1:nzf
178         for i=1:nyf
179             for j=1:nxf
180                 indice=indice+1;
181                 grid( indice ,1)=X( i , j , k );
182                 grid( indice ,2)=Y( i , j , k );
183                 grid( indice ,3)=Z( i , j , k );
184             end
185         end
186     end
187 end

```

### LISTING : compute\_distances.m

```

1 function [probe2mic , coef_probe] = compute_distances( L , blkx , blkz , nbptsvelx ,
2     nbptsvelz , probes , c , V_inf , mic , flow_file , Vconv , max_try , tolerance )
3
4 % There is no freestream
5 if strcmp( 'none' , flow_file )==1
6     % Directly compute distances
7     probe2mic = sqrt( bsxfun( @plus , sum( probes .^2 , 2 ) , sum( mic .^2 , 2 ) ) - 2*( probes *
8         mic ) );
9
10    % Number of probes
11    nb_probes=size( probes , 1 );
12    % Number of microphone
13    Nmic=size( mic , 1 );
14    % Number of microphone used by a probe
15    coef_probe=ones( nb_probes , 1 ) * Nmic;
16 else
17
18    % Number of microphone
19    Nmic=size( mic , 1 );
20
21    % Load velocity field
22    flow=load( flow_file );
23    % Velocities
24    freestream=flow( : , [4 , 5 , 6] ) * V_inf;
25    % Mesh coordinates

```

```

23     x_tmp=flow (: ,1)*L;
24     y_tmp=flow (: ,2)*L;
25     z_tmp=flow (: ,3)*L;
26     clear flow
27
28     % Mesh limits
29     xlm=[min([ probes (: ,1) ; mic (: ,1) ; x_tmp ]) ,max([ probes (: ,1) ; mic (: ,1) ; x_tmp ])
        ]*1.05;
30     ylm=[min([ probes (: ,2) ; mic (: ,2) ; y_tmp ]) *1.1 ,max([ probes (: ,2) ; mic (: ,2) ; y_tmp ])
        ]*1.2];
31     zlm=[min([ probes (: ,3) ; mic (: ,3) ; z_tmp ]) ,max([ probes (: ,3) ; mic (: ,3) ; z_tmp ])
        ]*1.05;
32
33     % The data must be interpolated in a meshgrid
34     % Number of blocks in x,y,z
35     nb_blkx=numel( blkx )-1;
36     nb_blkz=numel( blkz )-1;
37     nb_blkz=numel( blkz )-1;
38     % Scale the grid
39     blkx=blkx*L;
40     blkz=blkz*L;
41     blkz=blkz*L;
42     % Vectors to define the grid
43     % X
44     vecx=blkx(1);
45     for xg=1:nb_blkx
46         vecx=[vecx , blkx(xg):( blkx(xg+1)-blkx(xg) ) / nbptsvelx(xg) : blkx(xg+1) ];
47     end
48     % Y
49     vecy=blkz(1);
50     for yg=1:nb_blkz
51         vecy=[vecy , blkz(yg):( blkz(yg+1)-blkz(yg) ) / nbptsvelz(yg) : blkz(yg+1) ];
52     end
53     % Z
54     vecz=blkz(1);
55     for zg=1:nb_blkz
56         vecz=[vecz , blkz(zg):( blkz(zg+1)-blkz(zg) ) / nbptsvelz(zg) : blkz(zg+1) ];
57     end
58
59     % Check if the mesh has to be extended
60     % X
61     if xlm(1)<vecx(1)
62         vecx=[xlm(1):( blkx(2)-blkx(1) ) / nbptsvelx(1) : vecx(1) , vecx ];
63     end
64     if vecx(end)<xlm(2)
65         vecx=[vecx , vecx(end):( blkx(end)-blkx(end-1) ) / nbptsvelx(end) : xlm(2) ];
66     end
67     % Y
68     if ylm(1)<vecy(1)
69         vecy=[ylm(1):( blkz(2)-blkz(1) ) / nbptsvelz(1) : vecy(1) , vecy ];
70     end

```

```

71     if vecy(end)<ylm(2)
72         vecy=[vecy, vecy(end):(blkz(end)-blkz(end-1))/nbptsvely(end):ylm(2)];
73     end
74     % Z
75     if zlm(1)<vecz(1)
76         vecz=[zlm(1):(blkz(2)-blkz(1))/nbptsvelz(1):vecz(1), vecz];
77     end
78     if vecz(end)<zlm(2)
79         vecz=[vecz, vecz(end):(blkz(end)-blkz(end-1))/nbptsvelz(end):zlm(2)];
80     end
81
82     % Keep unique points
83     vecx=unique(vecx);
84     vecy=unique(vecy);
85     vecz=unique(vecz);
86
87     % Generate grid
88     [x,y,z] = meshgrid(vecx, vecy, vecz);
89
90     % Interpol freestream
91     u0 = griddata(x_tmp, y_tmp, z_tmp, freestream(:,1), x, y, z, 'linear');
92     v0 = griddata(x_tmp, y_tmp, z_tmp, freestream(:,2), x, y, z, 'linear');
93     w0 = griddata(x_tmp, y_tmp, z_tmp, freestream(:,3), x, y, z, 'linear');
94     clear freestream
95
96     % For linear indices computation
97     siz=size(u0);
98     k = [1 cumprod(siz(1:end-1))];
99
100    % Add values where there is NaN, cavity only
101    putfreestream=find(isnan(u0)==1 & y>0);
102    putzero=find(isnan(u0)==1 & y<=0);
103    u0(putfreestream)=V_inf;
104    u0(putzero)=0;
105    v0([putfreestream; putzero])=0;
106    w0([putfreestream; putzero])=0;
107
108    % Write the flowfield for checks
109    % loop over number of points
110    % Open output file
111    name=strcat('check_velocity.tec');
112    nbpx=numel(vecx);
113    nbpy=numel(vecy);
114    nbpz=numel(vecz);
115    tec_output=fopen(name, 'w');
116    fprintf(tec_output, 'TITLE      = "Beamforming"\n');
117    fprintf(tec_output, 'VARIABLES = "X" "Y" "Z" "U" "V" "W"\n');
118    fprintf(tec_output, 'ZONE T="Velocity field"\n');
119    fprintf(tec_output, 'STRANDID=0, SOLUTIONTIME=0\n');
120    fprintf(tec_output, 'I=%d, J=%d, K=%d, ZONETYPE=Ordered\n', nbpx, nbpy, nbpz);
121    fprintf(tec_output, 'DATAPACKING=POINT\n');

```

```

122     fprintf(tec_output, 'DT=(DOUBLE DOUBLE DOUBLE DOUBLE DOUBLE DOUBLE)\n');
123     for kt=1:nbpz
124         for it=1:nbpy
125             for jt=1:nbpx
126                 fprintf(tec_output, '%e %e %e %e %e %e\n', x(it, jt, kt), y(it, jt, kt),
127                     z(it, jt, kt), u0(it, jt, kt), v0(it, jt, kt), w0(it, jt, kt));
128             end
129         end
130     end
131     fclose(tec_output);
132     command= strcat({'preplot'}, name);
133     system(command{1});
134     delete(name)
135
136
137     clear x y z
138
139     figure(2)
140     % Plot mesh limits
141     [x1, y1, z1] = meshgrid(xlm(1):(xlm(2)-xlm(1)):xlm(2), ...
142         ylm(1):(ylm(2)-ylm(1)):ylm(2), ...
143         zlm(1):(zlm(2)-zlm(1)):zlm(2));
144
145     plot3(reshape(x1, numel(x1), 1), reshape(y1, numel(x1), 1), reshape(z1, numel(x1), 1)
146         , 'd');
147
148     hold on
149     % Plot microphones
150     plot3(mic(:, 1), mic(:, 2), mic(:, 3), 'or', 'MarkerFaceColor', [1, 0, 0]);
151
152     % Plot first probe
153     plot3(probes(1, 1), probes(1, 2), probes(1, 3), 'og', 'MarkerFaceColor', [0, 1, 0]);
154
155
156     % Number of probes
157     nb_probes=size(probes, 1);
158
159
160     % Real distance between a probe and a microphone at a velocity c
161     probe2mic=zeros(nb_probes, Nmic);
162
163
164     % Compute distances probe to microphone, compoments
165     dist_comp_x=bsxfun(@minus, mic(:, 1), probes(:, 1)');
166     dist_comp_y=bsxfun(@minus, mic(:, 2), probes(:, 2)');
167     dist_comp_z=bsxfun(@minus, mic(:, 3), probes(:, 3)');
168
169     % Total distances
170     Dist=sqrt(dist_comp_x.^2+dist_comp_y.^2+dist_comp_z.^2);
171
172
173     % Maximum and mean distance error
174     max_error=0;
175     mean_error=0;
176
177
178     % Number of microphone used by a probe
179     coef_probe=zeros(nb_probes, 1);
180
181
182     parfor p=1:nb_probes

```

```

171         probe=probes(p,:);
172         display(num2str(p))
173
174         % Distance computation
175         V0=bsxfun(@divide,[dist_comp_x(:,p),dist_comp_y(:,p),dist_comp_z(:,p)]*c
           ,Dist(:,p));
176
177         % Compute the probe position in the position array (for stream3 function)
178         ymin=find(vecx<probe(1),1,'last');
179         ymax=find(vecx>=probe(1),1);
180         sxi=(ymax-ymin)*(probe(1)-vecx(ymin))/(vecx(ymax)-vecx(ymin))+ymin;
181         ymin=find(vecy<probe(2),1,'last');
182         ymax=find(vecy>=probe(2),1);
183         syi=(ymax-ymin)*(probe(2)-vecy(ymin))/(vecy(ymax)-vecy(ymin))+ymin;
184         ymin=find(vecz<probe(3),1,'last');
185         ymax=find(vecz>=probe(3),1);
186         szi=(ymax-ymin)*(probe(3)-vecz(ymin))/(vecz(ymax)-vecz(ymin))+ymin;
187
188         %% For each microphone
189         for m=1:Nmic
190             % Set velocities
191             u = u0+V0(m,1);
192             v = v0+V0(m,2);
193             w = w0+V0(m,3);
194
195             % Compute trajectory from probe
196             traj=stream3_fast(vecx,vecy,vecz,u,v,w,sxi, syi, szi);
197
198             minimum=1e10;
199             tried=1;
200             while 0==0
201                 % Compute the distance between the trajectory and the microphone
202                 dist=sum(bsxfun(@minus,traj,mic(m,:)).^2,2); %#ok<*PFBNS>
203
204                 % Find the closest point to microphone
205                 [minimum,id_min]=min(dist);
206
207                 if id_min<2
208                     id_min=2;
209                     minimum=dist(id_min);
210                 end
211                 if id_min>size(traj,1)
212                     id_min=size(traj,1);
213                     minimum=dist(id_min);
214                 end
215
216                 % For the trajectory point find the corresponding velocity
217                 % Compute the difference between velocity grid and the trajectory
                % positions
218                 % Then find the the closest point for each trajectory point
219                 [~,idx]=min(abs(bsxfun(@minus,traj(1:id_min-1,1),vecx)),[],2);

```

```

220     [~, idy]=min(abs(bsxfun(@minus, traj(1:id_min-1,2), vecy)), [], 2);
221     [~, idz]=min(abs(bsxfun(@minus, traj(1:id_min-1,3), vecz)), [], 2);
222     indice = 1 + (idy-1)*k(1) + (idx-1)*k(2) + (idz-1)*k(3);
223     vel=sqrt(u(indice).^2+v(indice).^2+w(indice).^2);
224
225     % Compute the equivalent distance probe to microphone for each
           sections
226     probe2mic_xyz=sqrt(sum(bsxfun(@minus, traj(2:id_min,:), traj(1:
           id_min-1,:)).^2, 2));
227
228     % Total trajectory length
229     probe2mic(p,m)=sum(probe2mic_xyz);
230
231     % Compute the mean velocity on the trajectory
232     c_traj = sum(bsxfun(@times, probe2mic_xyz, vel))/probe2mic(p,m);
233
234     if minimum<tolerance || tried>max_try
235         break
236     end
237
238     % Offset from microphone
239     offset=traj(id_min,:)-mic(m,:);
240     % New velocities taking into account flowfield
241     V0(m,:)=V0(m,:)-offset*c_traj/(probe2mic(p,m)*Vconv);
242     % Normalize velocity to c
243     V0(m,:)=V0(m,:)*c/sqrt(sum(V0(m,:).^2));
244
245     % Set velocities
246     u = u0+V0(m,1);
247     v = v0+V0(m,2);
248     w = w0+V0(m,3);
249
250     traj=stream3_fast(vecx, vecy, vecz, u, v, w, sxi, syi, szi);
251     tried=tried+1;
252 end
253
254 if find( (traj(:,1)<0 | traj(:,1)>L | traj(:,3)<-0.1*L | traj(:,3)
           >0.1*L) & traj(:,2)<0 )
255     % This trajectory is impossible, put a non coherent value
256     probe2mic(p,m)=rand*999999;
257 else
258     % Take into account the velocity effect
259     probe2mic(p,m)=probe2mic(p,m)*c/c_traj;
260     % Add 1 to the probe coefficient
261     coef_probe(p)=coef_probe(p)+1;
262 end
263
264 % Maximum error
265 max_error=max(max_error, minimum);
266 mean_error=mean_error+minimum;
267

```

```

268         if p==1
269             % Save trajectory
270             parsave(traj(1:id_min,:),m)
271             % Figure with velocities
272             figure(3)
273             plot(traj(1:id_min-1,2),vel)
274             hold on
275         end
276     end
277 end
278
279 display(strcat('Maximum trajectory to microphone error of ',num2str(max_error,
280             '%.3f'),'.'));
281 display(strcat('Mean trajectory to microphone error of ',num2str(mean_error/(
282             nb_probes*Nmic),'%.3f'),'.'));
283
284 % Figure with velocities
285 figure(3)
286 % Set eps options
287 screensize = get(0,'ScreenSize');
288 sz=[400 500];
289 xpos = ceil((screensize(3)-sz(2))/2);
290 ypos = ceil((screensize(4)-sz(1))/2);
291 set(gcf,'Position',[xpos ypos sz(2) sz(1)]);
292 xlim(gca,[-0.51 2.0]);
293 xlabel(gca,'Z (m)','FontSize',18,'FontWeight','bold');
294 ylabel(gca,'Wave Velocity (m/s)','FontSize',18,'FontWeight','bold');
295 set(gca,'FontSize',16,'FontWeight','bold','FontName','Arial');
296 grid(gca,'on');
297 set(gcf,'color',[1 1 1]);
298 figure(2)
299
300 for m=1:Nmic
301     % Load trajectory set 1
302     traj=load(strcat('tmp_',num2str(m,'%03d'),'*.dat'));
303     % Plot trajectory to verify shape
304     plot3(traj(:,1),traj(:,2),traj(:,3),'-k');
305 end
306 delete('tmp*.dat');
307 end
308 coef_probe=coef_probe/max(coef_probe);
309 coef_probe(coef_probe==0)=99999;
310 coef_probe(coef_probe<99999)=1;
311 end
312
313 function parsave(traj,m) %#ok<*INUSL>
314 save(strcat('tmp_',num2str(m,'%03d'),'*.dat'),'traj','-ascii');
315 end

```

### LISTING : compute\_fft.m

```

1 function [ fft_data , freq ] = compute_fft(ym,f_samp , windowing)
2

```

```

3   % Size of signal
4   signal_len=size(ym,2);
5   NFFT = 2^nextpow2(signal_len);
6   % Frequency range
7   freq = f_samp/2*linspace(0,1,NFFT/2+1);
8   % Window the signal
9   if windowing==1
10      window=hamming(signal_len)';
11      ym=bsxfun(@times,ym,window);
12  end
13
14  % Compute the FFT
15  fft_data = (2/signal_len)*fft(ym,NFFT,2);
16  fft_data = fft_data(:,1:NFFT/2+1);
17
18  figure
19  plot(freq,20*log10(abs(fft_data(1,:)))/2e-5)
20
21  end

```

#### LISTING : BF3D\_function.m

```

1  function [Power]=BF3D_function(Nmic, sound_speed, freq_min, freq_max, beamf, diagelim,
    N_sources, dist, nx, ny, nz, fft_signal, freq, txtout, coef_probe)
2
3  % This function implements the conventional beamformer algorithm,
4  % the Robust Adaptive beamforming and the MUSIC technique in the case of a
5  % 3D array of microphones.
6  % The program takes in input position and signal of a sensor array
7  % and gives as output the noise map on the scan volume.
8  % -----
9  % The notation used here is the one used by Simley in his thesis
10 % "Development of an Acoustic Array for Wind Turbine Aeroacoustic Noise
11 % Analysis" from which this script is derived. In particular, a short
12 % description of the three algorithms used here can be found in Chapter 2
13 % and a MATLAB code is also included in the Appendix A for reference.
14 % -----
15
16 if freq_max<freq_min
17     error('fmax must be larger than fmin');
18     return %#ok<*UNRCH>
19 % Extract frequency range from FFT
20 % If the width is null
21 elseif freq_min==freq_max
22     freq_min=freq_min-0.01;
23     freq_max=freq_max+0.01;
24 end
25 % Find the frequency range that correspond to fmin fmax
26 fid = find(freq > freq_min & freq < freq_max);
27 % Number of bins
28 nbin=length(fid);
29
30 % There is no bin, define the interval that contains fmin fmax

```

```

31 if nbin==0
32     % Difference between frequency and freq_min
33     difference=freq-freq_min;
34     % The first positive element is the max of the window
35     fid = find(difference >0,1);
36     fid=[fid-1,fid];
37     nbin=1;
38
39 % initialisation fft array
40     fft_data = zeros(Nmic,1);
41     if txtout==1
42         fprintf(1, '1 bin between %.2f and %.2f Hz\n',freq_min ,freq_max);
43     end
44
45 % Frequency window
46     frequency=[freq(fid(1)),freq(fid(2))];
47     coef1=(freq_min-frequency(1))/(frequency(2)-frequency(1));
48     coef2=(freq_max-frequency(1))/(frequency(2)-frequency(1));
49
50     for i = 1 : Nmic % cycle on the sensors
51         % FFT value at extremities
52         valfft=[fft_signal(i ,fid(1)),fft_signal(i ,fid(2))];
53         fftmin=valfft(1)+(valfft(2)-valfft(1))*coef1;
54         fftmax=valfft(1)+(valfft(2)-valfft(1))*coef2;
55         fft_data(i)=(fftmin+fftmax)*(freq_max-freq_min)*0.5;
56     end
57
58 % More than 1 element
59 else
60     % Take the two extremas for partial integration
61     fid=[fid(1)-1,fid ,fid(end)+1];
62     nbin=nbin+1;
63
64 % initialisation fft array
65     fft_data = zeros(Nmic,nbin);
66     fprintf(1, '%d bins between %.2f and %.2f Hz\n',nbin ,freq_min ,freq_max);
67
68     for f=1:nbin % Cycle on bins
69
70         % Frequency window
71         frequency=[freq(fid(f)),freq(fid(f+1))];
72         if f==1
73             coef=(freq_min-frequency(1))/(frequency(2)-frequency(1));
74         elseif f==nbin
75             coef=(freq_max-frequency(1))/(frequency(2)-frequency(1));
76         end
77
78         for i = 1 : Nmic % cycle on the sensors
79             % FFT value at extremities
80             valfft=[fft_signal(i ,fid(f)),fft_signal(i ,fid(f+1))];
81             % First bin, compute the interpolated value of fft at freq_min

```

```

82         if f==1
83             fftmin=valfft(1)+(valfft(2)-valfft(1))*coef;
84             fftmax=valfft(2);
85             fmin=freq_min;
86             fmax=frequency(2);
87         elseif f==nbin
88             fftmin=valfft(1);
89             fftmax=valfft(1)+(valfft(2)-valfft(1))*coef;
90             fmin=frequency(1);
91             fmax=freq_max;
92         else
93             fftmin=valfft(1);
94             fftmax=valfft(2);
95             fmin=frequency(1);
96             fmax=frequency(2);
97         end
98
99         fft_data(i,f)=(fftmin+fftmax)*(fmax-fmin)*0.5;
100     end
101 end
102 end
103
104 % diagonal elimination
105 if diagelim == 1 % remove diagonal
106     mask_array = ones(Nmic) - eye(Nmic);
107 else % keep diagonal
108     mask_array = ones(Nmic);
109 end
110
111 num_points=nx*ny*nz;
112
113 %-----
114 % Noise map computation
115 % (the Noise map shows the power detected P at each grid point)
116 %-----
117
118 % cross-spectral matrix Rk initialisation
119 Rk = zeros(Nmic,Nmic);
120 % Pk (def. power detected at the kth frequency bin) initialisation
121 Power_detected = zeros(nbin,num_points);
122
123 % initialisation of the steering vector
124 % (def. ek is a nsensors x 1 vector containing weights and phase delays
125 % information of the sensors for an assumed source location)
126 %ek = zeros(nsensors,1);
127
128 for f=1:nbin
129     if nbin>1
130         fprintf(1,'%d/%d\n',f,nbin);
131     end
132     % creation of the cross-spectral matrix Rk (S matrix in Schmidt paper)

```

```

133 % (def.  $R_k = Y_k * Y_k'$ , where ' is the hermitian transpose operator and  $Y_k$ 
134 % the  $n_{\text{sensors}} \times 1$  vector representing amplitude and phase at the frequency
135 %  $\omega_k$  of the signals detected at the sensors (def.  $Y_k =$  Fourier transform of
    ym);
136 % therefore  $R_k$  is a  $n_{\text{sensors}} \times n_{\text{sensors}}$  matrix)
137 angles(:,1) = fft_data(:,f)'; % phase of the fft
138  $R_k = R_k + \text{mask\_array} .* (\text{conj}(\text{angles}) * \text{conj}(\text{angles}'))$ ;
139
140 % Frequency we are looking for
141  $\omega_k = 2 * \text{pi} * \text{freq}(\text{fid}(f))$ ;
142  $\text{tmp} = i * \omega_k / \text{sound\_speed}$ ;
143
144 % computation of the steering vector of each sensor  $e_k$ 
145  $e_k = \exp(\text{tmp} * \text{dist})$ ;
146
147 % power detected at the  $k$ th frequency bin computation
148 if (beamf == 0) % conventional beamforming
149     %  $P_k$  computation – formula 2.2.0.10 of Simley thesis
150     %  $\text{Power\_detected}(f,:) = e_k' * R_k * e_k$ ;
151      $\text{Power\_detected}(f,:) = \text{sum}((e_k' * R_k) .* \text{conj}(e_k'), 2)$ ;
152 elseif (beamf == 1) % MUSIC
153     % for the computation of  $P_k$  in MUSIC the following matrix is used,
154     % instead of the normal  $R_k$  (see formula 2.4.3.4 of Simley thesis)
155      $[\text{EVCT}, \sim] = \text{eig}(R_k, 'nobalance')$ ;
156      $R_{k\_music} = \text{zeros}(N_{mic}, N_{mic})$ ;
157     for  $k1 = 1 : (N_{mic} - N_{sources})$ 
158          $R_{k\_music} = R_{k\_music} + \text{EVCT}(:, k1) * \text{EVCT}(:, k1)'$ ;
159     end
160     %  $P_k$  computation – formula 2.4.3.5 of Simley thesis
161      $\text{Power\_detected}(f,:) = 1 ./ \text{sum}((e_k' * R_{k\_music}) .* \text{conj}(e_k'), 2)$ ;
162 end
163 end
164 clear dist_mic1 dist_g
165
166 % correct for negative values encountered in diagonal elimination
167  $\text{Power\_detected}(\text{Power\_detected} < 1e-15) = 1e-15$ ;
168  $\text{Power\_detected}(\text{isinf}(\text{Power\_detected})) = 1e-15$ ;
169
170 %-----
171 % Group all frequencies
172 %-----
173
174 % power detected computation
175 if  $n_{bin} == 1$ 
176      $\text{Power} = \text{Power\_detected}' ./ \text{coef\_probe}$ ;
177 else
178      $\text{Power} = \text{sum}(\text{Power\_detected})' ./ \text{coef\_probe}$ ;
179 end
180 end

```

## C.2 Cavity Flow Model

The cavity flow model was written in Matlab and is a single function *standing\_waves\_modelling.m*. This function reads a file containing unsteady stream-wise velocity along a line chosen by the user. Then it computes a third order upwind advection of generated pressure waves, and outputs the result in the file *modelling.dat*, containing the total pressure field for each point and timestep. The theory and the results are described chapter 5 of the thesis.

### LISTING : *standing\_waves\_modelling.m*

```

1 % Simulation of waves traveling , upwind scheme
2 function [] = standing_waves_modelling_dynamic_downstreamvortexes ()
3 close all
4
5 % Conditions
6 Minf=0.85; % Mach Number
7 L=1.0; % Cavity length
8 gamma=1.4;
9 Rs=287;
10 T=305.06;
11 c=sqrt(gamma*Rs*T); % Sound Speed
12 Uinf=Minf*c; % Free-stream Velocity
13
14 % Computation parameter
15 dt=0.000001; % Timestep
16 dx=0.005; % Grid spacing
17 minimum_signal_amplitude=0.05; % Signal amplitude to kill
18 reflexivity=0.93; % Reflectivity at walls (Rw.At)
19 % End time
20 tf=2.0; % Output signal length
21 % Flow axial velocity
22 % Upstream velocity stored in file (non dimensional)
23 % 1 2 3 ... N
24 % time (s) velocity(x1) velocity(x1) ... velocity(xn)
25 velocity_file_upstream{1}='velocity_x_085_M219nodoor_000_unsteady_max.dat';
26 % Downstream velocity vortexes_speed*Uinf
27 vortexes_speed=0.69;
28 % Coeficient to scale result (Pa)
29 coef_output=3920;
30
31 % Input signal
32 freq=1.0:1:3000; % Frequency to include in input signal
33 % FFT parameter
34 nowindows=1;
35 poverlap=50;
36 % Position of probe to save
37 probe_x=[0:0.05:1.0]*L;

```

```

38 % Time between each written timestep
39 dt_output=1.7e-4;
40 % Initialisation time to not to take into account in output (s)
41 transit_time=0.0;
42 % Timestep for fft input
43 dt_fft=dt_output;
44 % Signals to plot = 1 : total signal; 2: layer signals; 3: all; 0:none
45 plot_signal=3;
46 % Plot signal every steps
47 plot_every=200;
48 % 1 : Mean velocity, 0 : unsteady velocity
49 use_mean_vel=0;
50 % 1 : standing waves in a tube, 0 : Cavity flow driven by flowfield
51 use_zero_vel=0;
52 % Save Plots
53 save_plot=1;
54 % Output file name
55 output='unsteady';
56
57 %% Program
58 % Computational domain
59 % Point to script folder
60 addpath('/home/cfd/gloupy/PROJECT/utilities/postprocessing_scripts');
61
62 x=0:dx:L;
63 npoint=length(x);
64 lambda=dt/dx;
65
66 % Number of reflections
67 nb_reflexions=ceil(log(minimum_signal_amplitude)/log(reflexivity));
68
69 % Find the probe position
70 [~,probe_pos]=min(abs(bsxfun(@minus,x,probe_x)).[],2);
71 n_positions=numel(probe_pos);
72 grid_out=x(probe_pos)';
73
74 % Time
75 timestep=0:dt:tf;
76 n_steps=length(timestep);
77
78 % The output will be written every
79 step_output=floor(dt_output/dt);
80 timestep_out=[timestep(1:step_output:n_steps),0];
81 nb_step_output=numel(timestep_out)-1;
82
83 % Output image
84 if save_plot==1
85     % Set eps options
86     sz=[600,300];
87     screensize = get(0,'ScreenSize');
88     xpos = ceil((screensize(3)-sz(1))/2);

```

```

89     ypos = ceil((screensize(4)-sz(2))/2);
90     pngfig = hgexport('factorystyle');
91     pngfig.Format = 'png';
92     pngfig.Resolution = 300;
93     mkdir('signal-plot');
94 end
95
96 % Input noise
97 noise=zeros(1,n_steps);
98 for f=freq
99     noise=noise+(freq(end)-f)*sin(2*pi*timestep*f+rand()*2*pi)/freq(end);
100 end
101 noise=noise'/max(abs(noise));
102 window = n_steps / (floor(1+((nowindows-1)*(1-(poverlap/100)))));
103 overlap = floor(window*(poverlap/100));
104 [pxx,f] = pwelch(noise-mean(noise),window,overlap,[],1/dt);
105
106 % Plot single-sided amplitude spectrum.
107 figure(10)
108 plot(f,pxx)
109 xlim(gca,[0,250])
110 title('Single-Sided Amplitude Spectrum of y(t)')
111 xlabel('Frequency (Hz)')
112 ylabel('|Y(f)|')
113
114 % Number of advections
115 nb_adv=nb_reflexions+1;
116 % Initialise the solution p(x,t)
117 pres=zeros(npoint*nb_adv,1);
118 figure(1)
119
120 % Load upstream velocity
121 file=velocity_file_upstream{1};
122 velocity_mean=load(file);
123 velocity_mean(2:end,2:end)=velocity_mean(2:end,2:end)*Uinf;
124 % Velocities
125 % Axial positions
126 x0=velocity_mean(2:end,1)*L;
127 % Interpolate on x
128 % Flip the result as the wave begin by the end
129 vq = interp1(x0,velocity_mean(2:end,2:end),x,'spline');
130 c_back=flipud(c-vq);
131
132 % Make downstream velocity
133 c_ford=ones(size(c_back))*vortexes_speed*Uinf;
134
135 % Use time averaged velocity
136 if use_mean_vel==1
137     c_back=bsxfun(@times,ones(size(c_back)),mean(c_back,2));
138 end
139 % Use no velocity

```

```

140 if use_zero_vel==1
141     c_back=ones(size(c_back))*c;
142     c_ford=ones(size(c_ford))*c;
143 end
144
145 % Time of each velocity
146 time_velocity=velocity_mean(1,2:end);
147 clear velocity_mean
148 % Number of timestep before max(time_velocity)
149 num_timestep_velocity=numel(timestep(timestep<max(time_velocity)));
150 timestep2velocity=zeros(num_timestep_velocity,1);
151 for t=1:num_timestep_velocity
152     difference=abs(time_velocity-timestep(t));
153     [~, timestep2velocity(t)]=min(difference);
154 end
155
156 h=plot(bsxfun(@times,x',ones(size(c_ford(:,1:20:end))))),c_ford(:,1:20:end),'color'
        ,[0.7,0.7,0.7],'Linewidth',1);
157 hidelegend(h);
158 hold on
159 h=plot(bsxfun(@times,flipud(x'),ones(size(c_back(:,1:20:end))))),c_back(:,1:20:end),'
        color',[0.4,0.4,0.4],'Linewidth',1);
160 hidelegend(h);
161 hold on
162 plot(x,mean(c_ford,2),'-','color',[1.0,0.5,0.5],'Linewidth',2,'DisplayName','cw+
        steady');
163 hold on
164 plot(flipud(x'),mean(c_back,2),'-c','Linewidth',2,'DisplayName','cw- steady');
165 plot(x',ones(size(x,2),1)*c,'-','color',[0.7,0.7,0.7],'DisplayName','cw+ unsteady',
        'Linewidth',1);
166 hold on
167 plot(x',ones(size(x,2),1)*c,':','color',[0.4,0.4,0.4],'DisplayName','cw- unsteady',
        'Linewidth',1);
168 hold on
169 plot(x',ones(size(x,2),1)*c,'-','color',[0.0,0.0,0.0],'DisplayName','cw ideal',
        'Linewidth',1);
170 hold on
171
172 % Set eps options
173 sz=[400 800];
174 screensize = get(0,'ScreenSize');
175 xpos = ceil((screensize(3)-sz(2))/2);
176 ypos = ceil((screensize(4)-sz(1))/2);
177 epsfig = hgexport('factorystyle');
178 epsfig.Format = 'eps';
179 set(gcf, 'Position', [xpos ypos sz(2) sz(1)]);
180 xlim(gca,[0 L]);
181 xlabel(gca,'Distance from front lip (X/L)','FontSize',18,'FontWeight','bold');
182 ylabel(gca,'Wave Speed (m/s)','FontSize',18,'FontWeight','bold');
183 set(gca, 'FontSize', 16,'FontWeight','bold','FontName','Arial');
184 grid(gca,'on');

```

```

185 set(gcf, 'color', [1 1 1]);
186 % Legend
187 legend(gca, 'Location', 'eastoutside');
188
189 % Save velocity data for tecplot
190 data_tmp=[x', ones(size(x,2),1)*c.mean(c_ford,2), flipud(mean(c_back,2)), c_ford(:,1:20:
        end), zeros(size(x,2),1), flipud(c_back(:,1:20:end))];
191 save('velocities_pressure_waves.dat', 'data_tmp', '-ascii');
192 clear data_tmp;
193
194 % Pressure signal
195 pressure=zeros(nb_step_output,1+n_positions);
196 pressure(:,1)=timestep_out(1:end-1);
197
198 % Identify the direction
199 direction=(-1).^(1:nb_adv);
200 % Correct spatial positions
201 pres_order=(1:npoint*nb_adv)';
202 % Loop on advection vectors
203 for adv=1:nb_adv
204     % if wave traveling upstream
205     if direction(adv)==-1
206         pres_order((npoint*(adv-1)+1):(npoint*adv))=flipud(pres_order((npoint*(adv-1)
                +1):(npoint*adv)));
207     end
208 end
209 pres_order2d=reshape(pres_order, npoint, nb_adv);
210 pres_order_probes=pres_order2d(probe_pos, :);
211 pause(0.1);
212 disp('Starting simulation...');
213
214 % Advection points
215 p=3:npoint-1;
216 % Output step
217 out_step=1;
218
219 for step=1:n_steps
220     % Actual time
221     time=timestep(step);
222     % Back and ford velocity
223     ct=[c_ford(:, timestep2velocity(max(1, mod(step, num_timestep_velocity)))) , c_back(:,
            timestep2velocity(max(1, mod(step, num_timestep_velocity))))];
224     % Reflections
225     pres(npoint*(1:nb_adv-1)+1)=pres(npoint*(1:nb_adv-1))*reflexivity;
226     % First point
227     pres(1)=noise(step);
228
229     % Loop on advection vectors
230     for adv=1:nb_adv
231         % if wave traveling streamwise
232         if direction(adv)==1

```

```

233         c=ct(:,1);
234         % Traveling backward
235     else
236         c=ct(:,2);
237     end
238
239     % Store pressure
240     P=pres(npoint*(adv-1)+1:npoint*adv);
241     % Passage from t to t+1
242     % Order 3 upwind
243     pres(npoint*(adv-1)+2)=P(1);
244     p2=p+npoint*(adv-1);
245     pres(p2)=P(p)-lambda*c(p).*(2*P(p+1)+3*P(p)-6*P(p-1)+P(p-2))/6;
246     pres(npoint*adv)=pres(npoint*adv-1);
247 end
248
249 % Store the pressure
250 if timestep(step)==timestep_out(out_step)
251     pressure(out_step,2:end)=sum(pres(pres_order_probes),2)';
252     out_step=out_step+1;
253 end
254
255 % Plot the signal if needed
256 if mod(step,plot_every)==0
257     figure(2)
258     disp(num2str(time,'%2f'));
259
260     if plot_signal==1 || plot_signal==3
261         plot(x,sum(pres(pres_order2d),2),'-b','linewidth',3);
262     end
263     if plot_signal==3
264         hold on
265     end
266     if plot_signal==2 || plot_signal==3
267         for adv=1:nb_adv
268             plot(x,pres(pres_order2d(:,adv)),'-', 'linewidth',1.5);
269             hold on
270         end
271     end
272     if plot_signal>0
273         grid on
274         ylim(gca,[-2,2])
275         xlim(gca,[0,L])
276         set(gcf, 'Position', [xpos ypos sz(2) sz(1)]);
277         set(gca, 'FontSize', 16, 'FontWeight', 'bold', 'FontName', 'Arial');
278         xlabel(gca, 'Distance from front wall (X/L)', 'FontSize', 18, 'FontWeight', '
                bold');
279         ylabel(gca, 'Signal', 'FontSize', 18, 'FontWeight', 'bold');
280         set(gcf, 'color', [1 1 1]);
281         File=strcat('signal_plot/',output, '_', num2str(step, '%06d'), '.png');
282         hgexport(gcf, File, pngfig, 'Format', 'png');

```

```
283         end
284         hold off
285         pause(0.000001)
286     end
287 end
288
289 % Resampling
290 % Compute how many steps to withdraw
291 transit_steps=transit_time / dt_output+1;
292 dstep=round(dt_fft / dt_output);
293 pressure=pressure(transit_steps:dstep:end,:);
294 % Scale output
295 pressure(:,2:end)=pressure(:,2:end)*coef_output;
296 save('modelling.dat','pressure','-ascii');
297 % Save the grid
298 save('grid.dat','grid_out','-ascii');
299 dt_output=dt_output*dstep;
300 n_steps=length(pressure);
301 plot(pressure(:,1),pressure(:,2))
302
303 % PSD
304 figure(3)
305 window = n_steps / (floor(1+((nowindows-1)*(1-(poverlap/100)))));
306 overlap = floor(window*(poverlap/100));
307 [pxx, f] = pwelch(pressure(:,2)-mean(pressure(:,2)),window,overlap,[],1/dt_output);
308
309 % Plot single-sided amplitude spectrum.
310 plot(f,20*log10(pxx))
311 xlim(gca,[0,1200])
312 title('Single-Sided Amplitude Spectrum of y(t)')
313 xlabel('Frequency (Hz)')
314 ylabel('|Y(f)|')
315 end
```

# References

- [1] “GBU-12 drop test from F-35,” <http://upload.wikimedia.org/>, Last accessed 18<sup>th</sup> January 2015.
- [2] “GBU-32 Pitch down,” <http://skiesmag.com>, Last accessed 18<sup>th</sup> January 2015.
- [3] “Tupolev Tu-2 weapon bay,” <https://en.wikipedia.org/>, Last accessed 18<sup>th</sup> August 2017.
- [4] “Boeing B-52 weapon bay,” <https://www.pinterest.com/>, Last accessed 18<sup>th</sup> August 2017.
- [5] “Boeing B-52 weapon bay interior,” <http://blogspot.com/>, Last accessed 18<sup>th</sup> August 2017.
- [6] “General Dynamics F-111 weapon bay interior,” <http://www.f-111.net/>, Last accessed 18<sup>th</sup> August 2017.
- [7] “Rockwell B-1B weapon bay,” <https://www.pinterest.com/>, Last accessed 18<sup>th</sup> August 2017.
- [8] “Lockheed Martin F-22 weapon bay,” <http://www.f-16.net/>, Last accessed 18<sup>th</sup> August 2017.
- [9] “Boeing X-32 weapon bay,” <http://www.jsf.mil/>, Last accessed 18<sup>th</sup> August 2017.
- [10] “Boeing X-45 weapon bay,” <https://upload.wikimedia.org/>, Last accessed 18<sup>th</sup> August 2017.
- [11] “Lockheed Martin F-35 weapon bay,” <https://theaviationist.com/>, Last accessed 18<sup>th</sup> August 2017.
- [12] “Lockheed Martin F-35 weapon bay interior,” <http://www.sflorg.com/>, Last accessed 18<sup>th</sup> January 2015.
- [13] Rossiter, J. E., “Wind Tunnel Experiments on the Flow Over Rectangular Cavities at Subsonic and Transonic Speeds,” Technical Report 64037, Royal Aircraft Establishment, Bedford, UK, October 1964.

- [14] Schmit, R., Grove, J., Semmelmayr, F., and Haverkamp, M., “Nonlinear feedback mechanisms inside a rectangular cavity,” *AIAA Journal*, Vol. 52, No. 10, 2014, pp. 2127 – 2142, doi:10.2514/1.J052804.
- [15] Cenko, A., Deslandes, R., Dillenius, M., and Stanek, M., “Unsteady Weapon Bay Aerodynamics - Urban Legend or Flight Clearance Nightmare,” *Proceedings of the 46<sup>th</sup> AIAA Aerospace Sciences Meeting and Exhibit*, Reno, Nevada, USA, 7-10 January 2008, doi:10.2514/6.2008-189.
- [16] Davis, M., Yagle, P., Smith, B., Chankaya, K., and Johnson, R., “Store Trajectory Response to Unsteady Weapons Bay Flowfields,” *Proceedings of the 47<sup>th</sup> AIAA Aerospace Sciences Meeting*, Paper No. AIAA 2009-547, Orlando, FL, United States, 2009, doi:10.2514/6.2009-547.
- [17] Barakos, G., Lawson, S., Steijl, R., and Nayyar, P., “Numerical Simulations of High-Speed Turbulent Cavity Flows,” *Flow, Turbulence and Combustion*, Vol. 83, No. 4, December 2009, pp. 569–585, doi:10.1007/s10494-009-9207-1.
- [18] Plentovich, E., Stallings, Jr., R., and Tracy, M., “Experimental Cavity Pressure Measurements at Subsonic and Transonic Speeds,” Technical Paper 3358, NASA, 1993.
- [19] Chappell, P. and Gilbey, R. W., “Drag of a rectangular planform cavity in a flat plate with a turbulent boundary layer for Mach numbers up to 3. Part II: Open and transitional flows.” Tech. Rep. ESDU 00007, London, UK, February 2002.
- [20] H.E., P., J.S., G., and Lasstier, L., “A Theoretical and Experimental Investigation of the Acoustic Response of Cavities in an Aerodynamic Flow,” Technical Report WADD-TR-61-75, US Air Force, 1962.
- [21] Tam, C. and Block, P., “On the tones and pressure oscillations induced by flow over rectangular cavities,” *Journal of Fluid Mechanics*, Vol. 89, No. 2, 1978, pp. 373–399, doi:10.1017/S0022112078002657.
- [22] Heller, H., Holmes, D., and Covert, E., “Flow-Induced Pressure Oscillations In Shallow Cavities,” *Journal of Sound and Vibration*, Vol. 18, No. 4, 1971, pp. 545 – 553, doi:10.1016/0022-460X(71)90105-2.
- [23] Krishnamurty, K., “Acoustic Radiation From Two-Dimensional Rectangular Cutouts in Aerodynamic Surfaces,” Tech. Rep. Technical Note 3487, National Advisor Committee For Aeronautics, August 1955.
- [24] Heller, H. and Bliss, D., “Aerodynamically Induced Pressure Oscillations in Cavities – Physical Mechanisms and Suppression Concepts,” Technical Report AFFDL-TR-74-133, Air Force Flight Dynamics Laboratory, 1975.
- [25] Wagner, J., Casper, K., Beresh, S., Arunajatesan, S., Henfling, J., Spillers, R., and Pruett, B., “Relationship between acoustic tones and flow structure in transonic cavity flow,” *Proceedings of the 45th AIAA Fluid Dynamics*

- Conference, AIAA AVIATION Forum*, Paper No. AIAA 2015-2937, American Institute of Aeronautics and Astronautics Inc, Dallas, TX, United States, 2015, doi:10.2514/6.2015-2937.
- [26] Bilanin, A. and Covert, E., “Estimation of Possible Excitation Frequencies for Shallow Rectangular Cavities,” *AIAA Journal*, Vol. 11, No. 3, March 1973, pp. 347–351, doi:10.2514/3.6747.
- [27] Handa, T., Miyachi, H., Kakuno, H., Ozaki, T., and Maruyama, S., “Modeling of a feedback mechanism in supersonic deep-cavity flows,” *AIAA Journal*, Vol. 53, No. 2, 2015, pp. 420–425, doi:10.2514/1.J053184.
- [28] Alvarez, J., Kerschen, E., and Tumin, A., “A theoretical model for cavity acoustic resonances in subsonic flow,” *Proceedings of the 10th AIAACEAS Aeroacoustics Conference*, Paper No. AIAA 2004-2845, American Institute of Aeronautics and Astronautics Inc, Manchester, UK, 2004, doi:10.2514/6.2004-2845.
- [29] Kegerise, M., Spina, E., Garg, S., and Cattafesta, L., “Mode-Switching and Nonlinear Effects In Compressible Flow Over a Cavity,” *Physics of Fluids*, Vol. 16, No. 3, 2004, pp. 678–687, doi:10.1063/1.1643736.
- [30] Delprat, N., “Low-frequency components and modulation processes in compressible cavity flows,” *Journal of Sound Vibration*, Vol. 329, oct 2010, pp. 4797–4809, doi:10.1016/j.jsv.2010.05.013.
- [31] Murray, N. and Jansen, B., “Effect of door configuration on cavity flow modulation process,” *AIAA Journal*, Vol. 50, No. 12, 2012, pp. 2932 – 2937, doi:10.2514/6.2011-2773.
- [32] Nightingale, D., Ross, J., and Foster, G., “Cavity Unsteady pressure measurements - Examples from Wind-Tunnel Tests,” Tech. Rep. Version 3, Aerodynamics & Aeromechanics Systems Group, QinetiQ, Bedford, UK, November 2005.
- [33] Sheta, E., Harris, R., George, B., Ukeiley, L., and Luke, E., “Loads and Acoustics Prediction on Deployed Weapons Bay Doors,” *Journal of Vibration and Acoustics, Transactions of the ASME*, Vol. 139, No. 3, 2017, doi:10.1115/1.4035701.
- [34] Bacci, D., Saddington, A., and Bray, D., “Transient aerodynamics and aeroacoustics of complex-geometry weapon bays,” *Proceedings of the 50th 3AF International Conference on Applied Aerodynamics*, Paper No. FP08-2015-bacci, La Société Savante de l’Aéronautique et de l’Espace, Toulouse, France, 2015.
- [35] Blair, A. and Stallings, R., “Cavity door effects on aerodynamic loads of stores separating from cavities,” *Journal of Aircraft*, Vol. 26, No. 7, 1989, pp. 615 – 620, doi:10.2514/3.45811.

- [36] Kannepalli, C., Chartrand, C., Birkbeck, R., Sinha, N., and Murray, N., “Computational modeling of geometrically complex weapons bays,” *Proceedings of the 17th AIAA/CEAS Aeroacoustics Conference 2011*, Paper No. AIAA 2011-2774, American Institute of Aeronautics and Astronautics Inc, Portland, Oregon, United States, 2011, doi:10.2514/6.2011-2774.
- [37] Casper, K., Wagner, J., Beresh, S., Hening, J., Spillers, R., and Pruett, B., “Complex Geometry Effects on Cavity Resonance,” *AIAA Journal*, Vol. 54, No. 1, 2016, doi:10.2514/1.J054273.
- [38] Panickar, M., Murray, N., Jansen, B., Joachim, M., Birkbeckand, R., Kannepalli, C., and Sinha, N., “Reduction of noise generated by a half-open weapons bay,” *Journal of Aircraft*, Vol. 50, No. 3, 2013, pp. 716 – 724, doi:10.2514/1.C031747.
- [39] Probst, Z., Reeder, M., Johnson, R., and Grove, J., “Flight-Test Experiments on Cavity Flow in an SUU-41 Pod,” *Journal of Aircraft*, 2017, doi:10.2514/1.C034203.
- [40] Wagner, J., Casper, K., Beresh, S., Hunter, P., Spillers, R., Henfling, J., and Mayes, R., “Fluid-structure interactions in compressible cavity flows,” *Physics of Fluids*, Vol. 27, No. 6, 2015, doi:10.1063/1.4922021.
- [41] Wagner, J., Casper, K., Beresh, S., Hunter, P., Spillers, R., and Henfling, J., “Response of a store with tunable natural frequencies in compressible cavity flow,” *Journal of Aircraft*, Vol. 53, No. 4, 2016, pp. 2351–2360, doi:10.2514/1.J054688.
- [42] Casper, K., Wagner, J., Beresh, S., Spillers, R., and Henfling, J., “Study of Fluid-Structure Interactions on a Tunable Store in Complex Cavity Flow,” *Proceedings of the 47th AIAA Fluid Dynamics Conference*, Paper No. AIAA 2017-3125, American Institute of Aeronautics and Astronautics Inc, Denver, Colorado, United States, 2017, doi:10.2514/6.2017-3125.
- [43] Arunajatesan, S., Bharadwaj, M., Riley, W. C., and Ross, M., “One-Way Coupled Fluid Structure Simulations of Stores in Weapons Bays,” *Proceedings of the 51<sup>st</sup> AIAA Aerospace Sciences Meeting including the New Horizons Forum and Aerospace Exposition*, Grapevine, Texas, USA, 7-10 January 2013, doi:10.2514/6.2013-665.
- [44] Babu, S., Loupy, G., Dehaeze, F., Barakos, G., and Taylor, N., “Aeroelastic simulations of stores in weapon bays using Detached-Eddy Simulation,” *Journal of Fluids and Structures*, Vol. 66, October 2016, pp. 207–228, doi:10.2514/6.2017-3252.
- [45] Menter, F. and Egorov, Y., “The Scale-Adaptive Simulation Method for Unsteady Turbulent Flow Predictions. Part 1: Theory and Model Description,” *Flow, Turbulence and Combustion*, Vol. 85, No. 1, 2010, pp. 113–138, doi:10.1007/s10494-010-9264-5.

- [46] Atkins, D., "Flight Test Results of a GBU-38 Separating from the B-1B Aircraft," *Proceedings of the 46th AIAA Aerospace Sciences Meeting and Exhibit*, Paper No. AIAA 2008-184, American Institute of Aeronautics and Astronautics Inc, Reno, Nevada, United States, 7-10 January 2008, doi:10.2514/6.2008-184.
- [47] Lee, J. and Cenko, A., "Evaluation of the GBU-38 Store Separation from B-1 Aft Bay," *Proceedings of the 46th AIAA Aerospace Sciences Meeting and Exhibit*, Paper No. AIAA 2008-185, Reno, Nevada, USA, 7-10 January 2008, doi:10.2514/6.2008-185.
- [48] Sickles, W., Hand, T., Morgret, C., Masters, J., and Denny, A., "High-fidelity, time-accurate CFD store separation simulations from a B-1B bay with comparisons to quasi-steady engineering methods," *Proceedings of the 46th AIAA Aerospace Sciences Meeting and Exhibit*, Paper No. AIAA 2008-186, Reno, NV, United States, 7-10 January 2008, doi:10.2514/6.2008-186.
- [49] Spinetti, R. and Jolly, B., "Time-Accurate Numerical Simulation of GBU-38s Separating from the B-1B Aircraft with Various Ejector Forces, Store Properties, and Load-Out Configurations - IHAAA Store Separation Cavity (SSC) Project," *Proceedings of the 46th AIAA Aerospace Sciences Meeting and Exhibit*, Paper No. AIAA 2008-0187, Reno, NV, United States, 7-10 January 2008, doi:10.2514/6.2008-187.
- [50] Dix, R. and Bauer, R., "Experimental and Theoretical Study of Cavity Acoustics," Tech. Rep. AEDC-TR-99-4, Tennessee, United States, April 2000.
- [51] Cary, A. and Wesley, L., "Airframe Integration of Modern Stores (AIMS) Delivery Order 0031: Phase II and III Analytical Predictions and Validation Testing," Tech. Rep. AFRL-VA-WP-TR-2006-3079, Dayton, OH, United States, January 2006.
- [52] Murray, N., Jansen, B., Gui, L., Seiner, J., and Birkbeck, R., "Measurements of Store Separation Dynamics," *Proceedings of the 47th AIAA Aerospace Sciences Meeting including the New Horizons Forum and Aerospace Exposition*, Paper No. AIAA 2009-105, Orlando, Florida, USA, 5-8 January 2009, doi:10.2514/6.2009-105.
- [53] Flora, T., Reeder, M., Lofthouse, A., and Kraft, N., "Dynamic store release of ice models from a cavity into Mach 2.9 flow," *Journal of Aircraft*, Vol. 51, No. 6, 2014, pp. 1927-1941, doi:10.2514/1.C032459.
- [54] Merrick, J. and Reeder, M., "Sphere release from a rectangular cavity at Mach 2.22 freestream conditions," *Journal of Aircraft*, Vol. 53, No. 3, 2016, pp. 822-829, doi:10.2514/1.C033636.
- [55] Finney, L., *Investigation of Cavity Flow Effects on Store Separation Trajectories. Trident Scholar Project Report No. 388*, Ph.D. thesis, U.S. Naval Academy, May 2010.

- [56] Johnson, R., Davis, M., and Finley, D., "Relaxed Fidelity CFD Methods Applied to Store Separation Problems," *RTO-MP-AVT-108 - Proceedings of the RTO AVT Symposium on Functional and Mechanical Integration of Weapons and Land and Air Vehicles*, Paper No. 27, Williamsburg, VA, USA, 7–9 June 2004.
- [57] Smith, M. and Schwimley, S., "X-45A/Small Smart Bomb Separation Analysis," *Proceedings of the 44<sup>th</sup> AIAA Aerospace Sciences Meeting and Exhibit*, Paper No. AIAA 2006-827, Reno, Nevada, USA, 9-12 January 2006, doi:10.2514/6.2006-827.
- [58] Johnson, R. and Cary, A., "F-111 Store Trajectory Analysis," *RTO-MP-AVT-108 - Proceedings of the RTO AVT Symposium on Functional and Mechanical Integration of Weapons and Land and Air Vehicles*, Paper No. 28, Williamsburg, VA, USA, 7–9 June 2004.
- [59] Nayyar, P., Barakos, G. N., and Badcock, K. J., "Numerical study of transonic cavity flows using large-eddy and detached-eddy simulation," *The Aeronautical Journal*, Vol. 111, No. 1117, 2007, pp. 153164, doi:10.1017/S0001924000004413.
- [60] Lee, J., Piranian, A., Martel, J., Crowe, D., and Rizk, M., "Store Separations in Jet Flow Environments," *Proceedings of the 48<sup>th</sup> AIAA Aerospace Sciences Meeting*, Paper No. AIAA 2010-510, Orlando, Florida, USA, 4-7 January 2010, doi:10.2514/6.2010-510.
- [61] Crowe, D., Martel, J., Lee, J., and Rizk, M., "Numerical simulation of a GBU-12 emergency jettison from the F-35B (STOVL variant)," *Proceedings of the 28th AIAA Applied Aerodynamics Conference*, Paper No. AIAA 2010-4242, American Institute of Aeronautics and Astronautics Inc, 2010, doi:10.2514/6.2010-4242.
- [62] Kim, D., Choi, J., and Kwon, O., "Detached eddy simulation of weapons bay flows and store separation," *Computers and Fluids*, Vol. 121, August 2015, pp. 1–10, doi:10.1016/j.compfluid.2015.07.022.
- [63] Westmoreland, W. S., "Trajectory Variation Due to an Unsteady Flow-Field," *Proceedings of the 47<sup>th</sup> AIAA Aerospace Sciences Meeting*, Paper No. AIAA 2009-550, Orlando, FL, United States, 2009, doi:10.2514/6.2009-550.
- [64] Kraft, N. and Lofthouse, A., "Non-Repeatability of Store Separation Trajectories from Internal Weapon Bays Due to Unsteady Cavity Flow Effects - Lessons Learned from a 2D Investigation," *Proceedings of the 49<sup>th</sup> AIAA Aerospace Sciences Meeting including the New Horizons Forum and Aerospace Exposition*, Orlando, Florida, USA, 4-7 January 2011, doi:10.2514/6.2011-1238.
- [65] Yan, P. P., Zhang, Q. F., and Li, J., "Numerical Study of Strong Interplay Between Cavity and Store During Launching," *Journal of Mechanics*, 2017, pp. 1–10, doi:10.1017/jmech.2017.45.

- [66] Babu, S., Zografakis, G., Barakos, G. N., and Kusyumov, A., "Evaluation of scale-adaptive simulation for transonic cavity flows." *International Journal of Engineering Systems Modelling and Simulation*, Vol. 8, No. 2, 2016, pp. 106–124, doi:10.1504/IJESMS.2016.075510.
- [67] Cattafesta, L., Williams, D., Rowley, C., and Alvi, F., "Review of Active Control of Flow-Induced Cavity Resonance," *Proceedings of the 33rd AIAA Fluid Dynamics Conference, Orlando, FL, June 23–26*, Paper No. AIAA-2003-3567, American Institute of Aeronautics and Astronautics Inc, Orlando, FL, United States, 2003, doi:10.2514/6.2003-3567.
- [68] Rowley, C. and Williams, D., "Dynamics and Control of High Reynolds Number Flow Over Open Cavities," *Annual Review of Fluid Mechanics*, Vol. 38, 2006, pp. 251–276, doi:10.1146/annurev.fluid.38.050304.092057.
- [69] Zhang, X., Rona, A., and Edwards, J., "The Effect of Trailing Edge Geometry on Cavity Flow Oscillation Driven by a Supersonic Shear Layer," *The Aeronautical Journal*, Vol. 102, No. 1013, March 1998, pp. 129–136, doi:10.1017/S0001924000065416.
- [70] Das, S. and Cohen, J., "Effect of Rear Face Geometry on the Open Cavity Oscillatory Flow at  $M=0.9$ ," *Proceedings of the 8th AIAA Flow Control Conference*, Paper No. AIAA 2016-3175, American Institute of Aeronautics and Astronautics Inc, Washington, D.C., United States, 2016, doi:10.2514/6.2016-3175.
- [71] Shaw, L., Clark, R., and Talmadge, D., "F-111 Generic Weapons Bay Acoustic Environment," *Journal of Aircraft*, Vol. 25, No. 2, February 1988, pp. 147–153, doi:10.2514/3.45555.
- [72] Baysal, O., Yen, G.-W., and Fouladi, K., "Navier-Stokes Computations of Cavity Aeroacoustics with Suppression Devices," *Journal of Vibration and Acoustics*, Vol. 116, January 1994, pp. 105–112, doi:10.1115/1.2930385.
- [73] Lawson, S. and Barakos, G., "Assessment of Passive Flow Control Devices for Transonic Cavity Flows Using Detached Eddy Simulation," *Journal of Aircraft*, Vol. 46, No. 3, May/June 2009, pp. 1009–1029, doi:10.2514/1.39894.
- [74] Lawson, S. and Barakos, G., "Review of Numerical Simulations For High-Speed, Turbulent Cavity Flows," *Progress in Aerospace Sciences*, Vol. 47, No. 3, 2011, pp. 186 – 216, doi:10.1016/j.paerosci.2010.11.002.
- [75] Ross, J. and Peto, J., "The Effect of Cavity Shaping, Front Spoilers and Ceiling Bleed on Loads Acting on Stores, and on the Unsteady Environment Within Weapon Bays," Technical Report DERA/AS/HWA/CR97010/1, Royal Aircraft Establishment, March 1997.
- [76] Malhotra, A. and Vaidyanathan, A., "Aft Wall Offset Effect on Open Cavities in Confined Supersonic Flows," *Experimental Thermal and Fluid Science*, Vol. 74, 2016, pp. 411–428, doi:10.1016/j.expthermflusci.2015.12.015.

- [77] Roberts, D. A. and MacManus, D. G., “Passive Control of Transonic Cavity Aeroacoustics,” *Journal of Fluids Engineering*, Vol. 134, No. 11, 2012, doi:10.1115/1.4007593.
- [78] Saddington, A. J., Thangamani, V., and Knowles, K., “Comparison of Passive Flow Control Methods for a Cavity in Transonic Flow,” *Journal of Aircraft*, Vol. 53, No. 5, 2016, pp. 1439–1447, doi:10.2514/1.C033365.
- [79] Rossiter, J. and Kurn, A., “Wind Tunnel Measurements of the Unsteady Pressures In and Behind a Bomb Bay (T.S.R.2),” , No. AERO.2677, August 1963.
- [80] Ukeiley, L., Ponton, M., Seiner, J., and Jansen, B., “Suppression of Pressure Loads in Cavity Flows,” *AIAA Journal*, Vol. 42, No. 1, January 2004, pp. 70–79, doi:10.2514/1.9032.
- [81] Levasseur, V., Sagaut, P., Mallet, M., and Chalot, F., “Unstructured Large Eddy Simulation of the Passive Control of the Flow in a Weapon Bay,” *Journal of Fluids and Structures*, Vol. 24, 2008, pp. 1204–1215, doi:10.1016/j.jfluidstructs.2008.06.016.
- [82] Ashworth, R., *DES of a Cavity with Spoiler, Notes on Numerical Fluid Mechanics and Multidisciplinary Design – Advances in Hybrid RANS-LES Modelling: Second Symposium on Hybrid RANS-LES methods, Corfu, Greece, June, 2007.*, edited by S.-H. Peng and W. Hasse, Vol. 97, Springer, 2008, pp. 162–171, ISBN: 978-3-540-77813-4.
- [83] Duben’, A. P., Zhdanova, N. S., and Kozubskaya, T. K., “Numerical investigation of the deflector effect on the aerodynamic and acoustic characteristics of turbulent cavity flow,” *Fluid Dynamics*, Vol. 52, No. 4, Jul 2017, pp. 561–571, doi:10.1134/S001546281704010X.
- [84] Abdrashitov, R. G., Arkhireeva, E. Y., Dan’kov, B. N., Korotaev, V. S., Kosenko, A. P., Popov, O. Y., Strel’tsov, O. K., and Chuchkalov, I. B., “Numerical and experimental investigation of the means for reducing the aeroacoustic loads in an extended rectangular cavity at subsonic and transonic freestream velocities,” *Fluid Dynamics*, Vol. 52, No. 2, Mar 2017, pp. 239–252, doi:10.1134/S0015462817020089.
- [85] Luo, K., Zhe, W., Xiao, Z., and Fu, S., “Improved delayed detached-eddy simulations of sawtooth spoiler control before supersonic cavity,” *International Journal of Heat and Fluid Flow*, Vol. 63, 2017, pp. 172 – 189, doi:10.1016/j.ijheatfluidflow.2017.01.012.
- [86] Schmit, R., Schwartz, D., Kibens, V., Raman, G., and Ross, J., “High and Low Frequency Actuation Comparison for a Weapons Bay Cavity,” *Proceedings of the 43rd AIAA Aerospace Sciences Meeting and Exhibit*, Paper No. AIAA 2005-0795, American Institute of Aeronautics and Astronautics Inc, Reno, NV, United States, 2005, doi:10.2514/6.2005-0795.

- [87] Arunajatesan, S., Shipman, J., and Sinha, N., “Hybrid RANS-LES Simulation of Cavity Flow Fields with Control,” *Proceedings of the 40th AIAA Aerospace Sciences Meeting and Exhibit*, Paper No. AIAA 2002-1130, American Institute of Aeronautics and Astronautics Inc, Reno, NV, United States, 2002, doi:10.2514/6.2002-1130.
- [88] Smith, B., Welterlen, T., Maines, B., Shaw, L., Stanek, M., and Grove, L., “Weapons Bay Acoustic Suppression from Rod Spoilers,” *Proceedings of the 40th AIAA Aerospace Sciences Meeting and Exhibit, Reno, NV, USA, January 14–17*, Paper No. AIAA 2002-0662, American Institute of Aeronautics and Astronautics Inc, Reno, NV, United States, 2002, doi:10.2514/6.2002-0662.
- [89] Comte, P., Daude, F., and Mary, I., “Simulation of the reduction of unsteadiness in a passively controlled transonic cavity flow,” *Journal of Fluids and Structures*, Vol. 24, No. 8, 2008, pp. 1252 – 1261, doi:10.1016/j.jfluidstructs.2008.08.001.
- [90] Omer, A. and Mohany, A., “Suppression of Acoustic Resonance in Rectangular Cavities Using Spanwise Control Cylinder,” *Proceedings of the ASME Pressure Vessels and Piping Conference*, Paper No. PVP2015-45634, The American Society of Mechanical Engineers, Boston, Massachusetts, United States, 2015, doi:10.1115/PVP2015-45634.
- [91] Lawson, S. J., Steijl, R., Woodgate, M., and Barakos, G. N., “High performance computing for challenging problems in computational fluid dynamics,” *Progress in Aerospace Sciences*, Vol. 52, No. 1, 2012, pp. 19–29, doi: 10.1016/j.paerosci.2012.03.004.
- [92] Steijl, R. and Barakos, G. N., “Sliding mesh algorithm for CFD analysis of helicopter rotor-fuselage aerodynamics,” *International Journal for Numerical Methods in Fluids*, Vol. 58, No. 5, 2008, pp. 527–549, doi: 10.1002/d.1757.
- [93] Steijl, R., Barakos, G. N., and Badcock, K., “A framework for CFD analysis of helicopter rotors in hover and forward flight,” *International Journal for Numerical Methods in Fluids*, Vol. 51, No. 8, 2006, pp. 819–847, doi: 10.1002/d.1086.
- [94] Hirt, C. W., Amsten, A. A., and Cook, J. L., “An Arbitrary Lagrangian-Eulerian Computing Method for All Flow Speeds,” *Journal of Computational Physics*, Vol. 14, No. 3, 1974, pp. 227–253, doi: 10.1006/jcph.1997.5702.
- [95] Osher, S. and Chakravarthy, S., “Upwind Schemes and Boundary Conditions with Applications to Euler Equations in General Geometries,” *Journal of Computational Physics*, Vol. 50, No. 3, 1983, pp. 447–481, doi:10.1016/0021-9991(83)90106-7.
- [96] van Leer, B., “Towards the ultimate conservative difference scheme. V.A second-order sequel to Godunov’s Method,” *Journal of Computational Physics*, Vol. 32, No. 1, 1979, pp. 101–136, doi:10.1016/0021-9991(79)90145-1.

- [97] van Albada, G., van Leer, B., and Roberts, W., *A Comparative Study of Computational Methods in Cosmic Gas Dynamics, Upwind and High-Resolution Schemes*, edited by M. Y. Hussaini, B. van Leer, and J. Van Rosendale, Springer Berlin Heidelberg, Berlin, Heidelberg. Germany, 1997, pp. 95–103, doi:10.1007/978-3-642-60543-7\_6.
- [98] Axelsson, O., *Iterative Solution Methods*, Cambridge University Press, Cambridge, MA, United States, 1994, pp. 504–557, doi:10.1017/CBO9780511624100.
- [99] Godunov, S. K., “A Finite-Difference Method for the Numerical Computation of Discontinuous Solutions of the Equations of Fluid Dynamics,” *Matematicheskii Sbornik*, Vol. 47, No. 3, 1959, pp. 271–306.
- [100] van Leer, B., “Towards the Ultimate Conservative Difference Scheme. IV. A New Approach to Numerical Convection,” *Journal of Computational Physics*, Vol. 23, No. 1, 1977, pp. 276–299, doi: 10.1016/0021-9991(77)90095-X.
- [101] Mavriplis, D. J., “Revisiting the Least-Squares Procedure for Gradient Reconstruction on Unstructured Meshes,” *Proceedings of the 16th Computational Fluid Dynamics Conference*, Paper No. AIAA 2003-3986, Orlando, Florida, USA, 2003, pp. 1–13, doi:10.2514/6.2003-3986.
- [102] Lax, P. D., *Hyperbolic Systems of Conservation Laws and the Mathematical Theory of Shock Waves*, Philadelphia: SIAM Publications, 1973.
- [103] Reynolds, O., “On the dynamical theory of turbulent incompressible viscous fluids and the determination of the criterion,” *Phil. Trans. R. Soc. London*, Vol. A 186, 1894, pp. 123–161.
- [104] Pope, S. B., *Turbulent Flows*, Cambridge University Press, 2000.
- [105] Gatski, T. B. and Bonnet, J. P., *Compressibility, Turbulence and High Speed Flow*, Elsevier, Amsterdam, 2009.
- [106] White, F. M., *Viscous Fluid Flow*, McGraw Hill, New York, 1974.
- [107] Nayyar, P., *CFD Analysis of Transonic Turbulent Cavity Flows*, Ph.D. thesis, University of Glasgow, August 2005.
- [108] Spalart, P., Jou, W.-H., Strelets, M., and Allmaras, S., “Comments on the Feasibility of LES for Wings, and on a Hybrid RANS/LES Approach,” *Proceedings of the 1st AFOSR International Conference On DNS/LES, Columbus, OH, August 4-8, 1997*.
- [109] Smagorinsky, J., “General Circulation Experiments with the Primitive Equations,” *Monthly Weather Review*, Vol. 91, No. 3, March 1963, pp. 99–164.
- [110] Lawson, S. and Barakos, G., “Evaluation of DES for Weapons Bays in UCAVs,” *Aerospace Science and Technology*, Vol. 14, No. 6, 2010, pp. 397 – 414, doi:10.1016/j.ast.2010.04.006.

- [111] Wilcox, D., “Multiscale Model for Turbulent Flows,” *AIAA Journal*, Vol. 26, No. 11, 1988, pp. 1311–1320, doi: 10.2514/3.10042.
- [112] Menter, F., “Two–Equation Eddy–Viscosity Turbulence Models for Engineering Applications,” *AIAA Journal*, Vol. 32, No. 8, August 1994, pp. 1598–1605, doi: 10.2514/3.12149.
- [113] Wilcox, D., “Simulation of Transition with a Two-Equation Turbulence Model,” *AIAA journal*, Vol. 32, No. 2, 1994, pp. 247–255, doi: 10.2514/3.59994.
- [114] Menter, F., Kuntz, M., and Bender, R., “A Scale-Adaptive Simulation Model for Turbulent Flow Predictions,” *Proceedings of the 41<sup>st</sup> Aerospace Sciences Meeting and Exhibit*, Reno, Nevada, USA, 6-9 January 2003, doi:10.2514/6.2003-767.
- [115] Menter, F. and Egorov, Y., “Revisiting The Turbulent Length Scale Equation,” *Proceedings of the IUTAM Symposium: One Hundred Years of Boundary Layer Research*, Gottingen, 2004.
- [116] Menter, F. and Egorov, Y., “A Scale Adaptive Simulation Model using Two-Equation Models,” *Proceedings of the 43<sup>rd</sup> AIAA Aerospace Sciences Meeting and Exhibit*, San Diego, California, USA, 24-27 June 2005, doi:10.2514/6.2005-1095.
- [117] Egorov, Y., Menter, F., Lechner, R., and Cokljat, D., “The Scale-Adaptive Simulation Method for Unsteady Turbulent Flow Predictions. Part 2: Application to Complex Flows,” *Flow, Turbulence and Combustion*, Vol. 85, No. 1, 2010, pp. 139–165, doi:10.1007/s10494-010-9265-4.
- [118] Egorov, Y. and Menter, F., *Development and Application of SST-SAS Turbulence Model in the DESIDER Project, Advances in Hybrid RANS-LES Modelling: Papers contributed to the 2007 Symposium of Hybrid RANS-LES Methods, Corfu, Greece, 17-18 June 2007*, edited by S.-H. Peng and W. Haase, Springer Berlin Heidelberg, Berlin, Heidelberg, 2008, pp. 261–270, doi:10.1007/978-3-540-77815-8\_27.
- [119] Jarkowski, M., Woodgate, M., Barakos, G., and Rokicki, J., “Towards Consistent Hybrid Overset Mesh Methods for Rotorcraft CFD,” *International Journal for Numerical Methods in Fluids*, Vol. 74, No. 8, 2014, pp. 543–576, doi:10.1002/fld.3861.
- [120] Jimenez-Garcia, A. and Barakos, G. N., “CFD Analysis of Hover Performance of Rotors at Full-and Model-Scale Conditions,” *The Aeronautical Journal*, Vol. 120, No. 1231, 2016, pp. 1386–1424, doi: 10.1017/aer.2016.58.
- [121] Childers, D., *Modern Spectrum Analysis*, Chapter 2, pp. 23-148. IEEE Press, New York, 1978.

- [122] Larcheveque, L., Sagaut, P., and Comte, P., “Large-Eddy Simulation of a Compressible Flow in a Three-Dimensional Open Cavity at High Reynolds Number,” *Journal of Fluid Mechanics*, Vol. 516, 2004, pp. 265–301.
- [123] Pierce, A., *Acoustics: An Introduction to its Physical Principles and Applications*, Woodbury, New York: Acoustical Society of America, 1989.
- [124] Bussow, R., “An algorithm for the continuous Morlet wavelet transform,” *Mechanical Systems and Signal Processing*, Vol. 21, No. 8, 2007, pp. 2970–2979, doi:10.1016/j.ymssp.2007.06.001.
- [125] Cabral, B. and Leedom, L., “Imaging Vector Fields using Line Integral Convolution,” *Proceedings of the 20th annual conference on Computer graphics and interactive techniques, SIGGRAPH*, ACM, Anaheim, CA, United States, 1993, pp. 263–270.
- [126] Knowles, R., Finnis, M., Saddington, A., and Knowles, K., “Planar Visualization of Vortical Flows,” *Proceedings of the Institution of Mechanical Engineers, Part G: Journal of Aerospace Engineering*, Vol. 220, No. 6, 2006, pp. 619–627, doi:10.1243/09544100JAERO75.
- [127] Khanal, B., Knowles, K., and Saddington, A., “Computational Investigation of Cavity Flow Control Using a Passive Device,” *The Aeronautical Journal*, Vol. 116, No. 1176, 2012, pp. 153–174.
- [128] Khanal, B., Knowles, K., and Saddington, A., “Computational Study of Flowfield Characteristics In Cavities With Stores,” *The Aeronautical Journal*, Vol. 115, No. 1172, 2011, pp. 669–681.
- [129] Liu, Z., “Line Integral Convolution and Flow Visualisation Techniques,” [www.zhanpingliu.org/Research/FlowVis/LIC/LIC.htm](http://www.zhanpingliu.org/Research/FlowVis/LIC/LIC.htm), 2007, Last accessed: 10<sup>th</sup> August 2017.
- [130] Peng, S.-H., *M219 Cavity Flow, DESider A European Effort on Hybrid RANS-LES Modelling*, edited by W. Haase, M. Braza, and A. Revell, Vol. 103, Springer International Publishing, Berlin, Heidelberg, 2009, pp. 270–285, doi:10.1007/978-3-540-92773-0.
- [131] Lee, B., “Effect of Captive Stores on Internal Weapons Bay Floor Pressure Distributions,” *Journal of Aircraft*, Vol. 47, No. 2, March-April 2010, pp. 732–735, doi:10.2514/1.46684.
- [132] Allen, R., Mendona, F., and Kirkham, D., “RANS and DES turbulence model predictions of noise on the M219 cavity at M=0.85,” *International Journal of Aeroacoustics*, Vol. 4, No. 1, 2015, pp. 135–151, doi:10.1260/1475472053730039.
- [133] Temmerman, L., Tartinville, B., and Hirsch, C., *URANS Investigation of the Transonic M219 Cavity, Progress in Hybrid RANS-LES Modelling: Papers*

- Contributed to the 4th Symposium on Hybrid RANS-LES Methods, Beijing, China, September 2011*, edited by S. Fu, W. Haase, S.-H. Peng, and D. Schwamborn, Springer Berlin Heidelberg, Berlin, Heidelberg, 2012, pp. 471–481, doi:10.1007/978-3-642-31818-4\_41.
- [134] Ross, J. A., “PIV Measurements of the flowfields in an Aerodynamically Deep Cavity,” Tech. rep., Aerodynamics & Aeromechanics Systems Group, QinetiQ, Bedford, UK, October 2002.
- [135] Flaherty, W., Reedy, T., Elliott, G., Austin, J., Schmit, R., and Crafton, J., “Investigation of cavity flow using fast-response pressure-sensitive paint,” *AIAA Journal*, Vol. 52, No. 11, 2014, pp. 2462–2470, doi:10.2514/1.J052864.
- [136] Long, D., “Spatial structure of cavity pressure fluctuations at transonic speeds,” *AIAA Journal*, Vol. 44, No. 9, 2006, pp. 1983–1992, doi:10.2514/1.5236.
- [137] Schmidt, R. O., “MULTIPLE EMITTER LOCATION AND SIGNAL PARAMETER ESTIMATION.” *IEEE Transactions on Antennas and Propagation*, Vol. AP-34, No. 3, 1986, pp. 276–280.
- [138] Simley, E., *Development of an Acoustic Array for Wind Turbine Aeroacoustic Noise Analysis.*, Ph.D. thesis, University of Colorado, April 2010.
- [139] Prime, Z. and Doolan, C., “A comparison of popular beamforming arrays,” *Proceedings of the Annual Conference of the Australian Acoustical Society 2013*, Australian Acoustical Society, Victor Harbor, SA, Australia, 2013, pp. 151–157.
- [140] Ryan, J. G., “Criterion for the minimum source distance at which plane-wave beamforming can be applied,” *The Journal of the Acoustical Society of America*, Vol. 104, No. 1, 1998, pp. 595–598, doi:10.1121/1.423289.
- [141] Kegerise, M., Spina, E., and Cattafesta, L., “An experimental investigation of flow-induced cavity oscillations,” *Proceedings of the 30th Fluid Dynamics Conference*, Paper No. AIAA 99-3705, Norfolk, VA, United States, 1999, doi:10.2514/6.1999-3705.
- [142] Garg, S. and Cattafesta III, L., “Quantitative schlieren measurements of coherent structures in a cavity shear layer,” *Experiments in Fluids*, Vol. 30, No. 2, 2001, pp. 123–134, doi:10.1007/s003480000147.
- [143] Lurton, X., *An Introduction to Underwater Acoustics: Principles and Applications*, Praxis Publishing, 1st ed., 2002, p. 63.
- [144] Hirsch, C., *Numerical Computation of Internal and External Flows: The Fundamentals of Computational Fluid Dynamics*, Butterworth-Heinemann, 2nd ed., 1980, p. 197.
- [145] Loupy, G., Barakos, G., and Taylor, N., “Cavity Flow Over a Transonic Weapon Bay During Door Operation,” *Journal of Aircraft*, 2017, doi:10.2514/1.C03344.

- [146] Taylor, N., “Initial Aero and Structural Datapack (for use in accordance with GS31072009),” Tech. Rep. AERO/IRAD/11/M-034, MBDA UK Ltd., 2011.
- [147] *Real Eigenvalue Analysis, NX Nastran Basic Dynamic Analysis Users Guide*, Siemens Product Lifecycle Management Software Inc, 2008, pp. 3–1 – 3–18.
- [148] Ho, N., “Finding optimal rotation and translation between corresponding 3D points,” <http://nghiaho.com/>, Last accessed 9<sup>th</sup> November 2017.
- [149] Shepard, D., “A Two-dimensional Interpolation Function for Irregularly-spaced Data,” *Proceedings of the 1968 23rd ACM National Conference*, New York, NY, USA, 1968, pp. 517 – 524, doi:10.1145/800186.810616.
- [150] Biava, M. and Barakos, G. N., “Optimisation of Ducted Propellers for Hybrid Air Vehicles Using High-Fidelity CFD,” *The Aeronautical Journal*, Vol. 120, No. 1232, 2016, pp. 16321657, doi:10.1017/aer.2016.78.
- [151] R.J.Renka, “Multivariate Interpolation of Large Sets of Scattered Data,” *ACM Trans. Math. Softw.*, 1988, pp. 139 – 148, doi:10.1145/45054.45055.
- [152] Bonet, J. and Peraire, J., “An alternating digital tree (ADT) algorithm for 3D geometric searching and intersection problems,” *International Journal for Numerical Methods in Engineering*, Vol. 31, No. 1, 1991, pp. 1–17, doi:10.1002/nme.1620310102.
- [153] Siouris, G., *Missile Guidance and Control Systems*, Springer-Verlag New York Inc., 1st ed., 2008, pp. 15–51.
- [154] Fox, J., “Generic Wing Pylon, and Moving Finned Store. TN. 37389-6001,” Arnold Engineering Development Center (AEDC), Arnold AFB, USA, 2000.
- [155] Prewitt, N., Belk, D., and Maple, R., “Multiple-Body Trajectory Calculations Using the Beggar Code,” *Journal of Aircraft*, Vol. 36, No. 5, 1999, pp. 802–808, doi:10.2514/2.2513.
- [156] Demir, H. and Alemdaroglu, N., “Trajectory Calculation of a Store Released from a Fighter Aircraft,” *Proceedings of the 43<sup>rd</sup> AIAA Aerospace Sciences Meeting and Exhibit*, Paper No. AIAA 2005-847, San Diego, California, USA, 24-27 June 2005, doi:10.2514/6.2005-847.
- [157] Lijewski, L. and Suhs, N., “Time-Accurate Computational Fluid Dynamics Approach to Transonic Store Separation Trajectory Prediction,” *Journal of Aircraft*, Vol. 31, No. 4, 1994, pp. 886–891, doi:10.2514/3.46575.
- [158] Davis, M. and Welterlen, T., “Minimized Domain CFD for Store Separation,” *Proceedings of the 41<sup>st</sup> Aerospace Sciences Meeting and Exhibit*, Paper No. AIAA 2003-1245, Reno, Nevada, USA, 6-9 January 2003, doi:10.2514/6.2003-1245.

- [159] Yang, H., Kannan, R., and Przekwas, A., “A Nonlinear Reduced Order Method with Overset Adaptive Cartesian/Unstructured Grid for Moving Body Simulation,” *Proceedings of the 50<sup>st</sup> AIAA Aerospace Sciences Meeting*, Paper No. AIAA 2012-0414, Nashville, Tennessee, USA, 6-9 January 2012, doi:10.2514/6.2012-414.
- [160] Oktay, E., Merttopcuoglu, O., and Akay, H., “An Approach for Parallel CFD Solutions of Store Separation Problems,” *Parallel Computational Fluid Dynamics 2007*, Vol. 67 of *Lecture Notes in Computational Science and Engineering*, Springer Berlin Heidelberg, 2009, pp. 393–400, doi:10.1007/978-3-540-92744-0\_49.
- [161] Panagiotopoulos, E. and Kyparissis, S., “CFD Transonic Store Separation Trajectory Predictions with Comparison to Wind Tunnel Investigations,” *International Journal of Engineering*, Vol. 3, No. 6, January 2010, pp. 538 – 553.
- [162] Snyder, D., Koutsavdis, E., and Anttonen, J., “Transonic Store Separation Using Unstructured CFD with Dynamic Meshing,” *Proceedings of the 33<sup>rd</sup> AIAA Fluid Dynamics Conference and Exhibit*, Paper No. AIAA 2003-3919, Orlando, Florida, USA, 23-26 June 2003, doi:10.2514/6.2003-3919.
- [163] Hooker, J. and Gudenkauf, J., “Application of the Unstructured Chimera Method for Rapid Weapons Trajectory Simulations,” *Proceedings of the 45<sup>th</sup> AIAA Aerospace Sciences Meeting and Exhibit*, Paper No. AIAA 2007-75, Reno, Nevada, USA, 8-11 January 2007, doi:10.2514/6.2007-75.
- [164] Noack, R. and Boger, D., “Improvements to SUGGAR and DiRTlib for Overset Store Separation Simulations,” *Proceedings of the 47<sup>th</sup> AIAA Aerospace Sciences Meeting including The New Horizons Forum and Aerospace Exposition*, Paper No. AIAA 2009-340, Orlando, Florida, USA, 5-8 January 2009, doi:10.2514/6.2009-340.
- [165] Tang, L., Yang, J., and Lee, J., “Hybrid Cartesian Grid/Gridless Algorithm for Store Separation Prediction,” *Proceedings of the 48<sup>th</sup> AIAA Aerospace Sciences Meeting Including the New Horizons Forum and Aerospace Exposition*, Paper No. AIAA 2010-508, Orlando, Florida, USA, 4-7 January 2010, doi:10.2514/6.2010-508.
- [166] Tennekes, H. and Lumley, J., *A First Course in Turbulence*, MIT Press, 1972.
- [167] Laghari, W., Baloch, M., Mengal, M., and Shah, S., “Performance Analysis of Analog Butterworth Low Pass Filter as Compared to Chebyshev Type-I Filter, Chebyshev Type-II Filter and Elliptical Filter,” *Circuits and Systems*, Vol. 5, No. 9, 2014, pp. 209–216, doi:10.4236/cs.2014.59023.
- [168] Taylor, N., “Missile CFD Test Case (CFD\_OTC1),” Tech. Rep. AERO/IRAD/16/M-085, MBDA UK Ltd., 2016.

- 
- [169] Smirnov, P. E. and Menter, F. R., “Sensitization of the SST Turbulence Model to Rotation and Curvature by Applying the Spalart-Shur Correction Term,” *Journal of Turbomachinery*, Vol. 131, No. 4, 2009, pp. 041010–041010–8, doi:10.1115/1.3070573.
- [170] Hellsten, A., “New Advanced  $k - \omega$  Turbulence Model for High-Lift Aerodynamics,” *AIAA Journal*, Vol. 43, No. 9, 2005, pp. 1857–1869, doi:10.2514/1.13754.
- [171] Berkooz, G., Holmes, P., and Lumley, J., “The Proper Orthogonal Decomposition in the Analysis of Turbulent Flows,” *Annual Review of Fluid Mechanics*, Vol. 25, 1993, pp. 539–575.
- [172] Lumley, J., *Stochastic Tools in Turbulence, Volume 12*, Applied Mathematics and Mechanics, An International Series of Monographs, Academic Press, 1970.